Channeling and related effects in the motion of charged particles through crystals*

Donald S. Gemmell

Argonne National Laboratory, Argonne, Illinois 60439

The motion of energetic charged particles inside a monocrystalline solid can be strongly influenced by channeling and blocking effects. The present article reviews the theory, the experimental studies, and some of the applications of these effects. The coverage of the published literature extends through June 1973.

CONTENTS

Glossary of Symbols 129
1. Introduction 130
2. General Concepts 132
   2.1. The channeling effect 132
   2.2. The relationship between channeling and blocking 133
   2.3. Potentials 134
   2.4. Classical theory of channeling 135
      2.4a. Applicability of classical mechanics 135
      2.4b. The continuum model 136
      2.4c. Rules of angular and spatial averages 140
      2.4d. Calculations on the shapes of channeling dips 141
         2.4d1. Axial case 141
         2.4d2. Planar case 147
      2.4e. Depth dependence 149
         2.4e1. Surface oscillations 150
         2.4e2. Dechanneling 151
      2.4f. Distribution of particle flux 156
   2.5. Quantum mechanical considerations 158
   2 6. Energy losses 160
      2.6a. Basic considerations 160
      2.6b. Influence of channeling 162
3. Experimental Considerations 165
   3.1. Apparatus 165
   3.2. Monocrystalline targets 166
4. Channeling with Heavy ($M_1 > m_e$) Positive Projectiles 167
   4.1. Surface effects 167
   4.2. Bulk effects 168
      4.2a. Rutherford scattering 168
      4.2b. Blocking 176
      4.2c. Nuclear reactions 178
      4.2d. Characteristic x-ray production 179
      4.2e. Ranges 181
      4.2f. Radiation damage 181
      4.2g. Response of scintillating crystals 183
   4.3. Transmission effects 183
      4.3a. Star patterns 184
      4.3b. Anomalous energy losses 185
      4.3c. Detailed measurements of trajectories and potentials 189
      4.3d. Measurements with super-collimated beams 192
      4 3e. Hyperchanneling 193
      4.3f. Charge states of transmitted ions 194
      4.3g. Light emission from channeled ions 195
      4.3h. Breakup of molecular ions 195
   4.4. Channeling in nonsimple crystals 195
5. Channeling with Electrons and Positrons 198
6. Applications 205
   6.1. Ion implantation 206
   6.2. Location of dopant and impurity atoms 206
   6.3. Studies of lattice disorder 207
   6.4. Studies of surfaces and epitaxial layers 209
   6.5. Crystallography 210
   6.6. Measurement of nuclear lifetimes 210
   6.7. Production of polarized beams 213
   6.8 Particle detectors 214
Appendix A. Useful Data for Quick Estimates of Channeling Properties 214
Appendix B. Guide to Channeling Measurements performed on Various Target Materials 216
References 219

* Work performed under the auspices of the U.S. Atomic Energy Commission.

GLOSSARY OF SYMBOLS

The following list contains the symbols most frequently used in this article. An effort has been made to employ a consistent set of symbols throughout.

a	Thomas–Fermi screening radius; Eq. (2.3)
a_0	Bohr radius, $\hbar^2/(m_e e^2) = 0.529$ Å
b	Impact parameter in an atomic collision
c	Velocity of light
d	Distance between atoms in a row
d_p	Interplanar distance
e	Electronic charge; $e^2 = 14.4$ eV - Å
$f_{ch}(x)$	Channeled fraction at depth x
f_{RS}, f_{RV}, f_{PS}, f_{PV}	See Eqs. (2.17), (2.24)
$g(E_\perp, x)$	Distribution in transverse energy at depth x
$2\pi\hbar$	Planck's constant
k	Relativistic correction; Eq. (2.45)
m_e	Electron rest mass
n	Number of atoms per unit area in a plane
n_e	Number of electrons per unit volume
$\mathbf{r}$	Position measured in the plane normal to an axis
t	Target thickness parallel to beam direction
u_1	Rms thermal vibration amplitude in one direction; Eq. (2.44)
u_2	Rms thermal vibration amplitude in two directions; Eq. (2.51)
v	Incident particle velocity
v_0	Bohr velocity, $e^2/\hbar = 2.2 \times 10^8$ cm/sec
v_F	Fermi velocity for an electron gas $(3\pi^2 n_e)^{1/3}\hbar/m_e = 3.6 n_e^{1/3} \times 10^8$ cm/sec, where n_e is in units of $(\text{Å})^{-3}$
x	Depth in target measured parallel to beam direction
$x_{1/2}$	Half-thickness for dechanneling; Eq. (2.111)
z	Distance measured normal to planes; see Fig. 21
$A(E_\perp)$	Area accessible to particles with transverse energy $E_\perp$; Eqs. (2.91), (2.117)
C	Lindhard's constant; $C \approx \sqrt{3}$
D	Diffusion constant; Eq. (2.108)
$D(E_\perp)$	Diffusion function; Eq. (2.98)
E	Incident particle energy
$E_\perp$	Energy" associated with transverse motion, i.e., "transverse energy"
E^*	Detected particle energy
F_{RS}, F_{RV}, F_{PS}, F_{PV}	See Eqs. (2.36) and (2.43)
I	Mean electronic excitation energy; Eq. (2.121)
K	Bloch constant; Eq. (2.122)
K_S	Ratio of energies in elastic scattering; Eq. (2.113)
L	Number of atomic layers contributing to surface peak; Eq. (2.70)

L_3 Contribution of surface amorphous layers to L; Eq. (2.73)
L_e, L_n Electronic and nuclear stopping numbers; Eqs. (2.83) and (2.87)
M_1, M_2 Rest masses of incident ion and target atom, respectively
N Number of atoms/unit volume
$P(x)$ Gaussian distribution of thermal displacements; Eq. (2.44)
P_{NE} Nuclear encounter probability; Eq. (2.65)
$P_{ms}(\varphi)$ Multiple-scattering distribution; Eq. (2.89)
$P_R(\rho)$ Gaussian distribution of radial thermal displacements; Eq. (2.51)
R_0 Classical collision diameter; Eq. (2.9)
S Subscript denoting "static"
T Temperature
U_{RS}, U_{RV}, U_{PS}, U_{PV} Lattice continuum potentials; Eqs. (2.30) and (2.31)
V Subscript denoting "vibrating" (thermally)
$V(r)$ Ion-atom potential; Eq (2.1)
V_{RS}, V_{RV}, V_{PS}, V_{PV} Continuum potentials for isolated rows and planes; Eqs. (2.14), (2.20), and (2.75)
X $\frac{1}{4}\lambda_{ch}$ for planar channeling; Fig. 21
$Y(\varepsilon^*)$ Normalized backscattering energy spectrum; Fig. 31
Z_1, Z_2 Atomic numbers of incident ion and target atom, respectively
$Z_1^* e$, $Z_2^* e$ Effective charges of incident ion and target atom, respectively
α_R Factor relating $\psi_{1/2}$ to ψ_1 for axial channeling; Eq. (2.38)
β $\beta = v/c$
γ $\gamma = (1-\beta^2)^{-1/2}$
ε Ratio of channeled to random energy loss; Eq. (2.136)
$\varepsilon_\perp$ Reduced transverse energy; Eq. (2.92)
ε^* Reduced energy detected in backscattering; Fig. 31
κ Bohr's Coulomb scattering parameter; Eq. (2.10)
λ_{ch} Classical wavelength of oscillation for channeled trajectory
$2\pi\lambda$ De Broglie wavelength of a particle
$\nu(b)$ Distribution of impact parameters
$\nu'(\alpha_{ab})$ Double alignment factor; Eq. (4.1)
ρ Distance of a particle from a row or plane
ρ_c Critical distance of closest approach to a row or plane
ρ_{min} Distance of closest approach to a row or plane
$\varphi(r/a)$ Atomic screening function; Eq. (2.1)
$\chi(x)$ Normalized yield for close-encounter process, Fig. 3
χ_3 Contribution to χ_{min} from surface impurity layers; Eq. (2.47)
$\chi_{max}(x)$ Maximum value of $\chi(x)$; Fig. 3
$\chi_{min}(x)$ Minimum value of $\chi(x)$; Fig. 3
$\chi'_{min}(\alpha_{ab})$ Minimum yield in double alignment; Eq. (4.1)
ψ_0 Angle of beam incidence relative to a channeling direction
$\psi_{1/2}(x)$ Half-angular width of channeling dip or peak; Fig. 3
ψ_1 Characteristic angle for axial channeling; Eq. (2.12)
ψ_2 Characteristic angle for axial channeling; Eq. (2.28)
ψ_a Characteristic angle for planar channeling; Eq. (2.23)
ψ_c Critical angle for channeling
ψ_e Exit angle relative to a channeling direction
ψ_H Critical angle for hyperchanneling; Eq. (4.21)
$\omega/2\pi$ Electronic orbital frequency
ω_p Plasma frequency of an electron gas; Eq. (2.132)
Δ Beam divergence (Δ^2 is variance of Gaussian distribution)
Φ Debye function; Fig. 116
Θ_D Debye temperature; Appendices A, B
$\Pi(E_\perp)$ Probability distribution for transverse energy; Eq. (2.52)
Ω Rms multiple scattering angle; Eq. (2.89)

1. INTRODUCTION

A great variety of physical phenomena can occur when an energetic beam of charged particles is incident upon a solid target, e.g., Rutherford scattering, energy-loss processes, secondary-electron emission, nuclear reactions, x-ray production. All of these processes have cross sections which depend on the impact parameters b involved in collisions with individual target atoms. If the target material is homogeneous and isotropic, the impact-parameter distribution $\nu(b) \approx 2\pi b$ is independent of the relative orientations of the beam direction and the target. Therefore, if surface effects can be ignored, the observed yields of interaction processes between beam and target are also orientation-independent.

When the target material is monocrystalline, the situation becomes quite different. The distribution of impact parameters and the yields of physical processes are found to be very strongly dependent on the relative orientations of beam and target. This effect is commonly called the "channeling" effect. It obviously is related to other orientation-dependent effects, such as particle diffraction, and these relationships will be discussed in detail later. From a simple classical standpoint, one may qualitatively

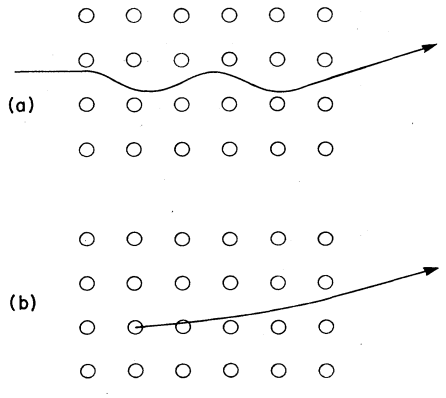

FIG. 1. Schematic illustration of (a) channeling and (b) blocking effects. The drawings are highly exaggerated. In reality, the oscillations of channeled trajectories occur with wavelengths typically several hundreds or thousands of lattice spacings.

understand the channeling effect as follows: If the direction of a charged particle incident upon the surface of a crystal lies close to a major crystal direction (i.e., close to a high-symmetry axis), the particle will with high probability suffer a small-angle scattering as it passes through the first plane of atoms in the crystal. The probability is also high (usually $>$ 90% for axial channeling) that this first deflection will be small enough so that the particle will suffer a similar small-angle scattering at the next atomic plane. Because of the ordered structure of the target, such a particle will undergo a correlated series of gentle small-angle collisions. Similar behavior can be expected for incidence parallel to atomic planes. This results in a steering effect which causes such particles to follow trajectories which (for positively charged particles) oscillate to and fro in the open "channels" between atomic rows or planes as shown schematically in Fig. 1a. Under these conditions, the yields of close-encounter processes are sharply reduced. (Strictly speaking, the incident beam particles need not be charged. The essential point is that the distance between relevant scattering events must be of the same order as lattice distances. Thus, neutrons interact too weakly, but interactions of atoms are strong enough.)

The possibility that such effects might exist was pointed out over 60 years ago by Stark [St12a, b]. His suggestions were not pursued at that time; possibly they were overshadowed by the prevailing interest in the new and powerful techniques then becoming available with x-ray diffraction. In any event, 50 years passed before channeling was actually discovered. In 1960, Rol *et al.* [Rol 60] published results showing that the sputtering ratio for ions bombarding a single crystal depends markedly on the crystal orientation. In the same year, Davies and co-workers [Dav60a, b] reported anomalously long ranges for heavy ions stopping in polycrystalline aluminum and tungsten. The measurements of Almén and Bruce [Alm 61] on the orientation dependence of the saturation value of collected ions and also of the sputtering yield for a Cu crystal bombarded with 45-keV Kr^+ ions, prompted Robinson [Ro 62] to comment on the likelihood and significance of the orientation dependence of ion penetration in crystals. In 1963 Robinson and Oen [Ro63a, b], performing computer calculations on the slowing down of 1–10-keV Cu atoms in various crystals, found abnormally large penetrations for those ions with initial velocities lying close to principal axial directions. These computations indicated that the long ranges observed by Davies and co-workers were attributable to ion channeling in the polycrystalline targets. This was soon confirmed by further experimental work with monocrystalline targets [Pie63, 64; Lu63].

These discoveries marked the beginning of a period in which interest in the channeling effect grew rapidly. Lehmann and Leibfried [Le63] made an analytic calculation of the trajectories of low-energy Cu ions channeled in a Cu crystal. Nelson and Thompson [Ne63] found that the penetration of 75-keV protons through thin crystals of Au was greatly enhanced along major crystal directions. They also observed sharp minima in the scattering of 50-keV H^+, He^+, Ne^+, and Xe^+ ions from a Cu crystal whenever the incident-beam direction coincided with low-index axes or planes of the target crystal. Dearnaley [De64] reported the observation of channeling effects at much higher velocities. He observed reduced energy losses for 2.1-MeV protons penetrating a 37-μm-thick Si crystal along low-index directions. Further channeling experiments with 3-MeV protons and 30-MeV ^3He ions were soon reported [Er64]. In 1964, the strong dependence of nuclear reaction yields on target-crystal orientation was observed for (p,γ) reactions in a Si crystal [Bø64] and for (p,n) reactions in a Cu crystal [Th64].

That the trajectories of particles with energies of several MeV can be so strongly influenced by potentials of the order of a few eV is a consequence of the collective nature of the channeling process. Nelson and Thompson [Ne63] showed that channeling could result from a series of glancing collisions with lattice atoms, and they derived an effective transverse potential governing the oscillatory trajectories of the particles. Lehmann and Leibfried [Le63], Lindhard [Li64a] and Erginsoy [Er65] developed the theory further, introducing the concept of an average or continuum potential and obtaining expressions for the intensities and angular widths of channeling anomalies. Much of the basic theory of the channeling process can be found in the treatment published by Lindhard in 1965 [Li65].

Channeled trajectories are those that lie close to a major crystal direction and which (for positive particles) originate in the open spaces between atomic rows or planes. In 1965, strongly anisotropic effects were discovered for positive-particle trajectories originating at lattice sites within a crystal. These effects were seen for α particles emitted from radioactive ^{222}Rn atoms substitutionally located in a W crystal [Do65a,b]. They were also seen in the wide-angle scattering or protons, deuterons, and α particles by Si and Ge crystals [Ge65], of protons by W crystals [Tu65a,b], and of protons originating in (d,p) reactions inside a Si crystal [Ge65]. These "blocking" effects, shown schematically in Fig. 1(b), are closely related to channeling effects. The relationship between the two, first delineated by Lindhard [Li65], will be discussed in more detail in Sec. 2.2.

During the comparatively short time that has elapsed since the first measurements on channeling, the experimental and theoretical work in this field proceeded at a rapidly increasing rate. Channeling and related effects have been studied with particle beams ranging from electrons and positrons to heavy ions and with energies ranging from a few keV to hundreds of MeV. In addition to the intrinsic interest apparent in the physics of the channeling process itself, several important applications have been found in such diverse areas as, for example, in the location of dopant atoms in semiconductors and in the measurement of short nuclear lifetimes.

The objective of this article is to survey and review the existing channeling theory, experiments, and applications, to acquaint the reader with the present status of the field, and to enable him to locate the published papers needed for further study. (The survey covers the literature through June 1973.) The attention of the reader is drawn to the existence of previous review articles (e.g., [Li65; Tu65c; Da67; Th68a]) and to the existence of the published proceedings of several conferences on channeling and related effects, especially Solid-State Physics Research with Accelerators, Brookhaven National Laboratory Report BNL-50083 (1968); "Atomic Collision and Penetration Studies," Can. J. Phys **46**, 449–782 (1968);

Atomic Collision Phenomena in Solids (North-Holland, Amsterdam, 1970); *Atomic Collision Phenoma in Solids* [(Gordon and Breach, London, 1972), also published in Radiation Effects **12** and **13** (1972, 1973)]; Interaction of Energetic Charged Particles with Solids, Brookhaven National Laboratory Report BNL-50336 (1973); Fifth International Conference on Atomic Collisions in Solids, Gatlinburg, Tennessee, September 24-28, 1973 (to be published).

Throughout the text, the reader may assume that, unless otherwise specified, the beam particles referred to are positively charged and have masses greater than or equal to that of the proton. This convention is adopted to avoid the necessity for repeatedly specifying the type of particle being considered. The channeling of negative and of light particles is, however, treated in several places (especially in Sec. 5). For the most part, monatomic cubic lattice structures are assumed, and a simplified notation for crystallographic axes and planes is employed. (More complex crystal structures are discussed in Sec. 4.4.) Furthermore, center-of-mass and relativistic effects are, for the most part, ignored; this leads to a simplification and a lack of clutter in many expressions. The manner in which such effects may be included is usually obvious.

2. GENERAL CONCEPTS

2.1. The channeling effect

Figure 2, a schematic diagram of a typical experimental arrangement for measurements on the channeling effect, serves to introduce some of the terms to be used throughout this review. A well-collimated beam of particles is incident upon a monocrystalline target mounted in a goniometer. The target is oriented so that there is a small angle ψ between some axial or planar direction in the crystal and the beam direction. Channeling measurements usually consist of determining either the ψ dependence of either the yield of close-encounter processes (e.g., with detector No. 1 in Fig. 2) or the distributions in space and/or momentum of the transmitted beam (in experiments with thin target crystals). In such measurements, the angle ψ is usually varied over a small range centered on $\psi = 0$.

In measurements on the yield of close-encounter processes, care must be taken to distinguish possible orientation-dependent effects on the outgoing detected radiation (e.g., blocking effects for emerging charged particles and diffraction effects for emerging x-rays). These effects,

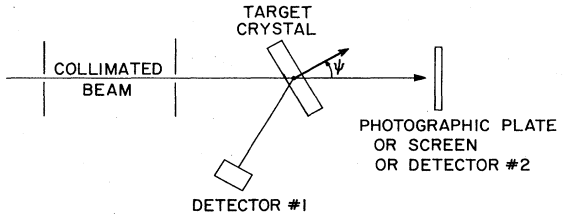

FIG. 2. Schematic arrangement for a typical channeling experiment. A tightly collimated beam is incident upon a monocrystalline target mounted in a goniometer with orients it so that a major crystal direction lies close to the beam direction. The angle ψ between these two directions is varied over a small range centered on $\psi = 0$ and the yield of close-encounter processes is measured (e.g., by detector #1) as a function of ψ. For thin targets, the transmitted beam can be examined with a photographic plate, a fluorescent screen or detector #2.

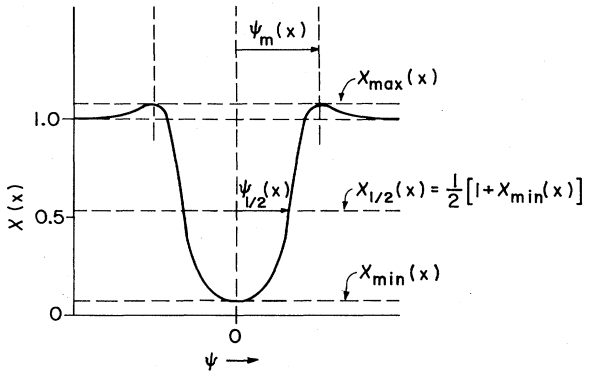

FIG. 3. The normalized depth-dependent yield of a close-encounter process, measured in a channeling experiment such as that depicted in Fig. 2.

which may be very strong, are usually avoided either by carefully placing the detector at a "random" direction (i.e., in an angular range containing no major crystal directions), by making the solid angle for the detector large enough that such effects will be averaged out, or by moving the detector with the target crystal so that the relative orientation of detector and target does not change.

The typical orientation dependence of the yield of a close-encounter process measured in a channeling experiment is illustrated in Fig. 3. The yield χ is normalized to random, i.e., the yield $\chi = 1$ is the yield that would be measured from a hypothetical amorphous target having otherwise the same characteristics as the one under investigation. (The nontrivial problem of determining the random yield experimentally is discussed in Sec. 3.) When $\psi = 0$, the channeled fraction of the incident beam is a maximum, and thus the yield of close-encounter processes is at its minimum value $\chi_{\min}$. As the crystal is tilted away from the beam, the channeled fraction decreases, and χ rises to a maximum value $\chi_{\max}$, which can be somewhat greater than unity. At still larger angular deviations, the yield approaches the random value. The quantities $\psi_{1/2}$ and ψ_m shown in Fig. 3 are defined to be the half-width at half-minimum and at the angle at which $\chi = \chi_{\max}$, respectively. The measured yield χ is dependent upon the depth x at which the close-encounter process occurs inside the target crystal. It follows that the angular width and the shape of the dip are also depth-dependent, as emphasized in Fig. 3 by writing the various yields and angles as functions of x. The depth dependence of χ is primarily a consequence of multiple scattering of the beam as it progresses through the crystal. In what follows, it may be assumed that if no depth is specified, then the values of the yields and of angular quantities such as those shown in Fig. 3 are surface values, i.e., values determined by extrapolation to zero depth.

Experimentally, one may measure the depth dependence of channeling parameters by varying the thickness of the target and in a variety of other ways. In Rutherford scattering measurements, for example, the energy loss of the emerging particle indicates the depth at which the close-encounter process (scattering) occurred; for x-ray production, the absorption in the target can give some depth information; for nuclear reactions, sharp

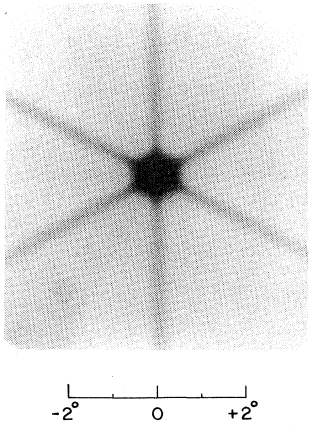

FIG. 4. Star pattern recorded in transmission (see Fig. 2) for 2.43-MeV protons incident along the ⟨111⟩ direction of a 60-μm-thick Ge crystal. The dark regions in the figure correspond to regions of high particle intensity. The range of 2.43-MeV protons in amorphous Ge is approximately 43 μm [Gor69].

resonances can be used to localize the depth from which the yield is observed.

Typically, values of $\psi_{1/2}$ lie in the range from a few hundredths of a degree to a few degrees. Values of χ_{min} typically range down to about 0.1 for planar channeling and to about 0.01 for axial channeling.

The trajectories of planar-channeled particles usually remain between two adjacent planes of atoms. In the axial case, however, the channeled trajectories can (and usually do) mount the small potential barrier between neighboring channels and wander from one axial channel to another. If special experimental precautions are taken, it is possible to establish trajectories that remain in one axial channel during passage through a crystal, in which case one refers to proper channeling or hyperchanneling (Sec. 4.3e).

If the target crystal is thin enough, the incident beam will be transmitted. For the transmitted particles, the energy and angle distributions are strongly dependent on several factors (to be discussed in detail in Secs. 4 and 5) but notably on the target thickness. For targets thin enough to transmit the beam but thick enough to cause significant multiple-scattering effects, the transmitted beam becomes concentrated along the major crystal planes and axes near the beam direction. Under these conditions, characteristic star patterns can be observed on a fluorescent screen or on a photographic plate located downstream from the target [Sc65]. An example is shown in Fig. 4. These patterns are useful aids in determining crystal orientations in channeling experiments. For very thin crystals, the patterns of transmitted particles are somewhat more complex; measurements on them give detailed information on channeled trajectories.

Since their paths do not closely approach the centers of atoms forming the channel walls, channeled ions sample only the regions of low electron density in the open channels. Thus, in the velocity range in which electronic stopping dominates the energy-loss process, the rate of energy loss for channeled ions is lower than that for nonchanneled ones (typically about half). For low-velocity ions, nuclear stopping also is strongly reduced by channeling.

2.2. The relationship between channeling and blocking

The blocking effect occurs for positively charged particles whose trajectories originate at lattice sites inside a crystal. From a practical standpoint, this implies either the emission of particles from nuclei in the crystal atoms or the large-angle Rutherford scattering of incident beam particles. Since the impact parameters involved in large-angle scattering are several orders of magnitude smaller than the zero-point thermal-vibration amplitudes for atoms in crystals, there usually is no practical difference between the two types of particle emission. A typical experimental arrangement for a blocking measurement is shown in Fig. 5. A beam of particles is incident upon a monocrystal in a random direction. A tightly collimated detector measures particles emerging at an angle ψ with respect to a high-symmetry crystal direction. The blocking measurement consists of determining the yield of emitted particles as a function of ψ as ψ is varied (usually by moving the detector) over a small range centered about $\psi = 0$.

Here, the function of the incident beam is merely to create particles that emerge from lattice sites. The incident beam does not need to be tightly collimated, nor need it consist of charged particles. Collimation becomes important when one wishes to define the recoil direction of compound nuclei formed in nuclear reactions induced by the incident beam, as in the nuclear lifetime measurements discussed in Sec. 6.6.

When the collimated detector is located on a major crystal direction ($\psi = 0$), the detected yield of emerging particles is a minimum; as ψ is increased, the detected yield rises. The result is a blocking dip similar in shape to the channeling dip shown in Fig. 3. The same considerations of normalization and of depth dependence apply to the blocking case.

Lindhard [Li65] pointed out that not only should blocking and channeling dips be similar, but under certain idealized conditions (e.g., when no slowing-down processes are involved) they should be identical when blocking and channeling measurements are compared for the same particles, energies, crystals, crystal directions, etc. The two processes are related by a rule of reversibility. In measuring a channeling dip, one determines the probability that a well-collimated incident beam will hit an atomic nucleus in the crystal. This probability is measured for various relative orientations of the incident beam and the crystal. Similarly the blocking measurement determines the probability that a particle emerging from an atomic nucleus in the crystal will hit a well-

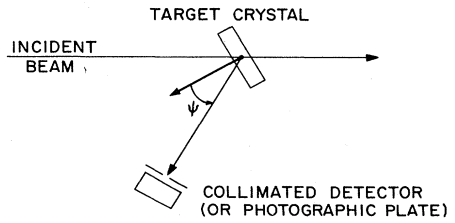

FIG. 5. Schematic arrangement for a typical blocking measurement. A beam of particles is incident upon a target crystal, usually in a random direction. Particles emitted from nuclear reactions or from wide-angle Rutherford scattering are counted in a collimated detector. The vector from the target to the detector makes an angle ψ with a major crystal direction. The detector is moved, and the yield of emerging particles is measured as ψ varies over a small range centered on $\psi = 0$. A photographic plate is also frequently used to record the blocking pattern.

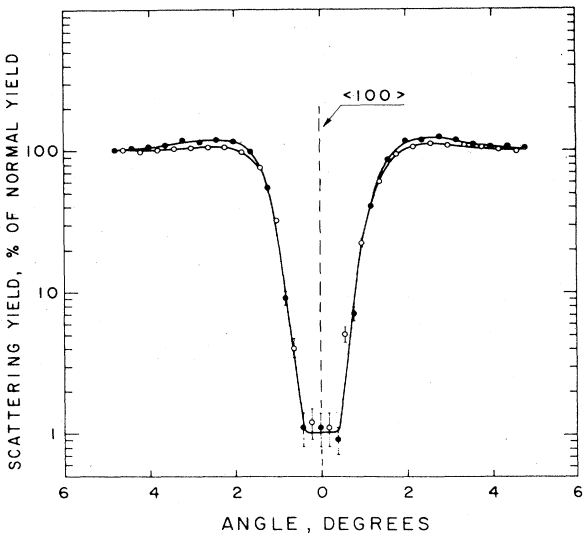

FIG. 6. Comparison of channeling and blocking yields for 1-MeV protons backscattered at 135° from a W crystal [Bø67b]. The thickness of the scattering zone is ~1000 Å. The depth of the scattering zone beneath the surface is ~3000 Å. Solid circles denote channeling results; open circles, blocking results. The small discrepancies in the shoulder regions of the curves are not considered significant. They are probably caused by very slight differences in experimental geometry for the two measurements.

collimated detector. This probability is measured for various relative orientations of the detector and the crystal. Clearly, in the absence of energy-loss processes, channeling and blocking trajectories are related to one another by time reversal. In a statistical-mechanical treatment [Li65], the probabilities for direct and inverse processes such as these can be shown to be the same. This is a special case of a general reciprocity relation based on Liouville's theorem. Analogous reciprocity theorems are well known in nuclear physics (e.g., [Bl52]) and in optics; e.g., if a source of radiation and a point of observation are interchanged, the intensity measured at the new place of observation is the same as at the old. The reversibility rule relating channeling and blocking has been verified experimentally by Bøgh and Whitton [Bø67b], whose result is shown in Fig. 6. (See also [An68; Scher69].)

By employing a photographic plate (Fig. 5) to detect particles emerging from the target, one can observe the blocking equivalent of a star pattern. In this case, the pattern is caused by an absence of detected particles along major crystal directions. (Examples are shown in Figs. 62, 73, and 112.)

In a double alignment geometry, the beam is incident along a channeling direction, and the emerging particles are detected along a blocking direction. In this arrangement, the sensitivity to particles emerging as a result of interactions between beam and crystal is minimized, and hence the sensitivity to interstitial atoms or to crystal defects is maximized. This geometry can therefore be used to advantage in studies of impurity atoms and of defects in crystals (Secs. 4.2a, 6.2, and 6.3).

2.3. Potentials

The potential describing the interaction in a collision between an ion (atomic number Z_1) and an isolated atom (atomic number Z_2) can generally be expected to be a rather complicated function of several parameters such as the nuclear separation distance r, the relative velocity v, the masses (M_1 and M_2) and atomic numbers of the collision partners, and the impact parameter b. In order to reduce the complexity of theoretical treatments of ion-atomic scattering, it is customary to make approximations that minimize the number of parameters upon which the assumed interaction potential depends. Thus, for example, it is usual to assume that a two-body potential function is adequate to describe the scattering. Furthermore, although the screening due to the electron clouds surrounding the ion and the atom contains dynamic features, any velocity dependence of the ion–atom potential is usually assumed to be negligibly small. A related assumption is that inelastic scattering can be neglected. The validity of these assumptions is frequently difficult to assess. Even at low ion velocities, where the electrons might be expected to adjust adiabatically to the motion of the nuclei to which they are bound, nonadiabatic effects, e.g., those brought about by level-crossing mechanisms, are known to result in significant internal electronic rearrangements in the collision partners (see, e.g., [Bar72]). It is generally assumed that the influence of such complex processes on channeled trajectories is small since channeling involves only relatively gentle small-angle collisions.

If the velocity dependence of the ion-atom field may be neglected, the interaction can be described with a static potential similar to that applying to the case of diatomic molecules. This, of course, is still a complex problem to treat theoretically because it requires a precise calculation of the electronic wave functions as functions of the nuclear separation distance. Such calculations (like static Hartree calculations of the ground state energy of a diatomic molecule) are complicated, require extensive machine computation and, in any case, only provide an interaction potential for one specific pair of collision partners. (The potential derived in this manner does, however, embody features such as electronic shell effects.) In order to further simplify the static ion-atom potential, a statistical (Thomas–Fermi) model can be employed. One can then write the interaction potential as

$$V(r) = (Z_1 Z_2 e^2/r)\varphi(r/a), \tag{2.1}$$

where $\varphi(r/a)$ is a screening function of Thomas–Fermi type and a is a screening length characteristic of any two given collision partners. For a discussion of the approximations involved in writing the potential in the form given in Eq. (2.1), the reader is referred to an article by Lindhard, Nielsen, and Scharff [Li68] and to references contained therein. Two very significant features of Eq. (2.1) are, firstly, that for a given ion–atom pair the potential is a function only of the nuclear separation distance and, secondly, that the simplified form of the screening function implies similarity properties for all combinations of ion–atom pairs.

The Thomas–Fermi screening function cannot, of course, exhibit such detailed features as shell structure, but otherwise it does approximate the results of Hartree calculations reasonably well (although tending to be somewhat too large at large distances, as seen in the comparisons presented by Gombas [Go56], for example). An explicit analytical form does not exist for the Thomas–Fermi screening function; it can be expressed only

in the form of a differential equation (numerically calculated values are tabulated by Gombas [Go56]). However, there exists a good analytical approximation due to Molière [Mol47]:

$$\varphi(r/a) = \sum_{i=1}^{3} \alpha_i \exp(-\beta_i r/a), \tag{2.2}$$

where $\{\alpha_i\} = \{0.1, 0.55, 0.35\}$ and $\{\beta_i\} = \{6.0, 1.2, 0.3\}$. In addition to its simple analytical form, Molière's approximation has the merit that at large distances it tends to fall below the Thomas–Fermi result and to come closer to the Hartree value.

In the Thomas–Fermi theory, the screening length a in Eq. (2.1) depends on Z_2 according to the relation

$$a = (9\pi^2/128\, Z_2)^{1/3}(\hbar^2/m_e e^2) = 0.8853 a_0 Z_2^{-1/3}, \tag{2.3a}$$

where a_0 is the Bohr radius. Strictly speaking, Eq. (2.3a) gives the screening length appropriate to the potential distribution in an isolated Thomas–Fermi atom. However, if $Z_1 = 1$ and $Z_2 \gg 1$, one would expect approximately the same potential distribution. Similarly, one might expect the screening distance to be given approximately by Eq. (2.3a) if the ion (in the ion–atom pair) were a fully ionized atom with nuclear charge $Z_1 e$. If the ion Z_1 is not fully ionized, then the question arises as to whether the Thomas–Fermi screening function can be written as a function of a single argument. Firsov [Fi57] showed that a relation such as Eq. (2.1) does, in fact, continue to be a good approximation if, in considering the interaction between two neutral Thomas–Fermi atoms, one uses the screening distance

$$a = 0.8853 a_0 (Z_1^{1/2} + Z_2^{1/2})^{-2/3}. \tag{2.3b}$$

Equation (2.3b) is also commonly used in cases in which the ion Z_1 is partially ionized. Although the screening lengths thus calculated are then expected to be somewhat too small, they should be more accurate than those calculated from Eq. (2.3a).

Throughout the remainder of this article, the parameter a will be assumed to be the Thomas–Fermi screening length given by Eq. (2.3a) if the ion has either $Z_1 = 1$ or is fully ionized and by Eq. (2.3b) otherwise. The reader is cautioned that other functional forms for Eq. (2.3b) are also frequently encountered in the literature. For example, the formula $a = 0.8853 a_0 \{Z_1^{2/3} + Z_2^{2/3}\}^{-1/2}$ is often used (e.g., [Li68]). For practical purposes the difference between this and Eq. (2.3b) can usually be ignored.

A screening function which does not differ markedly in value from the Thomas–Fermi screening function but which is mathematically simple and thus lends itself readily to computational purposes has been defined by Lindhard [Li65], who writes

$$\varphi(r/a) = 1 - [1 + Ca/r)^2]^{-1/2}, \tag{2.4}$$

where C is a standard constant which Lindhard sets equal to $\sqrt{3}$. Equation (2.4) expresses the nuclear and electronic contributions to the potential separately. The second term in Eq. (2.4) implies that the radial density distribution for the atomic electrons has the simple form

$$n_e(r) = (3/4\pi) Z_2 \{(Ca)^2/[r^2 + (Ca)^2]^{5/2}\}. \tag{2.5}$$

The Molière expression (2.2) and the Lindhard expression (2.4) for the screening function are the ones most widely used to describe ion–atom interactions in channeling.

Other screening functions are sometimes used in channeling calculations. For example, the exponential screening function due to Bohr [Boh48] is given by

$$\varphi(r/a_B) = \exp(-r/a_B), \quad a_B = a_0 (Z_1^{2/3} + Z_2^{2/3})^{-1/2}. \tag{2.6}$$

Although this simple screening function has been fairly widely used, it has the disadvantage (a significant one for channeling applications) that at large distances ($r > a_B$) it provides excessive screening and the potential decreases much too rapidly to fit actual ion–atom interactions.

The Born–Mayer screening function [Bor32] can be written

$$\varphi(r/a_{BM}) = A_{BM}(r/a_{BM}) \exp(-r/a_{BM}), \tag{2.7}$$

where A_{BM} and a_{BM} are usually determined phenomenologically, e.g., by fitting elastic moduli. This results in a purely exponential interaction potential which, since it does not have a hard Coulomb "core", is not very suitable for describing close ion–atom encounters. For this reason, the Born–Mayer potential is of most value in providing a simple functional form for ion–atom and atom–atom interactions at large distances. Its application to descriptions of interactions between particles and solids is therefore usually restricted to cases where the "particles" are heavy ions with energies in the keV range.

A further form for the screening function is that due to Nielsen [Ni56]:

$$\varphi(r/a_B) = a_B/2r, \tag{2.8}$$

where a_B is defined in Eq. (2.6). This results in a very simple functional form for the potential, but, like the Born–Mayer potential, it is only applicable at large distances ($r > 2a_B$).

For further details concerning the approximations discussed in this section and for treatments of the classical scattering of ions by screened Coulomb fields, see, for example, the articles by Bohr [Boh48], Everhart, Stone, and Carbone [Ev55], Lindhard, Nielsen, and Scharff [Li68], and Robinson [Ro70].

2.4. Classical theory of channeling

Most of the channeling effects seen for particles with masses equal to or greater than the proton mass can be well described within the framework of classical mechanics. In this section, the applicability of the classical theory is discussed and some of its more general features and results are given.

2.4a. Applicability of classical mechanics

Consider, for the moment, a pure (unscreened) Coulomb scattering between two particles with charges $Z_1 e$ and $Z_2 e$. We assume particle Z_1 to be incident upon particle Z_2 with velocity v and impact parameter b. (We neglect here center-of-mass motion and relativistic effects.) Bohr [Boh48] has discussed the conditions under which a classical orbital picture may be used to describe such a collision. He points out that for a wave packet of width δb there are two contributions to the uncertainty in the scattering angle θ. Firstly, the contribution from diffraction is $\delta\theta_{\text{diff}} \approx \lambda\!\!\!^{-}/(\delta b)$, where $\lambda\!\!\!^{-} = \hbar/M_1 v$ is the DeBroglie wavelength of the incident particle, and, sec-

ondly, the uncertainty in scattering angle caused by the uncertainty in position is $\sim \delta b \cdot \theta'(b)$, where the prime notation implies differentiation with respect to impact parameter. For a well-defined classical orbit having a definite impact parameter, we require both $\delta\theta_{\text{diff}} \ll \theta_{\text{class}}$ and $\delta b \ll b$, where θ_{class} is the classical scattering angle. For a pure (unscreened) Coulomb potential and for small scattering angles, one can write $\theta_{\text{class}} \approx R_0/b$, where the classical collision diameter R_0 is given by

$$R_0 = 2Z_1 Z_2 e^2/M_1 v^2. \tag{2.9}$$

Thus the requirement for a well-defined classical orbit is that simultaneously $\lambda\!\!\!^{-}/\delta b \ll R_0/b$ and $\delta b \ll b$. This can be satisfied if $R_0/\lambda\!\!\!^{-} \gg b/\delta b \gg 1$. That is, if $R_0/\lambda\!\!\!^{-} \gg 1$, then for any impact parameter b it is possible to make $\delta b \ll b$ and, at the same time, to limit diffraction to angles small compared to θ_{class}. Under these conditions, one may visualize a classical orbit and Bohr's condition may be written

$$\kappa = R_0/\lambda\!\!\!^{-} = (2Z_1 Z_2 e^2/\hbar v) \approx (2Z_1 Z_2/137\beta) \gg 1, \tag{2.10}$$

where $\beta = v/c$. The parameter κ is a measure of the strength of the Coulomb interaction in a scattering process. As κ decreases to $\kappa \lesssim 1$, classical orbital pictures completely lose their validity. Since κ is a decreasing function of velocity, Eq. (2.10) indicates that for most Rutherford scattering processes, there is an upper energy limit beyond which classical mechanics loses its significance.

For a screened Coulomb potential, Lindhard [Li65] has shown that a somewhat stronger condition than Eq. (2.10) is necessary for a classical trajectory. With the screened potential defined by Eq. (2.4), the requirement is

$$\kappa \gg 1 + (b/a)^2. \tag{2.11}$$

Thus, at sufficiently high energies or at sufficiently small angles of deflection, a quantal treatment is necessary. For 5-MeV protons bombarding Si, for example, the two sides of Eq. (2.11) are equal when $b \approx a$.

Since, in channeling, one is concerned with small-angle scatterings ($b \approx a$) of energetic particles, Eq. (2.11) would suggest that classical mechanics is not applicable. Lindhard [Li65] demonstrated that classical mechanics can, in fact, be applied to the channeling case (involving a *series* of collisions) even though individual scatterings may not be amenable to classical treatment. For axial channeling, he treated two approximations, the continuum string and the perfect string, both of which are discussed further in Sec. 2.4b. In the continuum-string approximation, the potential due to a row of atoms is considered to be uniformly smeared out along the row. In Lindhard's theory, the continuum approximation is valid if the angle of incidence of the particle upon a row is less than

$$\psi_1 = (2Z_1 Z_2 e^2/dE)^{1/2}, \tag{2.12}$$

where E is the energy of the incident particle and d is the spacing between atoms in the row. For incidence at the angle ψ_1, the distance of closest approach to the center of the string is $\sim a$. If the Bohr condition is now applied to the motion transverse to the string, i.e., if we require that $a \gg \lambda\!\!\!^{-}/\psi_1$, c.f., Eq. (2.10), then it follows that we require

$$2[(M_1/m_e)Z_1 Z_2^{1/3}(a_0/d)]^{1/2} \gg 1, \tag{2.13}$$

where m_e is the electron mass. This condition is certainly fulfilled for particles with masses large compared to that of the electron. Quantal tunneling to the center of the string does not occur if Eq. (2.13) is satisfied. A similar argument can be extended to the planar case.

In the perfect string approximation, Lindhard treats the atoms as static and located at fixed intervals d along rows. He demonstrates that if a channeled trajectory is determined by a whole series of correlated collisions with many atoms, then the angular uncertainties $\delta\theta_{\text{diff}}$ and the uncertainties δb in position do not continue to grow by random addition of the contributions from individual atoms in a string. The width of the wave packet for a channeled particle remains essentially constant during a set of collisions with a string. Consequently, as Lindhard shows, quantal corrections to the classical description actually decrease as the energy of the incident particle is increased.

The remainder of Sec. 2.4 will be confined to purely classical theories of channeling; the discussion of quantum mechanical considerations will be resumed in Secs. 2.5 and 5.

2.4b. The continuum model

From a classical viewpoint, a positively charged particle can be considered to be channeled with respect to a row of atoms if it is incident upon the row at some angle ψ small enough that it is reflected away again from the row by a correlated series of many consecutive glancing collisions with atoms in the row. As the incidence angle becomes greater than some critical angle ψ_c, the particle begins to approach the row so closely that the trajectory no longer can remain channeled. Instead, the particle begins to feel individual atoms and will rapidly be scattered away from the row by single (or at most a few) collisions. For $\psi \gg \psi_c$, the particle can be considered to be traveling randomly with respect to to the row. Similar considerations apply to a plane of atoms.

Thus, it is central to the classical ideal of channeling that the encounters of channeled particles with rows or planes of atoms be determined by many small-angle scatterings and that the particles do not feel individual atoms. Under these conditions, the continuum model [Le63; Li64a,65; Er65] asserts that to a good approximation the motion of channeled particles is determined by a continuum potential, i.e., a potential obtained by replacing the actual periodic potential of the row or plane by a potential averaged over a direction parallel to the row or plane. This is illustrated in Fig. 7 in which the crystal is pictured, for the moment, as an idealized simple static array of identical atoms. For the case of an isolated atomic row, the continuum potential at a distance ρ from the row is

$$V_{RS}(\rho) = \frac{1}{d}\int_{-\infty}^{\infty} V[(\rho^2 + x^2)^{1/2}]\,dx, \tag{2.14}$$

where the potential V is given by an expression of the type in Eq. (2.1) and the subscripts R and S denote row and static. This may be written

$$V_{RS}(\rho) = (2Z_1 Z_2 e^2/d) f_{RS}(\rho/a) \tag{2.15}$$

$$= E\psi_1^2 f_{RS}(\rho/a), \tag{2.16}$$

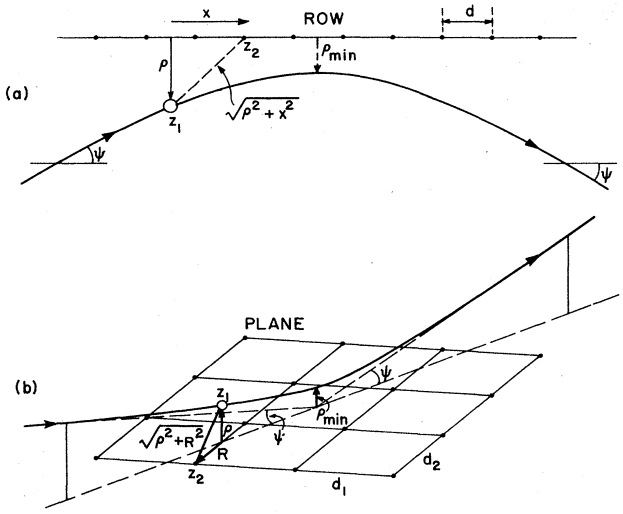

FIG. 7. Collisions of channeled particles with idealized static linear and planar arrays of atoms. The diagrams are distorted for illustrative purposes. In fact, many hundreds of atoms would typically be involved in the reflections of the projectiles.

where ψ_1 is defined in Eq (2.12) and

$$f_{RS}(\xi) = \int_0^\infty (\xi^2 + \eta^2)^{-1/2} \varphi[(\xi^2 + \eta^2)^{1/2}]\, d\eta. \quad (2.17)$$

For Molière's screening function, this becomes

$$f_{RS}(\xi) = \sum_{i=1}^{3} \alpha_i K_0(\beta_i \xi), \quad (2.18)$$

where K_0 is the zero-order modified Bessel function of the second kind (see, e.g., [Wa58]). For Lindhard's screening function

$$f_{RS}(\xi) = \ln(1 + C^2/\xi^2)^{1/2}. \quad (2.19)$$

The corresponding expressions for the continuum planar potentials are

$$V_{PS}(\rho) = n \int_0^\infty 2\pi R\, dR\, V[(\rho^2 + R^2)^{1/2}] \quad (2.20)$$

$$= 2\pi n Z_1 Z_2 e^2 a f_{PS}(\rho/a) \quad (2.21)$$

$$= E\psi_a^2 f_{PS}(\rho/a), \quad (2.22)$$

where n is the areal density of atoms in the plane, ψ_a is a characteristic planar channeling angle defined by

$$\psi_a = (2\pi n Z_1 Z_2 e^2 a/E)^{1/2}, \quad (2.23)$$

and

$$f_{PS}(\xi) = \int_0^\infty \varphi[(\xi^2 + \eta^2)^{1/2}]\, d\eta. \quad (2.24)$$

The subscripts P and S denote planar and static, respectively.

For Molière's potential, one obtains

$$f_{PS}(\xi) = \sum_{i=1}^{3} (\alpha_i/\beta_i) \exp(-\beta_i \xi), \quad (2.25)$$

and for Lindhard's potential,

$$f_{PS}(\xi) = (\xi^2 + C^2)^{1/2} - \xi. \quad (2.26)$$

For the corresponding expressions for f_{RS} and f_{PS} appropriate to the Bohr and Born–Mayer potentials [Eqs. (2.6) and (2.7)], see [Er65; Da67].

The conditions for the validity of the continuum approximation in axial channeling have been discussed by Lindhard [Li65]. He finds the high-energy condition

$$\psi < \psi_1 = (2Z_1 Z_2 e^2/dE)^{1/2} \quad (2.27)$$

when $\psi_1 \lesssim a/d$, and the low-energy condition

$$\psi < \psi_2 = [Ca\psi_1/(d\sqrt{2})]^{1/2} \quad (2.28)$$

when $\psi_1 > a/d$. The energy at which $\psi_1 = a/d$ is given by

$$E' = 2Z_1 Z_2 e^2 d/a^2. \quad (2.29)$$

For the ⟨110⟩ axis in Si, for example, this energy is $E' \approx 40$ keV. Most of the experiments performed to date have been in the high-energy range, and this is the region that will be discussed almost exclusively here.

The static continuum potentials may be regarded as the first (constant) term of a Fourier expansion of the periodic lattice potential. The coefficients of the succeeding (periodic) terms in the expansion decrease rapidly with distance from a row or plane as shown, for example, by Lehmann and Leibfried [Le63]. Even at distances small enough that these additional terms are not negligible compared to the constant term, their influence upon a channeled trajectory averages out close to zero since a large number of atoms participate in the steering of a channeled particle. For an example of an axial channeling calculation that takes account of the periodic lattice potential, the reader is referred to a paper by Kurakin and Romanyuk [Ku69].

Inside a crystal lattice, the continuum potential experienced by an axially channeled particle will be the sum of the potentials due to all of the rows of atoms in the crystal. Thus, for the static case the total potential measured at a position $\mathbf{r}$ in the plane normal to the axial direction is given by

$$U_{RS}(\mathbf{r}) = \sum_i V_{RS}(|\mathbf{r} - \mathbf{r}_i|) - U_{RS}^{\min}, \quad (2.30)$$

where the $\mathbf{r}_i$ are the positions of the atomic rows measured in the normal plane and $U_{RS}^{\min}$ is a constant subtracted in order to make the minimum value of $U_{RS}(\mathbf{r})$ equal to zero. Similarly, for planes, one has

$$U_{PS}(z) = \sum_i V_{PS}(|z - z_i|) - U_{PS}^{\min}, \quad (2.31)$$

where z and z_i are measured in a line normal to the set of planes being studied. Figures 8 and 9 show examples of the functions U_{RS} and U_{PS}. The transverse motions of channeled particles are affected by the symmetries of the channels involved. Thus the motion in an axial channel (or its projection onto the normal plane) is usually complex, whereas that in a planar channel is usually a fairly simple oscillatory motion in the transverse direction.

For a channeled particle traveling at small angles with respect to atomic rows or planes, the longitudinal component of the velocity may be treated as constant (if energy-

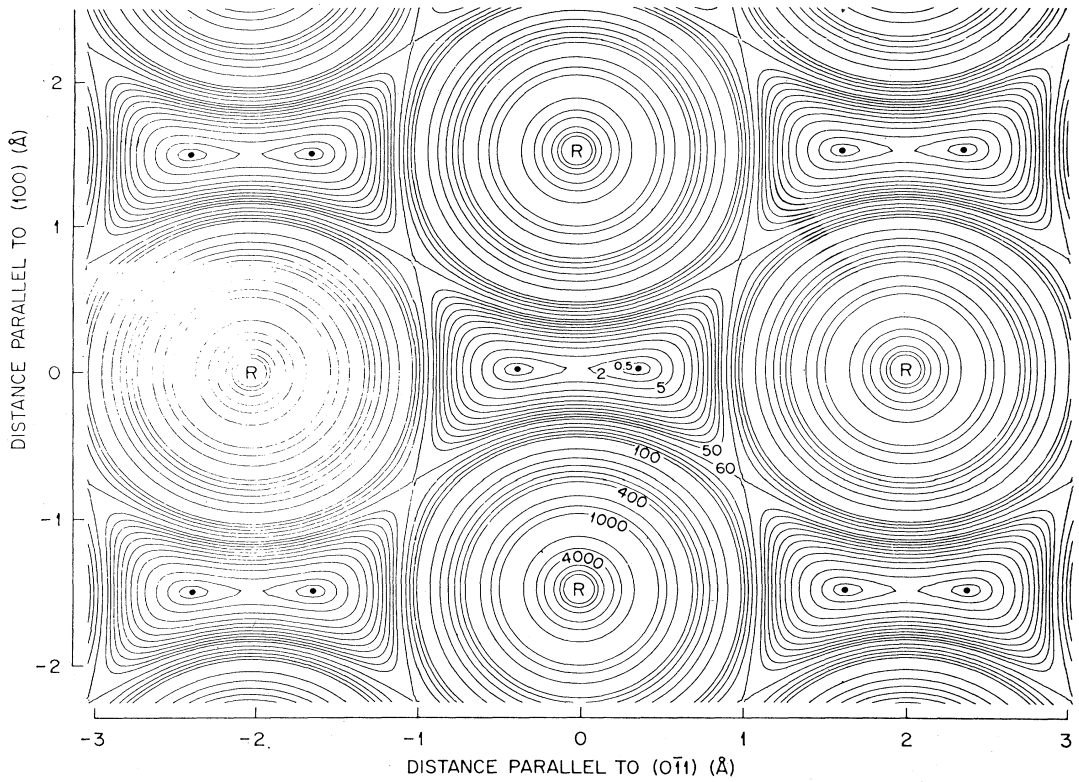

FIG. 8. Continuum potential energy contours (labeled in eV) for iodine ions channeled in the ⟨110⟩ direction in a static lattice of Ag atoms. The calculations are based on an empirically determined ion–atom potential given by Robinson [Ro71b]. The positions of the rows are marked by *R*'s and the positions of minimum energy by dots [Ap72a].

loss processes are neglected). Then, in the continuum model, the trajectory of the particle can be completely described in terms of the motion in the transverse direction. Consider a channeling collision with an isolated static string of atoms. At large distances ρ from the string, let the angle between the particle trajectory and the row be ψ_0. For small ψ_0, the transverse momentum is $M_1 v \psi_0$ and the kinetic energy associated with the transverse motion (usually and somewhat loosely called the transverse energy) is $E\psi_0^2$. The distance of closest approach to the row is given by the solution of

$$1 - (b/\rho_{\min})^2 - V_{RS}(\rho_{\min})/(E\psi_0^2) = 0, \qquad (2.32)$$

where b is now the impact parameter of the collision when projected onto the normal plane. In the special case in which the particle trajectory and the atomic row are coplanar, Eq. (2.32) reduces to

$$E\psi_0^2 = V_{RS}(\rho_{\min}). \qquad (2.33)$$

The critical angle of incidence ψ_0, beyond which the distance of closest approach becomes less than the critical distance ρ_c for sustaining a stable channeling trajectory, is given by

$$\psi_c = [V_{RS}(\rho_c)/E]^{1/2} \qquad (2.34)$$

$$= F_{RS}(\rho_c/a)\psi_1, \qquad (2.35)$$

where

$$F_{RS}(\xi) = [f_{RS}(\xi)]^{1/2}. \qquad (2.36)$$

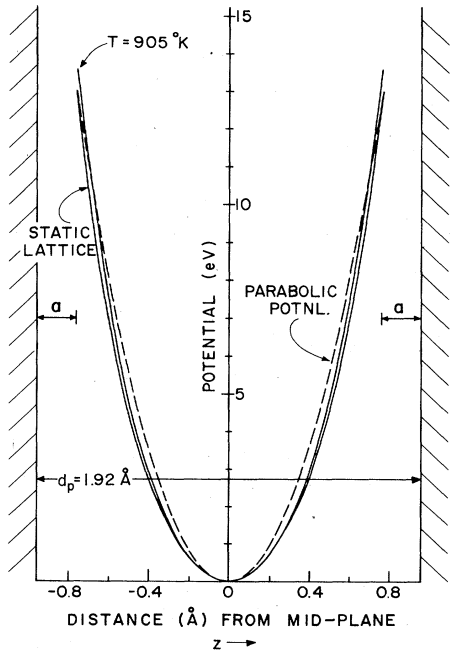

FIG. 9. Continuum potential energy for protons channeled in the (110) planes of Si. The calculations are based on Molière's ion–atom potential One of the solid curves is for the static case, with U_{PS} given by Eq. (2.31); the other is for a temperature of 905 °K, with U_{PV} derived from V_{PV} given in Eq. (2.75). For comparison, the dashed curve is a simple parabolic potential set equal to the value of U_{PS} at $z = (\frac{1}{2}d_p - a)$.

A graph of the function $F_{RS}(\xi)$ is given in Fig. 117, Appendix A. From this, it can be seen that ψ_c is on the same order of magnitude as ψ_1; if ρ_c lies between $0.1a$ and $2.4a$, then $F_{RS}(\rho_c/a)$ lies between $0.5\psi_1$ and $1.6\psi_1$. The critical angle ψ_c depends on E and d only through its dependence on ψ_1.

As a rough estimate of ρ_c in the ψ_1-region (Eq. 2.27), Lindhard [Li64, 65] suggested $\rho_c \approx a$. Inserting this value in Eq. (2.35) yields $\psi_c = 0.83\psi_1$, but such an exact evaluation was not intended in Lindhard's treatment; e.g., it ignores thermal vibration effects that certainly can be expected to influence the value of ρ_c. In an appendix to his 1965 paper, Lindhard discussed the accuracy of the continuum model for isolated rows of static atoms. Using the impulse approximation to derive the scattering at successive atoms, he showed that in order for the transverse motion to be described by a continuum potential, the requirement that must be fulfilled is

$$E > \tfrac{1}{8}d^2 V''_{RS}(\rho_c), \tag{2.37}$$

where the prime notation implies double differentiation with respect to ρ. Replacing the inequality in Eq. (2.37) with an equality defines an energy-dependent value of ρ_c. As the energy increases, ρ_c decreases. (See also [Mo68, 70a, 71; Mar70; Var70, 72].)

Several different meanings of the term critical angle are encountered in the published literature. In the present article, it is defined as the maximum angle at which a particle may be incident upon a row or plane of atoms and be reflected away again by a correlated series of collisions in such a manner as to conserve transverse energy and and justify the use of the continuum model. In actual experiments, it is not easy to determine ψ_c. Most commonly the angle measured is the half-angle $\psi_{1/2}$ defined in Fig. 3. For this, Lindhard [Li64a, 65] suggested

$$\psi_{1/2} = \alpha_R \psi_1, \tag{2.38}$$

where α_R has a value in the range 1 to 2.

In a static lattice (as distinct from an isolated static row), the critical angle for axial channeling becomes

$$\psi_c = [U_{RS}(\rho_c)/E]^{1/2}, \tag{2.39}$$

where the potential U_{RS} given by Eq. (2.30) is assumed to be cylindrically symmetric close to a row ($\rho \approx \rho_c$), and the angle ψ_c between the axis and the trajectory of a critically channeled particle is measured at a point where $U_{RS=0}$. For a major (high-symmetry) axial direction, the contributions from neighboring rows to the potential for any one row are usually small. In such cases, the much simpler expressions in Eqs. (2.34) and (2.35) can be expected to be reasonably good approximations.

Similarly, for the static planar case, the critical angle is given by

$$\psi_c = [U_{PS}(|\tfrac{1}{2}d_p - \rho_c|)/E]^{1/2}, \tag{2.40}$$

where d_p is the distance between planes and the potential $U_{PS}(z)$ given in Eq. (2.31) is assumed to be zero at $z = 0$, which by definition is at the midpoint between two neighboring planes. (We consider here only simple lattice structures with all planes identical and equally spaced and with all rows the same in any given axial direction. More complicated structures are considered in Sec. 4.4.)

The continuum potential between major crystal planes is frequently well approximated by including only the contributions from the two adjacent planes, and in such cases

$$\psi_c = [U_{PS}^{(2)}(|\tfrac{1}{2}d_p - \rho_c|)/E]^{1/2} \tag{2.41}$$

$$= F_{PS}(\rho_c/a, d_p/a)\psi_a, \tag{2.42}$$

where

$$F_{PS}(\xi, \eta) = [f_{PS}(\xi) + f_{PS}(\eta - \xi) - 2f_{PS}(\eta/2)]^{1/2}. \tag{2.43}$$

Graphs of the function $F_{PS}(\xi, \eta)$ are given in Fig. 118, Appendix A.

Thus far, we have discussed only static lattices. Clearly, if thermal vibrations are taken into account, both the continuum potential and the critical distance of closest approach ρ_c will be affected. The velocity of channeled particles is usually such that the interaction times with individual atoms are much shorter than the thermal vibration periods. Thus the particles see a lattice that is in effect stationary. The continuum potential experienced by the particles is that obtained by averaging over the thermal displacements of the atoms. Expressions for the continuum potentials for rows and for planes of thermally vibrating atoms have been given by Appleton *et al.* [Ap67] and also by Barrett [Ba71] whose expression for the planar case is given in Eq. (2.75). These derivations assume that the individual atoms vibrate independently and that in each of the translational degrees of freedom the probability $P(x)$ of a displacement x has the Gaussian distribution

$$P(x) = (2\pi u_1^2)^{-1/2} \exp[-x^2/(2u_1^2)], \tag{2.44}$$

where the root-mean-square displacement is assumed to be $u_1 = \langle x^2 \rangle^{1/2} = \langle y^2 \rangle^{1/2} = \langle z^2 \rangle^{1/2}$ and its value may be computed by use of the Debye theory of thermal vibrations (see Appendix A). Temperature-dependent continuum potentials for protons interacting with the $\langle 110 \rangle$ rows and the (110) planes in Si are shown in Fig. 10 (and also in Fig. 9). As might be expected, these potentials begin to differ markedly from the static-lattice values only when ρ is comparable to or smaller than the thermal vibration amplitudes.

The continuum model predicts that both axial and planar critical angles should vary as $E^{-1/2}$. Experimentally, this functional dependence on the bombarding energy is found to be obeyed very well. At higher energies, at which relativistic effects become important, the inverse-square-root relation continues to be valid provided that the kinetic energy E is replaced by the quantity kE, where

$$k = (E + 2M_1c^2)/(2E + 2M_1c^2). \tag{2.45}$$

This follows from the fact that the relativistic transverse momentum is $\gamma M_1 v\psi$, where $\gamma = [1 - \beta^2]^{-1/2}$, and thus the associated transverse kinetic energy is given by $\gamma M_1 v^2\psi^2/2$, for small values of ψ.

The minimum yields $\chi_{\min}$ predicted by the continuum model are in essence the geometrically determined fractional areas for which channeling trajectories are not possible when a beam is aligned with an axis or plane. Within these areas, the initial transverse energy is above the critical value. Thus the value for an axis is

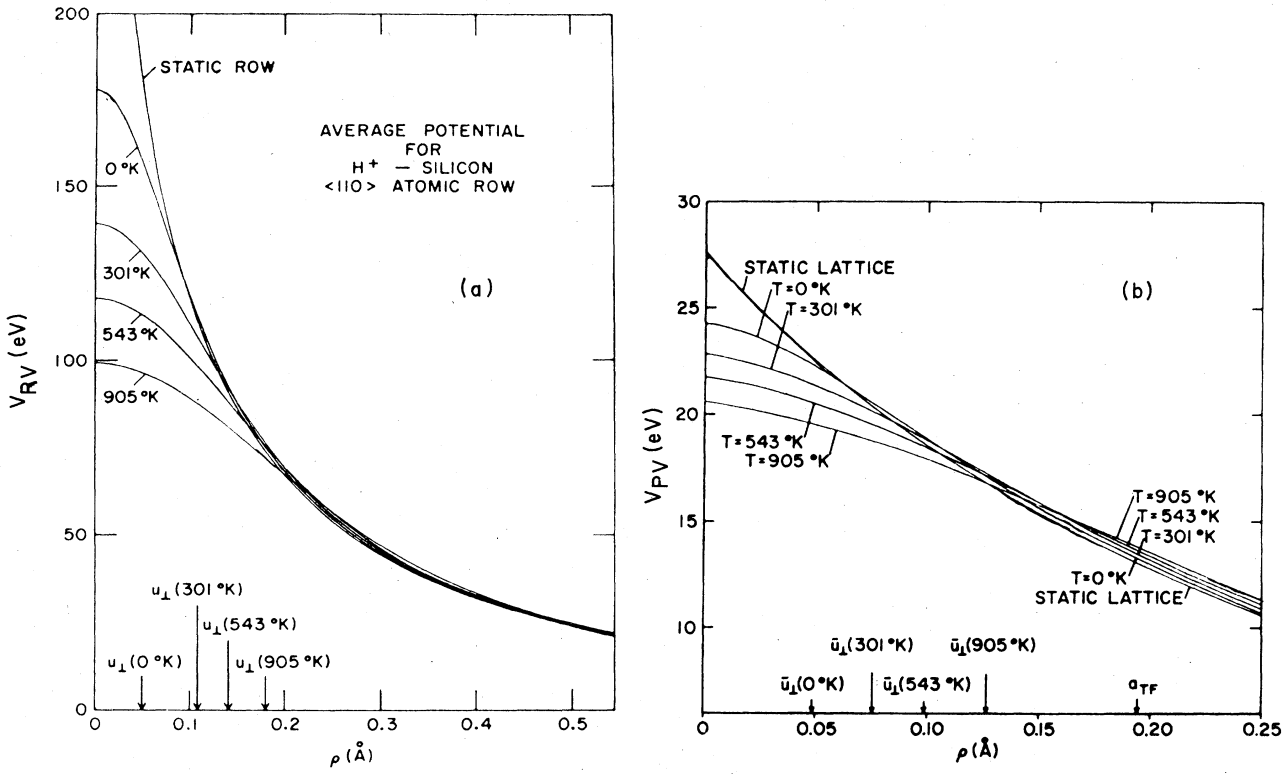

FIG. 10. Continuum potentials based on the Molière ion–atom potential evaluated by Appleton *et al* [Ap67]for protons at various distances from (a) the ⟨110⟩ rows and (b) the (110) planes of Si. Results are shown for a static lattice and for various temperatures. The Thomas–Fermi screening distance in this case is 0.194 Å. The quantities $\bar{u}_\perp$ and $u_\perp$ in the figure are equal to u_1 and $\sqrt{2}u_1$, respectively, where u_1 is defined in Eq. (2.44).

$$\chi_{\min} = Nd\pi\rho_c^2, \tag{2.46}$$

where N is the number of atoms per unit volume in the crystal. Lindhard [Li65] suggested the relation

$$\chi_{\min} = Nd\pi(u_2^2 + a^2) + \chi_3 \tag{2.47}$$

for the axial minimum yield just below the crystal surface Here, $u_2 = \langle x^2 + y^2\rangle^{1/2} = \sqrt{2}\,u_1$ is the rms value of the thermal vibration amplitude normal to the axis and χ_3 is a contribution from any amorphous or impurity layers on the crystal surface. The minimum yield for the planar case is predicted by the continuum model to be

$$\chi_{\min} = 2\rho_c/d_p, \tag{2.48}$$

and the expression suggested by Lindhard is

$$\chi_{\min} = 2a/d_p. \tag{2.49}$$

The continuum model has been treated here in some detail because in general it fairly successfully predicts such important features as angular widths and minimum yields and their dependences on several fundamental parameters (e.g., Z_1, Z_2, E). Furthermore, it is common to express the results of channeling calculations and experiments in terms of quantities derived from the continuum model. Thus far we have neglected the slowing down of particles inside a crystal and the orientation dependence of the stopping power. Also, we have ignored multiple-scattering, which leads to changes in the transverse energy and to dechanneling effects. These phenomena that may be regarded as consequences of channeled motion but that to a first approximation do not determine the motion are discussed in later sections.

2.4c. Rules of angular and spatial averages

Some of the features observed in channeling can be explained in a qualitative way in terms of statistical mechanical concepts [Li65]. In addition to the rule of reversibility (Sec. 2.2), Lindhard has outlined a rule of angular averages and a rule of spatial averages. These rules lead to the concept of compensation, which can be explained as follows: We compare the magnitude of some definite physical effect (e.g., the frequency of nuclear encounters, energy loss per unit distance, or rate of production of K-shell vacancies) that would be observed for a particle beam interacting in a random medium with the magnitude of the same effect in a medium that differs from this only in that the atoms are ordered in a crystal lattice. For the random system, the effect occurs at a certain rate independent of direction; for the crystal, channeling effects may drastically alter the magnitude of the effect within small solid angles. The rule of angular averages states that for effects that are not affected by the slowing down of the particles, the rate averaged in angle is the same for the crystal as it is for the random medium. That is, if the rate is lower than this average in some crystal directions, then the rate in other directions must be higher than average to compensate for this.

As an example, consider a crystal containing α-emitting radioactive atoms located on some lattice sites, and

let us suppose the dimensions of the crystal to be much smaller than the range of the α particles. The angular distribution of emerging α particles will show strong blocking minima along major crystal directions. However, the total integrated flux of α particles out of the crystal is independent of the ordered structure of the material. Therefore there must be directions in which the rate of emergence of α particles is higher than the average (or random) rate. These directions will lie fairly close to major blocking directions since most of the blocked particles will not have been scattered through very large angles. Thus, there will be "compensation shoulders" on the blocking dips. Application of the rule of reversibility immediately shows that corresponding shoulders will be seen for channeling dips.

On the basis of considerations similar to those for angular averages, Lindhard also stated a rule of spatial averages. This type of average is discussed in Sec 2.4f in connection with flux peaking.

2.4d. Calculations on the shape of channeling dips

In this section we describe both analytical and Monte Carlo methods of calculating the shape of a channeling (or blocking) dip such as that shown in Fig. 3. We still maintain, for the moment, the approximations in which energy losses and multiple scattering are ignored; thus, the results may be regarded as pertaining to the region just below the crystal surface. Many of the calculations describe blocking rather than channeling. Within the approximations made in this section, the results apply equally well to both processes.

2.4d1. Axial case

A detailed analytical treatment of the motion of axially channeled particles in a lattice is difficult even if one introduces the simplification of the static-continuum potential. The motion of particles in potentials of the type given in Eq. (2.30) is generally complex. The theoretical description is greatly simplified if one considers channeled particles as interacting only with isolated rows of atoms. That is, in a collision with a row, the influence of all other rows is neglected. For major axial directions this might be expected to be a reasonable assumption because the continuum potential falls off rapidly with distance. Then, in the static-continuum approximation, the transverse energy of a channeled particle,

$$E_\perp = E\varphi^2 + V_{RS}(\rho), \tag{2.50}$$

will be conserved, where φ is the instantaneous angle between the particle trajectory and the axis and ρ is the distance of the particle from the row. On the basis of this simple model, Lindhard [Li65] derived an expression for the probability distribution $\Pi(E_\perp)$ of the transverse energies of particles being emitted from lattice atoms into directions around a major crystal axis. He assumed that the emitting atoms were vibrating thermally and that after being emitted, the blocked particles experienced only the static-continuum potential. From Eq. (2.44) one finds that the probability distribution for the radial displacement (normal to an axis) of a thermally vibrating atom is

$$P_R(\rho) = (2\rho/u_2^2)\exp(-\rho^2/u_2^2), \tag{2.51}$$

where $u_2 = \sqrt{2}\,u_1$. In the simple continuum model, the probability distribution function for $E_\perp$ is then

$$\Pi(E_\perp) = \int_{\hat\rho}^{\infty} P_R(\rho)\,d\rho \tag{2.52}$$

$$= \exp(-\hat\rho^2/u_2^2), \tag{2.53}$$

where $\hat\rho$ is defined by

$$E_\perp = V_{RS}(\hat\rho). \tag{2.54}$$

With the aid of Lindhard's potential, this leads to

$$\Pi(E_\perp) = \exp\{(-C^2a^2/u_2^2)[\exp(2E_\perp/E\psi_1^2) - 1]^{-1}\}. \tag{2.55}$$

From this one obtains the blocking angular distribution from the relation

$$E\psi_e^2 = E_\perp, \tag{2.56}$$

where ψ_e is the angle of emission from the row. As Lindhard pointed out, this calculation has the disadvantages that it does not include compensation (the exponential in Eq. (2.53) cannot exceed unity) and that it leads to $\chi_{\min} = 0$. Furthermore, it is expected to be valid only when $\psi_1 < u_2/d$. However, within these limitations, the model does reproduce some of the features of more detailed calculations and of experiment (as seen in Fig. 16), and at the same time it provides some physical insight into the processes involved (often difficult to obtain in more detailed calculations).

From Eq. (2.53), it follows [Pi69; An70] that the angular half-width of the dip is given by

$$\psi_{1/2} = \alpha_R(u_2/a)\psi_1, \tag{2.57}$$

where, for Lindhard's potential,

$$\alpha_R(u_2/a) = \{\tfrac{1}{2}\ln[1 + C^2a^2/(u_2^2\ln 2)]\}^{1/2}. \tag{2.58}$$

In an appendix to his 1965 paper, Lindhard showed that the continuum model can be refined if one considers the transverse energy to be conserved only when measured on the transverse planes located midway between atoms in a string. Figure 11 defines the geometric quantities in the half-way plane model used by Lindhard in his derivation of the blocking angular distribution. The transverse energy is now

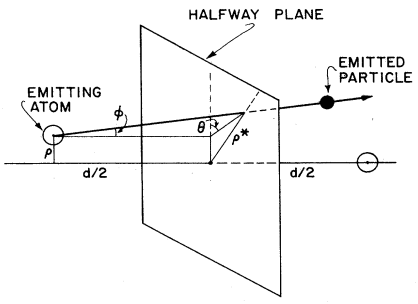

FIG. 11. Geometry considered for Lindhard's halfway plane calculation on the emission of particles from atoms inside a crystal.

$$E_\perp = E\varphi^2 + V_{RS}(\rho^*), \tag{2.59}$$

where

$$\rho^* = [\rho^2 + (\varphi d/2)^2 + \rho\varphi d \cos\theta]^{1/2}, \tag{2.60}$$

and θ is the azimuthal angle shown in Fig. 11. From this it follows that the distribution function for the transverse energy is

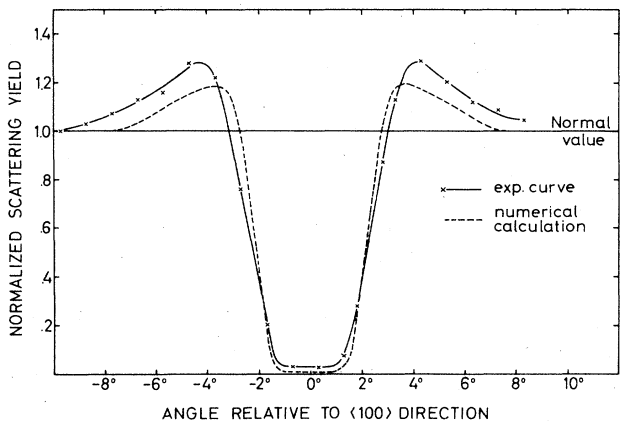

FIG. 12. Experimental and calculated dips for axial channeling of 480-keV protons in the ⟨100⟩ directions of W at 309°K [An67]. The calculations were based on Eqs. (2.61) and (2 62).

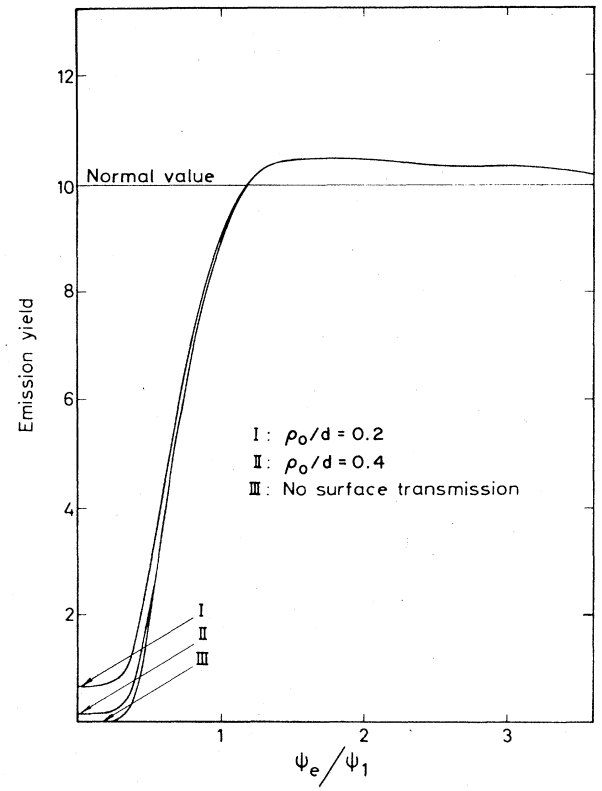

FIG. 13. The influence of surface transmission on the calculated ⟨100⟩ axial channeling dip, Eq. (2.62), for 500-keV protons in tungsten at 1470 °K [An67]. The actual value of ρ_0/d is 0.4.

$$\Pi(E_\perp) = \int_0^{\rho_0} P_R(\rho)\,d\rho \int_0 d(E\varphi^2) \times \int_0^{2\pi} (d\theta/2\pi)\,\delta[E_\perp - V_{RS}(\rho^*) - E\varphi^2], \tag{2.61}$$

where ρ_0 is given by $\pi\rho_0^2 = (Nd)^{-1}$. For a given value of $E_\perp$ in Eq. (2.61), the integrals are carried out over the values that satisfy Eq. (2.59). The modification of the distribution in transverse energy at the crystal surface was also included by Lindhard. Outside the crystal, the distribution becomes

$$P_e(E\psi_e^2) = \int_0^{\rho_0} \frac{2\rho\,d\rho}{\rho_0^2 - \hat{\rho}^2[E\psi_e^2 + V_{RS}(\rho)]}\,\Pi[E\psi_e^2 + V_{RS}(\rho)], \tag{2.62}$$

where $\hat{\rho}$ is defined by Eq. (2.54). The assumption in applying this surface transmission factor is that by the time particles reach the surface, statistical equilibrium has been reached in the sense that on the transverse plane all exit points for which $V_{RS}(\rho) \leq E_\perp$ are equally likely.

Andersen [An67] has evaluated the formulas in Eqs. (2.61) and (2.62) by numerical integration. Some of his results are shown in Figs. 12–15. Figure 12 shows one of his fits to experimental data, in this case for tungsten. The angular width of the dip is well reproduced. The experimental χ_{min} is higher than the calculated value, perhaps because of experimental rather than theoretical difficulties. The calculations predict compensating shoulders which, as seen in Fig. 14, smear out as $u_2/(\psi_1 d)$ increases. In actual experiments, the shoulder region is strongly influenced by planar effects, so quantitative agreement with the results calculated from Eq. (2.62) is not necessarily to be expected. The main influence of the surface transmission is in the region at the bottom of the dip (Fig. 13). The results of the calculations shown in Fig. 14 demonstrate that as the crystal temperature is raised, χ_{min} increases and $\psi_{1/2}$ decreases. This is in good accord with experiment (Sec. 4.21). The surface transmission does not affect $\psi_{1/2}$ very much. Consequently Andersen was able to

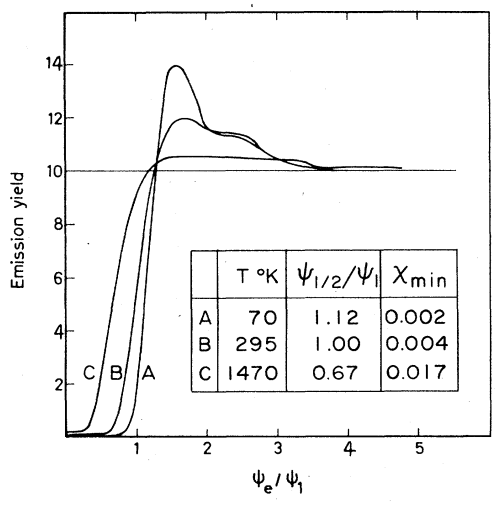

FIG. 14 The influence of the vibrational amplitude u_2 on the shape of the calculated ⟨100⟩ axial channeling dip for 500-keV protons in tungsten at various temperatures [An67]. The calculation is based on Eq. (2.62).

find the ratio $\psi_{1/2}/\psi_1$ as a function of only the two parameters $u_2/(Ca)$ and $\psi_1/(Ca/d)$. This ratio, which was called α_R in Eq. (2.57), is plotted in Fig. 15. It is interesting to note that for $\psi_1 < Ca/d$, the calculated α_R is almost constant. If also $\psi_1 < u_2/d$, this constant value is close to the value given by Eq. (2.58). Although the fit to the experimental data for tungsten is gratifying, the fit to channeling data for many other crystals is not nearly so good. Thus, for example, the values of α_R obtained from the experiments of Andersen and Laegsgaard [An72a] fall to about 70% of the calculated values when u_2/a is large, as seen in Fig. 42.

The axial blocking dip has also been calculated analytically by Tulinov [Tu65a,b] and Oen [Oe65], both of whom employed the exponential screening function, Eq. (2.6). Tulinov discussed two angular widths which approximately correspond to the values ψ_m and $\psi_{1/2}$ in Fig. 3. In his model, ψ_m is determined solely by blocking at the nearest-neighbor atom in a row and is not temperature dependent. The result for ψ_m is

$$\psi_m = \{(2R_0/d)[K_0(R_0^{1/2}d^{1/2}/a) + 2]\}^{1/2}, \quad (2.63)$$

where R_0 is given in Eq. (2.9) and K_0 is the zero-order modified Bessel function of the second kind (see, e.g., [Wa58]). In his derivation of the half-width $\psi_{1/2}$, Tulinov treated a row of atoms as a cylinder of radius g filled with independent classically vibrating atoms. Then for each particle emitted by an atom in the row, he calculated the multiple scattering as it moves along and radially out of this cylinder in which the number of atoms per unit volume is determined by the interatomic spacing d. After leaving the cylinder, the particle is further deflected by the continuum potential. The result total deflection is then

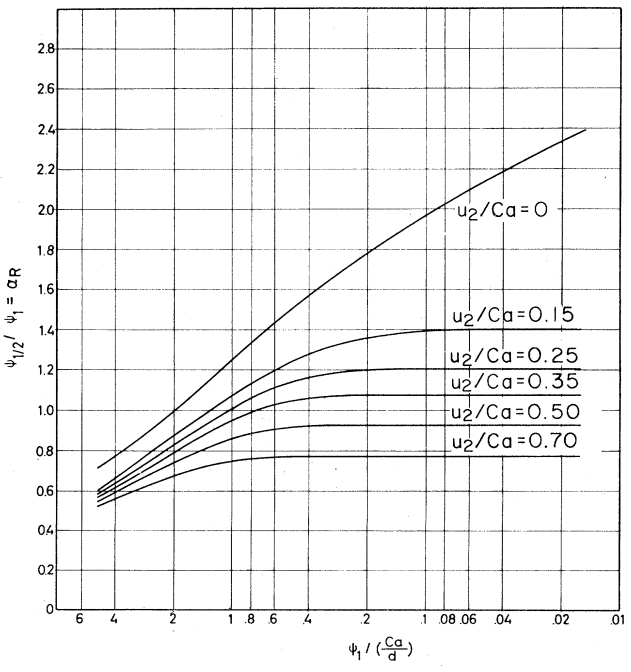

FIG. 15. The ratio $\alpha_R = \psi_{1/2}/\psi_1$, calculated from Eq. (2.62) as a function of the two parameters $\psi_1/(Ca/d)$ and u_2/Ca [An67].

$$\psi_{1/2} = \left[\left(\frac{3R_0^2}{2gd}\ln\frac{a}{R_0}\right)^{2/3} + \frac{2R_0}{d}K_0\left(\frac{g}{a}\right)\right]^{1/2}. \quad (2.64)$$

The values calculated from Eqs. (2.63) and (2.64) gave reasonable fits to the proton blocking data measured at 80 and 300°K by Tulinov *et al.* [Tu65a, b] when the value $g = \sqrt{3}\,u_2$ was used for the radius of the cylinder.

Oen [Oe65] calculated the blocking of 5.49-MeV α particles in tungsten in order to make a comparison with the data of Domeij and Björkqvist [Do65a]. In this model, only two atoms are considered; the emitting atom and the nearest-neighbor atom in the $\langle 111\rangle$ row. The two atoms are allowed to vibrate relative to one another. An exact analytical expression of general applicability for the angular emission pattern was obtained. The result shows $\psi_{1/2}$ decreasing and $\chi_{\min}$ increasing with increasing temperature. The angular width fits the experimental value quite well, but it is not possible to fit $\chi_{\min}$ and $\chi_{\max}$ simultaneously. If one fits the region around $\chi_{\max}$ and assumes that the poor fit then found around $\chi_{\min}$ is due to experimental problems, then the implied two-dimensional thermal vibration amplitude has the unusually low value $u_2 = 0.0024$ Å. Oen postulates that this implies a high degree of correlation between the thermal vibrations of neighboring atoms. He also points out that scattering by the second-nearest neighbor increases $\psi_{1/2}$ by about 10%.

Ibel and Sizmann [Ib68], Varelas and Biersack [Var70] and Varelas and Sizmann [Var72] have made analytical calculations to investigate the conditions that determine the maximum transverse energy sustainable by an isolated static row of atoms. These authors have computed the total deflections of incident ions by summing the contributions (calculated by means of the impulse approximation) from each atom in the row. The critical distance of closest approach is found to decrease with increasing incident energy {c.f. Eq. (2.37); see also [Li65; Mo68; 70a, 71; Mar70]}. We denote this energy-dependent critical distance of closest approach by ρ_{cS}, where the subscript S denotes that the value is for a static row. Varelas and Sizmann [Var72] found that for a thermally vibrating row a good approximation for the distance of closest approach is $\rho_{cV} \approx (\rho_{cS}^2 + u_2^2)^{1/2}$, where u_2 is defined in Eq. (2.51). Inserting ρ_{cV} into Eq. (2.34) was found to give a good fit to a wide variety of experimental values of $\psi_{1/2}$, including data recorded in both the ψ_1 and ψ_2 energy regions.

Following the initial work of Robinson and Oen [Ro63a, b], many authors (e.g., [No67, 69; To68, 69; Ho68; Ba68, 71; Mo68, 70a, 71; Ry68, 70, 72; An70; Ma70]) have made Monte Carlo calculations on axial channeling. Three types of calculation of the axial channeling dip were compared by Andersen and Feldman [An70]. Using a binary-collision model, they performed a Monte Carlo calculation on the emission of particles from atoms in an isolated string, and the results were compared with those calculated [An67] from Lindhard's halfway plane model, Eq. (2.61), and with the results of the simple continuum model, Eq. (2.55). Surface transmission effects were omitted. Figure 16 shows such comparisons in two materials. In general the results of the binary-collision model and the halfway plane model agree very well. In their binary-collision calculation, those authors also found that if all the atoms in a row were allowed to vibrate, the effect on the emitted angular

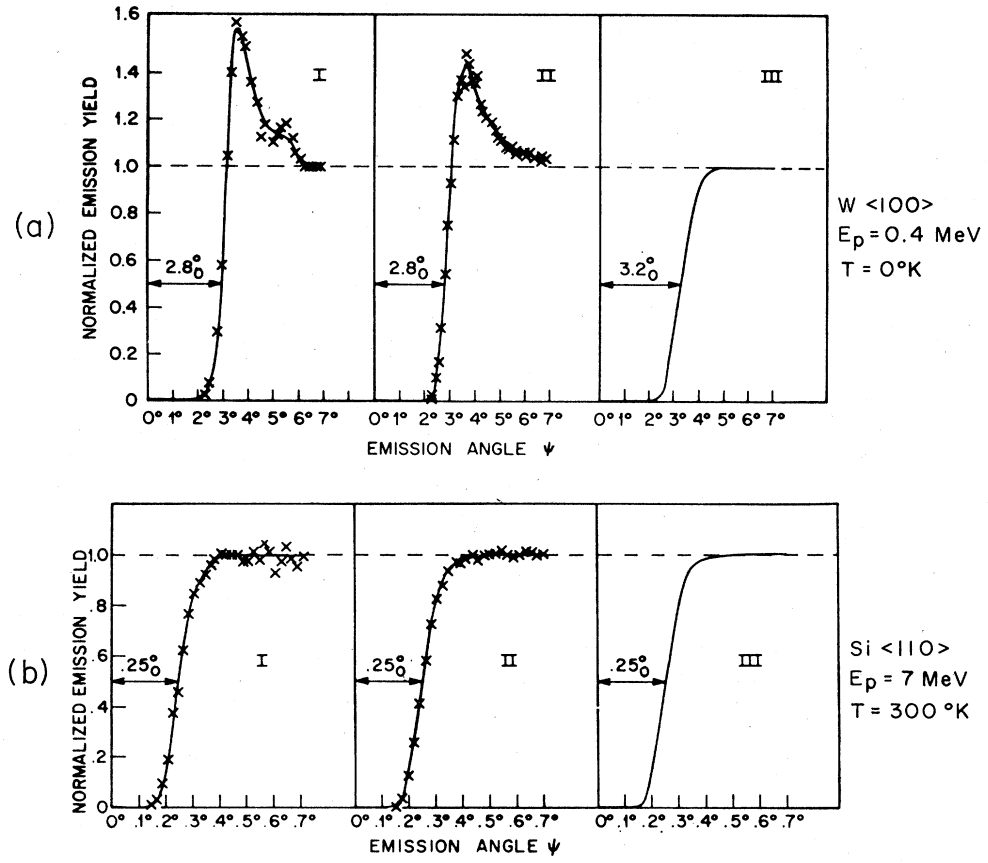

FIG. 16. Calculated axial dips for protons channeled (a) in tungsten and (b) in silicon. Results are given for (I) the binary-collision model with only the emitting atom vibrating, (II) the halfway plane model, and (III) the simple continuum model [An70].

distribution was quite small. When $\psi_1 \ll u_2/d$, as in the case shown in Fig. 16(b), then all three models are in good agreement.

The fact that these three models can give such good agreement among themselves and yet can give values of $\psi_{1/2}$ as much as 30 to 40% larger than the experimentally determined values, as has been found in many investigations (e.g., [Dav68a; Pi69a; An72a]), suggests an inherent difference between the channeling behavior for an isolated row of atoms and for a complete lattice. Unfortunately, analytical calculations taking account of the complete lattice are prohibitively complex, especially if thermal vibrations are included. Thus whole lattice calculations are almost invariably of the Monte Carlo type and are performed on large-scale electronic computers. Such calculations may be regarded as computer experiments and have been performed extensively in recent years, notably by Barrett [Ba68, 71], Morgan and Van Vliet [Mo68, 70a, b, 71]and Ryabov [Ry68, 70, 72].

The Monte Carlo calculations of Morgan and Van Vliet have emphasized comparisons with and checks on the validity of the continuum model. They have characterized the results of their calculations in terms of ρ_c, the critical distances of closest approach to rows or planes, and have developed simple empirical rules giving the dependence of ρ_c on ψ_1 and u_1. These authors have also computed particle-flux distributions in crystals (Sec. 2.4f) by Monte Carlo methods. In addition, they and several others (see Sec. 6.6) have computed the way in which blocking angular distributions are modified by the finite lifetimes of emitting nuclei as they recoil from lattice sites.

In 1971, Barrett published the results of a very detailed set of Monte Carlo computer calculations from which he was able to derive empirical formulas that fit not only the calculated results but also a great variety of experimental determinations of $\psi_{1/2}$ and $\chi_{\min}$. Classical trajectories of ions were followed through various simulated crystals (mostly, but not always, tungsten). The calculations were done mostly for the channeling case, i.e., an ion beam was considered to be incident upon the crystal surface at randomly chosen positions. Thermal vibrations were simulated by assuming the atoms to have independent displacements with probabilities given by Eq. (2.44). The Molière potential was used. The deflections at each binary encounter were computed by the impulse approximation. Energy losses were neglected, as was the effect of multiple scattering due to electrons. As a measure of close-encounter processes, a quantity called the normalized nuclear encounter probability was introduced. It is defined as

$$P_{NE} = \frac{\cos\psi}{2\pi u_1^2 N d \mathfrak{N}_c} \sum_{i=1}^{\mathfrak{N}_c} \exp\left(-\frac{\rho_i^2}{2u_1^2}\right), \qquad (2.65)$$

where ψ is the angle between the beam direction and the direction of the channel, i is an index number labeling a particular binary collision, ρ_i is the radial distance (i.e.,

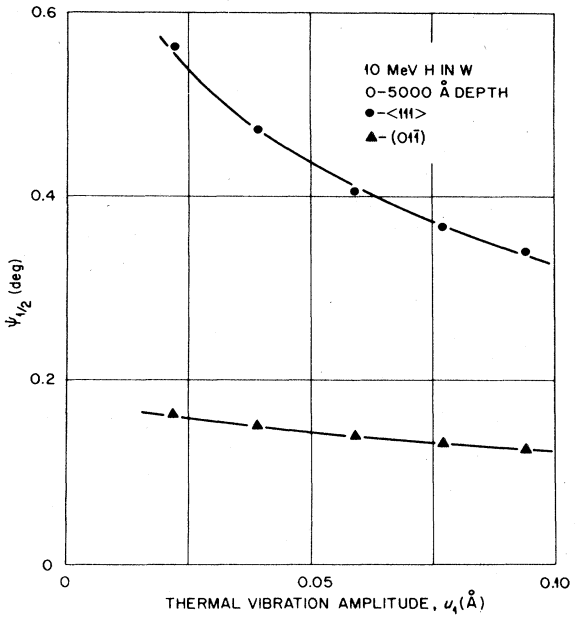

FIG. 17. Half-angles $\psi_{1/2}$ as a function of thermal vibration amplitude for axial and planar channeling [Ba71]. The points are the results of Monte Carlo calculations, and the curves are obtained from Eqs. (2.66) and (2.81) with values of $k = 0.83$ and $m = 1.2$ for the axial case and $k = 0.76$ and $m = 1.6$ for the planar case.

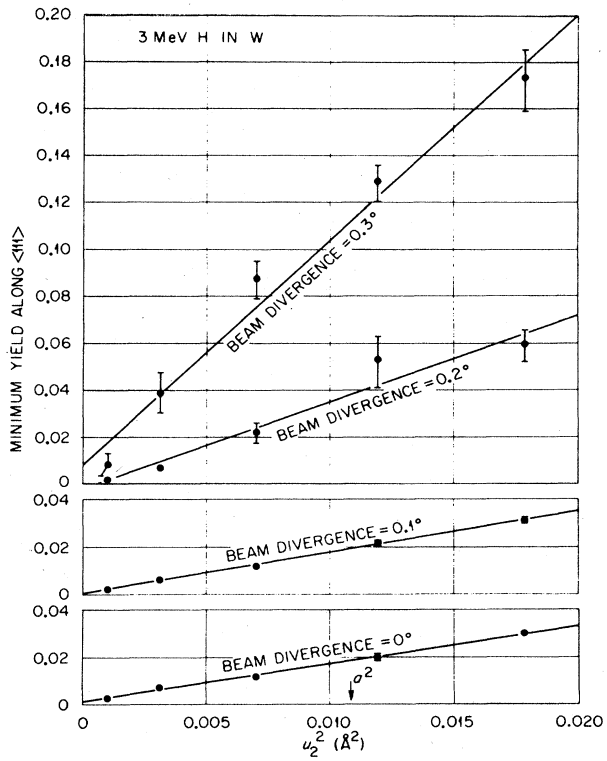

FIG. 18. Axial minimum yield χ_{min}, calculated [Ba71] as a function of the square of the thermal vibration amplitude for several beam divergences. The depth range considered is 340–1370 Å.

the distance measured in the plane normal to the axis of the channel) from the trajectory to the row containing the ith atom, and the number of collisions $\mathfrak{N}_c$ is given by the number of calculated trajectories multiplied by the thickness of the section of crystal being considered and divided by d. By evaluating Eq. (2.65) for a succession of thin slices parallel to the surface of the crystal, the depth dependence of P_{NE} can be obtained. At the crystal surface, $P_{NE} = 1$.

In the part of his calculations in which he studied $\psi_{1/2}$ and χ_{min}, Barrett treated mostly the case of 10-MeV protons incident on tungsten. He assumed that the beam divergence and the mosaic spread were zero. He considered a depth range of 0–5500 Å in order to average over surface oscillations in the value of P_{NE} (as discussed more fully in Sec. 2.4e1) and calculated for temperatures of 4.2, 298, 700, 1200, and 1800°K. The Debye temperature of W was taken to be 400°K [Gray63]. Some other authors, e.g., Andersen [An67, 72a], use a value of 310°K [Lo48]. Figure 17 shows the calculated values of $\psi_{1/2}$ at these temperatures. The curve through the points for axial channeling was obtained from

$$\psi_{1/2} = kF_{RS}(mu_1/a)\psi_1, \tag{2.66}$$

where F_{RS} is defined in Eqs. (2.18) and (2.36) and is plotted in Fig. 117, and the values $k = 0.83$ and $m = 1.2$ were found by adjustment to give the best fit to the points. Note that if Eq. (2.57), based on the simple continuum model, is evaluated for the Molière potential, the form obtained for $\psi_{1/2}$ is the same as Eq. (2.66) with $k = 1$ and $m = 1.18$.

Barrett also computed the dependence of $\psi_{1/2}$ on E and found the inverse-square-root law to be valid to within small errors. The best fit of Eq. (2.66) to the energy-dependent calculations was found with $k = 0.80$ and $m = 1.2$. The values of $\psi_{1/2}$ calculated from Eq. (2.66) with $k = 0.80$ and $m = 1.2$ were compared by Barrett with 35 different experimental values obtained with a great variety of targets, ion-beam species, energies, and orientations. The fit obtained was very good, in general calculated and measured values agreed to within 5 or 10%. This level of agreement is about as good as can be hoped for since most of the experimentally determined values were not accompanied by a specification of the direction (the so-called tilt plane) along which the scan through the axis was made. Variations in the direction of this tilt plane can give rise to variations of several percent in the measured values of $\psi_{1/2}$ [An68]. It is tempting to interpret Eq. (2.66) to mean that the distance of closest approach to a row is $\rho_c = mu_1$ and that the factor k relates ψ_c to $\psi_{1/2}$. However, in his paper Barrett states that the values of ρ_c that he determined did not have either a simple linear or a quadratic dependence on u_1.

The axial minimum yields calculated by Barrett for 3-MeV protons incident along the $\langle 111 \rangle$ of W are shown in Fig. 18 for various temperatures and for various beam divergences. It was found that, to a good approximation,

$$\chi_{min} = C_R(\Delta)Nd\pi u_2^2, \tag{2.67}$$

where the coefficient $C_R(\Delta)$ is a function of the standard deviation Δ of the assumed Gaussian distribution of incident-beam directions. For a perfectly collimated

beam, $C_R(0) = 3.0$. Barrett discussed the large value of C_R and the negligible magnitudes of any temperature-independent terms in Eq. (2.67), in contrast to Eq. (2.47), by considering two factors: an effectiveness factor and a density of trajectories factor. These together with their product are plotted in Fig. 19 as a function of transverse energy. For particles with transverse energies near to the maximum value of the continuum potential energy (~650 eV), the effectiveness factor for nuclear encounters is greater than unity. On the other hand, trajectories with low transverse energies are very numerous and consequently make a substantial contribution to $\chi_{\min}$ even for transverse energies lower than the continuum potential energy (~400 eV) evaluated at a distance u_2 from a row. In Fig. 19(c), the data for the simple geometrical model were obtained on the assumption that the effectiveness factor is 1 for all trajectories that strike within a distance u_2 from the row and is 0 for all others. This leads to $\chi_{\min} = Nd\pi u_2^2$, about a factor of 3 smaller than the Monte Carlo results. The result for the continuum-row model is about two-thirds that for the discrete-lattice model. The difference arises mostly from those trajectories that have been shifted upward in transverse energy, and hence to higher effectiveness factors, by strong collisions in the Monte Carlo calculations.

Barrett also found that the computed values of $\chi_{\min}$ were energy dependent. This is shown in Fig. 20(c) together with curves representing a generalized expres-

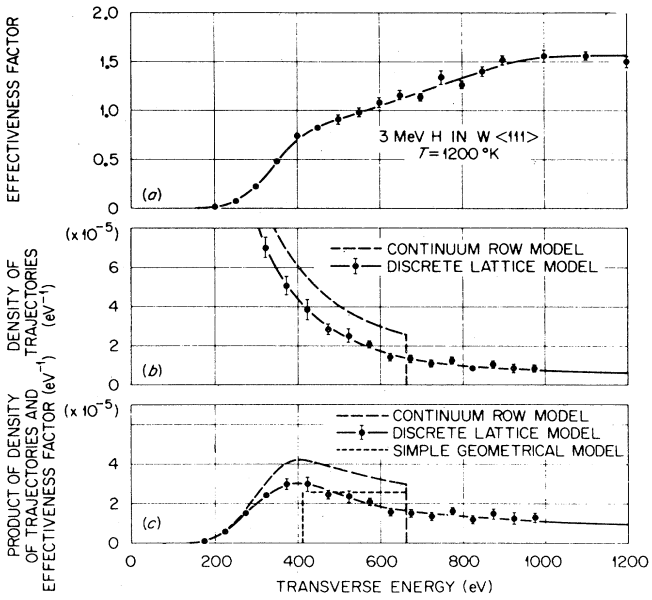

FIG. 19. Factors contributing to the calculated minimum yield for 3-MeV protons in the ⟨111⟩ direction of W plotted as functions of the proton transverse energy [Ba71].

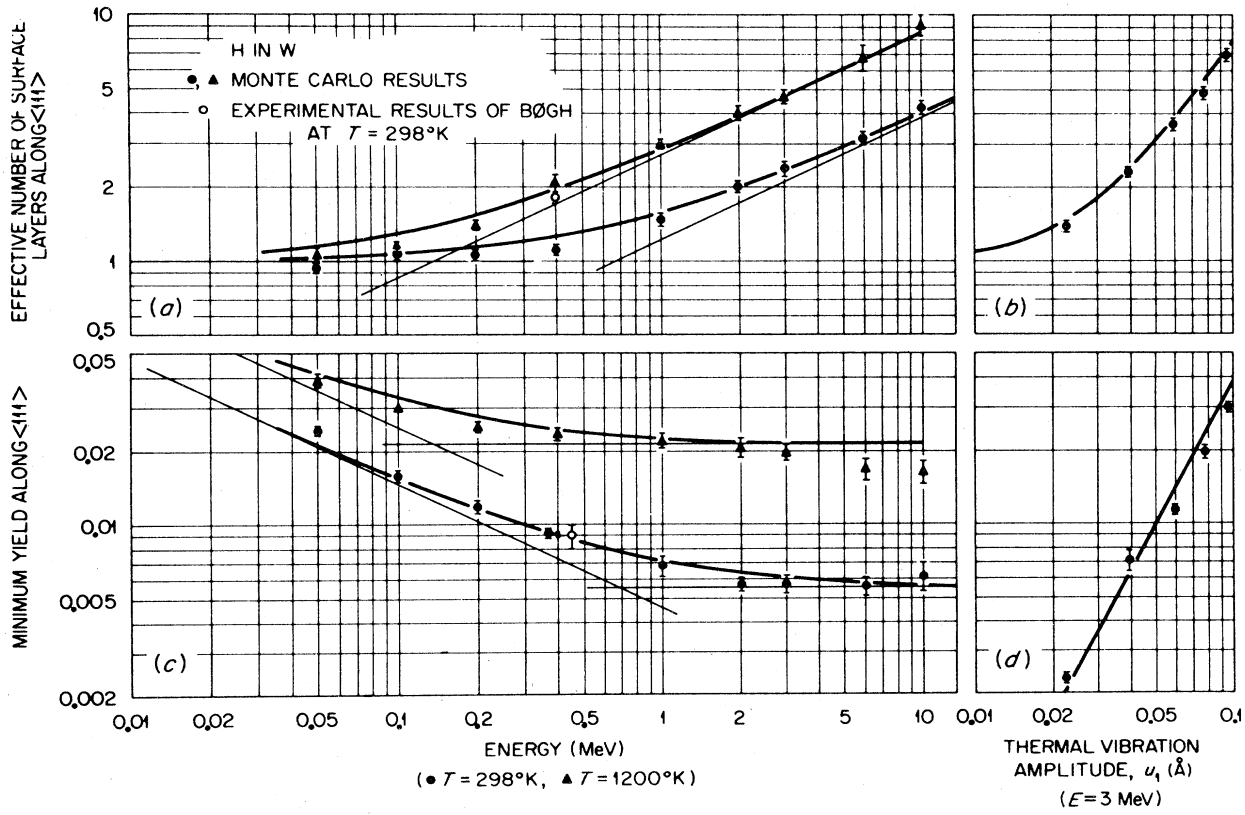

FIG. 20. The E and u_1 dependences of the calculated values of minimum yield and effective number of surface layers in ⟨111⟩ axial channeling of protons in tungsten [Ba71]. The experimental result of Bøgh [Bø67a] is shown for comparison.

sion which he found to fit the results of his calculations. This equation is

$$\chi_{\min} = C_R(\Delta) N d\pi u_2^2 (1 + \zeta^{-2})^{1/2}, \tag{2.68}$$

where

$$\zeta = 2.2 u_1/(\psi_{1/2} d). \tag{2.69}$$

The forms of Eqs. (2.68) and (2.69) were suggested on the ground that the value of $\chi_{\min}$ would be expected to be related to L, the effective number of surface layers contributing to the surface peak. Examples of surface peaks will be seen below in Figs. 25 and 26; the explanation for these is that P_{NE}, given by Eq. (2.65), is unity at the first layer in the crystal and then decreases rapidly with depth in the crystal because of the screening effect of the first few layers. The number L is defined as the area under the surface peak in a plot such as Fig. 25 divided by the spacing d between atoms in a row. At low energies, the screening by the first layer is totally effective and hence $L = 1$. At higher energies it might be expected to be of the form $L = \zeta$ with $\zeta \propto u_1/(\psi_{1/2} d)$. These two extremes of the energy range can be connected by

$$L = (1 + \zeta^2)^{1/2}, \tag{2.70}$$

where the value of ζ is as given in Eq. (2.69). Figures 20(a) and (b) show the values of L calculated from the areas under the surface peaks (points) and their fit to the curves representing Eq. (2.70). If one postulates that L and $\chi_{\min}$ are related by

$$\chi_{\min} \propto L\psi_{1/2} \propto L/\zeta, \tag{2.71}$$

this then leads to Eq. (2.68). At high energies ($\psi_1 \ll u_2/d$) Eq. (2.68) reduces to the form given in Eq. (2.67). Mainly because of difficulties in obtaining undamaged clean surfaces on crystals, there exist very few experimental data to compare with Eq. (2.68). A further source of difficulty is the fact that the calculated values of $\chi_{\min}$ assume a certain depth range in the crystal, whereas the measured values are usually determined for a fixed energy loss.

An amorphous surface region will increase $\chi_{\min}$ by an amount χ_3, which can be estimated by methods suggested by Lindhard [Li65] and Barrett [Ba71]. If it is assumed that scattering through an angle of $\psi_{1/2}$ or greater is required for a contribution to $\chi_{\min}$, the resulting estimate of χ_3 is

$$\chi_3 = \sum_s n_s N d\pi [Z_1 Z_s e^2/(E\psi_{1/2})]^2, \tag{2.72}$$

where the index s runs over the types of atoms in the surface region, Z_s is the atomic number, and n_s is the number of layers of type s. The contribution of the amorphous surface layer to L is

$$L_3 = \sum_s n_s (Z_s/Z_2)^2. \tag{2.73}$$

Barrett made Monte Carlo calculations on the effect of amorphous surface layers and the results agreed well with Eqs. (2.72) and (2.73). He pointed out that by making simultaneous measurements of $\chi_{\min}$ and L over a range of energies, it should be possible to determine the contributions to each from the amorphous surface layers and from the underlying lattice itself.

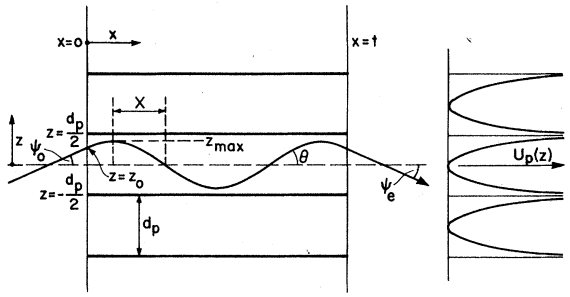

FIG. 21. Schematic diagram of planar channeling and the associated continuum potentials.

2.4d2. Planar case

The motion of a particle channeled between two planes is much easier to treat analytically in the continuum model than is the more complex motion of axially channeled particles. In the approximations used in this section, the motion is a relatively simple oscillation in the z direction normal to the planes (Fig. 21). There will be conservation of the transverse energy which, if we use the static continuum potential energy function defined in Eq. (2.31), can be written

$$E_\perp = E\varphi^2 + U_{PS}(z), \tag{2.74}$$

where z is the distance from the midplane of a channel to a point on the trajectory and φ is the angle between the planar direction and the trajectory at this point. Several authors (e.g., [An67; Ba68, 71; Pi69b; Ko70; Mo70c; Po71a; Ry72]) have calculated the shapes of planar channeling dips. Results obtained analytically by Poizat and Remillieux [Po71a] and from Monte Carlo calculations by Barrett [Ba71] will be quoted here for illustration.

Poizat and Remillieux made a continuum-model calculation of planar channeling. Instead of U_{PS} in Eq. (2.74), they used the temperature-dependent continuum potential that Appleton, Erginsoy, and Gibson [Ap67] derived from the Molière potential. In the form given by Barrett [Ba71], this potential at a distance ρ from an isolated plane is

$$V_{PV}(\rho, u_1) = E\psi_a^2 \sum_{i=1}^{3} \tfrac{1}{2}\gamma_i e^{\tau_i} \left\{ e^{-\beta_i \rho/a} \operatorname{erfc}\left[\frac{1}{\sqrt{2}} \left(\frac{\beta_i u_1}{a} - \frac{\rho}{u_1} \right) \right] + e^{\beta_i \rho/a} \operatorname{erfc}\left[\frac{1}{\sqrt{2}} \left(\frac{\beta_i u_1}{a} + \frac{\rho}{u_1} \right) \right] \right\}, \tag{2.75}$$

where

$$\operatorname{erfc}(x) = \frac{2}{\sqrt{\pi}} \int_x^\infty e^{-t^2} dt \tag{2.76}$$

is the complementary error function, $\gamma_i = \alpha_i/\beta_i$, and $\tau_i = \beta_i^2 u_1^2/(2a^2)$ with α_i and β_i as defined in Eq. (2.2). The subscript V denotes that the atoms are considered to be

vibrating with a Gaussian probability distribution, c.f. Eq. (2.44). Poizat and Remillieux approximated the interplanar continuum potential by the sum of the contributions from the two neighboring planes. In analogy with Eqs. (2.31) and (2.41), this will be denoted by $U_{PV}^{(2)}(z, u_1)$.

As a channeled particle with transverse energy $E_\perp$ penetrates a crystal, its distance from the midplane varies from $z = z_{\max}(E_\perp)$ to $z = 0$ as it moves forward a distance

$$X(E_\perp, u_1) = \int_0^{z_{\max}(E_\perp)} \{E/[E_\perp - U_{PV}^{(2)}(z, u_1)]\}^{1/2} dz, \quad (2.77)$$

where $z_{\max}(E_\perp)$ is defined by

$$U_{PV}^{(2)}[z_{\max}(E_\perp), u_1] = E_\perp, \text{ for } E_\perp \leq U_{PV}^{(2)}(\tfrac{1}{2}d_p, u_1), \quad (2.78a)$$

$$z_{\max}(E_\perp) = \tfrac{1}{2}d_p, \text{ for } E_\perp > U_{PV}^{(2)}(\tfrac{1}{2}d_p, u_1). \quad (2.78b)$$

For a particle incident at initial angle ψ_0 and distance z_0 from the midplane, the transverse energy is

$$E_\perp = E\psi_0^2 + U_{PV}^{(2)}(z_0, u_1). \quad (2.79)$$

Averaged over z_0, the normalized nuclear encounter probability is

$$\chi(\psi_0, u_1) = 2\int_0^{\frac{1}{2}d_p} [X(E_\perp, u_1)]^{-1} dz_0 \int_0^{z_{\max}(E_\perp)} P(\tfrac{1}{2}d_p - z) \times \{E/[E_\perp - U_{PV}^{(2)}(z, u_1)]\}^{1/2} dz, \quad (2.80)$$

where $P(x)$ is given by Eq. (2.44).

Equation (2.80) was evaluated by Poizat and Remillieux, and the result for the case of 3-MeV protons incident at angles near the (110) plane of Si at room temperature is shown as curve (a) in Fig 22. Somewhat similar results have also been obtained by Andersen [An67], Picraux and Andersen [Pi69b], and Komaki and Fujimoto [Ko70]. The most striking features are the very high and sharp compensation shoulders on the curve. These shoulders are broadened and greatly reduced in height by multiple scattering, whereas $\chi_{\min}$ and $\psi_{1/2}$ are affected much less. Curve (b) in Fig. 22 was calculated with only nuclear multiple scattering taken into account. For the shoulder regions of the curve, this can be expected to be a reasonable assumption, and, in fact, in these regions the curves agree well with experimental results. The rather weak temperature dependence of $\chi_{\min}$ and $\psi_{1/2}$ calculated from Eq. (2.80) is also in accord with experimental observations. However, the calculated values of $\chi_{\min}$ are about two-thirds of the experimental

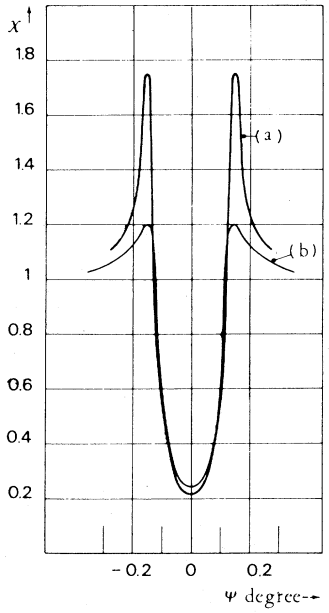

FIG. 22. Calculated planar channeling dips for 3-MeV protons incident along the (110) planes of Si at room temperature (u_1 = 0.075Å). The curves were calculated (a) without multiple scattering and (b) with multiple scattering included for a depth of 5000 Å [Po71a].

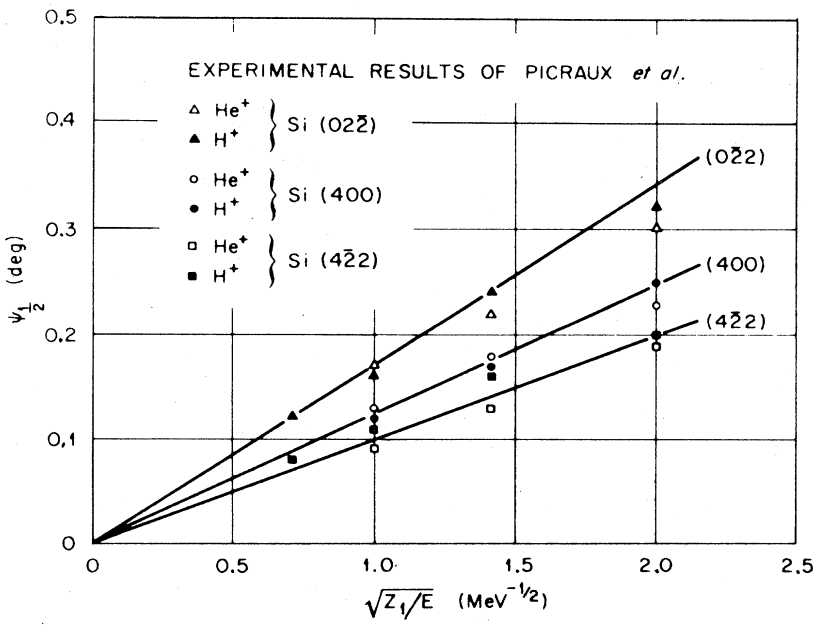

FIG. 23. Variation of planar $\psi_{1/2}$ with Z_1, E, and d_p for three planar channels in Si. The data points are those of Picraux *et al.* [Pi69a], and the straight lines are obtained from the empirical formula of Barrett [Ba71] given in Eq. (2.81) with $k = 0.72$ and $m = 1.6$.

values and those of $\psi_{1/2}$ are $\sim$10% too large. These differences are probably due to the above-average encounter probability for part of the initially unchanneled component of the incident beam [Alt70a].

In the course of his Monte Carlo calculations (outlined in Sec. 2.4d1), Barrett [Ba71] derived results for planar as well as axial channeling. The typical temperature dependence of $\psi_{1/2}$ is much weaker for planar than for axial channeling, as was seen in Fig. 17 in which the curve for planar channeling was obtained from

$$\psi_{1/2} = kF_{PS}(mu_1/a, d_p/a)\psi_a, \tag{2.81}$$

where F_{PS} is defined in Eqs. (2.25) and (2.43) and is plotted in Fig. 118, and the values $k = 0.76$ and $m = 1.6$ were found by adjustment to give the best fit to the points. Barrett also found that the inverse-square-root dependence of $\psi_{1/2}$ upon the bombarding energy held quite well for his calculations on planar channeling; the best fit to the energy-dependent values were found with $k = 0.72$ and $m = 1.6$ in Eq. (2.81). The experimentally determined dependence of $\psi_{1/2}$ on the interplanar spacing d_p is well reproduced by Eq. (2.81); an example is shown in Fig. 23. Barrett computed the values of $\psi_{1/2}$ from Eq. (2.81) with $k = 0.72$ and $m = 1.6$ and compared them with 32 different experimental values representing a wide range of combinations of target, bombarding energy, interplanar spacings, etc. The agreement was good, typically within about 10%.

The planar minimum yield calculated by Barrett for 10-MeV protons in the (110) planes of W was found to increase approximately linearly with the thermal vibration amplitude in contrast to the quadratic dependence for the axial case. The dependence of the calculated χ_{min} on E and u_1 is shown in Fig. 24 together with the effective number of surface layers L. The corresponding curves for the axial case were shown in Fig. 20. No general formula analogous to Eqs. (2.67) and (2.68) could be deduced for the planar χ_{min} from the Monte Carlo calculations. The value of χ_{min} determined experimentally for protons in the (110) planes of W by Davies *et al.* [Dav68] was found not to vary significantly in the energy range 2–6 MeV. This is consistent with the calculated weak energy dependence. The experimental result is also shown in Fig. 24. The agreement with the Monte Carlo calculation is good, in fact, much better than with the simple estimate given in Eq. (2.49).

2.4e. Depth dependence

As a beam incident in a channeling direction traverses the first layer of atoms in a crystal, there is, assuming quantum-mechanical diffraction effects to be negligible, no immediate channeling effect. Thus, for example, the yield of close-encounter processes from this first layer will be the same as for an amorphous target. However, a certain fraction of the beam that satisfies the requirements on transverse energy at the entrance to the crystal will become initially channeled as successive layers are traversed and as the ordered structure of the medium begins to assert itself. We denote this initially channeled fraction as $f_{ch}(0)$. As the beam progresses further through

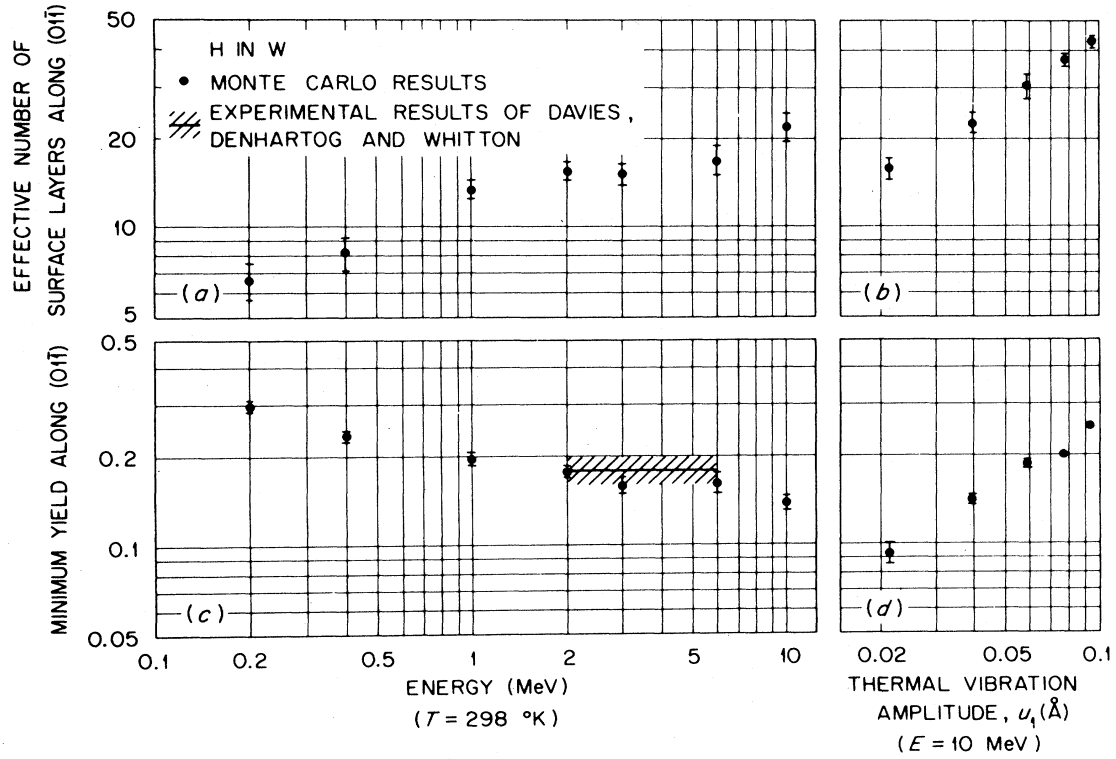

FIG. 24. The E and u_1 dependences of the calculated values of minimum yield and effective number of surface layers in (110) planar channeling of protons in tungsten [Ba71]. The experimental results of Davies *et al.* [Dav68] are shown for comparison.

the crystal, the channeled fraction decreases (becomes dechanneled) primarily as a consequence of electronic and nuclear multiple scattering. The nuclear encounter probability P_{NE} given by Eq. (2.65) also varies with depth. In the region just below the surface, typically at a depth of a few thousand angstroms, P_{NE} shows an oscillatory behavior; at larger depths, typically a few microns, P_{NE} increases because of dechanneling. These two regions of depth dependence will be discussed in Secs 2.4e1 and 2.4e2.

2.4e1. Surface oscillations

At the crystal surface, the normalized nuclear encounter probability P_{NE} in Eq. (2.65) is by definition equal to unity. At the second and successive layers that the beam encounters in the crystal, P_{NE} will be less than unity because of the screening effect of the first layer. The actual value of P_{NE} evaluated for the second layer, for example, will depend on such factors as the perfection of the crystalline structure at the surface, the thermal-vibration amplitudes, the correlations between vibrations of neighboring atoms, the lattice spacing, and the beam energy. After a few layers (in the axial case) or tens of layers (typical of the planar case), this screening effect becomes almost complete, and P_{NE} falls to a value close to zero. The initial high value of P_{NE} is referred to as the surface peak and is readily observable in Rutherford backscattering measurements, for example. The largest contribution to the surface peak comes from those particles whose initial transverse energies are too great for them to be channeled. In traversing the first few layers, the great majority of these particles scatter into small forward angles. Even though they are unchanneled, their motion in these first layers is still governed by the ordered structure of the lattice. Such particles are initially steered away from the channel walls. As they traverse the crystal they move across the center of the channel and then encounter the opposite wall where again P_{NE} reaches a peak. In his Monte Carlo calculations, Barrett [Ba71] has calculated the depth dependence of P_{NE} in the region near the surface. Figures 25 and 26 show some results for axial and planar channeling, respectively. The oscillations are more regular for the planar than for the axial case and occur approximately at intervals of $\frac{1}{2}\lambda_{ch}$, where λ_{ch} is the classical oscillation wavelength. As the beam moves into the crystal, the oscillations damp out because of a spread in the wavelengths associated with the spread in initial impact parameters and also because of the strong multiple scattering encountered by this compo-

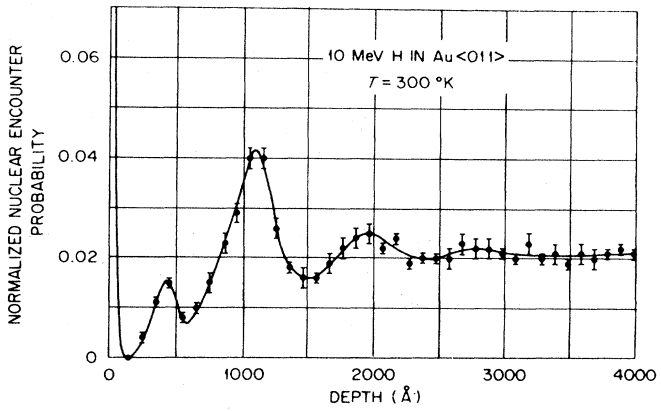

FIG. 25. Nuclear encounter probability calculated as a function of depth below the crystal surface for axial channeling [Ba71].

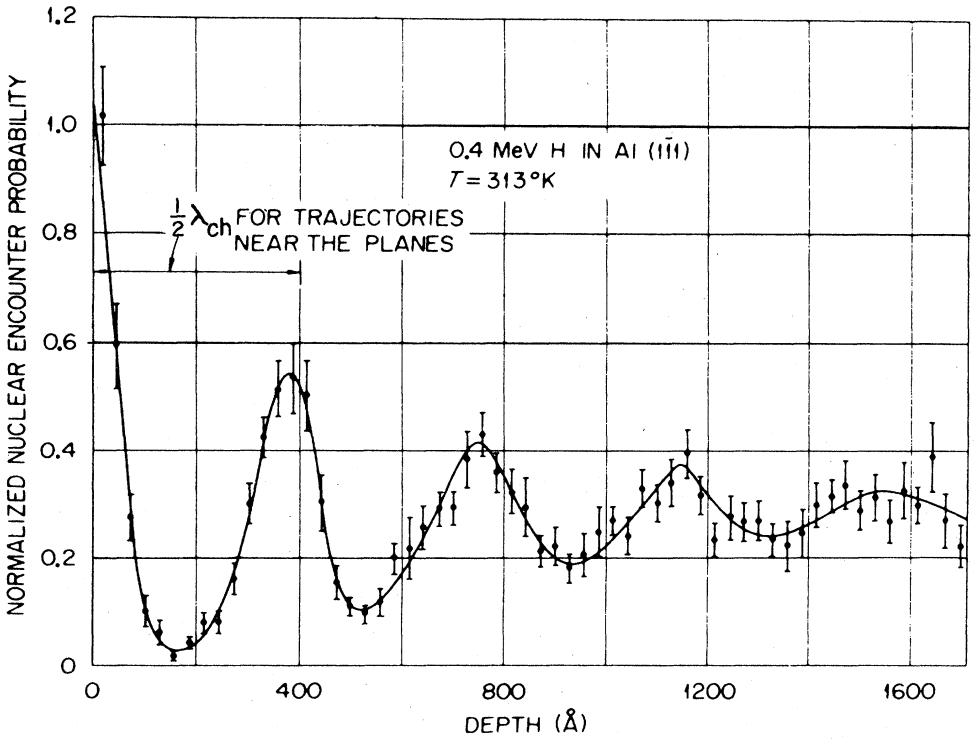

FIG. 26. Nuclear encounter probability calculated as a function of depth below the crystal surface for planar channeling [Ba71].

nent of the incident beam. For the axial case, the behavior is less regular because the motion between rows is more complex than that between planes. The depth at which the first peak shown in Fig. 25 occurs is in good agreement with that estimated by use of continuum potential energies and the assumption that it is due to collisions with the nearest-neighbor rows. Similarly, the second peak can be associated with the second-nearest-neighbor rows. The greater intensity in this peak may be due to a steering effect of the first-neighbor rows.

One can determine L, the effective number of surface layers contributing to the surface peak, by integrating the surface peak as a function of depth and then dividing by the spacing d between atoms in a row. Values of L have been computed by Barrett and are plotted in Figs. 20 and 24, for example. From a comparison between measured and calculated values of L, it is possible to extract information about the structure of the crystal surface.

In quoting values of $\chi_{\min}(0)$, it is customary to average over the surface oscillations, excluding, of course, the surface peak. Because the initially unchanneled particles can have an average nuclear encounter probability that is anomalously high, there is not necessarily a simple relationship between $\chi_{\min}(0)$ and $f_{ch}(0)$.

2.4e2. Dechanneling

Thus far, we have assumed that the transverse energy for channeled particles is a constant of their motion. This assumption is a reasonable one when considering channeling at small penetration depths, typically, up to a few thousand angstroms. However, at greater depths, the initial distribution in transverse energy becomes significantly modified through multiple scattering of the beam by the electrons and nuclei of the target and by defects and impurities in the target. In particular, the transverse energy of some of the initially channeled particles becomes larger than the critical value for stable channeling. These particles are then lost from the channeled fraction, which is thus steadily depleted as the beam progresses through the crystal. This dechanneling of the beam occurs over distances that are typically on the order of several microns for high symmetry directions.

Dechanneling was first described theoretically by Lindhard [Li65]. The treatment given in the present section will be essentially a high-energy one pertaining mainly to the Bethe–Bloch region (see Sec. 2.6a) and, in common with most discussions of the theory of dechanneling (e.g., [El67; Fel68; Kum70a; Fot70a, 71; Beh71, 72; Mor71b, 72; Bel72a, b, c; Bj72; Bond72; Pok72]), will lean heavily on concepts introduced by Lindhard in his 1965 article.

For a collimated beam of particles incident with energy E upon an amorphous target, the rate of increase of the mean-square angular deviation of the beam due to nuclear multiple scattering is given approximately by the following expression of Bohr [Boh48]:

$$(d\Omega^2/dx)_n = (M_2/M_1 E)(-dE/dx)_n, \qquad (2.82)$$

where M_1 and M_2 are the masses of the beam particles and target atoms, respectively. The rate of energy loss $(-dE/dx)_n$ due to nuclear scattering can be written [Li63,65]

$$(-dE/dx)_n = (4\pi Z_1^2 Z_2^2 e^4/M_2 v^2) N L_n, \qquad (2.83)$$

where Z_1 and Z_2 are the atomic numbers of the projectile and target atoms, respectively, v is the velocity of the incident beam, N is the number of target atoms per unit volume, and L_n is given approximately by

$$L_n = \ln[1.29 a M_2 E/Z_1 Z_2 (M_1 + M_2) e^2]. \qquad (2.84)$$

The screening distance a is defined in Eq. (2.3). Equations (2.83) and (2.84) apply when the expression in the square brackets in Eq. (2.84) is large compared with unity. This expression is approximately equal to the ratio of the screening distance to the classical collision diameter (Eq. 2.9) and, in the energy range being considered here, this ratio is certainly much greater than unity. Similarly, there is a contribution from multiple scattering due to electronic collisions:

$$(d\Omega^2/dx)_e = (m_e/2M_1 E)(-dE/dx)_e, \qquad (2.85)$$

where m_e is the electron mass and the electronic stopping power is given by

$$(-dE/dx)_e = S_e N Z_2. \qquad (2.86)$$

The electronic stopping cross section S_e can be written

$$S_e = (4\pi Z_1^2 e^4/m_e v^2) L_e. \qquad (2.87)$$

The factor L_e is approximately

$$L_e = \ln(2m_e v^2/I), \qquad (2.88)$$

where I is the mean excitation energy of the target atoms ($I \approx 10 Z_2$ eV). Section 2.6a contains a fuller discussion of energy losses.

Comparing Eqs. (2.82) and (2.85), one notes that for an amorphous medium, or for particles traveling randomly in a crystal, the electronic contribution to $(d\Omega^2/dx)$ is much smaller than the nuclear contribution by a factor of roughly $2Z_2 L_n/L_e$, which is typically on the order of a few times Z_2. From an initially well-collimated beam, there develops, due to multiple scattering, a Gaussian distribution in angular deviations φ given by

$$P_{ms}(\varphi) 2\pi\varphi d\varphi = (2\varphi d\varphi/\Omega^2)\exp(-\varphi^2/\Omega^2), \qquad (2.89)$$

where Ω^2 is found by summing Eqs. (2.82) and (2.85) and integrating over the depth x.

For particles channeled in a crystal, both the nuclear and the electronic contributions of the multiple scattering are reduced compared to the corresponding values for randomly traveling particles. Moreover, the reduction factors are dependent upon the range of impact parameters sampled by the channeled particles; i.e., there is a dependence upon the transverse energy. Further, for particles channeled with a given transverse energy, one expects the nuclear multiple scattering to be dependent upon the thermal vibration amplitude. The electronic multiple scattering should be only very weakly temperature-dependent since the electron density distribution experienced by a channeled particle does not vary much with temperature.

We consider firstly the case of axial channeling and use the approximation of isolated and randomly distributed strings of atoms; i.e., the possible influence of planes is disregarded. The transverse energy of a particle can then be written in the continuum approximation as

$$E_\perp = E\varphi^2 + V_{RS}(\rho), \tag{2.90}$$

where φ is the instantaneous angle between the particle's trajectory and the axis and $V_{RS}(\rho)$, the static continuum potential at a distance ρ from the row, is defined in Eqs. (2.14) through (2.19). For particles with a given transverse energy, the average rate of change of this transverse energy with penetration depth x is

$$\langle dE_\perp/dx\rangle = E\langle d\varphi^2/dx\rangle + \langle\varphi^2(dE/dx)\rangle, \tag{2.91}$$

where the average is taken over the area $A(E_\perp)$ in the transverse plane accessible to particles with transverse energy $E_\perp$. It is assumed here that statistical equilibrium has been reached in the sense that this accessible area is uniformly populated with particles of transverse energy $E_\perp$. The first term on the right-hand side of Eq. (2.91) gives the rate of increase of transverse energy due to multiple scattering, and the second term gives the rate of decrease due to energy loss, or damping. This latter contribution is relatively small [Bj72] as can be seen from Fig. 27 and will be ignored in the remainder of this section.

If the crystal is free of defects and impurities, then the multiple-scattering term in Eq. (2.91) may be written as the sum of nuclear and electronic contributions. It is convenient to express the transverse energy in units of the characteristic transverse energy $E\psi_1^2/2 = Z_1 Z_2 e^2/d$, where d is the spacing between atoms along the rows. Thus with

$$\varepsilon_\perp = E_\perp/(\tfrac{1}{2}E\psi_1^2), \tag{2.92}$$

Eq. (2.91) may be rewritten as

$$\langle d\varepsilon_\perp/dx\rangle = \langle d\varepsilon_\perp/dx\rangle_n + \langle d\varepsilon_\perp/dx\rangle_e. \tag{2.93}$$

Lindhard evaluated the nuclear contribution in Eq. (2.93) by considering the force fluctuations experienced by channeled particles as a consequence of thermal vibrations of the target atoms. Assuming that the vibration amplitude u_2, defined in Eq. (2.51), is small compared to the distance of the channeled particles from the rows and using Lindhard's expression for $V_{RS}(\rho)$, i.e., Eqs. (2.16) and (2.19), one finds

$$\langle d\varepsilon_\perp/dx\rangle_n = (2x_n)^{-1}\{\tfrac{1}{2}\exp(\varepsilon_\perp) + \tfrac{1}{3}\}\{1 - \exp(-\varepsilon_\perp)\}^3, \tag{2.94}$$

where

$$x_n = (C^2a^2/2u_2^2)(\pi Nd^2\psi_1^2)^{-1}. \tag{2.95}$$

Note that $\langle d\varepsilon_\perp/dx\rangle_n$ is proportional to u_2^2.

The electronic contribution to Eq. (2.93) can be found by analogy with the random case, Eqs. (2.85)–(2.88). The electronic stopping power is averaged over the area $A(E_\perp)$ taking into account the variation in the electron density distribution $n_e(\rho)$. This distribution is obtained by averaging the value given in Eq. (2.5) along the row direction. The result obtained by Lindhard is

$$\langle d\varepsilon_\perp/dx\rangle_e = (x_e)^{-1}\{1 - \exp(-\varepsilon_\perp)\}, \tag{2.96}$$

where

$$x_e = E/(\pi Z_1 e^2 L_e N d). \tag{2.97}$$

Note that $\langle d\varepsilon_\perp/dx\rangle_e$ is approximately independent of temperature.

The quantities given in Eqs. (2.91), (2.94), and (2.96) have been calculated by Björkquist *et al.* [Bj72] for axial proton channeling in W and Si. Their results are shown plotted in Fig. 27. It is worthy of note that, in contrast to the random case, the electronic contribution can be much larger than the nuclear contribution, especially for particles with low transverse energies, i.e., the best channeled particles. The use of a mean ionization potential, i.e. Eq. (2.88), in calculating the value of L_e in Eq. (2.97) leads to too small a result for $\langle d\varepsilon_\perp/dx\rangle_e$ since the channeled particles interact only very weakly with the most tightly bound electrons. A value of L_e based on a treatment in which the electrons are regarded as constituting a gas with locally varying density (curves (b) in Fig. 27) may be a better approximation.

These considerations lead to the following conceptually, if not computationally, simple picture of the dechanneling process. The initial, normalized, distribution $g(E_\perp, 0)$ of transverse energy for a beam incident parallel to a major axial direction is determined by its divergence outside the crystal, by the multiple scattering in any amorphous, e.g., oxide, layers on the crystal surface and by the transverse continuum potential energies acquired by the beam particles as they uniformly illuminate and enter the axially aligned rows of atoms. For a well-collimated beam and for a clean and structurally perfect crystal surface, the distribution $g(E_\perp, 0)$ is sharply peaked about $E_\perp = 0$; we assume that the minimum continuum potential between rows is adjusted to be zero as is done, for example, in Eq. (2.30). Under these conditions the development of $g(E_\perp, x)$ as the beam proceeds into the target will initially be determined mostly by the dominating electronic multiple scattering; the crystal is assumed to be free of defects and impurities. As the transverse energy increases, the nuclear multiple scattering plays a growing and, eventually, a dominant role. For individual beam particles the changes in trans-

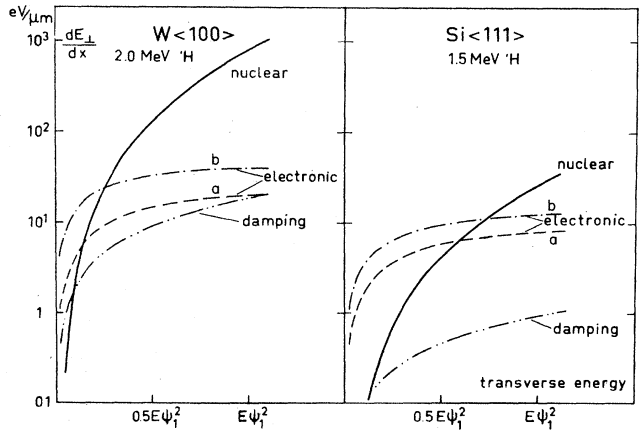

FIG. 27. The magnitude of the different contributions to $\langle dE_\perp/dx\rangle$ as a function of $E_\perp$ for 2.0-MeV protons channeled along the $\langle 100\rangle$ axis in W and for 1.5-MeV protons channeled along the $\langle 111\rangle$ axis in Si [Bj72]. The curves labeled *nuclear* are evaluated from Eq. (2.94). *Damping* refers to the second term on the right-hand side of Eq. (2.91). The curves labeled *electronic* are determined from Eq. (2.96) with (a) L_e given by Eq. (2.88) and (b) L_e calculated assuming an electron gas with locally varying density.

verse energy at successive scatterings are in the nature of a random walk process, there being a net drift toward higher transverse energies with a rate given by Eqs. (2.93)–(2.97). The distribution in transverse energy can therefore be described by a diffusion equation:

$$\frac{\partial g(E_\perp, x)}{\partial x} = \frac{\partial}{\partial E_\perp}\left(D(E_\perp)\frac{\partial}{\partial E_\perp} g(E_\perp, x)\right), \quad (2.98)$$

where $D(E_\perp)$ is a diffusion function. The validity of this diffusion approach and the functional relationship between $D(E_\perp)$ and $\langle dE_\perp/dx\rangle$ have been discussed by Lindhard [Li65] and by Bonderup *et al.* [Bond72]. Once the initial distribution $g(E_\perp, 0)$ is given, then $g(E_\perp, x)$ can be found by solving Eq. (2.98). If one makes the assumption that those beam particles with transverse energies greater than some critical value $E_{\perp,\text{crit}}$ are dechanneled, then the dechanneled fraction as a function of depth is given simply by

$$1 - f_{\text{ch}}(x) = \int_{E_{\perp,\text{crit}}}^{\infty} g(E_\perp, x)\, dE_\perp . \quad (2.99)$$

Dechanneling has been calculated in this fashion by Morita and Itoh [Mor71b, 72] by Kumakhov and coworkers [Kum70a; Bel72a, b, c] and Bonderup *et al.* [Bond72]. Figure 28 shows some results for axially channeled protons in Si and W.

The particles which dechannel at fairly shallow depths, e.g., in the first 10 μ for the case shown in Fig. 28, will be mostly those which began in the distribution $g(E_\perp, 0)$ with high values of the transverse energy. These particles have a large value of $\langle dE_\perp/dx\rangle$ determined mostly by nuclear multiple scattering. Such considerations, together with the computational difficulties involved in solving the diffusion equation, have led several authors (e.g., [Ca70, 71, 72a, b; Fot70a, b, 71; Beh71, 72; Bj72]) to adopt the so-called steady-increase approximation. In this, it is assumed that because of the rapid rate of increase of the transverse energy, the spreading introduced by diffusion is negligible in the depth required for the particles to dechannel. The rate of increase of $E_\perp$ for each particle is then set equal to $\langle dE_\perp/dx\rangle$. In this approximation, the transverse energy of a particle at a depth x is entirely determined by its initial value $E_{\perp,0}$. All particles that start off with the same value $E_{\perp,0}$ dechannel at the same depth found from

$$x(E_{\perp,0}) = \int_{E_{\perp,0}}^{E_{\perp,\text{crit}}} (\langle dE_\perp/dx\rangle)^{-1}\, dE_\perp , \quad (2.100)$$

where $\langle dE_\perp/dx\rangle$ is determined by Eqs. (2.92)–(2.97). Comparisons of the dechanneled fractions calculated this way with the values calculated including diffusion are shown in Fig. 28. The agreement is good for dechanneled fractions up to about 20%, but after that the steady-increase approximation gives dechanneled fractions which increase far too rapidly with depth.

The importance of the diffusion process has been emphasized by Bonderup *et al.* [Bond72]. Figure 29 illustrates the spreading of the calculated transverse-energy distribution with increasing depth for the case where the initial distribution is a delta function.

A somewhat different approach to the calculation of axial dechanneling has been given by Ellegaard and Lassen [El67]. Making some simplifying assumptions, these authors derived a formula which gave a good fit to their experimental data. They assumed the angular distribution of the beam inside the crystal to have the Gaussian form given by Eq. (2.89) and with

$$\Omega^2 = (x/L_1)\psi_1^2, \quad (2.101)$$

where L_1 is a constant equal to the depth required for Ω^2 to grow as large as ψ_1^2. The dechanneled fraction is then assumed to be

$$1 - f_{ch}(x) = \int_{\psi_1}^{\infty} P_{ms}(\varphi) 2\pi\varphi\, d\varphi = \exp(-\psi_1^2/\Omega^2) \quad (2.102)$$

$$= \exp(-L_1/x). \quad (2.103)$$

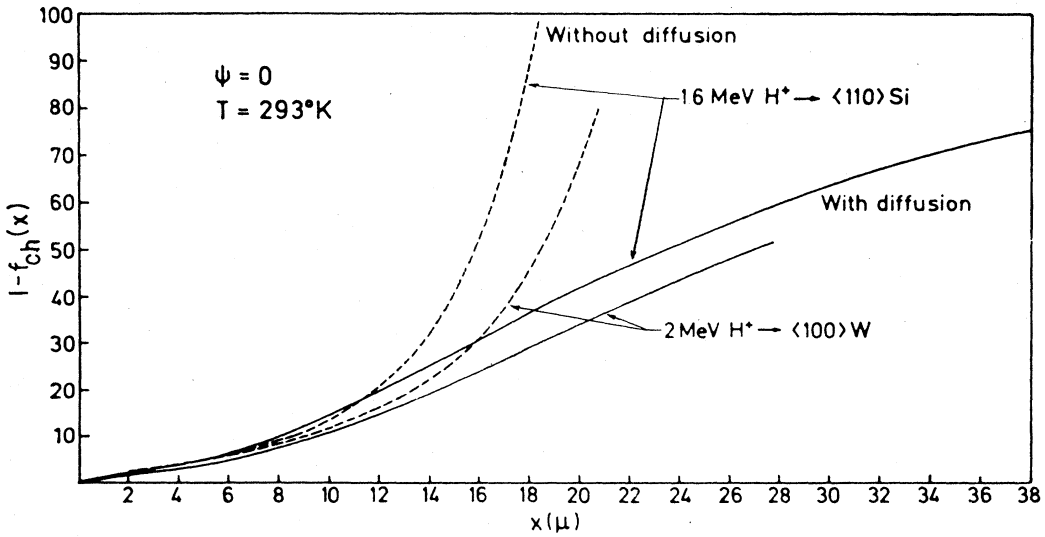

FIG. 28. Dechanneled fraction calculated as a function of depth for axially channeled protons in Si and W [Bond72]. The solid curves are from solution of the diffusion equations, and the dashed curves are calculated assuming a steady increase in transverse energy. The critical value of the transverse energy, see Eq. (2.99), used in the calculation is $E_{\perp\text{crit}} = V_{RS}(u_2)$.

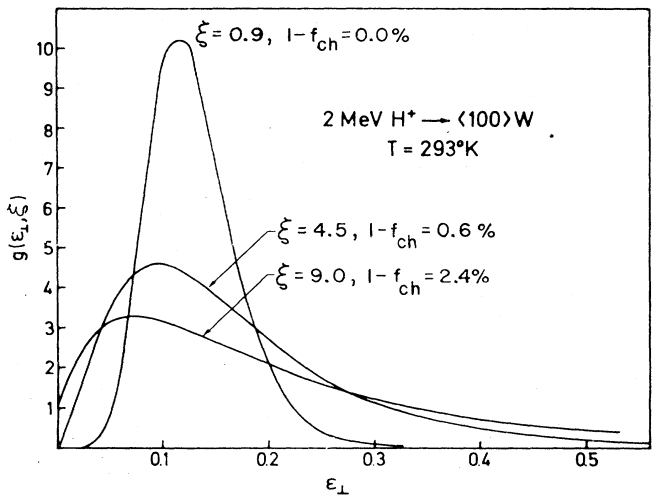

FIG. 29. Development of the distribution in transverse energy calculated for axially channeled protons in W [Bond72]. The energy and depth coordinates $\varepsilon_\perp$ and ξ are given in units of $\frac{1}{2}E\psi_1^2$ and x_n, respectively, see Eqs. (2.92) and (2.95). The initial distribution is taken as a delta function; i.e., $g(\varepsilon_\perp, 0) = \delta(\varepsilon_\perp - \varepsilon_{\perp,0})$, where $\varepsilon_{\perp,0} \approx 0.1$.

The minimum yield $\chi_{\min}(x)$ is then calculated on the assumption that it contains contributions both from the dechanneled beam with an effectiveness factor of unity and from the channeled beam with an effectiveness factor equal to $\chi_{\min}(0)$. This gives

$$\chi_{\min}(x) = \exp(-L_1/x) + [(1 - \exp(-L_1/x)]\chi_{\min}(0) \tag{2.104}$$

$$= \chi_{\min}(0) + [1 - \chi_{\min}(0)]\exp(-L_1/x). \tag{2.105}$$

For an amorphous medium, Eqs. (2.82) and (2.83) show that the distance required for the mean-square nuclear multiple scattering angle to grow as large as ψ_1^2 is approximately given by

$$l_n = 2/\pi N d^2 L_n \psi_1^2. \tag{2.106}$$

If one makes the rough approximation that the density of target atoms encountered by the channeled beam is about $\chi_{\min}(0)$ times the total density N, then

$$L_1 = l_n/\chi_{\min}(0). \tag{2.107}$$

With this value inserted into Eq. (2.105) Ellegaard and Lassen obtained excellent agreement with their axial dechanneling data obtained for proton bombardment of Bi at two different temperatures. Fujimoto and co-workers [Fuj70, 71a, b; 72b] have somewhat extended the theory of Ellegaard and Lassen by taking into account the beam divergence and surface effects; some results are given in Sec. 4.21.

For planar dechanneling, considerations apply similar to those already discussed for the axial case. A diffusion model for the escape of particles from planar channels was developed by Feldman *et al.* [Fel68] (see also [Th68b]). These authors wrote a diffusion equation for the distribution $n_{ch}(\theta, x)$ of crossing-angles θ (see Fig. 21) for planar channeled particles as a function of the depth x:

$$\partial n_{ch}(\theta, x)/\partial x = D[\partial^2 n_{ch}(\theta, x)/\partial\theta^2], \tag{2.108}$$

with the boundary conditions

$$n_{ch}(\psi_c, x) = n_{ch}(-\psi_c, x) = 0 \tag{2.109}$$

and

$$n_{ch}(\theta, 0) = \delta(\theta - \psi_0), \tag{2.110}$$

where ψ_0 is the angle of incidence and ψ_c is the critical angle for channeling. D is a diffusion constant. Morita [Mor72] has performed a similar calculation but introduced a diffusion function $D(\theta, x)$. These equations have analytical solutions. Leaving D as an adjustable parameter, Feldman *et al.* were able to obtain good fits to a variety of experimental data on planar dechanneling. For depths greater than a few microns, the calculated expression for the channeled fraction becomes approximately

$$f_{ch}(x) = \text{const. } \exp(-0.693x/x_{1/2}), \tag{2.111}$$

where $x_{1/2}$, the half-thickness for dechanneling, is proportional to ψ_c^2/D. If the diffusion constant is taken to be proportional to the average rate of increase of the mean square multiple-scattering angle, then, as can be seen from Eqs. (2.82)–(2.87), it should also be proportional to E^{-2}. This then predicts

$$x_{1/2} = \text{const. } E, \tag{2.112}$$

which is in good accord with experimental data on planar dechanneling (e.g., [Fel68; Dav68, 72a; Ca72a]).

Campisano *et al.* [Ca72a] have evaluated the nuclear and electronic multiple scattering contributions to planar dechanneling. They find that the electronic part dominates over a wide range of transverse energy. This is in sharp contrast with the axial case. The difference can be largely attributed to the fact that planar continuum potentials are generally not as shallow as axial ones, and channeled particles therefore do not approach the walls so closely. The electronic dechanneling contribution and the planar critical angle are only very weakly temperature dependent. Hence, one expects planar dechanneling not to exhibit a strong temperature dependence, and this expectation is borne out by experiment. Dechanneling is discussed further in Sec. 4.2a.

Although the present theoretical descriptions of dechanneling predict qualitatively the observed dependence upon various experimental parameters (e.g., the rate of dechanneling decreases with increasing E and M_1 and increases with higher temperatures), detailed comparisons with experiment leave much to be desired. There is at present no general formula capable of predicting depth-dependent yields. Figure 30 shows a comparison between theory and experiment typical of that presently achievable.

We conclude this section by listing some of the more obvious reasons for the generally poor agreement between theory and experiments on dechanneling:

(a) The calculated contribution of electronic multiple scattering is sensitively dependent upon the expression used for the electron-density distribution. Expressions used thus far are probably not very accurate at large distances.

(b) Planar effects are ignored in most calculations on axial dechanneling. However, experiments indicate that the feeding of particles from axial into planar channels is

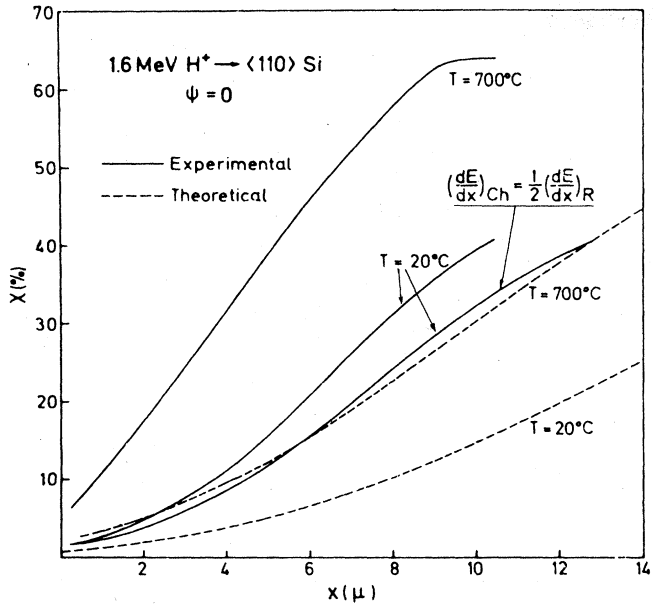

FIG. 30. Comparison of theoretical and experimental yield curves for axial channeling in Si at two temperatures [Bond72]. The experimental curves are for wide-angle Rutherford scattering, the top two are based on $\varepsilon = 1$, and the lower one is based on $\varepsilon = 1/2$, where $\varepsilon = (dE/dx)_{ch}/(dE/dx)_{random}$. The theoretical curves are calculated using diffusion theory; see Eqs. (2.98) and (2.99).

an important dechanneling mechanism (see, e.g., [Del73]).

(c) The calculated dechanneling is sensitive to the choice of $E_{\perp,crit}$. Various choices have been made. Some of these have included temperature-dependent effects; others have not.

(d) The assumption, implicit in Eq. (2.94), that u_2 is small compared to the distance of the channeled particles from the rows can be seriously in error for particles with high transverse energies.

(e) Dechanneling depends sensitively on the beam divergence, on the effects of amorphous surface layers and on the presence of defects and impurities inside the crystal. There is also evidence that strain in the crystal can strongly affect dechanneling (e.g., [Fel70a]). Factors such as these presumably account for the fact that even for Si targets (easily obtainable in the form of highly perfect crystals with low defect and impurity concentrations) experimental results on dechanneling determined in different laboratories differ markedly when comparisons are made for the same beam particles, energies, orientations and temperature (e.g., [Fot71; Bond72; Fon72]). The influence of defects and impurity atoms on dechanneling is discussed in Secs. 6.2 and 6.3. The effects of beam divergence and of surface layers have been treated by several authors (e.g., [Ca71; Fuj71a; Rim71, 72a; Bj72]; see also Sec. 6.4). For very thin amorphous surface layers, plural scattering theory (e.g., [Kei60; Mey71]) can be applied.

(f) In most theoretical treatments, it is usually assumed that rechanneling can be neglected. That is, the probability for transitions from the random beam into the aligned beam is assumed to be small. Morita and Itoh [Mor71b] have indicated that this assumption may be in error especially when χ_{min} is large.

(g) Most theoretical treatments derive the dechanneled fraction $1 - f_{ch}(x)$ as a function of depth, whereas most experiments measure the energy spectrum of particles Rutherford scattered through wide angles and compare the results for aligned and random orientations. Figure 31 illustrates schematically the type of data acquired in typical Rutherford backscattering experiments. The measured energy E^* of the detected particles is given in units of $K_S E$, where K_S is the ratio of the scattered to the incident energy in elastic scattering, viz.,

$$K_S = \left(\frac{M_1 \cos\theta + (M_2^2 - M_1^2 \sin^2\theta)^{1/2}}{M_1 + M_2} \right)^2, \qquad (2.113)$$

where θ is the laboratory scattering angle and we assume $M_1 < M_2$. Figure 32 shows a typical history of a dechanneled particle that is detected in a backscattering measurement. If the particle is initially well channeled, the transverse energy at $x = 0$ will be small. So too will the channeled stopping power, perhaps as little as one third of the random value (see Sec. 4.3b). As the particle

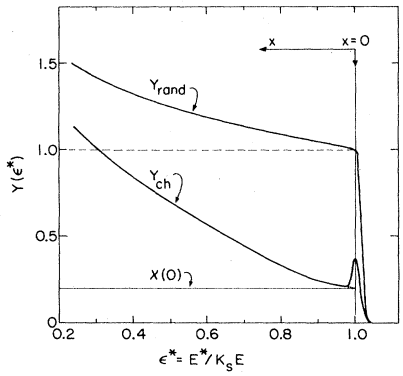

FIG. 31. Schematic illustration of the normalized random and aligned spectra observed in typical wide-angle Rutherford scattering measurements. The abscissa gives the detected energy in units of $K_S E$, where K_S is defined in Eq. (2.113).

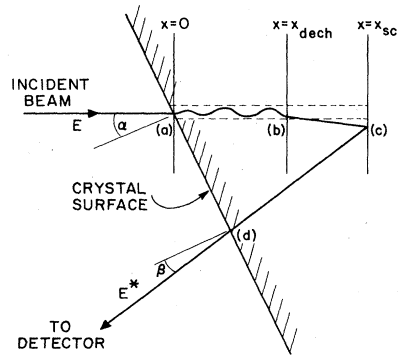

FIG. 32. Schematic diagram of the sequence of events in the dechanneling of a particle and its detection in a backscattering measurement. The incident beam lies in a channeling direction. The emerging particle is assumed not to come out in a channeling direction. The particle dechannels at point (b) and suffers a large-angle Rutherford scattering at point (c).

penetrates deeper, its transverse energy diffuses to higher values and so does the rate of energy loss. At some depth, point (b) in Fig. 32, the particle dechannels and with high probability scatters through only a very small angle. In the neighborhood of the point of dechanneling, the rate of energy loss may be higher than the random value. The particle then proceeds on a random path until, as at point (c) in Fig. 32, it suffers a large-angle scattering. The cross section for this scattering is usually strongly energy dependent ($\sim E^{-2}$ for Rutherford scattering). Immediately after the scattering the energy of the particle is reduced by the factor given in Eq. (2.113), $\theta \approx \pi - \alpha - \beta$, where the angles α and β are shown in Fig. 32. Along the return path to the crystal surface, the particle experiences the energy-dependent stopping power characteristic of an amorphous medium. Obviously there is no one-to-one correspondence between the detected energy E^* and the depth at which dechanneling occurs. Nor is there such a correspondence between E^* and the depth at which backscattering occurs. For a given value of E^*, there is a spread in possible dechanneling and backscattering depths, and this spread grows from zero at the surface to larger values for lower detected energies. In order to be able to compare experimental results obtained at different laboratories and at different energies and also to make some comparisons with theory, dechanneling data obtained via backscattering measurements are usually analyzed according to the so-called Aarhus convention, in which it is assumed that the random stopping power applies to both the ingoing and outgoing trajectories. With this assumption, the depth of scattering is uniquely determined, within the uncertainties due to straggling and the energy resolution of the detector, by the relation

$$E^*(x_{sc}) = K_S[E + \int_0^{x_{sc}} (dE/dx)\,dx] + \int_0^{x_{sc}(\cos\alpha/\cos\beta)} (dE/dx)\,dx, \qquad (2.114)$$

where dE/dx is the appropriate energy-dependent random stopping power along the trajectory shown in Fig. 32. It is widely appreciated that sizable errors are liable to be incurred in comparing theory with experimental data analyzed using a depth scale derived from Eq. (2.114). One of the curves in Fig. 30 demonstrates that lowering the stopping power along the incoming part of the trajectory to one-half the random value can have quite a large effect on the dechanneling rate deduced from an experiment. It is common procedure to determine the depth-dependent yield $\chi(x)$ from data such as those shown in Fig. 31 by evaluating

$$\chi(x) \approx Y_{\rm ch}(\varepsilon^*)/Y_{\rm rand}(\varepsilon^*), \qquad (2.115)$$

where $\varepsilon^* = E^*/K_S E$ and x is related to E^* according to Eq. (2.114). (Some authors make corrections for the energy dependence of the Rutherford scattering cross section.) There is some danger in treating the quantity given in Eq. (2.115) as representing the dechanneled fraction of the beam. The Monte Carlo calculations of Barrett [Ba71] and the transmission measurements of Altman *et al.* [Alt70a] both indicate this. For planar channeling, Altman *et al.* cite a case where the value of $\chi_{\rm min}(0)$ is about three times as large as the initially dechanneled fraction, $1 - f_{\rm ch}(0)$. This is thought to be due to the abnormally high scattering probability for many of the initially unchanneled particles.

An interesting attempt has been made by Jack [Ja72] to remove some of the ambiguities inherent in the usual type of analysis of backscattering data. He assumed that in a channeled energy spectrum of the type illustrated in Fig. 31, the contribution due to the dechanneling of initially channeled particles is

$$Y_{\rm dech}(\varepsilon^*) = Y_{\rm ch}(\varepsilon^*) - \chi(0) Y_{\rm rand}(\varepsilon^*). \qquad (2.116)$$

He then attempted to reproduce the distribution $Y_{\rm dech}(\varepsilon^*)$, determined from measurements of the quantities in Eq. (2.116), with a calculated one using various trial functions for the depth dependence of the dechanneling rate. He performed a detailed computer calculation allowing the channeled stopping power to vary and including such effects as the energy variation of the Rutherford scattering and the contributions from all the combinations of dechanneling and backscattering depths capable of producing a given value of ε^*. Excellent reproduction of the experimental data was obtained when he used a channeled fraction exponentially decaying with depth. This was interpreted as suggesting that the channeled particles eventually get dechanneled by discrete collisions with thermally displaced atoms.

2.4f. Distribution of particle flux

The existence of surface oscillations (Sec. 2.4e1) indicates that the flux of beam particles in the region just below the surface is far from uniform both in depth (x) and in position ($\mathbf{r}$ for the axial case, z for the planar case) on the transverse plane. Thus, for example, in planar channeling (see Fig. 26) the existence of a peak in P_{NE} at $x = \frac{1}{2}\lambda_{\rm ch}$, where $\lambda_{\rm ch}$ is the classical wavelength of the oscillating channeled trajectories, implies that there should be a peak in the particle flux at $x = \frac{1}{4}\lambda_{\rm ch}$, $z = 0$, since, for zero incidence angle, most of the beam particles will cross the center of the channel at about $x = \frac{1}{4}\lambda_{\rm ch}$. From statistical arguments Lindhard [Li65] has shown that, as the beam progresses more deeply into the crystal there is a trend towards equilibrium on the transverse energy shell. That is, at sufficiently large depths, particles of a given transverse energy are distributed uniformly over the area, in the axial case, or in the region of z, in the planar case, energetically accessible to them in the transverse plane. Lindhard has given some simple estimates of the depth required to reach equilibrium. However, values found experimentally (e.g. [Ar72]) are sometimes as much as ten times larger than these estimates. Typically, depths of a few microns are needed to reach equilibrium although the distance required varies markedly with factors such as the incident energy E and the crystal orientation.

For depths where equilibrium has been attained, the flux distribution can be calculated analytically. Thus, in the axial case, one can obtain the normalized distribution in transverse energy $g(E_\perp, x)$ by the methods discussed in the previous section. Then the normalized particle flux is

$$F(\mathbf{r}, x) = \int_{U_{RS}(\mathbf{r})}^{\infty} \frac{g(E_\perp, x)}{A(E_\perp)}\,dE_\perp, \qquad (2.117)$$

where $A(E_\perp)$ is the area in the transverse plane accessible to a particle with transverse energy $E_\perp$ and we have

employed the static continuum potential $U_{RS}(\mathbf{r})$ given by Eq. (2.30); we neglect the small effect due to the particles spending somewhat longer times near the channel walls than near the center of the channel. The normalization in Eq. (2.117) is such that $F(\mathbf{r}, x) = 1$ corresponds to the flux just before the beam enters the crystal; thus for random incidence, $F(\mathbf{r}, x) \approx 1$ at depths where multiple scattering has not dispersed the beam too much. Clearly, if $g(E_\perp, x)$ is peaked toward low transverse energies, the flux distribution will be sharply peaked near the center of the channel and in this region can attain values many times the random value. All of the factors mentioned in the previous section as influencing $g(E_\perp, x)$ also have an effect upon the flux peaking. In particular, the extent to which flux peaking occurs is highly sensitive to effects such as beam energy and divergence, amorphous surface layers, crystal defects and impurities, and temperature. In addition, flux peaking depends on the detailed shape of the potential since this influences the denominator in Eq. (2.117). This latter fact offers interesting possibilities in determining the potential at large distances from crystal atoms.

If one makes the greatly simplifying assumption that the transverse energy distribution is unaltered from its form at $x = 0$, and if we let A_i represent the area inside the ith potential contour (see Fig. 33) then Eq. (2.117) reduces to

$$F_i = \int_{A_i}^{A_0} dA/A = \ln(A_0/A_i), \qquad (2.118)$$

where F_i is the flux at the ith contour, A_0 is the cross-sectional area of the channel, and the incidence angle is assumed to be zero [An71a]; for analytical treatments of flux peaking effects, see also [Kal68; Kum70b, 72a, b, c]. Equation (2.118) gives a flux distribution sharply peaked towards zero transverse energy; F_i diverges logarithmically towards infinity at the channel center. In practice, electronic multiple scattering, if nothing else, would give the particles some transverse energy at the channel center and thus reduce the flux peak to some finite value.

Channeling techniques are widely used in locating dopant and impurity atoms in host crystals (see Sec. 6.2). Since the Rutherford scattering yield, for example, from such atoms is proportional to the local particle flux, an understanding of the flux distribution and the ways in which it varies with parameters such as depth, beam divergence, and incidence angle, are of central importance in these applications.

The significance of flux peaking in atom location measurements has prompted several authors (e.g., [Al70, 71, 72; Va71; Car72; Mo72]) to perform Monte Carlo computer calculations on the effect. Such computations are especially valuable in the depth region just below the surface where analytical methods of calculation are not readily applicable. Because of the sensitivity of flux peaking to factors such as thermal vibrations, nuclear and electronic energy losses, and multiple scattering, it is important to include them in calculations. Figures 34, 35, and 36 illustrate some of the results obtained in Monte Carlo calculations by Morgan and Van Vliet [Mo72]. Pronounced depth oscillations occur (Fig. 35) in the calculated midchannel flux; these may be compared with surface oscillations such as those shown in Fig. 25. As expected, these oscillations get washed out with increasing depth and as the transverse energy distribution is broadened either by multiple scattering or by poorer beam collimation. Figure 36 shows the effect of varying the incidence angle. The midchannel flux shows a very rapid falloff with increasing ψ_0. For positions off the channel center, the flux varies in a more complex fashion with incidence angle. These effects are discussed further

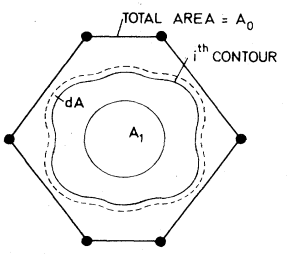

FIG. 33. Flux peaking effect in the ⟨110⟩ axial channel of Si. The diagram illustrates the area accessible to particles entering at a given height, the ith contour, on the transverse potential energy surface [An71a]. The area A_1 indicates the central flat portion of the channel potential that is accessible to the best-channeled particles, whose transverse energies are determined mainly by multiple scattering and beam divergence.

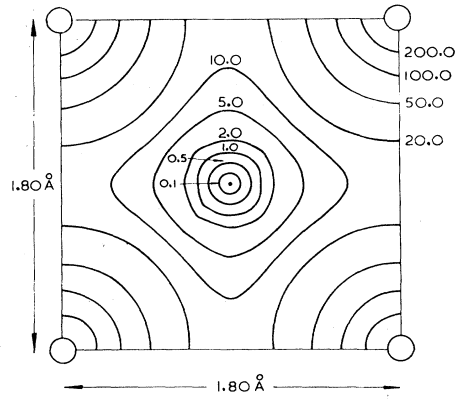

FIG. 34. Static continuum potential contours (Molière potential) for helium ions in the ⟨100⟩ axial direction of Cu [Mo72]. The energies are given in eV.

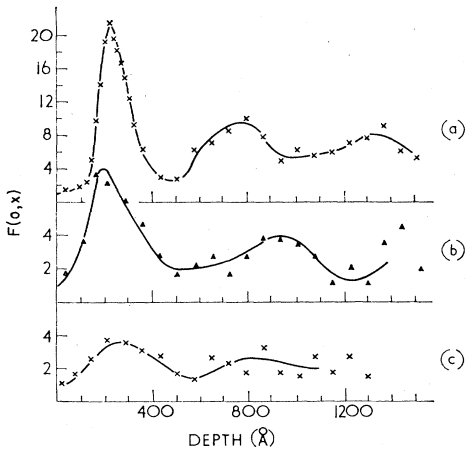

FIG. 35. Depth variation of the calculated mid-channel flux $F(0, x)$ of 1-MeV alpha particles in the ⟨100⟩ axial channel of Cu [Mo72]. The potential contours are shown in Fig. 34. The curves are (a) no multiple scattering included (b), multiple scattering, energy losses, thermal vibrations ($T = 273°K$) and beam divergence ($\pm 0.06°$) included, and (c) as for (b) but with a beam divergence of $\pm 0.23°$.

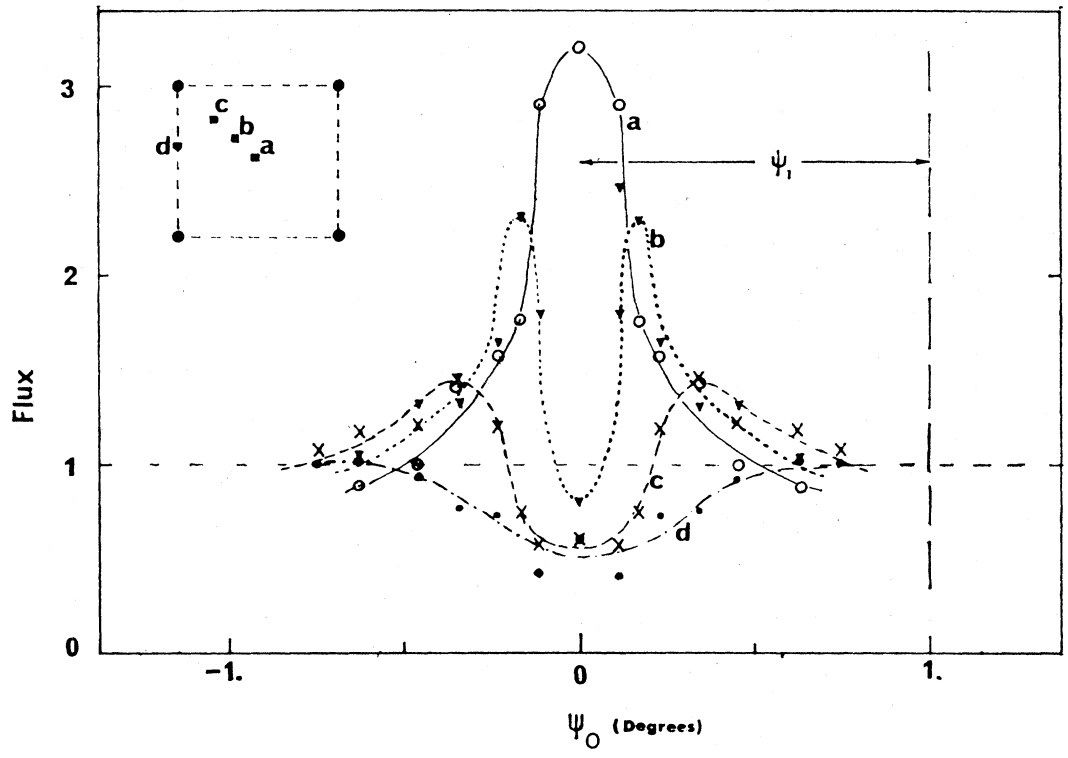

FIG. 36. Calculated particle flux $F(\mathbf{r}, x)$ as a function of the angle of incidence ψ_0. The calculations are for 1.5-MeV alpha particles in the $\langle 100 \rangle$ axial channel of Cu [Mo72]. The four curves correspond to points $\mathbf{r}$ in the transverse plane as shown in the insert, (c.f. Fig. 34). The depth is assumed large enough that statistical equilibrium has been reached. The angle ψ_1 (1.0°) is shown for comparison. The angle of tilt ψ_0 is such that the beam is incident in a (110) planar direction.

in Sec. 6.2. Suffice it for the moment to remark that in atom location experiments it is clearly of importance to make observations for several angles of incidence. Application of the rule of reversibility (Sec. 2.2) indicates that flux peaking can also play a significant role for particles emitted by atoms located near the center of channels. This has important implications in the use of the blocking technique to measure nuclear lifetimes (Sec. 6.6).

2.5. Quantum mechanical considerations

In the last few years, extensive studies in the field of high-voltage electron microscopy have established that particle diffraction effects undoubtedly play a major role in the interaction of 1-MeV electrons ($\lambda = 9 \times 10^{-11}$ cm) with crystals. For the case of 1-MeV protons ($\lambda = 3 \times 10^{-12}$ cm), the question arises as to whether diffraction effects will still be of importance since the particle wavelength is only a factor of 30 less than for electrons of the same energy. Several authors (e.g., [Li65, 70; Fo67; Ler67; Co68; How68, 70a; Th68b, Whe70a]) have given arguments justifying the use of classical mechanics to describe the channeling of particles as heavy as the proton at these energies (see also Sec. 2.4a). However, the question of the significance of diffraction effects has given rise to a vigorous discussion in the literature (see, e.g., [Ch66; Fo67; DeW67; DeS68; Co68; DeW70b]). The main proponents of the view that particle diffraction effects may be of significance even in heavy-particle channeling have been Chadderton and DeWames and collaborators [DeW66; Ch66; DeW67; To67; Ch68a, b; DeW68a, b, c; Ch70a; DeW70a, b; New71].

The interaction of particle waves with a crystal lattice can be discussed in terms of the dynamical diffraction theory originally developed to describe the anomalous transmission and absorption of x rays in thick highly perfect crystals (the Borrmann effect [Bo41]; see [Bat64] for a comprehensive review). In this theory, the solution of the Schrödinger equation for particles in the three-dimensional periodic lattice potential is obtained in terms of Bloch waves whose amplitudes are determined by requiring a match to the incident wave function at the crystal surface. The use of a complex lattice potential permits taking into account absorption and inelastic processes. For incident x rays, low-energy ($\lesssim$ 100 keV) electrons and neutrons, only two Bloch waves are excited with appreciable intensity. One of these has maxima at the atomic sites and is thus anomalously strongly absorbed. The other has nodes at the atomic sites and is anomalously transmitted. The number of excited Bloch waves increases as the energy and mass of the incident particles increase and as the interaction between particles and crystal gets stronger. When many waves are excited, computational complexities frequently make it difficult to compare theory and experiment. For a detailed description of the dynamical diffraction theory applied to high-voltage electron microscopy, the reader is referred to the book of Hirsch *et al.* [Hir65]. (See also [How70b; Whe70a, b] and Sec. 5.)

In order to be able to detect angular structure due to

wave-interference effects in planar channeling, it is necessary that the angular divergence Δ of the beam be small compared to the Bragg angle θ_B. If Δ is the limiting factor in the angular resolution, then the condition $\Delta \gg \theta_B$ makes a wave treatment unnecessary (see, e g., [Co68; How70a]). The condition $\Delta \ll \theta_B$ usually applies in the cases of x rays, low-energy electrons, and thermal neutrons. For protons in the MeV range, $\theta_B \approx 10^{-4}$. This is just around the limit of presently achievable proton beam divergences, especially if scattering in thin-surface oxide layers is present (see Sec. 3.1), and thus suggests that diffraction effects should be difficult to see. In cases where the ratio Δ/θ_B is large, the uncertainty ($\delta_z \approx \lambda/\Delta$) in the position of a particle measured in the direction normal to the crystal planes is small compared to the interplanar distance d_p (since $\lambda \approx 2d_p\theta_B$). That is, the particle can be localized in a particular planar channel, and thus a classical model should be appropriate. Even for a perfectly collimated beam ($\Delta = 0$), the Bragg resonance has an angular width $\delta\theta_B$. For the two-beam case and for particles of energy E, this width can be calculated to be $\delta\theta_B = |V_h|/(E \sin 2\theta_B)$, where, in the Fourier expansion of the lattice potential, V_h is the coefficient corresponding to the reciprocal lattice vector $\mathbf{k}_h$. This has led to the suggestion (e.g., [Ch68b; DeW68c]) that a sufficient condition for the applicability of classical theory to planar channeling might be written

$$\frac{\delta\theta_B}{\theta_B} = \left|\frac{4V_h\gamma M_1}{\hbar^2 k_h^2}\right| \gg 1, \qquad (2.119)$$

where γM_1 is the relativistic mass of the incident particles. The condition, Eq. (2.119), is also a necessary one if the experimental angular uncertainties are smaller than $\delta\theta_B$. Eq. (2.119) is probably not a strong enough condition for planar channeling; it is likely to be more appropriate for axial channeling. This can be seen from the following considerations based on phase-space arguments (see also Sec. 5).

The available phase space for particles channeled in a planar direction in which the critical angle is ψ_c is approximately given by $2\hbar k_0 \psi_c d_p$, where k_0 is the wave number of the incident beam. Thus the number of quantum states available to the particles as they move in the planar potential well is $n_P \approx 2\psi_c k_0/k_h$. A necessary condition for the applicability of a classical model to planar channeling is $n_P \gg 1$, because then the transverse energy will be quantized into many states whose separation is small compared with the channeling potential. Since the Bragg angle is given by $\theta_B \approx k_h/2k_0$, one may write $n_P \approx \psi_c/\theta_B$. The number of Bloch waves needed in a diffraction description is approximately $2\psi_c/\theta_B$ for the planar case [How70a]. Thus, as is to be expected, the condition $n_P \gg 1$ automatically signifies that many Bloch waves are required. For the axial case, similar arguments can be made (Sec. 5). If one considers an axis at the normal intersection of two (equivalent) planes whose critical angle and Bragg angle are ψ_c and θ_B, respectively, it can be seen that the number of Bloch waves then needed is approximately $(2\psi_c/\theta_B)^2$. An estimate for the number of quantum states for the axial channeling is thus $n_R \approx n_P^2$. The condition $n_R \gg 1$ is equivalent, within a factor of two, to Eq. (2.119) if one identifies the Fourier coefficient V_h with the critical value of the transverse energy in planar channeling. These considerations indicate that the conditions for a classical description are more easily met for axial than for planar channeling.

From Eq. (2.119) one sees that a classical model becomes more appropriate as the velocity and mass of the incident particles increase, as the atomic numbers of the incident ions and target crystal increase (larger $|V_h|$), and for higher symmetry planes rather than lower symmetry ones (larger values of $|V_h|/k_h^2$). Note that the velocity dependence enters only via the relativistic mass. Equation (2.119) indicates that the weak interaction potential is the main reason why a wave description is needed for neutron scattering by crystals in spite of the high value of the neutron mass.

For charged particles, the condition in Eq. (2.119) is usually met for values of M_1 greater than a few tens or hundreds of electron masses. High-energy electrons and positrons and charged mesons therefore occupy a unique position where neither the wave nor the particle description is fully applicable. Experiments with these projectiles should be of value in bridging the gap between the two descriptions. Chadderton [Ch68b] has related the quantum mechanical and diffraction descriptions of channeling with a correspondence principle. He points out certain analogous features in the two approaches; e.g., the wave mechanical oscillations of intensity with depth (the Pendellösung effect) have a period, the extinction distance, which is analogous to the wavelength of the classically oscillating trajectory (see also [How68; Ch70a]). He also suggests that the angular widths of proton Kikuchi bands should be proportional to the mass-independent geometrical mean $\sqrt{\theta_B\,\delta\theta_B}$. This then gives an expression for the angular width similar in form to Eq. (2.40) except that the continuum potential, U_{PS}, is replaced by the Fourier coefficient $|V_h|$.

If one neglects secondary processes such as energy loss and multiple scattering, then in the classical description the trajectories of channeled particles of a definite energy are independent of the particle mass, whereas in the quantum mechanical description, the mass affects the particle wavelength, and so in a direct way it affects such fundamental quantities as the Bragg angle. Thus the mass dependence of channeling angular distributions can be used as a measure of the extent to which a quantum mechanical description is required. DeWames *et al.* [DeW68b] have studied the mass dependence of particle emission patterns obtained from multiple-beam dynamical diffraction calculations. They find a strong mass dependence for $M_1 \approx m_e$. They find also that the angular width calculated for electrons can differ by a factor of up to 4 from that calculated for much higher mass particles of the same energy. Pathak and Yussouff [Pa70, 72] have also made dynamical diffraction calculations formulated like those of DeWames *et al.* and with similar results. The essential differences in the calculations lie in the models assumed for the lattice vibrations.

The observation [Fot70b; Gr72] of slight differences in the angular scans obtained in backscattering measurements with protons and deuterons of the same bombarding energy and for identical targets and orientations has led to the postulation [DeW70a; Gr72] that these are quantum mechanical effects. The measurements show oscillations in the shoulder region of the channeling dip. The oscillations vary with angle more rapidly for deuter-

ons than for protons in keeping with the expectation of a more classical behavior for the heavier particle (shorter DeBroglie wavelength).

As further evidence for quantum effects in proton channeling, Chadderton [Ch66] has cited the light and dark planar streaks observed in transmission star patterns (see Sec. 4.3a). Chadderton interpreted these in terms of the Kikuchi patterns familiar from electron microscopy. Thompson [Th68b] and Appleton and Feldman [Ap69] have shown that these streaks can also be simply explained using a classical description.

Lervig *et al.* [Ler67] have given a quantal treatment of directional effects for fast charged particles in crystals. These authors do not attempt a Bloch-wave formulation but instead use the fact that, for channeled particles, the velocity in the beam direction is nearly constant, thus permitting a time-dependent Schrödinger equation to be set up to describe the motion in the transverse plane. Only the lattice periodicity in the string direction is considered to affect the motion. The authors first use the sudden-collision approximation to derive a general formula for the scattering by a single atom and then obtain an expression for the probability of penetration to the atomic centers in a string of atoms. Their results show that appreciable penetration of particles into classically forbidden regions can occur only when $M_1 \lesssim m_e$. The questions of coherence and interference are also discussed. The mean free path for electronic energy losses is large (many times the lattice spacing) for high-incident velocities and low values of Z_1. This permits strong diffraction effects to be seen for electrons and positrons but would destroy coherence for high values of Z_1 (see also [Fo67; DeW67; How68, 70a, b]).

An interesting particle-diffraction calculation on the channeling effect has been performed by Kagan and Kononets [Ka70]. They make use of a powerful density-matrix formalism that permits the inclusion of the full three-dimensional lattice periodicity and, at least in principle, can take into account the incoherent inelastic scattering of particles within the crystal. Their results obtained for the planar case and ignoring inelastic energy losses reproduce qualitatively the major channeling characteristics as well as such details as depth oscillations of the nuclear encounter probability.

2.6. Energy losses

One of the most significant characteristics of channeled motion is the modification of the stopping power from the value experienced by randomly traveling particles. Experimentally, channeled particles are often identified through their anomalous energy losses. This important aspect of channeling is treated in some detail in many of the following sections. In the present section we give a resume of some of the fundamental considerations in the theory of energy-loss processes for charged particles in amorphous media and then discuss, in a general way, the influence of channeling on these processes in crystals.

2.6a. Basic considerations

The slowing down of charged particles in matter has been intensively studied for many years. There exist several reviews of the subject (e.g., [Boh48; Fa63; Li63, 69; Nor63, 70; Da67; Sau72; Schiø73] and references contained therein). Particles lose their energy primarily by a succession of Coulomb interactions. At very high energies, in the GeV range for protons, energy losses due to nuclear reactions become significant. Figure 37 illustrates in a schematic way the velocity dependence of the stopping power of a typical ion in an amorphous medium, or in a random direction in a crystal. At incident velocities large compared to the orbital velocity that electrons would have if captured by the incident ion, the incident ion rapidly becomes fully stripped of electrons as it enters the stopping medium. At these velocities (Region I in Fig. 37), the stopping power is a decreasing function of velocity and is almost entirely due to electronic collisions. (The contribution from "nuclear" stopping is usually on the order of a thousand times smaller.) For these collisions, a quantal perturbation treatment gives fairly accurate results (as expected from Eq. (2.10) evaluated for electrons) except when Z_1 becomes large. As the ion slows down, the electron capture probability increases, and the loss probability decreases. Also, the tightly bound inner shells of the target atoms begin to play a declining role in the stopping process. Shell corrections to the theory then become necessary (e.g., [Wal52, 56]). Bohr [Boh40, 41] suggested as an approximate criterion that an electron becomes bound to an ion if the ion velocity is less than the orbital velocity of the electron in its bound state (see also [La40]). For the first K electron, the critical velocity is $\sim Z_1 v_0$, where $v_0 = e^2/\hbar$ is the Bohr velocity, approximately 2.2×10^8 cm/sec, equivalent to about 25 keV/nucleon. For the outermost electrons, the critical velocity is $\sim v_0$. For an ion with charge state Q_1, Bohr proposed the critical velocity $Q_1 v_0/Z_1^{1/3}$, where the denominator represents an effective quantum number in conformity with the electron binding energies determined from the Thomas–Fermi statistical model. It follows that for an ion of velocity v, the mean fractional charge state of the ion is given roughly by

$$\bar{Q}_1/Z_1 \approx v/(v_0 Z_1^{2/3}). \tag{2.120}$$

Equation (2.120) is only modestly successful in predicting charge states (see [Betz72] for a recent review of the topic

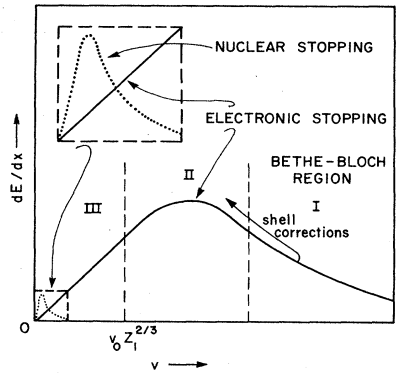

FIG. 37. Schematic classification of the regions of stopping (after Lindhard [Li69]). The solid curve represents electronic stopping, and the dotted curve (see insert) represents the nuclear stopping for a typical heavy ion. The curves are qualitative only, and the coordinates are not to scale.

of charge states of fast ions in matter; see also Sec. 4.3f). However the Thomas–Fermi velocity $v_0 Z_1^{2/3}$ does serve as a convenient unit when comparing stopping powers for different ions. The stopping power curve goes through a maximum that usually occurs slightly above this velocity (Fig. 37). As the ion velocity decreases further (Region III in Fig. 37), the electronic stopping power decreases, and the ion tends toward lower charge states. For heavy ions at very low velocities, nuclear stopping due to elastic collisions involving the screened nuclear Coulomb fields of the ion and atom can compete with electronic stopping.

At high velocities (Region I), the electronic stopping power may be written

$$-(dE/dx)_e = (4\pi Z_1^2 e^4/m_e v^2) N Z_2 L_e, \quad (2.121)$$

where N is the number of target atoms per unit volume and the dimensionless quantity L_e is the stopping number per atomic electron. There have been several theoretical treatments deriving expressions for L_e (see the review by Fano [Fa63]). The initial expression due to Bohr [Boh13] was obtained on a classical impact-parameter basis. However in Region I, Eqs. (2.10) and (2.11), the conditions for a classical treatment, are usually not fulfilled. Following the advent of quantum theory, Bethe [Be30] formulated the problem in terms of momentum transfer to the target electrons. He used the Born approximation to obtain the well-known (nonrelativistic) result

$$L_e = \ln(2m_e v^2/I), \quad (2.122)$$

where the quantity I is the mean excitation energy of the target atoms. Bloch [Blo33a, b] calculated the stopping power with a treatment based on generalized impact parameters (viz., the distances between the particle paths and the nuclei of the target atoms). He used the Thomas–Fermi model for the electron distribution in the target atoms and also took into account the perturbation of the electronic wave functions caused by the presence of the incident particle. Bloch's formula goes over to that of Bethe in the limit $\kappa \ll 1$ and to that of Bohr when $\kappa \gg 1$, where κ is defined in Eq. (2.10). Bloch also showed that the mean excitation energy is approximately given by $I = KZ_2$, where K is an empirically determined number (the Bloch constant) with a value of $\sim$10 eV. Both Bethe and Bloch extended their treatments to include modifications to the formulae for L_e for ions that are incident at relativistic velocities. At high velocities, Eq. (2.122) becomes

$$L_e = \ln(2m_e c^2\beta^2/I) - \ln(1-\beta^2) - \beta^2, \quad (2.123)$$

where $\beta = v/c$. Here we have omitted the small terms that take account of shell corrections and density effects (see [Fa63] for a discussion of these and other refinements to the theory). The Bethe–Bloch formulas generally reproduce the experimentally determined stopping powers in the high-velocity region to an accuracy of a few percent.

An impact-parameter derivation, similar to that of Bloch, of the stopping-power formula has been given by Datz *et al.* [Da67]. These authors show that the average energy loss due to ionization in a single collision between an incident particle and one target atom is given by

$$\Delta E(b) = (2/m_e)(Z_1 e^2\omega/v^2)^2[K_0^2(\omega b/v) + K_1^2(\omega b/v)], \quad (2.124)$$

where b is the nuclear impact parameter of the collision, K_0 and K_1 are, respectively, the zero-order and first-order modified Bessel functions of the second kind (as defined, for example, in [Wa58]), and ω is equal to $(E_f - E_i)/\hbar$, where E_f and E_i are the energies of the final and initial electronic states. If, for an amorphous material, one assumes an impact-parameter distribution

$$\nu(b)\,db = 2\pi b\,db, \quad (2.125)$$

and if the velocity is high enough so that $\omega b/v \ll 1$, then integrating Eq. (2.124) over impact parameters yields

$$L_e = \ln(b_{\max}/b_{\min}). \quad (2.126)$$

The lower limit $b_{\min}$ is determined by the positional uncertainty of an electron when the interaction is the closest possible, i.e., when the momentum $2m_e v$ is transferred to the electron. Thus

$$b_{\min} = \hbar/2m_e v. \quad (2.127)$$

The upper limit $b_{\max}$ is determined by the requirement that the collision be sudden, as originally suggested by Bohr. That is, the duration $\sim b/v$ of the collision should remain shorter than the reaction time $\sim\hbar/(E_f - E_i)$ of the electrons. Slower adiabatic collisions result in no energy loss. Therefore

$$b_{\max} = \hbar v/(E_f - E_i) \quad (2.128)$$

$$\approx 93(E/M_1)^{1/2}/(E_f - E_i)\ \text{Å}, \quad (2.129)$$

where E and M_1 are given in units of MeV and amu, respectively, and $(E_f - E_i)$ is expressed in eV. Substitution into Eq. (2.126) gives

$$L_e = \ln[2m_e v^2/(E_f - E_i)], \quad (2.130)$$

which may be compared directly with Eq. (2.122) As will be discussed in Sec. 2.6b, the effect of channeling is to modify the distribution of impact parameters from that given in Eq. (2.125).

In addition to the core excitations which are strongly dependent on impact parameter, there are energy losses to the loosely bound valence and conduction electrons. These electrons are fairly uniformly distributed in solids and may be treated to a good approximation as constituting a Fermi gas. The response of such an electron gas to the passage of a charged particle has been treated by Lindhard [Li54] and Lindhard and Winther [Li64b] in terms of the complex dielectric constant (see also [Kr47]). For high incident velocities, this leads to

$$-(dE/dx)_e = (4\pi Z_1^2 e^4 n_e/m_e v^2)\ln(2m_e v^2/\hbar\omega_p), \quad (2.131)$$

where

$$\omega_p = (4\pi n_e e^2/m_e)^{1/2} \quad (2.132)$$

is the plasma frequency of an electron gas of density n_e. The logarithmic term in Eq. (2.131) has an obvious similarity with those given in Eqs. (2.126) and (2.130) but with the limiting impact parameters replaced by limiting momentum transfers $2m_e v$ and $\hbar\omega_p/v$. This latter value

separates two regions of behavior of the electron gas. For much higher momentum transfers, the gas behaves like a collection of single particles; for much lower transfers, it behaves collectively exhibiting plasma oscillations of frequency ω_p. The logarithmic term in Eq. (2.131) contains contributions both from plasmon and single-particle excitations. Erginsoy [Er68] evaluated numerically the expressions for these contributions given by Lindhard and Winther and found that although the contributions themselves were not equal, the changes in them with velocity were equal when evaluated at high velocities. This verified numerically the equipartition rule given by Lindhard and Winther. A similar result was obtained by Brandt and Reinheimer [Br70a] in calculations on the properties of an electron gas with an energy gap in the limit where the gap width goes to zero (see also [Bon70]). As Erginsoy pointed out, these results do not imply equipartition of the stopping power of an electron gas.

Bohr [Boh48] discussed the total electronic stopping power of a solid in terms of contributions from close single-particle electronic collisions (large momentum transfers) and distant resonance-type excitations (small momentum transfers). The latter can be identified with processes in which the field exerted by the incident particle is fairly uniform over the volume occupied by bound electrons and with plasmon excitation in the case of valence and conduction electrons. Bohr showed that for high incident velocities the electronic stopping power is asymptotically contributed by close and distant collisions equally. The relevance of this equipartition rule to channeling is discussed in Sec. 2.6b.

In Region III (Fig. 37) the stopping power is proportional to the ion velocity. This is a result that Fermi and Teller [Fe47] derived when they calculated the slowing down of μ-mesons at low velocities in a free electron gas. Lindhard and co-workers [Li54,61,63,69] have developed the theory of the stopping of heavy ions in this low velocity range. They considered the electronic stopping in terms of the self-consistent dynamics of a Fermi gas. Their calculated stopping power is proportional to v and has a simple monotonic dependence on Z_1 and Z_2:

$$-\left(\frac{dE}{dx}\right)_e = \zeta_e 8\pi N e^2 a_0 \frac{Z_1 Z_2}{(Z_1^{2/3} + Z_2^{2/3})^{3/2}} \frac{v}{v_0}, \qquad (2.133)$$

where ζ_e is a numerical factor on the order of 1 to 2 ($\zeta_e \sim Z_1^{1/6}$). Equation (2.133) has been successful in predicting random, i.e., nonchanneled, stopping powers to an accuracy of about 20% in the velocity region $v < v_0 Z_1^{2/3}$. Lindhard [Li69] has remarked on the analogy between the velocity-dependent electronic stopping power in Region III and the familiar case of Ohm's law which describes a similar situation where particles (electrons) experience a slowing down or frictional force proportional to the particle velocity. In addition, the nuclear stopping in Region III has been calculated by Lindhard and co-workers [Li63,68]. Here a classical treatment is expected to be accurate. These authors derived a universal curve for the nuclear stopping power using the Thomas–Fermi model to determine the effects of screening.

An alternative calculation of the electronic stopping power in the velocity-proportional region has been performed by Firsov [Fi59]. His is a quasi-classical treatment in which it is assumed that for each individual encounter between the incident beam ions and the target atoms, there is a deceleration due to electron exchange. In the region of overlap of the electron distributions in such an encounter, the motion of the electrons is presumed to be governed by the Thomas–Fermi field of the ions. The energy loss is determined by a calculation of the net electron flux across a plane constructed perpendicular to a line joining the two colliding nuclei and located at the point of potential minimum on this line (Fig. 38). It is assumed that when an electron moves out of the potential field of one atom into that of the other, i.e., it crosses the plane S shown in Fig. 38, there is a momentum transfer equal to $m_e v$, where v is the relative velocity of the ions. The total energy loss in a collision is given by Firsov as

$$\Delta E = m_e \int \mathbf{R} \cdot d\mathbf{R} \int_S \tfrac{1}{4} n_e v' \, dS, \qquad (2.134)$$

where $\mathbf{R}$ and S are shown in Fig. 38, and the surface integral gives the electron flux across S. The density of electrons n_e and their mean velocity v' at the surface S are calculated by Firsov by use of the Thomas–Fermi model. The following result is then obtained for the energy loss in a collision with impact parameter b:

$$\Delta E(b) = \frac{4.3 \times 10^{-8}(Z_1 + Z_2)^{5/3} v}{[1 + 0.31(Z_1 + Z_2)^{1/3} b]^5} \text{ eV}, \qquad (2.135)$$

where v and b are given in units of cm/sec and angstroms, respectively. As Firsov concedes in his paper [Fi59], the theoretical basis for this model of stopping is far from rigorous. However, when Eq. (2.135) is integrated over impact parameter, the resultant stopping power agrees well with experimentally determined values (see, e.g., [Te62]) and gives results not too different from those derived by Lindhard and co-workers (e.g., [Li61,63]). The origin of the proportionality to velocity in Eq. (2.135) lies in Firsov's use of the impulse approximation for the nuclear motion. Thus both Lindhard's and Firsov's approaches result in a velocity-proportional stopping power, but for entirely different reasons. From the viewpoint of channeling, Eqs. (2.124) and (2.135) have the merit of providing an explicit dependence upon the impact parameter.

2.6b. Influence of channeling

For channeled trajectories, the distribution of impact parameters is drastically altered from that given in Eq.

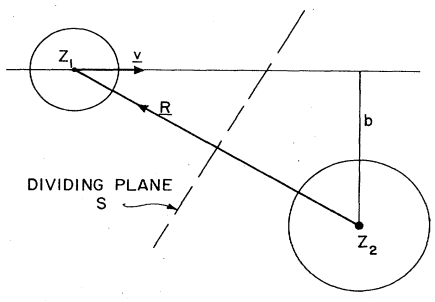

FIG. 38. Illustration of the quantities involved in calculating the electronic stopping power in the low-velocity region by the method of Firsov [Fi59].

(2.125). Since channeled particles do not make collisions with nuclear impact parameters much less than $\rho_{\min} \sim u_1$, the thermal vibration amplitude defined in Eq. (2.44), they experience a strongly reduced stopping power. The ratio of the channeled stopping power to the random stopping power depends on the transverse energy of the channeled particles. We define

$$\varepsilon(E_\perp) = (dE/dx)_{\rm ch}/(dE/dx)_{\rm rand}, \qquad (2.136)$$

where the stopping powers are measured at the same energy. The compensation rules discussed in Sec. 2.43 apply to stopping powers. Thus, for well-channeled particles, $\varepsilon < 1$, while for particles with transverse energies just above the critical value for channeling, $\varepsilon > 1$.

Citing the equipartition rules [Boh48; Li64b] discussed in Sec. 2.6a, Lindhard [Li64a,65] suggested that the reduction in stopping power experienced by channeled particles should be at most by a factor of "$\sim$2". The factor "$\sim$2" was widely interpreted at that time (ca. 1965) as indicating that ε should always satisfy $\varepsilon \geq 0.5$. (Although from a closer study of Lindhard's 1965 paper one can very quickly determine that values of $\varepsilon < 0.5$ are certainly not prohibited by equipartition. Lindhard relates the channeled stopping power to the electron density $n_e^{(\rm ch)}$ sampled by a channeled particle and also to a measure, α, of the locality of the stopping, $0.5 \leq \alpha \leq 1$, $\alpha \to 0.5$ at high velocities. He then finds $\varepsilon = 1 - \alpha\,[1 - n_e^{(\rm ch)}/n_e^{(\rm av)}]$, where $n_e^{(\rm av)}$ is the average electron density in the crystal.) When it was found in early measurements (e.g., [Er64]) that for protons channeled along the $\langle 110\rangle$ axis of Si, $\varepsilon_{\langle 110\rangle} \approx 0.5$, equipartition was thought to have been confirmed. However, examples of $\varepsilon < 0.5$ were soon found in some other target materials; for example, for protons in Ge, $\varepsilon_{\langle 110\rangle} = 0.3$ [Ap67; Sa67]. Thus it is clear that although the electronic stopping power in an amorphous medium may be equally partitioned between close and distant collisions, channeling experiments in crystals do not provide a means of cleanly separating these two contributing processes. The reason for this lies in the fact that *close* and *distant* in the sense used in the equipartition rules refer to large and small momentum transfers to atomic electrons, whereas channeling makes a purely spatial differentiation between large and small nuclear impact parameters.

We consider now the influence of channeling on the stopping power for incident ions in the high velocity range (Region I in Fig. 37). Theoretical treatments have been given by several authors (e.g., [Li65; Ap67; Bri68; Er68; Kum68a,71; Lun68,72; Po68a; Bon69,70; Var70; Oh71a,b,72a; Ki72]). The discussion given by Appleton *et al.* [Ap67] serves to illustrate many of the considerations involved. These authors treated separately the core electrons and the valence and conduction electrons. The latter are regarded as constituting a Fermi gas while the former are discussed in terms of the impact parameter treatment outlined in Sec. 2.6a. The simplest channeling case to treat is that in which, for the best channeled particles, i.e., those whose trajectories do not depart much from the center of a major axial or planar channel, the energy loss due to ionization vanishes. This will happen if the maximum impact parameter $b_{\max}$ defined by the adiabaticity criterion in Eq. (2.128) is less than the distance $\rho_{\max}$ from the center of the channel to the nearest row or plane forming part of the channel wall. That is,

$$\hbar v/\Delta E < \rho_{\max}, \qquad (2.137)$$

where $\Delta E = E_f - E_i$. Appleton *et al.* measured the effect of channeling on the stopping power of Si and Ge crystals for incident protons in the energy range 3–11 MeV. The (111) planar channels are the most open ones in the diamond lattice ($d_p = 2.35$ Å in Si; $d_p = 2.45$ Å in Ge). Thus for the best channeled particles in these directions we may take $\rho_{\max} \sim 1.2$ Å. At the lowest velocity used by Appleton *et al.*, i.e., the velocity having the best chance of satisfying Eq. (2.137), one finds for the K shell in Si ($\Delta E = 1839$ eV [Bea67]), $b_{\max} = 0.09$ Å. Thus K-shell excitation by the well-channeled particles in Si can be neglected. For the L shell in Si, the electron binding energies lie in the range 100–150 eV. If one takes $\Delta E = 100$ eV, then for the L shell, $b_{\max} \approx 1.6$ Å. Therefore ionization of the L shell cannot be entirely neglected even for the best channeled particles. Appleton *et al.* point out that energy loss scales approximately in the ratio $[\ln(b_{\max}/\rho_{\max})]/[\ln(2m_e v^2/\Delta E)]$. Thus the energy loss due to ionization of the L electrons should be reduced by about 90% for the best channeled protons in the (111) planar direction in Si. At bombarding energies higher than 3 MeV, this reduction becomes smaller. In Ge, ionization losses to the outer M-shell electrons remain large even at 3 MeV for well-channeled protons in the (111) planes.

Appleton *et al.* calculated the stopping power for the best channeled 3-MeV protons in the (111) planes of Si. They assumed that ionization losses to the K- and L-shell electrons could be neglected and that the stopping power is due only to the valence electrons which they treated as a Fermi gas. The stopping power of an electron gas can be partitioned according to the theory of Bohm and Pines [Pin64] into separate contributions from collective (plasma) excitations and from single-particle excitations. The stopping power calculated for the valence electrons only is given by the expression

$$-\left(\frac{dE}{dx}\right)_{\rm val} = \frac{4\pi Z_1^2 e^4}{m_e v^2} N\left(Z_{\rm val} \ln \frac{v}{v_F} + Z_{\rm loc} \ln \frac{2m_e v v_F}{\hbar\omega_p}\right), \qquad (2.138)$$

where $NZ_{\rm val}$ and $NZ_{\rm loc}$ are the effective electron densities for plasma and single-particle excitations, respectively, v_F is the Fermi velocity of the valence electron gas, $v_F = (\hbar/m_e)(3\pi^2 NZ_{\rm val})^{1/3} \sim 3.6\,(NZ_{\rm val})^{1/3} \times 10^8$ cm/sec, where $NZ_{\rm val}$ is given in units of electrons/Å^3, and ω_p is the plasma frequency defined in Eq. (2.132), $\hbar\omega_p \sim 37\,(NZ_{\rm val})^{1/2}$ eV, where $NZ_{\rm val}$ is given in electrons/Å^3. Appleton *et al.* equated the right-hand side of Eq. (2.138) (assuming $Z_{\rm val} = 4$ for Si) to the stopping power measured for the (111) planar channel and obtained a value of $Z_{\rm loc(111)} = 3.8$. In general the local electron density sampled by the channeled beam need not be the same as the valence-electron gas density because of nonuniformities in the spatial distribution of valence electrons. However, the measurements in Si indicate that for the (111) planes, $Z_{\rm loc}$ and $Z_{\rm val}$ are approximately equal. Appleton *et al.* also point out that collective excitations should not contribute appreciably to the straggling in the channeled energy loss. Assuming that the straggling is due only to close collisions with local electrons in the channel, they find $Z_{\rm loc(111)} = 4.1$ in reasonable agreement with the value determined from the channeled stopping power.

Because the value of ρ_{max} [Eq. (2.137)] for an axis is frequently close to the value of ρ_{max} for the most open planar channel intersecting in that axis, the channeled stopping power for the axial direction and for this most open planar direction are often about the same.

For narrow channels, for high incident velocities, and for small electron binding energies, the inequality given in Eq. (2.137) can be violated. Then core excitation remains an important energy-loss process even for well-channeled particles. Calculations of channeled stopping power taking into account the nonvanishing contributions of core excitations have been made by Luntz and Bartram [Lun68,72] (see also Sec. 4.2g). Bonsignori and DeSalvo [Bon69,70] have made calculations on the effect of channeling on the energy loss to valence electrons. These authors use a dielectric approach taking into account the lattice periodicity of the electron gas. They find that channeling has a very small (a few percent) effect on the stopping power even though the local electron density encountered by channeled particles is much less than the average electron density. This result is consistent with that of Appleton *et al.* [Ap67].

Ohtsuki and co-workers [Oh71a,b, 72a,b; Ki72] have calculated the dependence of the channeled stopping power on the distance from a row or a plane of atoms. They use an impact-parameter representation of the stopping power for each atom and then average over the row or planar direction. They compare their results with experimentally determined values derived by Robinson [Ro69,72a] (see also Sec. 4.3c). The agreement is poor at high velocities (Region I, Fig. 37), but good at low velocities (Region III, Fig. 37).

A somewhat different approach to the problem of energy losses in crystals has been taken by Brice [Bri68] who has made a diffraction calculation of the stopping power and straggling experienced by MeV H, D, and ^{3}He ions in Ge. He treats each crystal atom as consisting of a core and an outer shell of loosely bound electrons. The cores and the shells are considered to move independently. He finds that the effective number of electrons per atom that participate in collective modes depends on the channeling direction chosen; the narrower the channel, the larger the number of electrons participating.

All of these results for high velocities indicate that the largest part of the reduction in stopping power due to channeling is a consequence of the decrease in the probability for ionizing inner shells. The effect on contributions from valence and conduction electrons should depend on the nature of the target material, e.g., on whether it is a metal, semiconductor, ionic crystal, etc. Neither calculations nor experiments have thus far been performed that are capable of making these finer distinctions.

We now consider the low-velocity region (Region III in Fig. 37). Because nuclear stopping occurs mostly through collisions with small impact parameters, it is strongly reduced by channeling. This reduction is largely responsible for the anomalously long ranges of low-energy heavy ions in crystals, measurements of which gave the first experimental evidence for ion channeling [Dav60a, b; Pie63; Lu63]. In the absence of nuclear stopping, the slowing down of channeled low-energy ions is almost

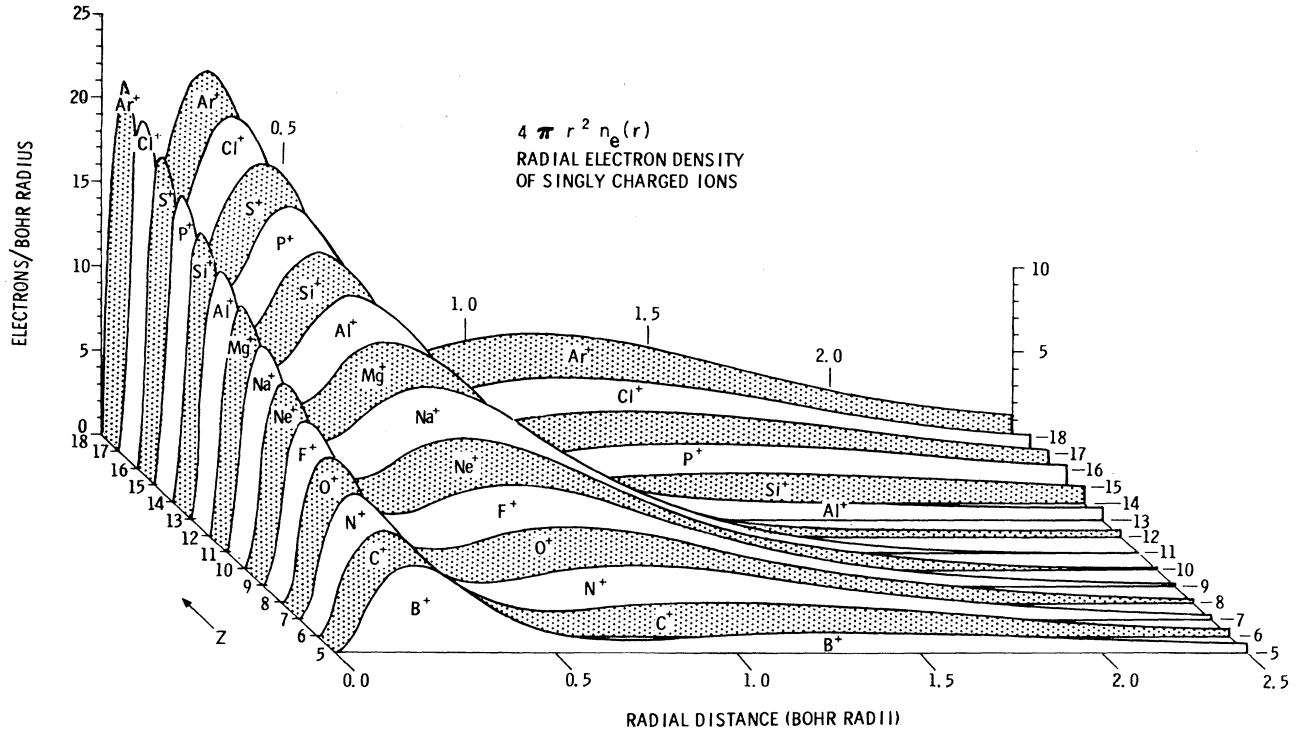

FIG. 39 The radial electron densities, $4\pi r^2 n_e(r)$ for singly charged ions from boron to argon [Ha68]. Periodicity of the type required to explain channeling data, such as those shown in Figs. 70 and 79 is readily apparent at large radial distances.

entirely due to electronic energy losses. Channeling thus provides a unique means of separating these two types of stopping process. The impact-parameter dependent electronic stopping power in the velocity-proportional region is well described by the formula due to Firsov [Fi59]; see Eq. (2.135).

Ormrod *et al.* [Or63,65; Mac66] and Fastrup *et al.* [Fas66] have observed an oscillatory Z_1 dependence of the stopping power for low-energy heavy ions in amorphous foils of boron, carbon, and aluminum. It was realized that these oscillations were indicative of shell effects influencing the electronic stopping power. For channeled ions, the strong reduction in nuclear stopping makes such effects much more pronounced (see, e.g., the experimental data of Eriksson *et al.* [Erik67a, b], Eisen [Ei68a], and Bøttinger and Bason [Bøtt69]; see also Secs. 4.2e and 4.3b). The Z_1 oscillations seen in channeling have been successfully accounted for by several authors (e.g., [Che68,69,70; Bh68,70; El-H68; Ha68; Wi68; Ke71,72; Kom73]) by modifying Firsov's formula to take into account the periodic variation with Z_1 of the electron density measured at large radial distances. A plot of radial electron densities for ions ranging from boron to argon is given in Fig. 39. These were calculated [Ha68] from the Hartree–Fock–Slater equations and show clearly an oscillatory behavior at large radial distances. For further theoretical discussion on the effects of channeling on dE/dx in the low-velocity region, the reader is referred to the following: [Ib68; Gu70; Oh72b]; see also Secs. 4.2e, 4.3b, and 4.3c.

3. EXPERIMENTAL CONSIDERATIONS

3.1. Apparatus

The experimental techniques used in channeling frequently have much in common with those of low-energy nuclear physics. The main difference usually lies in the greater angular precision required in channeling measurements. Channeling can, of course, be observed at much lower incident energies than can nuclear reactions. Furthermore, atomic (e.g., x-ray) detectors are often employed in addition to nuclear ones. For a detailed description of a typical apparatus for channeling experiments, see [Ge71]. Several authors have described goniometers for use in channeling measurements (e.g., [Ei68; Gi68a; Liv68; Beh69; Kn70; Fot71; Pe72; Bi73]). The determination of orientation and the alignment of target crystals is usually done either with x rays, or by observing the star pattern for transmitted particles (e.g., [De67]) or by observing the channeling minima for close-encounter processes such as characteristic x rays or Rutherford scattering (see, e.g., [Bord70]). Since $\psi_{1/2}(x)$ becomes smaller for increasing depths x (see Secs. 2.4e and 4.2a), it is frequently advantageous to orient crystalline targets by searching for backscattering minima determined at depths a few microns below the surface. Because of the repetitive nature of channeling measurements, computer control of the goniometer and of the data acquisition system is a great advantage [Ge71]. The computer can then also be programmed to align the target crystal. Frequently, channeling and blocking measurements require the determination of the spatial distribution of particles emerging from a crystal in directions close to some major axis or plane. This is usually done either with photographic plates or with cellulose-nitrate films (e.g., [Mars69]) or with a scanning detector (e.g., [Ho68; Ge71]) or with a position-sensitive surface-barrier detector (e.g., [Ge65; Ap67; Gi72b]). Fuschini *et al.* [Fu71] have described the use of a checker-board counter for such an application, and Anastassiades *et al.* [Ana69a] have described a mechanical scanning device based on a rotating cylinder in which a series of collimating holes have been drilled.

Obtaining and maintaining good angular resolution is normally a consideration of paramount importance in channeling measurements. Since the incident beam is usually very tightly collimated, care has to be taken to avoid degradation of the beam quality due to slit-edge scattering. A theoretical analysis of this problem has been given by Courant [Cou51] and is found to be in good accord with experiment (e.g., [Re69]). A method of producing a supercollimated beam from negative ions has been suggested by Rickey and Smythe [Ri62] and tested by Armstrong and Wegner [Ar71]. These latter authors passed a 4-MeV beam of negative hydrogen ions through two apertures 30 μm in diameter and 1 m apart. The emerging beam was then magnetically separated into its positive, neutral, and negative components. Because of the small electron binding energies in the H^- ion, any slit-edge scattering or scattering in the residual gas in the vacuum system is almost certain to convert H^- to either H^0 or H^+ at these velocities. Thus the emerging H^- beam is free of components degraded by scattering. Armstrong and Wegner were able to obtain a few pico-amperes of a 30-μm-diam H^- beam with an angular divergence of ± 1.5 mdeg. By way of comparison, an angular divergence of ± 3.8 mdeg can be obtained [Ge71] by normal collimating techniques, using two 0.5-mm-diam. apertures 7.6 m apart, without appreciable slit-edge scattering effects and with beam currents of a few hundred nanoamperes. It is worthy of note that, in order to make full use of beams with angular divergences in the millidegree range, extreme care must be taken to avoid detrimental effects due to amorphous surface layers, inadequate vacuum, mechanical vibrations, electrostatic charging of insulators near the beam, varying magnetic fields, etc. The rms angular spread introduced by multiple scattering in an oxide surface layer of typical thickness 30 Å on a Si crystal is approximately ± 20 mdeg for protons of a few MeV [Ar72].

Small beam-spot sizes at the target are usually desirable from considerations of angular resolution and of target characteristics. However, a small beam-spot size can result in an attendant high rate of radiation damage to the target crystal. Radiation damage can lead to effects such as lattice expansion in the sample ("dimpling," see, e.g., [Me71a]), swelling and surface blistering (for an instance where this was observed in the course of a channeling measurement, see [Mi73]), and possibly the eventual complete amorphization of the irradiated section of the target (see, e.g., [Ne67b; Ger72] and references contained therein; see also Sec. 4.2f). It is normally advisable before and during a channeling measurement to determine the rate at which target crystals deteriorate due to radiation damage, e.g., by monitoring χ_{min} in a particular channeling orientation. Radiation damage effects can often be minimized or even eliminated completely by heating the target crystal either continuously or at appropriate intervals during a measurement.

A severe problem often arises when the target crystal is an insulator. Electrostatic effects due to the passage of the beam may cause such crystals to strain and crack. This can frequently be overcome either by heating the target during bombardment, by evaporating a very thin conducting layer (e.g., of carbon or aluminum) onto the surface and grounding it, or by spraying electrons from a filament onto the target to neutralize it.

Conventional techniques of beam-current integration for normalization purposes often cannot be employed in channeling measurements. For example, in transmission measurements the angular divergence of the transmitted beam depends markedly on crystal orientation. For target crystals that are insulators, there are obvious problems with beam integration. One method of circumventing these difficulties is through the use of a beam chopping device (see e.g., [Ge71; Fon72]).

In order to determine accurately a normalized (depth dependent) channeling yield like that shown schematically in Fig. 3, the random yield (also depth-dependent) must be known with precision. Frequently the yield is assumed to be random when it is measured for an orientation in which the beam is not incident near any major crystal axis or plane. However, finding such an orientation can be time-consuming, and it is very difficult to avoid observation of some channeling effects. This method seems to be reproducible only to about $\pm 10\%$. Ziegler and co-workers [Zi72a, 73] have shown how to determine a random yield that is both reproducible ($\pm 1\%$) and accurate ($\pm 1\%$). Their method involves offsetting the target orientation so that the beam is incident at an angle of about ten times $\psi_{1/2}$ relative to a major axis and then measuring the yield as the crystal is rotated about this axis. Corrections must be made for geometrical factors arising from the angle of offset.

3.2. Monocrystalline targets

In channeling experiments, the preparation and characterization of monocrystalline targets often requires more effort than the actual measurement itself. Each different target material needs its own special treatment. The technology for the preparation of monocrystalline targets, especially very thin, uniformly planar ones, is developing rapidly. For a review of the topic, the reader is referred to the article of Whitton [Wh69].

Almost all channeling measurements performed thus far have employed exclusively inorganic crystalline targets. The extreme susceptibility of most organic crystals to radiation damage makes them generally unsuitable targets for such measurements.

Occasionally it is possible to grow monocrystalline targets of the size and thickness required for particular channeling measurements. More often, targets must be prepared either by sectioning a piece from a larger bulk crystal or by epitaxial growth. Samples prepared from bulk crystals can usually be obtained with high purity, low defect concentration, and small mosaic spread. However, it is often difficult to make them thin enough for transmission measurements. Epitaxially grown crystals, on the other hand, can be made thin and uniform, but tend to suffer from larger mosaic spread, twinning, and difficulties in mounting.

In cases where a sample can be obtained by cleaving a bulk crystal, the resulting planar surface is usually adequately clean and free of damage for channeling measurements. In other cases, e.g., when samples are sectioned from bulk crystals by techniques such as sawing, abrasive cutting, spark erosion, and acid etching, the resulting surface is usually uneven and damaged. The surface quality can be improved by lapping and mechanical polishing. The damage left by these processes can then be removed by one or a combination of various techniques such as vibratory polishing, anodic oxidation and dissolution, chemical- or electro-polishing, ion bombardment, and annealing. The final quality of the surface can be checked by a variety of methods but it is worthy of note that one of the best and possibly the most appropriate for the purpose is through use of the channeling effect (see Sec. 6.4).

Electrochemical thinning techniques (see e.g., [Bu71; Me71b] and references contained therein) frequently offer a means of obtaining self-supporting, large-area, uniformly thin monocrystalline films. With such techniques, Meek *et al.* [Me71b] have obtained highly uniform Si crystals with thicknesses in the range 5000–10000 Å and areas of a few square millimeters. Anodic oxidation followed by chemical stripping (see, e.g., [McC63; Pr69]) provides a method of accurately removing uniform layers of material in a very well-controllable fashion.

Those channeling measurements that require extremely clean surfaces must be performed in ultra-high vacuum. The surfaces must then usually be prepared either by cleaving *in vacuo* or by low-energy inert gas bombardment followed by annealing.

The thinnest crystals, typically a few hundred to a few thousand angstroms thick employed in channeling experiments have been epitaxially grown. The great majority of these have been gold crystals grown either on a silver-rocksalt substrate ($\langle 100 \rangle$ orientation) or on a silver-mica substrate ($\langle 111 \rangle$ orientation) (see, e.g., [Bas59; And66b; Gi68a; Zig68; Ch69a; Da69; No69; Hög70; Rei71; Kir72] and references contained therein). One of the principal difficulties with the use of rocksalt as a substrate lies in the steps in the cleaved surface which cause tearing of the epitaxially grown crystals upon removal from the substrate. Mica surfaces, on the other hand, do not have this difficulty, but crystals grown on them are frequently badly twinned; i.e., two orientations grow epitaxially at the same time. A twinned crystal of this type is believed to consist of a collection of crystallites on the order of a few microns in size and existing in one of two orientations which differ by a rotation of 180° about the $\langle 111 \rangle$ axis of epitaxial growth. The boundaries between these crystallites are thought to be only of the type perpendicular to the crystal surface; thus each incident beam particle in a channeling measurement traverses only one crystallite. By careful growth and annealing techniques, it is possible to obtain untwinned crystals of gold grown on mica. The extent of twinning in epitaxially grown crystals can be determined using channeling as a tool (see, e.g., [Gi68a; Kir72]).

Unless great care is taken in the preparation of epitaxially grown crystals, mosaic spreads with full widths at half-maximum of a degree or more can result. Noggle (e.g., [No67; Da69; No69; Ap72a,b; No72]) has been able to reduce the mosaic spread of thin crystals grown on rocksalt to about 0.1° for gold and to about 0.03° for

silver. Electron-microscope observations on these samples indicate that there are discrete defect-free crystal regions approximately 0.5–1.0 μ in diameter which are slightly misoriented from adjacent regions. These perfectly crystalline mosaic blocks constitute over 95% of the volume of the target samples. The orientation distribution of these blocks (mosaic spread) is measured by x-ray rocking curves. For gold crystals grown epitaxially on a silver-mica substrate. Gibson *et al.* [Gi68a] have reported mosaic spreads of less than 0.05°. Similarly, Reichelt and Lutz [Rei71] have reported mosaic spreads of 0.07° for Au crystals grown in this manner.

To conclude this section, we stress the great importance of adequate characterization of monocrystalline targets. All too often this topic is neglected or carelessly treated in published accounts of channeling experiments. It is especially important when the target crystal is thin as in the transmission measurements described in Sec. 4.3. In this connection the careful work of Noggle (e.g., [Da69; No72]) in using electron-microscope and x-ray diffraction techniques to characterize dislocation densities and mosaic spreads may be cited as worthy of emulation.

4. CHANNELING WITH HEAVY ($M_1 > m_e$) POSITIVE PROJECTILES

In this section we survey several types of channeling and blocking measurements performed with positive particles having masses large compared with that of the electron.

4.1. Surface effects

It is well known that many surface phenomena observed in the bombardment of single crystals with low-energy heavy ions, e.g., sputtering, surface scattering, and secondary electron emission, are strongly orientation dependent. Strictly speaking, these effects, of course, are not truly surface effects. Although the sputtered atoms, secondary electrons, etc. do indeed come from the crystal surface, the channeling mechanism responsible for the orientation dependence hinges upon the fact that the crystal has some depth to it.

These effects have been discussed extensively in the literature (e.g., [Ne68a; Mash72; Col69] and references contained therein) and will be mentioned here only in passing. The orientation dependences observed in single-crystal sputtering experiments (e.g., [Rol60; Alm61; Flu64]) played a central role in the discovery of channeling. Since then, many authors have pointed out the significance of channeling effects in sputtering (e.g., [Ne68a; On68; Fi69; Eli70; Fi70; Fr70; Chap72]) and in surface scattering (e.g., [Yu68, 72; Mash70, 72; Shu71; Ari72]) with low-energy heavy ions. Measurements on these phenomena provide one of the most important methods of studying the ψ_2 region; see Eq. (2.28). Using H, He, and N ions in the energy range 20–100 keV, Reuther and Bradford [Reu69] have made simultaneous measurements of the orientation- and energy-dependence of sputtering and backscattering from Au crystals. They found values of $\psi_{1/2}$ for the sputtered particles somewhat smaller than the corresponding values of $\psi_{1/2}(0)$ for backscattered particles. The difference was attributed to dechanneling effects influencing the value for sputtering (see also [Wij69]).

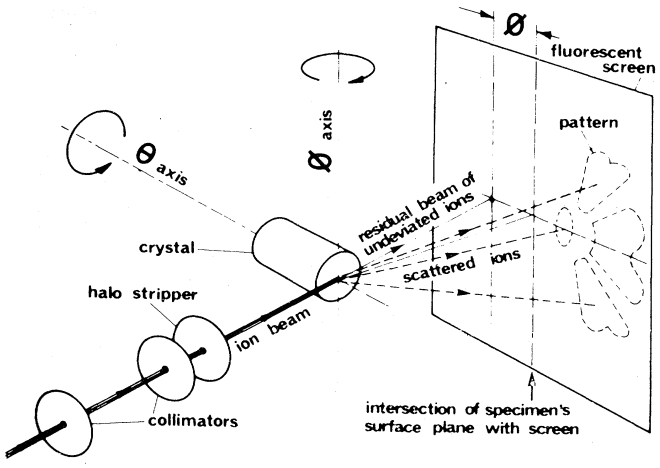

FIG. 40. Diagram of the experimental arrangement used by Farmery *et al.* [Fa70] in their surface reflection experiments. The spot drawn on the screen occurs at a scattering angle of 2ϕ. The $\langle 111 \rangle$ axis lies at a slightly greater angle; its associated blocking pattern is also shown sketched on the screen.

At the University of Sussex, the glancing-angle scattering of alpha-particle beams from surfaces of monocrystalline and amorphous tungsten has been studied [Far70; Marw71, 72]. The beam energies ranged from 30 keV to 2 MeV. The experimental arrangement is illustrated in Fig. 40. These measurements are technically rather difficult. They require beam-spot diameters of 100 μ or less and vacuum conditions that have to be stringently controlled to prevent the buildup of amorphous surface layers, even a few angstroms of such surface layers can be extremely deleterious because of the small incidence angle. In the arrangement shown in Fig. 40, the highly polished scattering surface lay close to a (110) planar direction in the W crystal. In the initial measurement [Far70], an angle θ was chosen (see Fig. 40) so that a major axis (e.g., the $\langle 111 \rangle$) lay in the plane containing the incident beam and the θ axis. The angle ϕ was varied from zero up to a few degrees, and data on the scattered beam were recorded by photographing a fluorescent screen; later measurements [Marw72] also employed a solid-state particle detector. For small angles of incidence ($\phi \lesssim \psi_1$) the scattered beam exhibited two components: an intense low-energy-loss specularly reflected spot and a higher-energy-loss blocking pattern. On the screen drawn in Fig. 40 these are indicated for the $\langle 111 \rangle$ case. The data showed that the spot was due to reflection not from the atomic rows but from the plane of the crystal surface. For the case depicted in Fig. 40, the authors postulated that the spot was due to planar channeling effects. The results observed in measurements of this type depend rather delicately on the relative orientations of the crystal's symmetry directions and its surface and also on the relative magnitudes of the (usually small) angular differences involved and the critical angles for axial and planar channeling. Marwick *et al.* [Marw72] have made extensive measurements on the distributions both in energy and in angle for the scattered particles. They point to the possible significance of semichanneling, i.e., a process whereby particles penetrate two or three layers below the

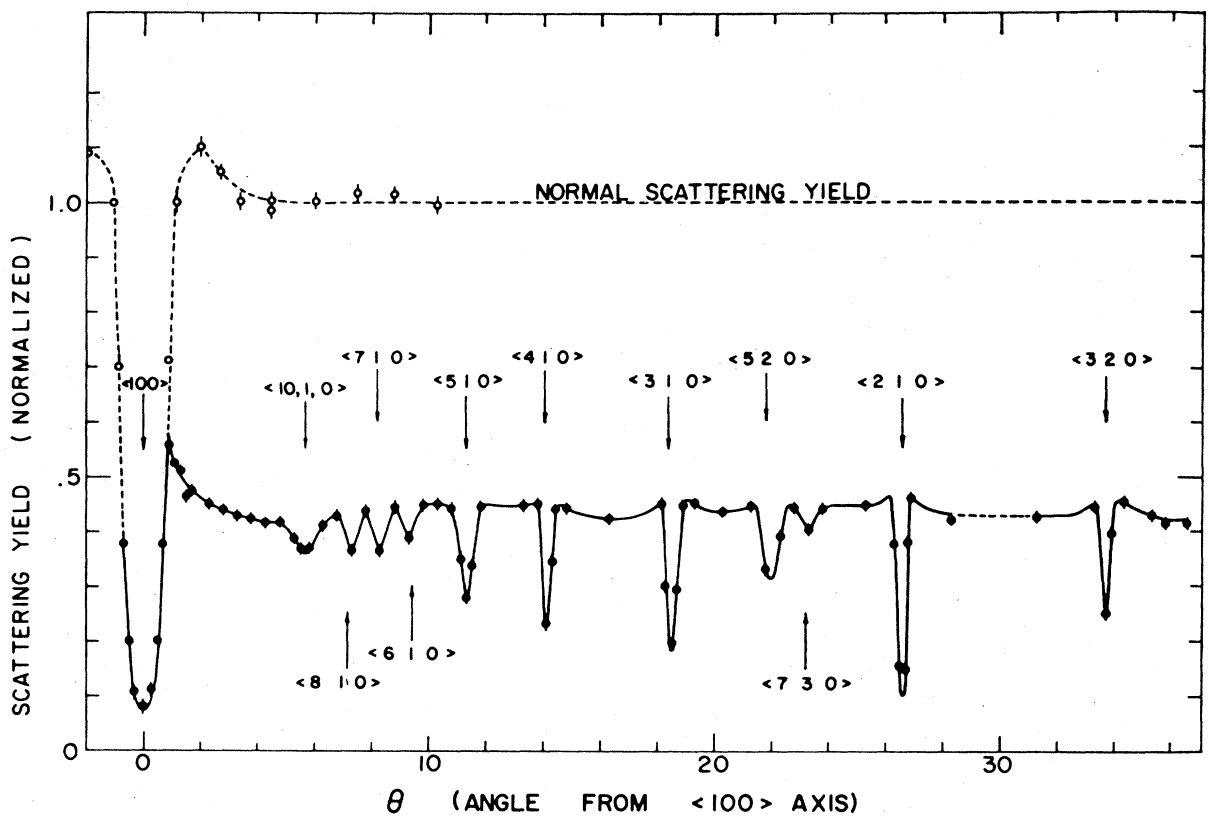

FIG. 41. Axial and planar channeling dips obtained in the backscattering of 10-MeV ^{4}He ions from W [Dav68a]. The solid dots are results when the incident beam direction lies in the (100) plane, and the open circles are data obtained when the direction of scan does not lie in any close-packed lattice plane. The yields shown are for a scattering zone about 3 μ beneath the surface.

surface before being reflected back out of the crystal. It is interesting to note the role of dechanneling in surface reflection experiments. In conventional channeling measurements, particles that acquire transverse energies greater than the critical value for channeling are fed into the random beam, but in surface scattering experiments many of them can rapidly reemerge from the crystal and can be studied directly (see also [Rau73]).

4.2. Bulk effects

4.2a. Rutherford scattering

The first direct evidence for the strong influence of channeling on Rutherford scattering yields was found by Nelson and Thompson [Ne63]. They observed sharp minima in the scattering of 50-keV H^+, He^+, Ne^+, and Xe^+ ions from a Cu crystal whenever the incident beam lay in a channeling direction. Later, Bøgh and Uggerhøj [Bø65a, b] measured the orientation-dependent yields for Rutherford scattering of 400-keV protons from crystals of Al and Ta. Since then, Rutherford scattering (usually backscattering) has become the most commonly used tool in channeling studies. It has the advantage of high cross sections, small impact parameters, and the availability of a wide variety of particle species and energies.

A typical experimental arrangement for backscattering is illustrated in Fig. 2 and some measurements on axial channeling dips are given in Figs. 6, 12, 51, 57, 66, 89, 107, and 108. Figure 41 shows the result of scanning the incidence angle along a major plane. Many axes with high Miller indices are observed indicating that care should be taken to avoid their effects when measuring a planar channeling dip; the yields shown in Fig. 41 correspond to a scattering depth of 3 μ where effects due to yet higher-order axes have been washed out by dechanneling.

For axial channeling, the measured shape of the dip in yield at zero depth, i.e., the depth-dependent yield $\chi(x)$ that has been smoothly extrapolated to $x = 0$, averaging over any surface oscillations and avoiding complications due to the surface peak, is generally in fairly good agreement with theoretical calculations of the type discussed in Sec. 2.4d1. Figure 42 shows a comparison between calculated and measured values of $\psi_{1/2}(0)$ for the axial channeling of protons in several materials and at several temperatures. For planar channeling, the situation is somewhat less satisfactory. However, the value of $\psi_{1/2}(0)$ can usually be predicted quite accurately with the expression due to Barrett [Ba71]; see Eq. (2.81) and Fig. 23. Although there is presently no simple formula capable of predicting $\chi_{\min}(0)$ in the planar case, there has been success in some instances in fitting the measured planar dips with calculated curves. An example is shown in Fig. 43 (see also Sec. 2.4d2).

There have been comparatively few channeling measurements on backscattering in the low-energy ψ_2 region; see Eq. (2.28). This is in part attributable to experimental difficulties with surface layers and with detection problems. Figure 44 shows some results obtained by Berg-

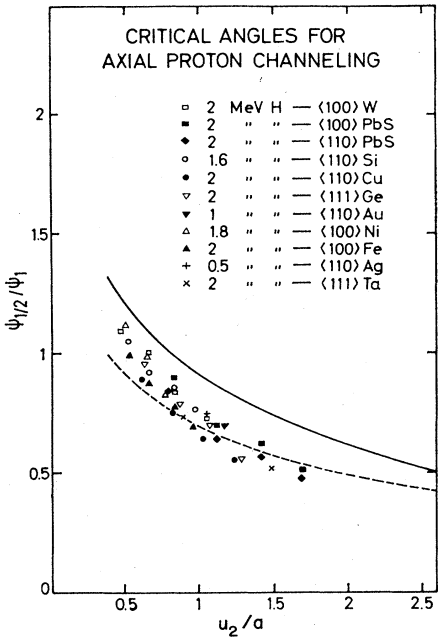

FIG. 42. Measured values of $\psi_{1/2}(0)/\psi_1$ as a function of the parameter u_2/a [An72a]. The same symbol is used to denote data points measured at different temperatures. The solid line corresponds to the analytical result calculated using the continuum approximation. Equation (2.58) is used for this, since, for the data shown here, $\psi_1 < u_2/d$. The dashed line is calculated from Eq. (2.66), with $k = 0.80$ and $m = 1.2$, derived by Barrett [Ba71] from his Monte Carlo results.

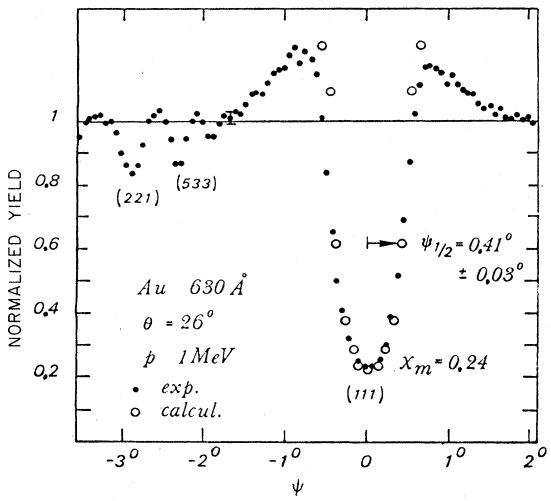

FIG. 43. Planar channeling dip for 1-MeV protons incident in the (111) direction in Au [Po72b]. The crystal thickness was 630 Å and the scattering angle 26°. The solid dots are the experimental points, and the open circles are the results of a calculation which includes multiple-scattering effects [see Sec. 2.4d2, Eq. (2.80), and Fig. 22].

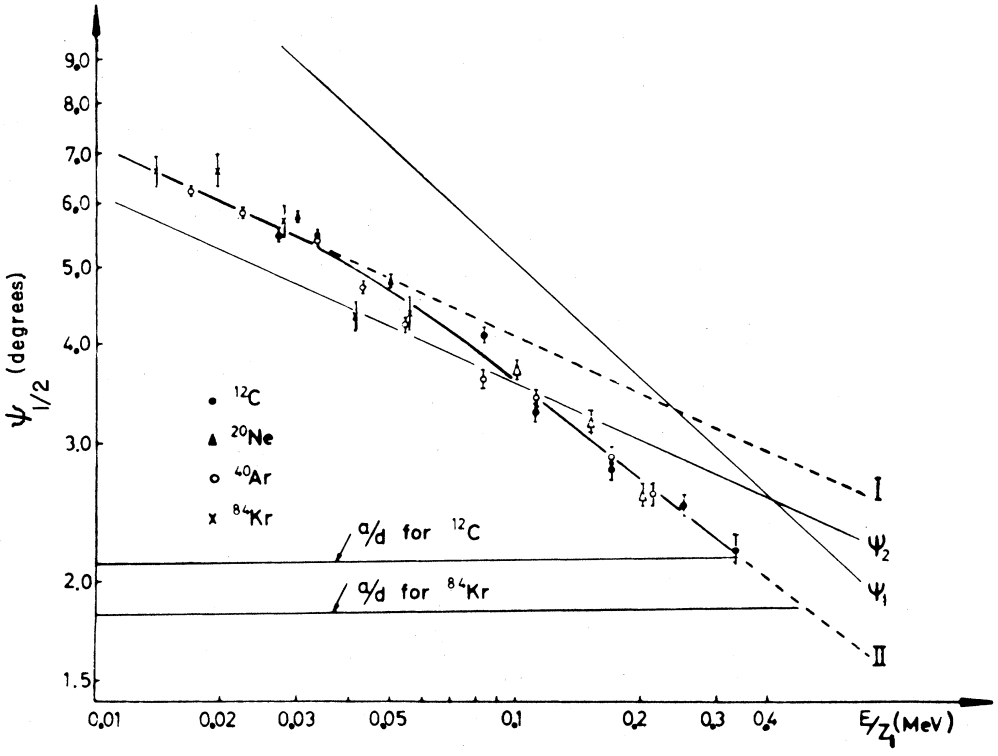

FIG. 44. Values of $\psi_{1/2}$ determined from backscattering, as a function of E/Z_1 for ^{12}C, ^{20}Ne, and ^{84}Kr ions channeled in the ⟨111⟩ direction of W [Berg68]. The values of ψ_1 and ψ_2 are also plotted (ψ_2 is not strictly a universal function of E/Z_1; it is plotted here for ^{40}Ar). Curve I is a straight line with the same slope as ψ_2 but fitted to the data in the low-energy region. Curve II is an extrapolation of the curve that fits the data.

ström *et al.* [Berg68] on the variation of $\psi_{1/2}$ with the parameter E/Z_1 for low-energy heavy ions axially channeled in W. Most of the data shown in Fig. 44 fall in the ψ_2 region (i.e., $\psi_1 > a/d$), but it is only for very low values of E/Z_1 that the data show the $E^{-1/4}$ energy dependence characteristic of ψ_2. Channeling and semichanneling effects have been reported by Feijen *et al.* [Fei73] for 3-keV H^+ ions scattered from a Cu crystal. Morita *et al.* [Mor71c] have measured values of $\psi_{1/2}$ for axial channeling in Si and Ge for protons in the energy range 20 keV–1.5 MeV. They find that the measured values are always about 0.8 times the values calculated by Andersen [An67] (Sec. 2.4d1).

For low incident velocities, Z_1 oscillations in the channeled stopping power are observed (see Secs. 2.6b, 4.2e, and 4.3b) These are attributable to shell effects that modify the electron density and thus affect the electronic stopping power. Since the electron distribution also affects the potential governing channeling, it might be expected that shell effects should be seen in other characteristics of channeled motion. Figure 45 illustrates some evidence for such effects seen in Z_1 oscillations in χ_{min} for various ions axially channeled in Au [Ne69a].

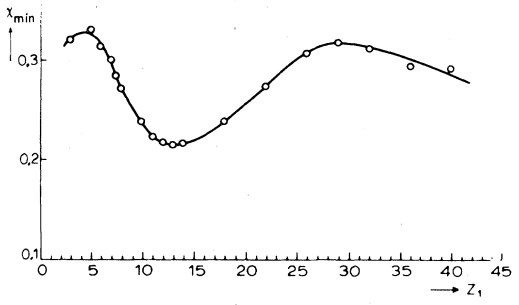

FIG. 45. Oscillatory behavior of χ_{min} as a function of Z_1 measured for various ions (E = 80keV) channeled in the ⟨110⟩ axial direction of Au [Ne69a].

The surface oscillations discussed in Sec. 2.4e1 are readily observable in Rutherford scattering measurements. They are most prominent in planar channeling. An example is shown in Fig. 46. For the first few hundred angstroms in depth before straggling effects begin to dominate, a considerable improvement in depth resolution can be achieved by using a magnetic spectrometer instead of a solid-state detector to measure the energies of scattered particles. This technique has been employed by Bøgh [Bø67a, 68a, b, 72]. Figures 47–49 show some of his results. Axial alignment is illustrated in Fig. 47. The surface peak corresponds to scattering from about the first two atomic layers of the target (c.f. Fig. 20), and thus the shape of the peak is essentially the instrumental line shape. The surface oscillations are not as pronounced as for the planar case (Figs. 46 and 48). This is consistent with the discussion of Sec. 2.4e1 and with the Monte Carlo calculations of Barrett [Ba71] (see Figs. 25 and 26). Figure 48 shows a planar case. The two curves are recorded for beam incidence 5° either side of the ⟨111⟩ axis. In the two cases the conditions of incidence are the same, but, for a given scattering depth the exit paths differ; the exit path lies in a random direction. Thus, for example, the peaks occurring at about 3190 G in Fig. 48 both correspond to scattering at a depth of $\lambda_{ch}/2$, where λ_{ch} is the classical wavelength of the planar channeled trajectory. The stopping power on the ingoing portion of the path for these particles is expected to be abnormally large. Using the data from two curves such as those in Fig. 48 one can determine this stopping power and also

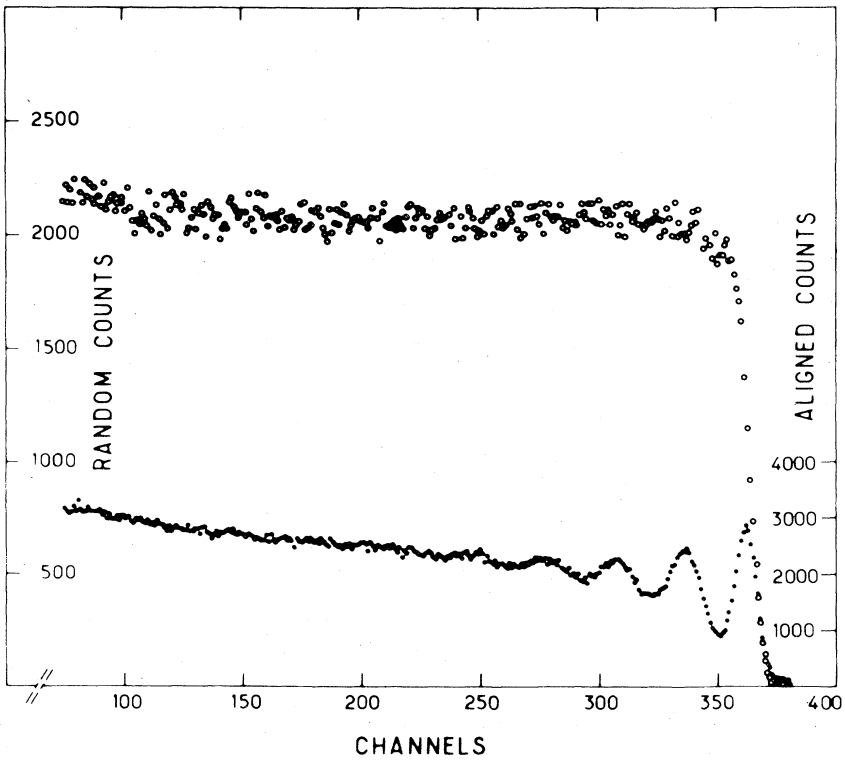

FIG. 46. Aligned and random spectra obtained in backscattering of 1.9-MeV ^{4}He from an Fe crystal [Abel72a]. The two spectra are normalized for equal numbers of incident beam particles. The aligned spectrum along the (100) plane exhibits clearly the surface oscillations referred to in Sec. 2.4e1. The energy dispersion is 2.24 keV/channel. The depth resolution near the surface is about 100 Å. From the aligned spectrum, a wavelength λ_{ch} = 640Å is calculated for the oscillating channeled trajectories.

the wavelength λ_{ch}. Figure 49 shows planar dips measured at depths corresponding to the first and third minima in the backscattering spectrum, i.e., dips measured for particles that have suffered one and three collisions. The most striking feature is the pronounced shoulders observed for the single-collision case and the large multiple scattering to which the particles must be subjected since the shoulders are strongly reduced already after three collisions (c.f. Fig. 22). It is remarkable too that after one collision, $\psi_{1/2}$ is approximately 20% larger than the value observed after three collisions; the latter corresponds to the value usually observed when a solid-state detector is used. It is evident that multiple scattering effects play a very significant role in planar channeling even at small depths. Further evidence for this is provided by data and calculations on the variation of the value of χ_{min} as a function of planar spacing (Fig. 50).

Figure 51 shows a typical example of backscattering data obtained with a solid-state detector and a thick target crystal. For progressively deeper scattering regions within the crystal, multiple scattering causes the shoulders on the channeling dip to disappear and the value of $\psi_{1/2}$ to get smaller. Similar effects are seen for low-energy heavy-ion bombardment (see, e.g., [Berg68]). The variation of $\psi_{1/2}$ with depth is a consequence of the increase in the rate of dechanneling as the direction of beam incidence deviates from being parallel to the channeling direction: the initial transverse energy distribution moves to higher values. Campisano *et al.* [Ca72b] have made experimental and theoretical studies of the depth and temperature dependence of $\psi_{1/2}$. Some of their measurements are shown in Fig. 52.

The first detailed studies of dechanneling were the backscattering measurements of Davies *et al.* [Dav68a]

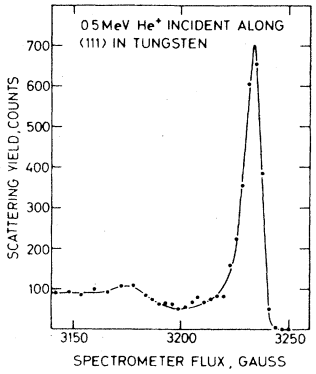

FIG. 47. Momentum spectrum measured with a magnetic spectrometer for α particles scattered at 90° from a W crystal [Bø72]. The incident beam of 0.5-MeV ^{4}He is aligned with the ⟨111⟩ crystal axis. The depth resolution near the surface is about 20 Å.

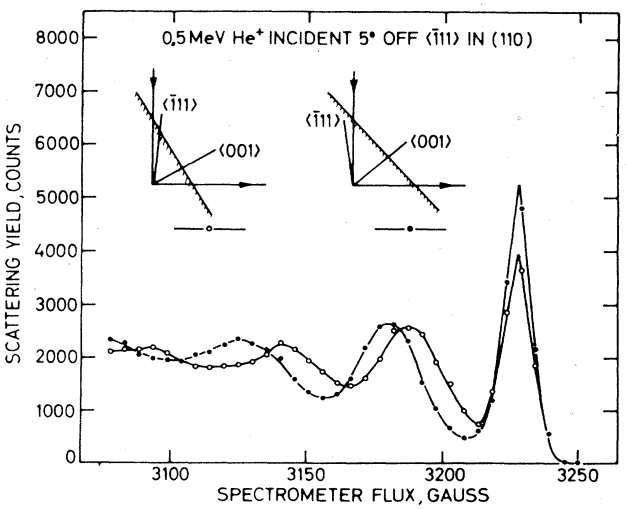

FIG. 48. Momentum spectra measured with a magnetic spectrometer for α particles scattered at 90° from a W crystal [Bø72]. The incident beam of 0.5-MeV ^{4}He is aligned with the (110) crystal planes. The two curves are for incidence 5° on either side of the ⟨111⟩ axis.

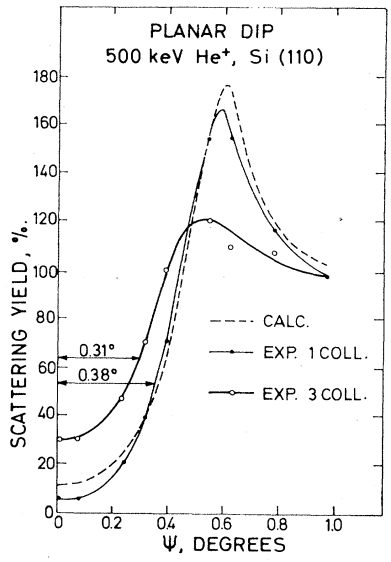

FIG. 49. Planar dip measured for 0.5-MeV α particles scattering at 90° from a Si crystal [Bø72]. Angular scans were made across the (110) planar direction and data were recorded for particles that have made only one collision (solid dots) and for those that have made three collisions (open circles). The dashed line represents a calculation based on a planar continuum potential (Sec. 2.4d2).

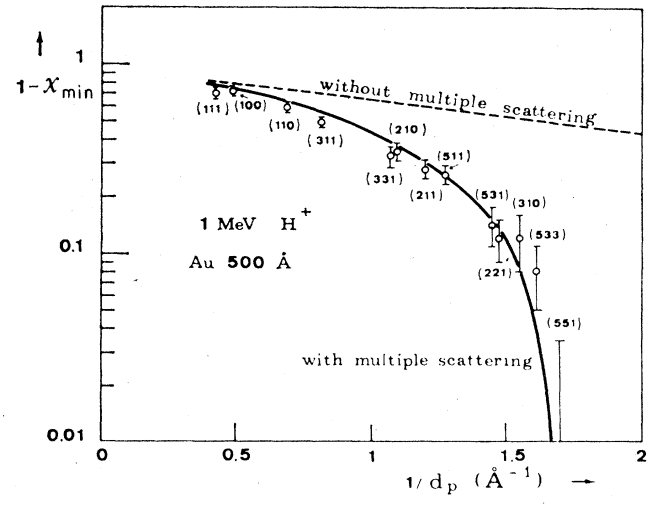

FIG. 50 Plot of $(1 - \chi_{min})$ versus $(1/d_p)$ for planar channeling of 1-MeV protons in a 500-Å-thick Au crystal [Po72a]. The value of χ_{min} refers to the whole depth of the crystal, not just the surface value, and d_p is the planar spacing. The dashed line shows the result of calculations excluding nuclear multiple scattering, and the solid line shows the calculated results with nuclear multiple scattering included.

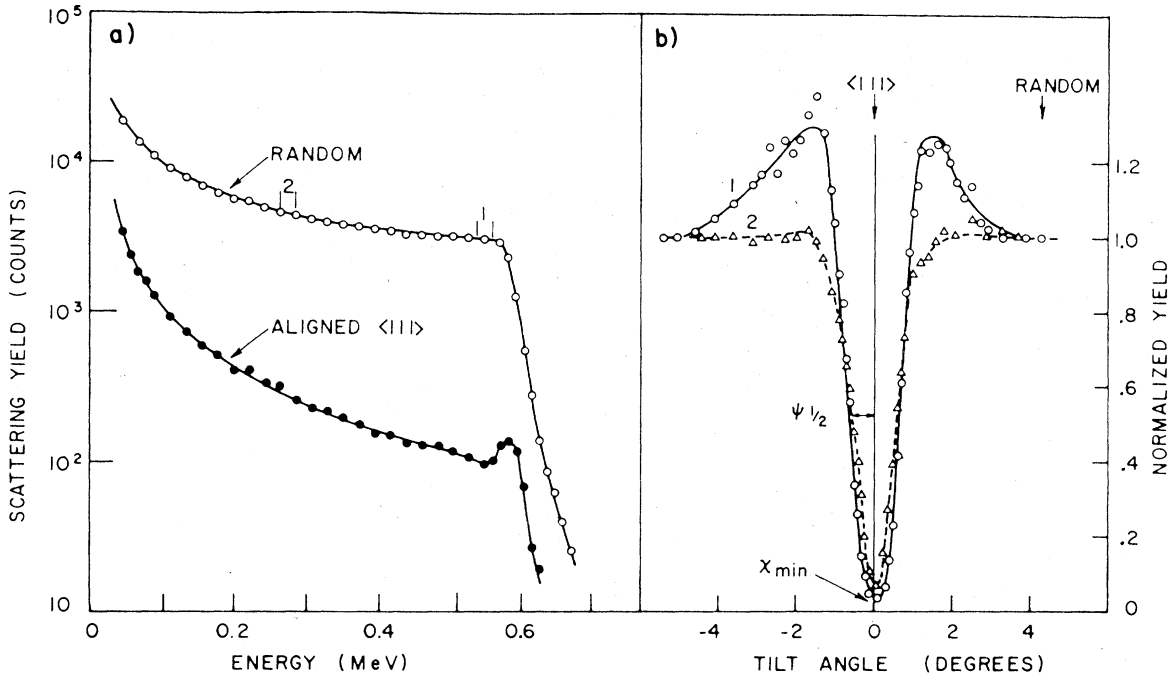

FIG. 51. (a) Aligned (⟨111⟩ axis) and random energy spectra for 1-MeV helium ions backscattered at 160° from a Si crystal. (b) Orientation dependence of the normalized yield obtained from the energy regions 1 and 2 marked in the spectra in (a) [Pi69a].

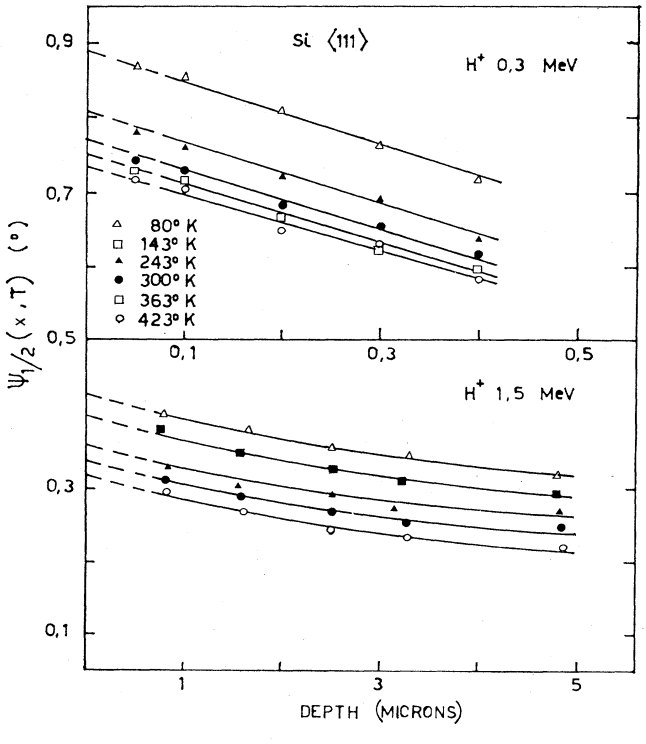

FIG. 52. Depth dependence of $\psi_{1/2}$ for 0.3- and 1.5-MeV protons in the ⟨111⟩ axial channel of Si at different temperatures [Ca72b]. The depth scale is determined from Eq. (2.114).

and the transmission measurements of Appleton *et al.* [Ap68]. Since then, dechanneling has been the subject of fairly intense investigation at several laboratories. Figures 53 and 54 show some typical backscattering data and illustrate the dependence of the channeling dip on depth and temperature. The fitted curves in Fig. 54 are calculated from the expression of Ellegaard and Lassen [El67], c.f. Eq. (2.105), modified to take into account surface scattering effects. Several authors (e.g., [Fuj70; Kon70a; Fot71; Howe71; Ca72; Mor72]) have been able to fit their measured temperature-dependent axial dechanneling rates with simple linear or exponential functions of u_2^2, where u_2 is the thermal vibration amplitude defined in Eqs. (2.44) and (2.51). However this is by no means a universal rule (see, e.g., the data of [Dav68a, 72a]). Similar diversity exists in abilities to fit the dependence upon the incident energy E. At the University of Catania, extensive experimental investigations have been carried out on the dechanneling of H and He ions in Si and Ge [Fot69, 70a, 71; Ca70, 71, 72a, b]. It is found that, for these materials, the dechanneling in a given axial direction as measured by $\chi_{min}(x) - \chi_{min}(0)$ is a simple, almost linear function of the single parameter xu_2^2/E, where x is the depth determined according to Eq. (2.114). Figure 55 shows some of the Catania data plotted in this way for two major axes in Si. The simplicity of this functional dependence and the vast amount of data it correlates are remarkable. There is no obvious theoretical reason why such a simple relation should exist (see Sec. 2.4e2). Data obtained at some other laboratories (e.g., [Dav72; Fon72]) do not obey this simple rule. In Sec 2.4e2 a list is given of some reasons why there is often poor agreement between dechanneling theory and experiment, and sometimes between the results of experiments conducted at different laboratories. Various methods

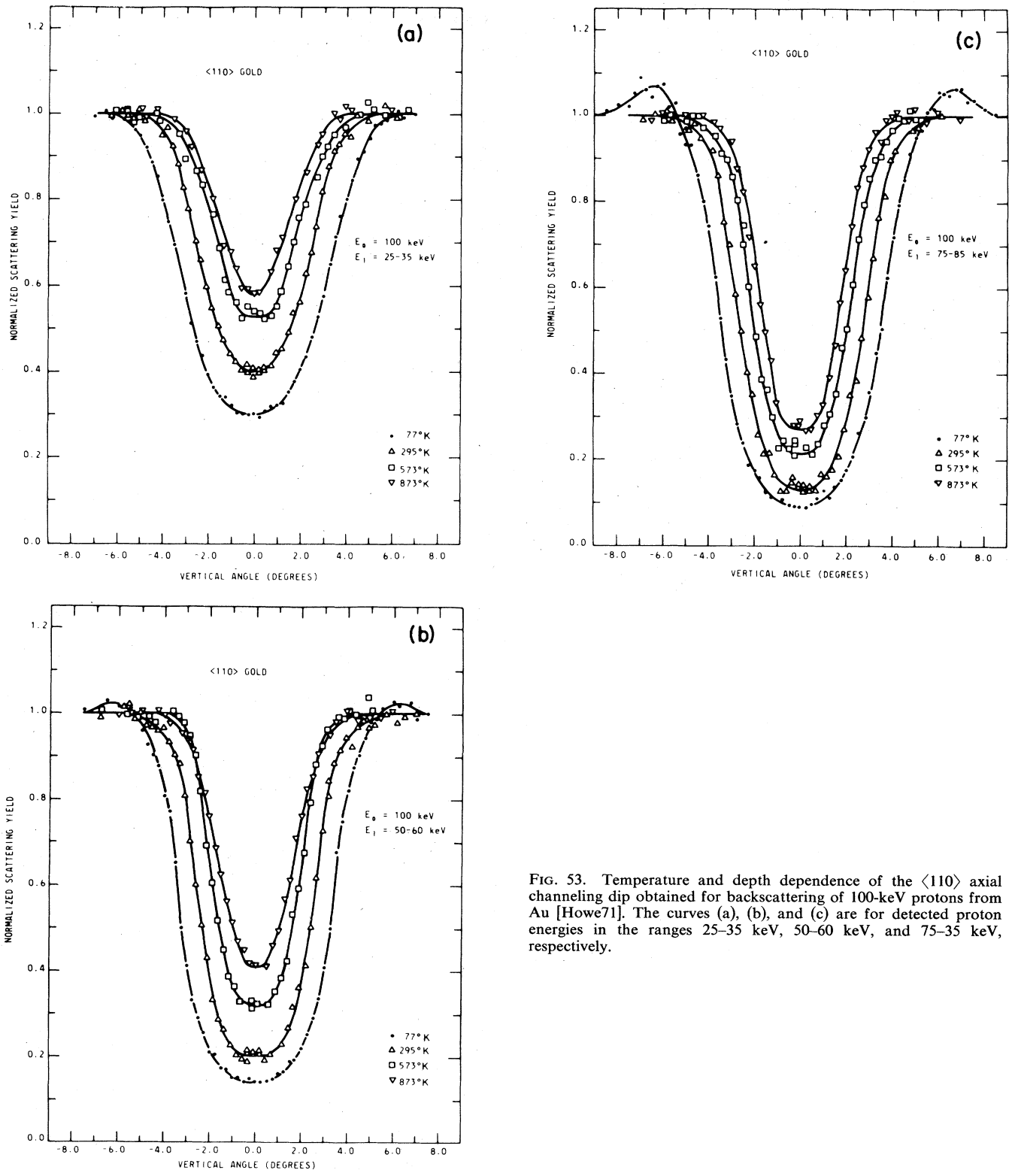

FIG. 53. Temperature and depth dependence of the ⟨110⟩ axial channeling dip obtained for backscattering of 100-keV protons from Au [Howe71]. The curves (a), (b), and (c) are for detected proton energies in the ranges 25–35 keV, 50–60 keV, and 75–35 keV, respectively.

have been used to overcome the problem of the uncertainty in determining the depths at which dechanneling and backscattering occur; see item (g) in the list given in Sec. 2.4e2. We have already alluded to the techniques used by Jack [Ja72] (Sec. 2.4e2) and by Bøgh [Bø72] (see Fig 48). By varying the angle of detection, one is able to vary the outgoing path length traversed in the crystal by the detected particles. The information obtained in this way can greatly reduce the uncertainty in the scattering depth. Another approach to this problem has been employed by Edge and Dixon [Ed70] who used the (p,α) reaction to measure the escape of 0.5-MeV protons from

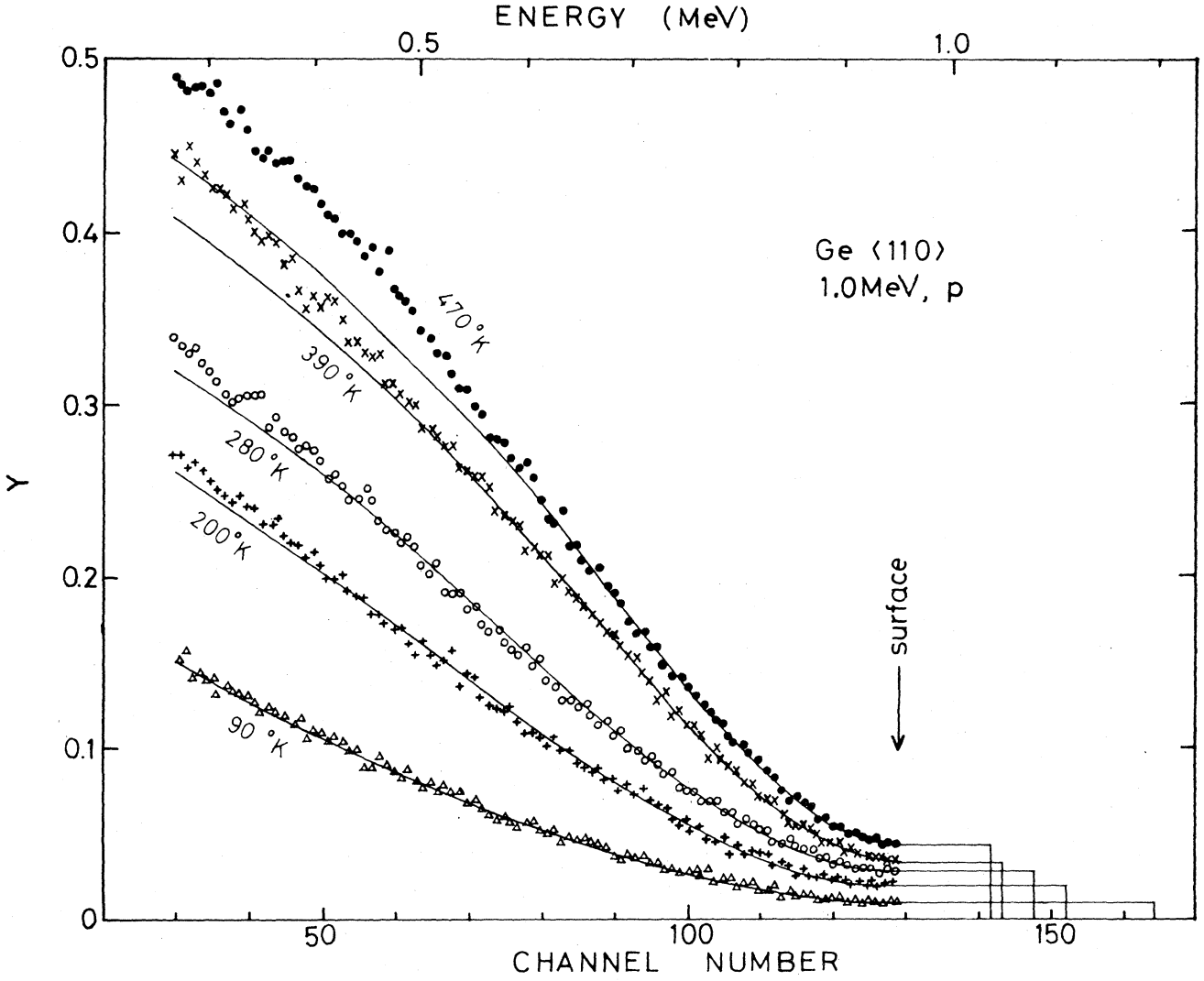

FIG. 54. Aligned (⟨110⟩ axis) spectra (normalized to random) obtained at various temperatures for backscattering of 1-MeV protons from Ge [Fuj72b]. The full lines are calculated from a modification of the formula [Eq. (2.105)] of Ellegaard and Lassen [El67].

axial channels in CaF_2 and LiF. They also were able to show that the channeled stopping power for those particles that later dechanneled was about the same as the random stopping power.

Backscattering measurements on planar dechanneling have been reported by Davies *et al.* [Dav68a, 72] for W and by Campisano *et al.* [Ca72a] for Si and Ge. It is found that the quantity $1 - \chi_{\min}(x)$ decreases approximately exponentially with x and that $x_{1/2}$ varies roughly linearly with E; see Eq. (2.111). Both of these functional dependences are in accord with theory based on the diffusion model (Sec. 2.4e2). The agreement is, however, a little bit surprising since for the planar case the discrepancy between $1 - \chi_{\min}(x)$ and $f_{ch}(x)$ is known to be large (e.g., [Alt70a]). The temperature dependence of planar dechanneling is very slight, certainly much less pronounced than for the axial case. This is illustrated in Fig. 56. A qualitative explanation of this has been given by Davies [Dav68a] (see also Sec. 2.4e2). These authors point out that even without thermal vibrations a planar channeled particle already encounters rather large force fluctuations in the steering process since relative to the particle's trajectory, the atoms are distributed randomly in the planes. The extra force fluctuations introduced by lattice vibrations therefore make a relatively smaller contribution to the rate of dechanneling for the planar than for the axial case. A further consideration is the fact that for major axial directions, the potential minimum in the channel tends to be shallow, and therefore even particles with fairly small transverse energies can approach close to the channel walls and so be strongly affected by changes in the thermal vibration amplitudes. The potential minima for planes tend not to be shallow (an example is shown in Fig. 9), and so only particles with high transverse energies approach the walls closely.

It was stressed in Sec. 2.4e2 that the divergence of the incident beam and the conditions at the crystal surface are of crucial importance in measurements on dechanneling. A group at Caltech [Rim71, 72a; Lug73] has made a series of experimental investigations of these effects.

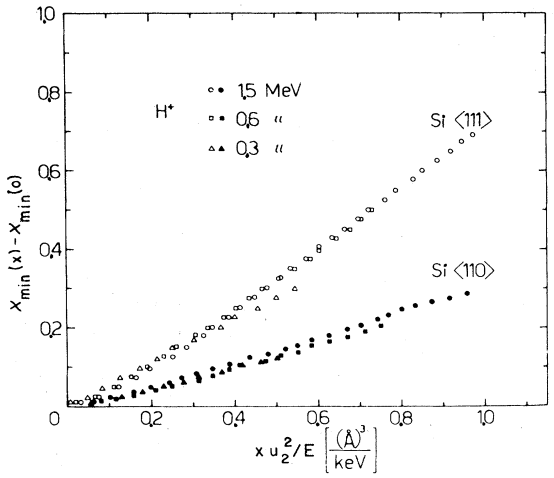

FIG. 55. The quantity $\chi_{min}(x) - \chi_{min}(0)$ plotted against the parameter xu_2^2/E for protons dechanneling in the ⟨110⟩ and ⟨111⟩ axial directions of Si [Fot71]. The data come from measurements at three incident beam energies and six different target temperatures in the range 80–423 °K. The depth scale is determined according to Eq. (2.114).

Some of their data showing the influence of amorphous surface layers upon the shape of the channeling dip are reproduced in Fig. 57. The authors obtained good agreement between their data and the results of calculations based on Meyer's treatment [Mey71] of plural scattering.

Morita and Itoh [Mor71a] and Morita [Mor72] have found a strong dependence of dechanneling rates on the mass M_1 of the incident ion (Fig. 58). They were able to fit the dechanneling rate, expressed as a probability per unit energy loss, to a linear function of $1/L_e$, a relationship predicted by their diffusion model treatment of dechanneling [Mor71b], where L_e is defined in Eq. (2.88). Their result is shown in Fig. 59.

A different type of mass-dependent effect has been found by Grasso and co-workers [Fot70b, Gr72]. These authors detected small differences in the shapes of the shoulders of channeling dips (measured near the crystal surface) depending on whether the incident particles were protons or deuterons. These differences have been interpreted [DeW70a; Gr72] as evidence for quantum effects in channeling (see the discussion in Sec. 2.5).

In addition to the articles already cited in this section, the reader is referred to the following, by no means complete, list of further papers on measurements on the depth and temperature dependences of Rutherford scattering [Far65; An68; Pal68; Pi69b; Mor70a; Beh68, 71, 72; Fuj71a, b; So71a, b, 72a, b; Bel72c; Del73; He73; Kub73] (see also Sec. 4.4).

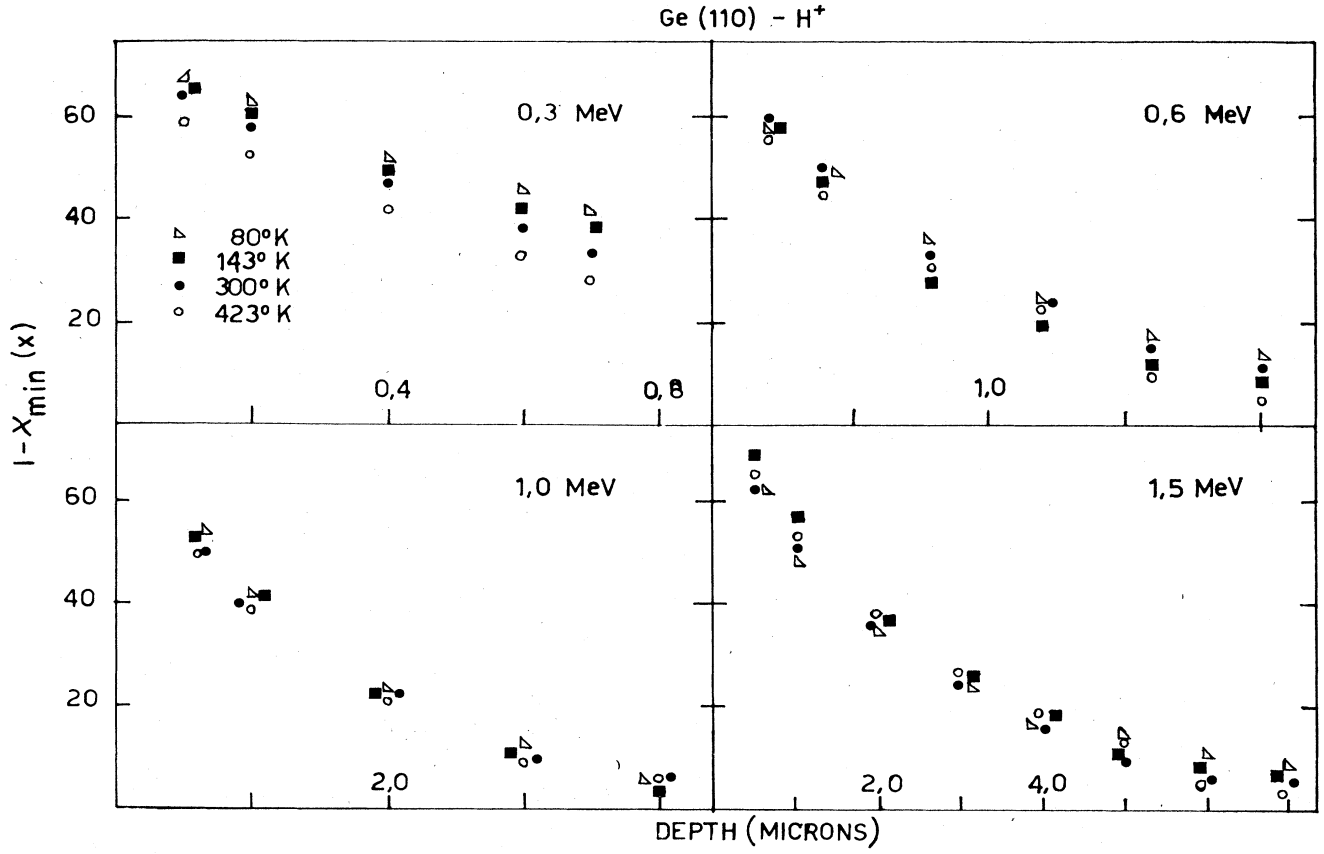

FIG. 56. Depth dependence of the quantity $1 - \chi_{min}(x)$ for protons channeled in the (110) planes of Ge at various temperatures and energies [Ca72a]. The depth x is determined according to Eq. (2.114).

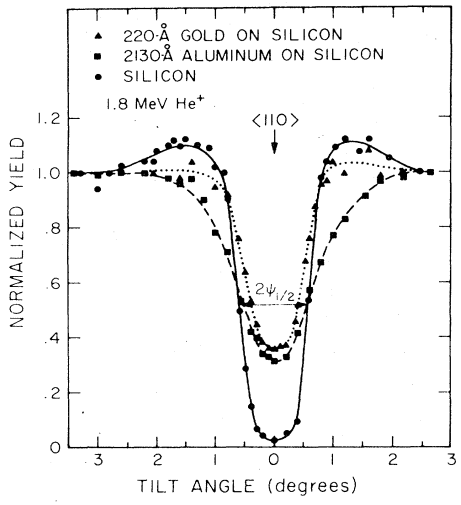

FIG. 57. Normalized channeling dips (⟨110⟩ axis) for 1.8-MeV He ions backscattered from a Si crystal [Rim72a]. The data show the effects of the presence of amorphous layers of Au and Al. The yields were measured for a scattering region approximately 0.1 μ below the crystal surface.

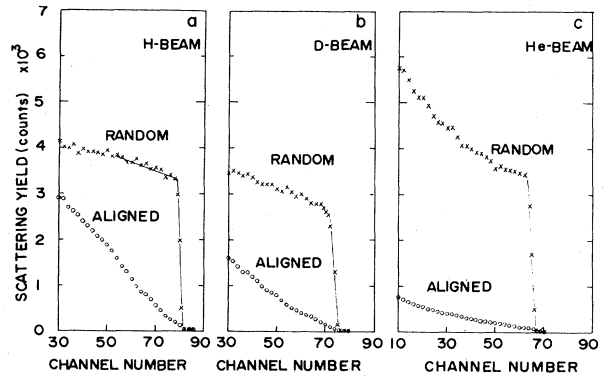

FIG. 58. Energy spectra for 1.5-MeV protons, deuterons, and helium ions backscattered from a Ge crystal [Mor72]. The aligned spectra were obtained for channeling along the ⟨100⟩ axial direction.

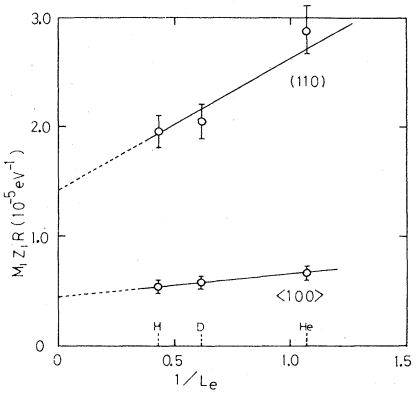

FIG. 59. Mass dependence of planar and axial dechanneling of 1.5-MeV protons, deuterons, and helium ions in Ge [Mor72]. The quantity $M_1 Z_1 R$ is predicted [Mor71b] to be proportional to $A + B/L_e$, where A and B are constants, M_1 and Z_1 are the mass and charge, respectively, of the incident ion, R is the measured dechanneling rate eV^{-1}, and L_e is defined in Eq. (2.88).

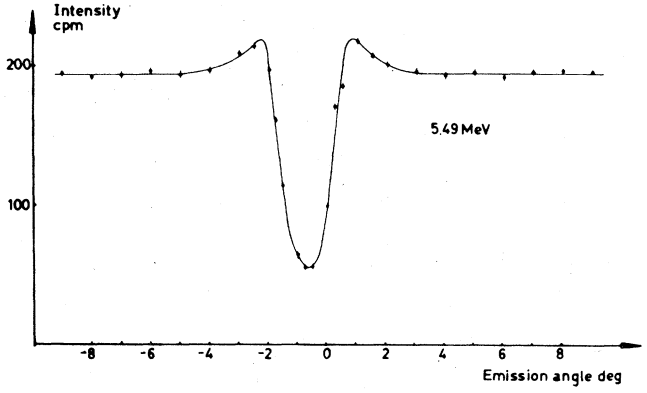

FIG. 60. Intensity as a function of emission angle for 5.49-MeV α particles from ^{222}Rn implanted in W [Do65a]. The dip is centered on the ⟨111⟩ axis of the W crystal. The mean depth of the Rn nuclei was measured to be 650 Å. The value of $\psi_{1/2}$ is 1.7° and χ_m is 0.28.

4.2b. Blocking

Following its discovery in 1965 [Do65; Ge65; Tu65a, b], the blocking effect has been studied intensively in connection with its applications in nuclear lifetime measurements and in atom location measurements. We defer until Secs. 6.2 and 6.6 a discussion of blocking effects in which the emitting atom does not occupy a normal position in the lattice. The relationship between channeling and blocking has been discussed in Sec. 2.2.

Domeij [Do65a, b, 66] has studied the angular distribution of α particles emitted from radioactive ^{222}Rn ions injected at 60 keV into a W single crystal. Figure 60 shows some of his results. The fact that χ_{min} is larger and $\psi_{1/2}$ is smaller than the corresponding values for α-particle channeling is probably due to lattice damage effects caused by the implantation and to the fact that some of the Rn atoms may be interstitially located. Multiple scattering and flux peaking effects may also be present (see also [Mat67, 69a]). For comparison with the data shown in Fig. 60, Oen [Oe65] has made a calculation based on the assumption that the blocking is due solely to the nearest neighbor atom. His calculation is discussed in Sec. 2.4d1.

An example of planar blocking effects seen in the wide-angle scattering of a proton beam is shown in Fig. 61. It is interesting to note the existence of a group of particles emerging in the planar direction and having anomalously low energy losses. These particles must have been scattered into the planar channel and thereafter experienced a reduced stopping power. This process somewhat complicates the analysis of data on nuclear lifetimes (Sec 6.6). Fujimoto *et al.* [Fuj71d] have made experimental and theoretical investigations of such channeling effects in blocking phenomena. The angular widths of the dip and peak in Fig. 61 are approximately the same and agree well with the corresponding value for planar proton channeling.

The temperature and depth dependences of blocking have been studied (e.g., [Tu65a, b; Ho68; Ana69b]) with

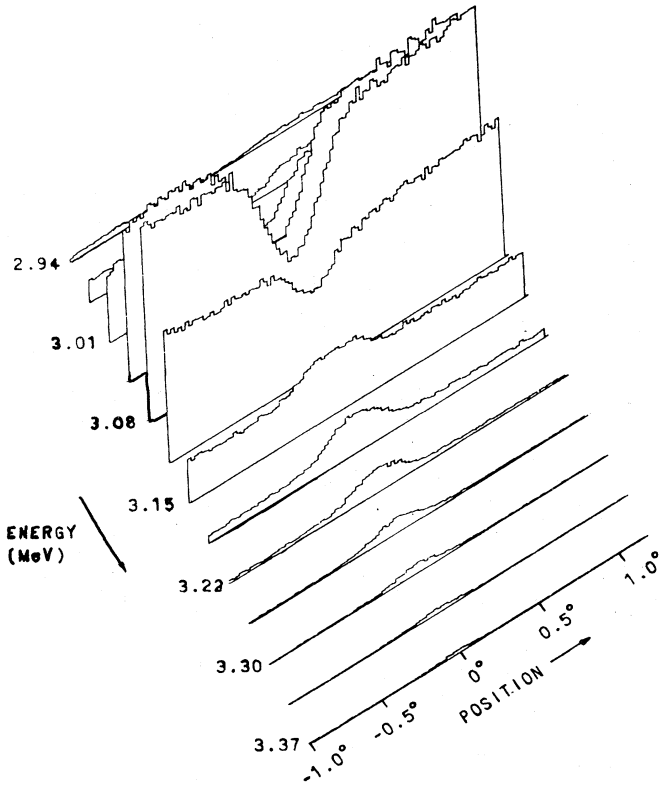

FIG. 61 Distribution in energy and in angular position of protons emerging near the (110) planar direction of a 35-μ-thick Si crystal [Ho68]. The incident 4-MeV proton beam was not channeled. The scattering angle for the detected protons was 15°.

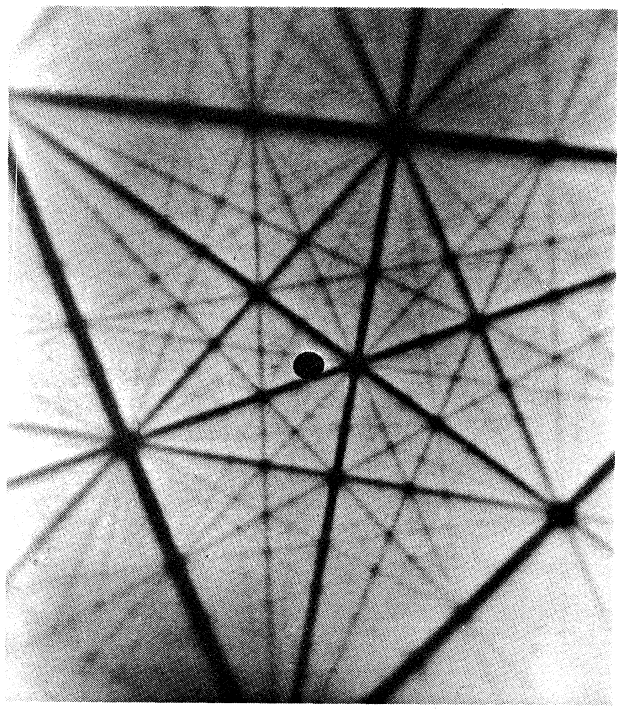

FIG. 62. Backscattering blocking pattern recorded for 150-keV protons incident on a Bi crystal near the ⟨111⟩ axial direction [En70]. The hole near the center of the picture is to permit the passage of the incident beam.

results similar to those found for the corresponding channeling measurements.

Blocking patterns are frequently recorded on photographic plates or on cellulose-nitrate film (e.g., [Ge65; Tu65b, d; Barr68, 69a, 70; Beh68; Ho68; Maz69; En70; Mat70; Mu70; Howe71; Pan72]). An example is shown in Fig. 62. A careful study of such patterns has revealed lines corresponding to planes whose Miller indices include integers as high as 9 [Ho68]. Mueller and White [Mu70] have found marked differences in blocking patterns for crystals having nearly identical structures but differing thermal vibration amplitudes (e.g., Pt and Au). The line intensities seen in blocking patterns have been interpreted by Barrett [Barr69b] in terms of the geometrical structure factors familiar from x-ray crystallography.

If, in a blocking measurement, the incident beam lies in a channeling direction, then the yield detected for close-encounter processes is drastically reduced. Such an experimental arrangement is referred to as double alignment and was first investigated by Kulikauskas *et al.* [Kul67] for the axial case and by Holland and Gemmell [Ho68] for the planar case. Since the sensitivity to scattering or reactions involving atoms at regular lattice sites is minimized in double alignment, then by the same token the sensitivity to processes involving displaced atoms is maximized. Advantage can be taken of this in studies of lattice disorder and in atom location measurements (Secs. 6.2 and 6.3). In these measurements, it is often difficult to avoid causing excessive beam-induced radiation damage to the target crystal due to technical problems in simultaneously aligning the beam and the detector. Feldman and Appleton [Fel69; Ap70] showed that these difficulties can be greatly reduced if unidirectional double alignment is employed, i.e., the channeling and the blocking directions are the same. This can be achieved using an annular detector to collect particles scattered close to 180° from the beam direction. An example of data recorded this way is shown in Fig. 63.

It may be expected that the minimum yield $\chi'_{\min}$ in a double alignment measurement should be proportional to the product $\chi^a_{\min}\chi^b_{\min}$, where $\chi^a_{\min}$ and $\chi^b_{\min}$ are the corresponding single alignment values for the ingoing and outgoing directions, respectively. There should also be a dependence on the angle α_{ab} between these two directions, since the displacements of the scattering atoms relative to the two directions involve geometrical factors. We write

$$\chi'_{\min}(\alpha_{ab}) = \nu'(\alpha_{ab})\chi^a_{\min}\chi^b_{\min}. \tag{4.1}$$

For the case where the two directions concerned have the same type of crystal symmetry, this becomes

$$\chi'_{\min}(\alpha) = \nu'(\alpha)\chi^2_{\min}. \tag{4.2}$$

Appleton and Feldman [Ap70] have derived analytically an expression for $\nu'(\alpha)$ based on the continuum model for axial channeling (Secs. 2.4b and 2.4d1). They included a modification of Lindhard's expression, Eq. (2.47), for $\chi_{\min}$ that allowed for a nonuniform distribution of particle

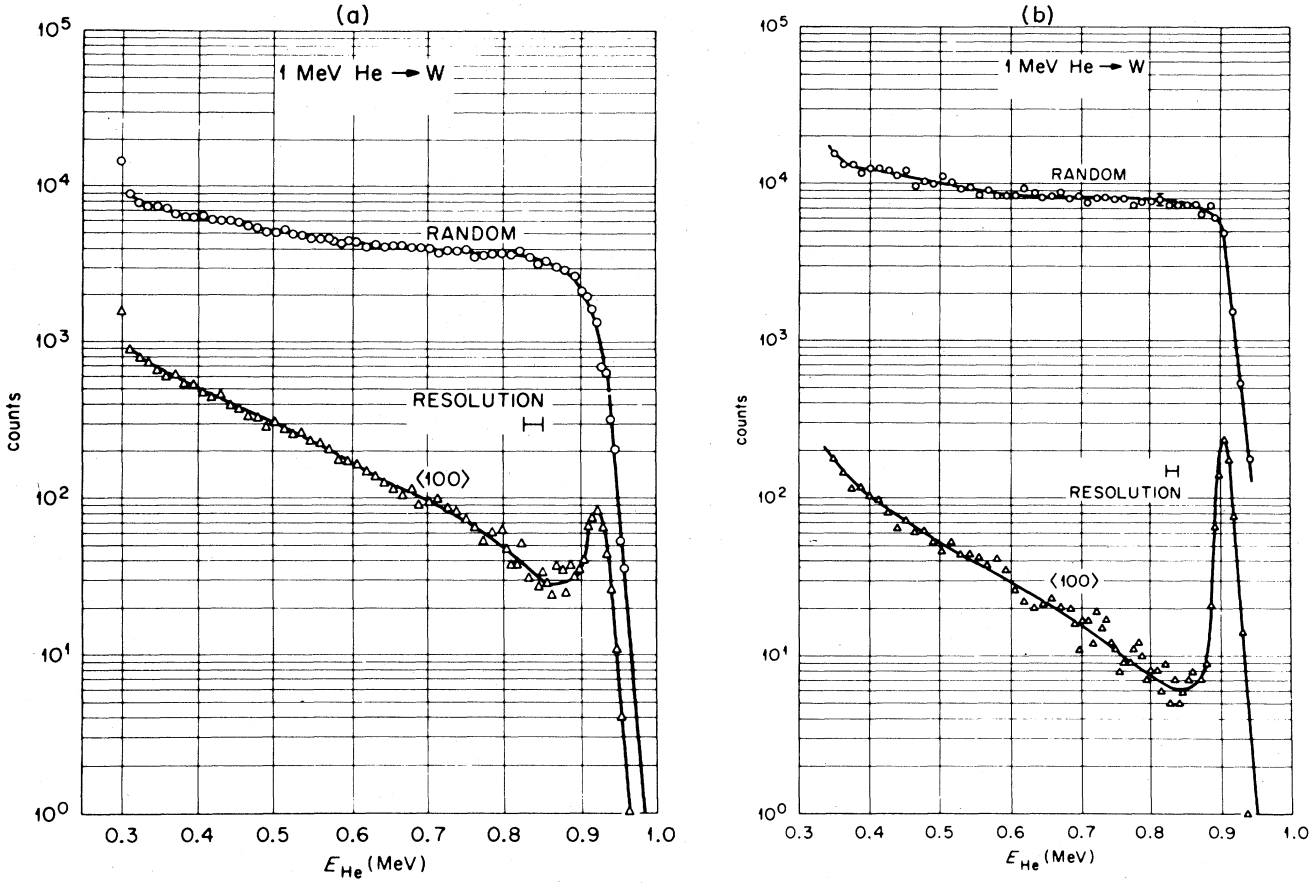

FIG. 63. Rutherford backscattering (near 180°) energy spectra for 1-MeV ^{4}He ions incident in a random direction (circles) and parallel to the ⟨100⟩ axis (triangles) of a W crystal [Ap70]. The data shown in (a) are for single alignment and in (b) are for uniaxial double alignment. The target temperature was 350 °K. Measured at a detected ^{4}He energy of 0.85 MeV, the normalized minimum yields are 0.01 ± 0.001 and 0.0009 ± 0.0001 for the data shown in (a) and (b), respectively.

flux. Their result is

$$\nu'(\alpha) = 2 - 0.5 \sin^2\alpha. \tag{4.3}$$

From Monte Carlo calculations Barrett [Ba71] found values of $\nu'(90°) = 1.1 \pm 0.1$ and $\nu'(0°) = 1.2 \pm 0.1$ for 1-MeV protons channeled in the ⟨110⟩ axial direction of Au. Thus both theories predict a value of $\nu'(\alpha)$ in the range 1 to 2 and predict that it should be somewhat larger for uniaxial than for biaxial geometry. Several values of $\nu'(\alpha)$ have been measured for the axial case (see, e.g., [Kul67; Bø68a, b, 69; Fel69; Ap70, 72c; Beh72; Pi72]) and are found to lie in the range from 2 to 10. Experimental problems, such as amorphous surface layers, may account for some part of the discrepancy, but it seems likely that the largest part may be attributable to factors that have thus far been neglected in theoretical treatments; e.g., if an incoming channeled particle strikes a target atom, the probability that such a particle will emerge from the crystal along a major symmetry direction is higher than that for particles emitted in normal single-alignment blocking.

For axial double alignment, Eq. (4.2) indicates that χ'_{min} should be strongly temperature dependent, approximately proportional to u_2^4; see Eqs. (2.47) and (2.68). This was experimentally verified by Appleton and Feldman [Ap70] who measured χ'_{min} for the ⟨100⟩ axis in W as a function of temperature. They found good agreement with Eq. (4.2) when Barrett's value, Eq. (2.68), of χ_{min} was used. However a value of $\nu'(\alpha) \approx 9$ was required. Picraux *et al.* [Pi72a] have measured the dependence of χ' on the incidence angle for 1-MeV ^{4}He ions bombarding Si. The measured value of $\psi_{1/2}$ for axial double alignment is found to be about 25% larger than the value for single alignment; part of this can be attributed to the reduced energy of the scattered α particles. Double alignment measurements are very susceptible to lattice damage [Kul67; Ap70], a fact that makes them well suited to determinations of such damage [Bø68a, b].

Gaillard *et al.* [Ga73b] have measured the dependence on bombarding energy for the minimum yield in planar double alignment. Their data display an oscillatory energy dependence which provides detailed information on the oscillating particle trajectories in planar channeling.

4.2c. Nuclear reactions

In crystals the interaction rates observed for nuclear reactions involving the absorption or emission of charged particles are highly orientation dependent. Most of the considerations discussed in the previous two sections apply. The main characteristics of nuclear reactions that

are of particular interest from a channeling standpoint are (i) the existence of reactions with high positive Q-values permitting the identification and separation of elements, especially light elements, which might be difficult by other means, e.g., backscattering, (ii) the existence of narrow resonances that can be used as depth gauges, e.g., in determining dechanneling rates, and (iii) recoil effects associated with the finite lifetimes of compound nuclei (Sec. 6.6). Figure 64 shows the orientation dependence of the γ-ray yield from the $^{19}F(p,\alpha\gamma)^{16}O$ reaction measured in a CaF_2 crystal.

The following list indicates some of the reactions for which channeling effects have been measured. The corresponding references are also given.

$^6Li(n,\alpha)^3H$	[Bi73]
$^6Li(p,\alpha)^3He$	[Ed70]
$^{12}C(d,p)^{13}C$	[Mat69a, 70]
$^{16}O(d,p)^{17}O$	[Abel69, 72b; Erik69a; Mat69a, 71]
$^{16}O(^3He,p)^{18}F$	[Cli72]
$^{19}F(p,\alpha\gamma)^{16}O$	[Ed70, 72a; Kob68, 70; He71a, b]
$^{27}Al(p,\gamma)^{28}Si$	[Bø64; An65; Blan69]
$^{28}Si(d,p)^{29}Si$	[Ge65; Ho68]
$^{29}Si(p,\gamma)^{30}P$	[Bø64]
$^{51}V(p,n)^{51}Cr$	[Po68b]
$^{65}Cu(p,n)^{65}Zn$	[Th64; Far65].

4.2d. Characteristic x-ray production

The influence of channeling on the rate of production of characteristic x rays in crystalline targets was first studied by Brandt and co-workers [Br65, 68] and was followed by an extensive set of measurements by Khan *et al.* [Kh66, 67a, b]. X-ray production is of special interest in channeling because the impact parameters involved, typically up to $10^{-10} - 10^{-9}$ cm, are much larger than those in Rutherford scattering, typically $10^{-13} - 10^{-11}$ cm. In fact, the impact parameters for x-ray production can be of the same order of magnitude as the critical distance of closest approach ρ_c to the channel walls. Where two-particle Coulomb collisions are the dominant mechanism for ionizing a particular atomic shell in the target atoms, a semiclassical impact-parameter treatment (e.g., [Bang59]) is known to reproduce the observed ionization cross sections in the region where Eq. (2.10) is satisfied. Under these conditions Bohr's adiabaticity criterion, Eq.

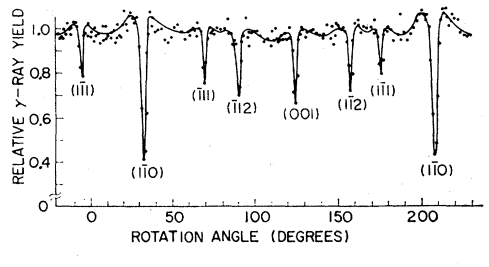

FIG. 64 Variation of the γ-ray yield from the $^{19}F(p,\alpha\gamma)^{16}O$ reaction when a CaF_2 crystal is rotated so that the beam direction follows a cone around the $\langle 110\rangle$ axis [Kob70]. The cone angle is 5° and the proton energy is 896.1 keV.

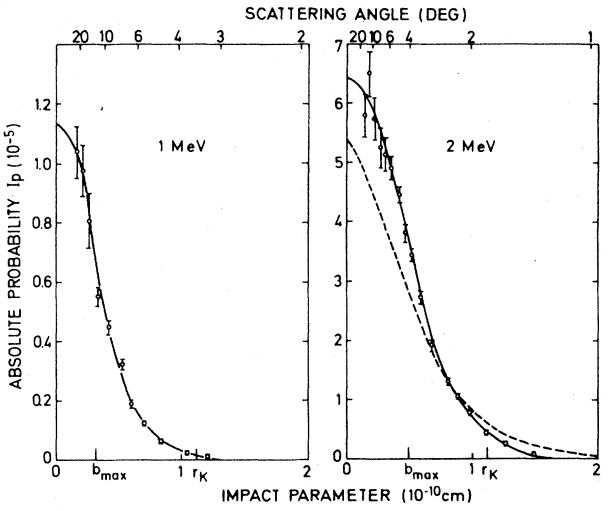

FIG. 65 K-shell ionization probability I_p as a function of impact parameter (or alternatively, scattering angle) for 1- and 2-MeV protons incident on Ag [Laeg72a]. The K-shell radius r_K is indicated together with the values of b_{max} calculated according to Eq. (4.4) The solid lines are drawn through the experimental points. For the 2-MeV case, the dashed line corresponds to the theoretical value of Hansteen and Mosebekk [Han72].

(2.127), provides an estimate of the maximum impact parameter for ionization by a particle of velocity v:

$$b_{max} = \hbar v/\Delta E \tag{4.4}$$

$$\approx 93(E/M_1)^{1/2}/\Delta E \text{ Å}, \tag{4.5}$$

where the energy E and the mass M_1 of the bombarding particle are given in units of MeV and amu, respectively, and the binding energy of the shell in question, ΔE, is given in eV. The validity of this estimate in the cases of ionization of the K shells in Cu, Se, and Ag by protons of about 2-MeV energy has recently been demonstrated by Laegsgaard and co-workers [Laeg72a, b; Br73a] (Fig. 65). One might expect that if b_{max} were much less than ρ_c, typically about one or two times u_2, the thermal vibration amplitude defined in Eqs. (2.44) and (2.51), then the corresponding x-ray yield should vary with orientation in the same way as backscattering or nuclear reaction yields. If, on the other hand, b_{max} and ρ_c are comparable in size, the channeling dip for x rays might be expected to be shallower and narrower than those for backscattering or nuclear reactions. These expectations have been verified by Davies and co-workers [Dav69; Pi69a]. Figure 66 shows some of their data for 1.4-MeV ^4He ions incident on W. For the case shown in Fig. 66, b_{max} is about 0.005 Å for the L shell and about 0.02 Å for the M shell. For W at room temperature, $u_2 \approx 0.07$Å if a Debye temperature of 310°K is assumed [Lo62]; for a Debye temperature of 400°K [Gray63], $u_2 \approx 0.05$ Å. Thus, the channeling dips for the L x rays and for backscattering should be the same, whereas one might expect the dip for the M x rays to be slightly different as is observed in the data shown in Fig. 66.

When the incident beam consists of heavy ions, quasi-molecular excitation (Pauli excitation) of inner-shell vacancies in both the beam and the target atoms may occur [Fa65; Bar72]. This type of process is known to dominate

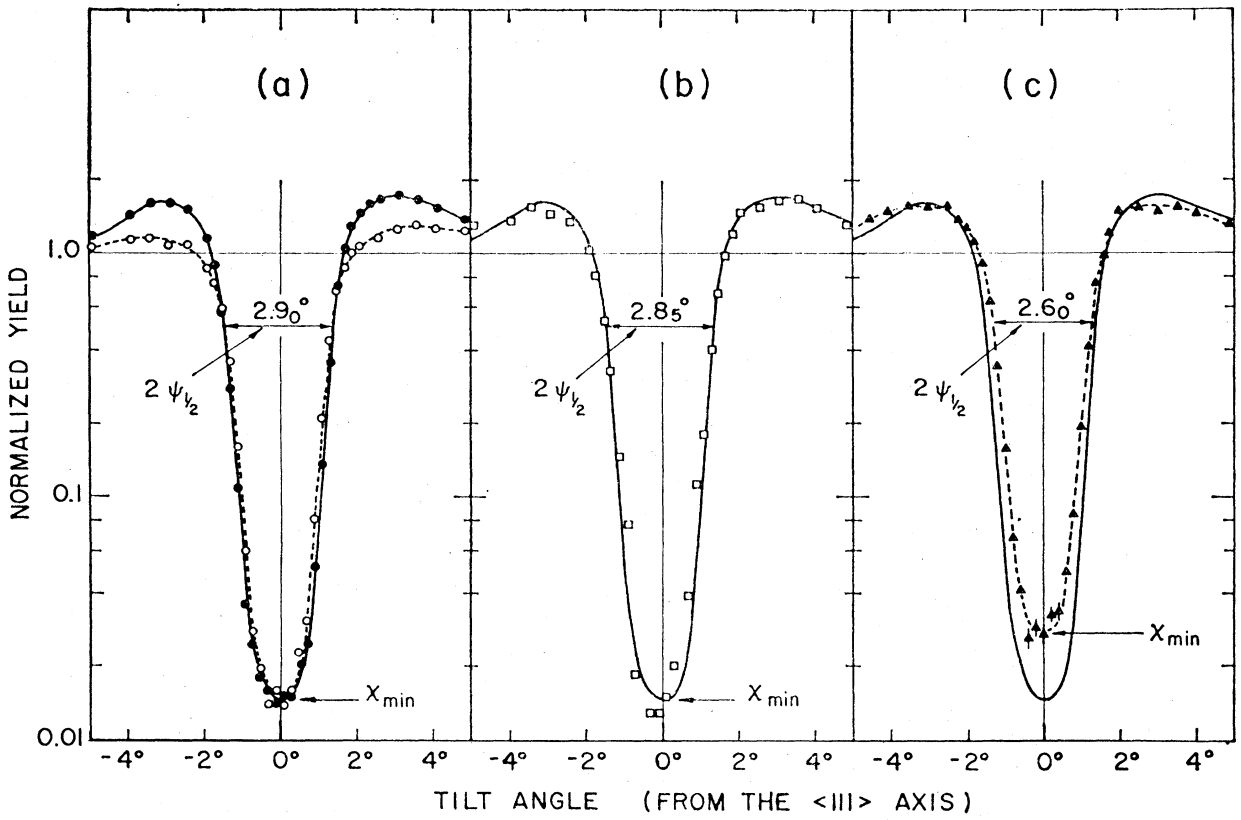

FIG. 66. Comparison of Rutherford scattering and L and M x-ray yields in W as a function of incidence angle relative to the $\langle 111 \rangle$ axis for 1.4-MeV ^{4}He ions [Dav69]. In each of the three sets of data, the full line represents the Rutherford scattering curve obtained for a scattering depth of 1200 Å. In (a) is also shown (open circles) the Rutherford scattering curve for a depth of 5000 Å. In (b) the points shown represent the L x-ray yield and in (c) the points show the M x-ray yield.

in the keV/nucleon energy range (see, e.g., [For69; Br70b]). Recent experiments [Ste70; Da71] have indicated that this mechanism may still play a dominant role even at bombarding energies in the MeV/nucleon range. Under these circumstances, a better estimate of the maximum impact parameter for ionization to occur may be the level-crossing distance as calculated, for example, from the model of Barat and Lichten [Bar72]. This estimate gives a good fit to the measured impact-parameter dependence of the probability of L-shell vacancy production for bombardment of Te with 30-MeV ^{127}I ions [Ste70]. It is not too different from the sum of the radii of the two interacting electronic shells.

The interpretation of channeling measurements on characteristic x-ray production can be complicated by the rapid variation of the cross section with bombarding energy, by dechanneling effects and by the absorption in the target of the emitted x rays. All of these complications can be minimized by using thin targets. For the thick target data shown in Fig. 66, the 1.4-MeV ^{4}He beam lost energy in the W sufficiently rapidly that 95% of the L and M x rays originated within 6000 Å of the surface. The dechanneling in this distance is negligible ($< 1\%$) for the $\langle 111 \rangle$ axis. The strong self-absorption of the M x rays further limited the effective measured depth for them to about 2000 Å. This situation is to be contrasted with, say, an angular scan across the (100) plane of a thick Ge crystal using 4-MeV protons. In this case the x-ray absorption distances together with the dechanneling and energy loss of the beam combine in such a way that scarcely any dip is observable for the K x rays (10 keV) whereas quite a pronounced dip is seen for the L x rays (1.2 keV).

Measurements comparing the effect of channeling on backscattering and on x-ray production have been performed by several authors (e.g., [Dav69; Pi69a; Ge72a, b; Ja72]). In some instances (e.g., [Pi69a; Roth70; Ge72a, b]), characteristic x rays have been used to study sublattices in polyatomic crystals (see Sec. 4.4). For this application the high efficiency and good resolution of the Si(Li) detector are of great value. Cairns *et al.* [Cai72] have studied the production of L x rays in a Cu crystal bombarded by low-energy (150–350 keV) Ne^+, Ar^+, Kr^+, and Xe^+ ions. The values of $\psi_{1/2}$ that were found for the $\langle 110 \rangle$ axis exhibit a dependence on (Z_1/E) that is intermediate between the dependences expected for ψ_1 and ψ_2 (c.f. Fig. 44). Saris *et al.* [Sar69] found a peak in the yield of Ar L x rays observed in a $\langle 110 \rangle$ axial channeling direction when they bombarded a Cu crystal with 35-keV Ar^+ ions. These results, suggestive of flux peaking, were interpreted as being due to collisions between the beam and Ar ions that had become implanted interstitially in the $\langle 110 \rangle$ direction. When the bombarding energy was raised to 90 keV the yield displayed a dip instead of a peak, possibly because at this energy the x rays were predominantly due to Ar–Cu collisions.

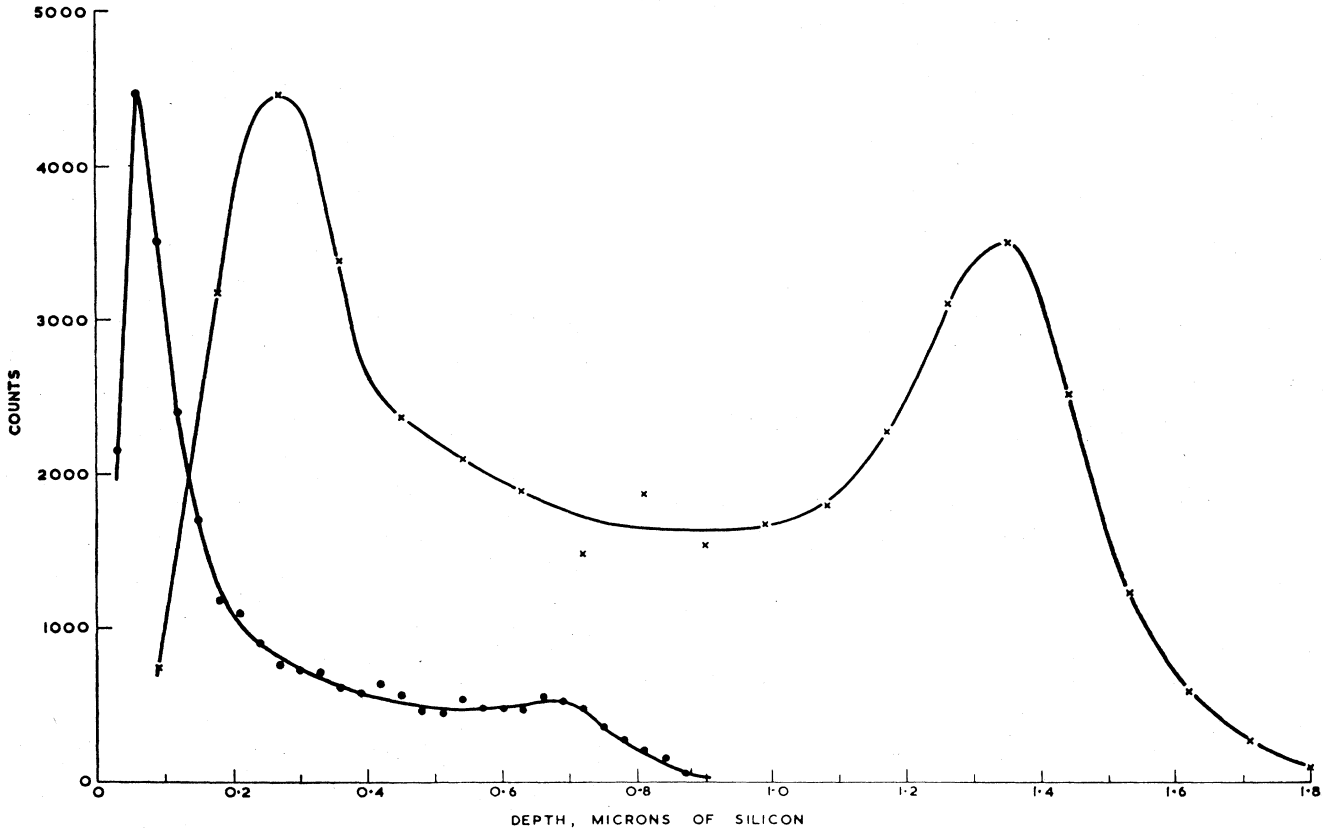

FIG. 67. Range profiles for 40-keV (dots) and 110-keV (crosses) ^{32}P ions incident along the ⟨110⟩ axial direction of Si at room temperature [De68c].

4.2e. Ranges

Because channeled particles experience an anomalously low rate of energy loss their maximum ranges in crystalline solids are abnormally large. This phenomenon led initially to the first observations of channeling [Dav60a, b; Pie63; Lu63]. Since then the topic has been studied intensively particularly with respect to applications in ion implantation in semiconductor materials (Sec. 6.1). In this section we give a few illustrative examples of the influence of channeling on ranges. For more detailed discussions and reviews of the extensive literature on this subject, the reader is referred to [Se66; Da67; Dav67a, 68b, 72b; Wh67, 68; Ne68a; May70; Mar71b; Dem72].

A common technique for measuring range profiles is that of bombardment with radioactive ions followed by anodic oxidation and chemical stripping (Sec. 3.2). Figure 67 shows data obtained in this way for ^{32}P ions channeled in Si (see also [Ei68a; Red72]). The detailed shape of the range profile depends on the dechanneling rate, which in turn, for a given crystal orientation, depends on factors such as temperature (see Fig. 68), lattice defects which can be produced by the ion bombardment itself, incidence angle with respect to the channeling direction, and the many other factors discussed in Sec. 2.4e.

By differentiating a curve of maximum range versus incident energy, the stopping power for channeled ions can be derived. This is illustrated in Fig. 69 for Xe ions injected along the ⟨100⟩ axis of W. It can be seen that the velocity-proportional electronic stopping dominates down to energies of about 4 keV; for amorphous W, the corresponding value is about 2.5 MeV. The electronic stopping power measured at constant velocity was found by Eriksson *et al.* [Erik67a] to exhibit the Z_1 oscillations discussed in Sec. 2.6b. An example is shown in Fig. 70.

4.2f. Radiation damage

Since atomic displacements are caused mostly by close collisions, the rate of radiation damage in single crystals bombarded by ion beams is strongly orientation-dependent. This was first observed by Noggle and Oen [No66]. These authors found a factor of 14 reduction, as determined by spot densities in electron micrographs, in the damage induced in thin Au crystals when an incident beam of 51-MeV ^{127}I ions was aligned with the ⟨110⟩ axis as compared with a random direction of incidence. The damage rate showed a characteristic channeling dip as a function of incidence angle (see also [No69]). Merkle [Me68] saw similar effects in the bombardment of Au crystals at 4.2°K with 120-keV protons and 120-keV Xe^+ ions. Schober and co-workers [Schob68, 69a, b; Tho69] have observed the formation of vacancy clusters caused by the dechanneling of keV Au ions in Au. To ensure that only channeled ions entered the Au, these authors used an epitaxial layer of Ag as a filter.

A striking example of the orientation dependence of radiation damage in Si bombarded by 80-keV Ne^+ ions

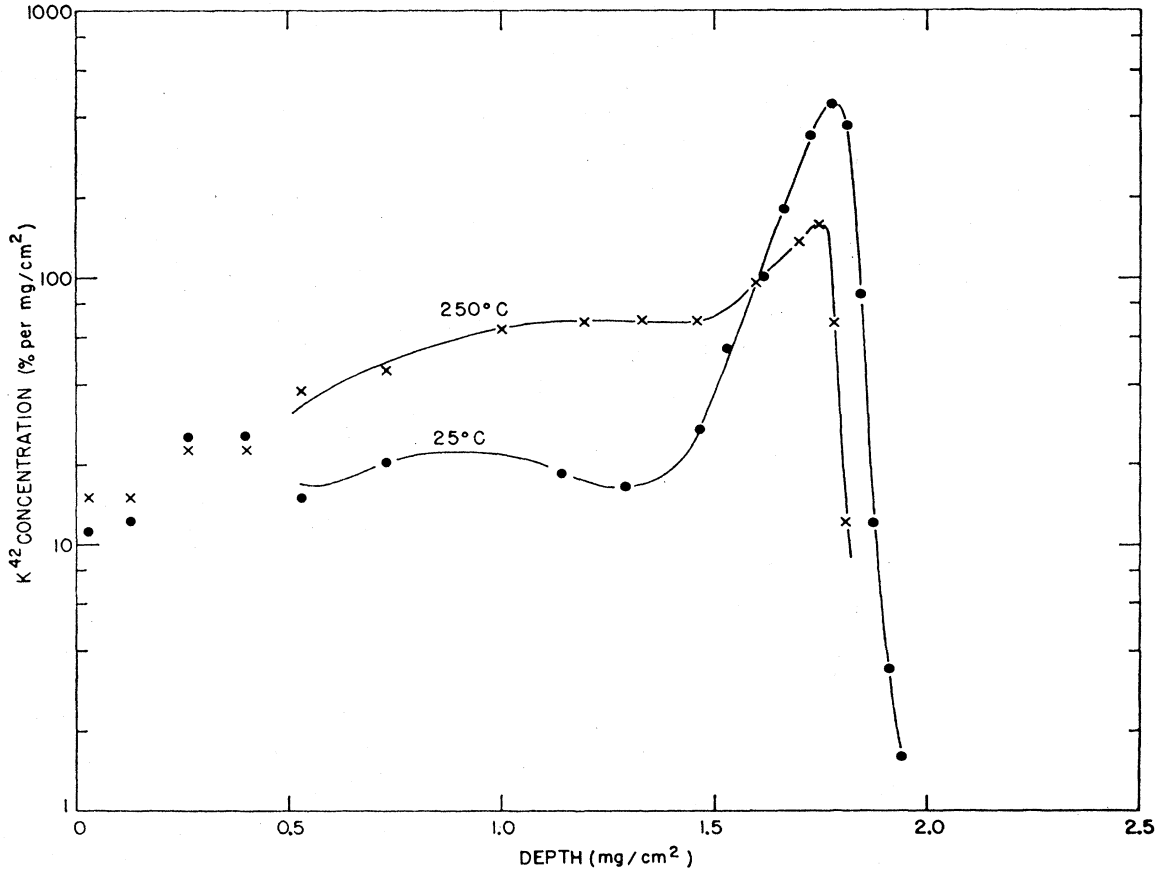

FIG. 68. The influence of target temperature on the range distribution of 500-keV ^{42}K ions injected along the ⟨111⟩ axial direction in W [Erik67b].

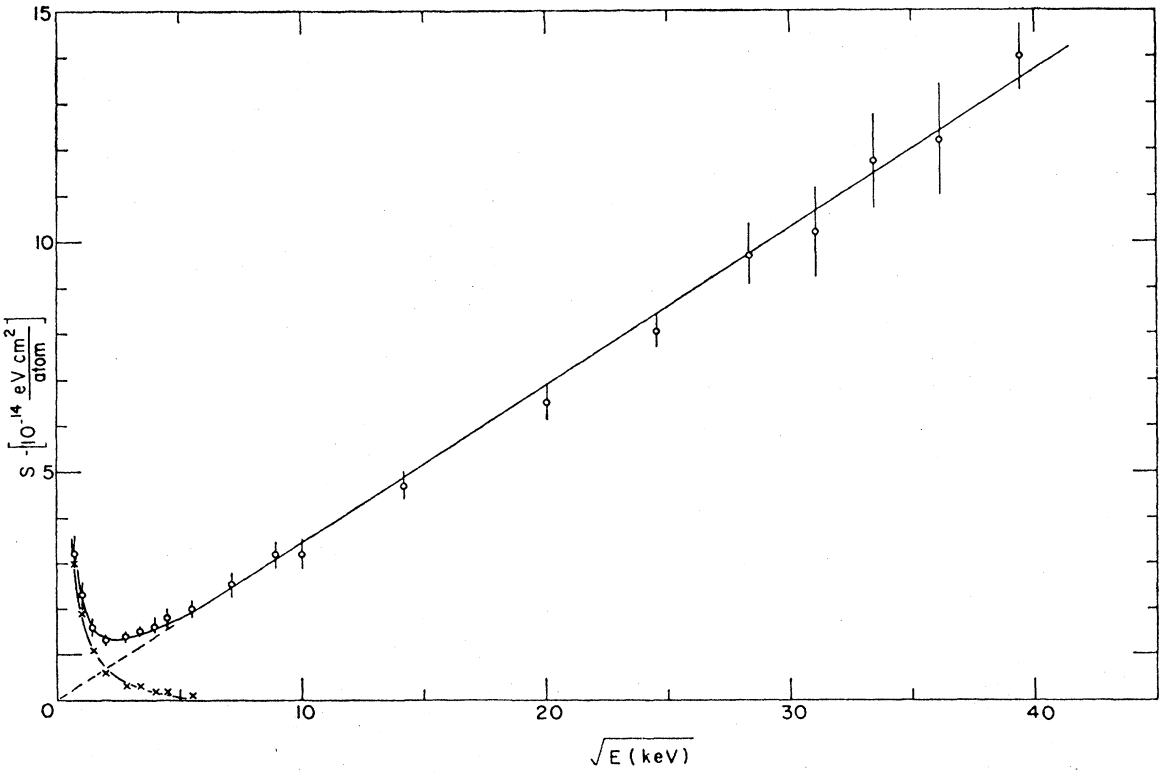

FIG. 69. Experimentally derived values of the total stopping cross section (open circles) as a function of $E^{1/2}$ for well channeled Xe ions incident along the ⟨100⟩ axis of a W crystal [Erik67a]. The dotted line is an extrapolation of the electronic contribution to lower energies. Crosses indicate the nuclear stopping obtained by subtracting the extrapolated electronic stopping from the measured total values.

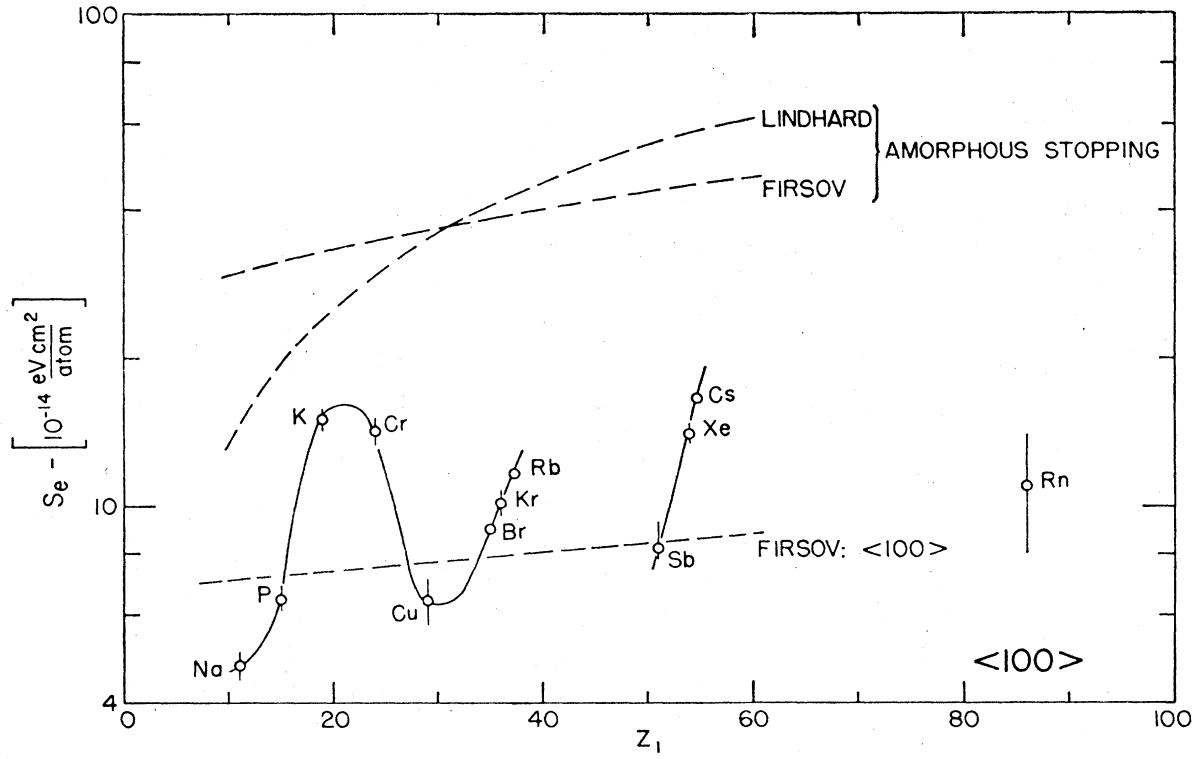

FIG. 70. Z_1 oscillations in the electronic stopping cross sections (measured at $v = 1.5 \times 10^8$ cm/sec) for well-channeled ions in the $\langle 100 \rangle$ axial direction in W [Erik67a]. The upper two dashed lines show the calculated values for amorphous W using the theories of Lindhard *et al.* [Li63] and of Firsov [Fi59]. The lower dashed curve labeled *Firsov*: $\langle 100 \rangle$ is computed from Eq. (2.135).

has been given by Nelson and Mazey [Ne67b, 68a, b]. At high doses the damaged surface of Si assumes a milky appearance. The data shown in Figs. 71 and 72 demonstrate how this is reduced when the beam is channeled.

For further discussion on the effects of channeling on rates of radiation damage, the reader is referred to [Ei68b; Kum68b, 69; Ne68a; Jo69; No69; May70; Mor70b; Roth70; Bulg71; Mat71b; Ge72a, b].

4.2g. Response of scintillating crystals

In 1968 Luntz and Bartram [Lun68] calculated the stopping powers for well-channeled ions (^{4}He – ^{20}Ne) over the velocity range 1–10 MeV/amu in crystals of NaI(Tl) and CsI(Tl). They predicted that since the scintillation efficiency in these crystals is a decreasing function of dE/dx at large values of dE/dx, the luminescent-response should show a maximum when the incident ions are channeled. The reduced ionization density for channeled particles favors radiative recombination of electrons and holes at Tl^+ sites over competing nonradiative recombination. This effect was verified experimentally in 1970 by Altman *et al.* [Alt70b] for the cases of 7.5-MeV ^{4}He and 10-MeV ^{16}O ions planar channeled in NaI(Tl). Similar effects have been seen for protons in CaF_2(Eu) [Ato70] and KCl(Tl) [Hu71], for α particles in CsI(Tl) [Kul72; Sh73], and for ^{4}He and ^{16}O in NaI(Tl) and KI(Tl) [Alt73; Mas73]. The theory has been further developed by Luntz and Heymsfield [Lun72].

For comparison, it is interesting to note that the optical fluorescence yield measured for 5.48-MeV α particles in a pure anthracene crystal shows a minimum under channeling conditions [Berk64; Wick67; Br68]. In this case, the fluorescence yield is an increasing function of dE/dx [Bir64].

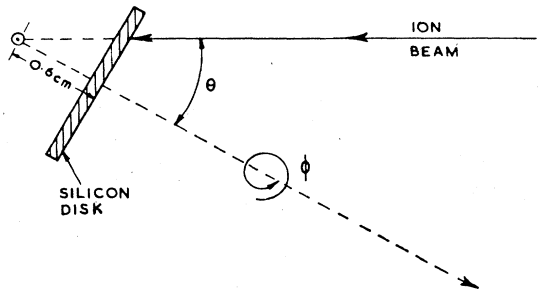

FIG. 71. Schematic drawing of the experimental arrangement used by Nelson and Mazey [Ne67b, 68a, b] to produce the data shown in Fig. 72. The 2.5-cm-diam Si target was rotated continuously about the ϕ axis. The angle θ was stepped in such a way that the entire crystal surface received a uniform dose. The incident beam of 80-keV Ne^+ ions was collimated to a diameter of 0.8 mm and to an angular divergence of ~0.01°. (Reproduced with permission of J. Mat. Sci., Chapman & Hall, London.)

4.3. Transmission effects

The anomalous transmission of ions due to channeling effects was first seen by Nelson and Thompson [Ne63] for the case of 75-keV H^+ and He^+ ions incident on an Au foil ~ 3000 Å thick. Sharp maxima in the transmitted ion

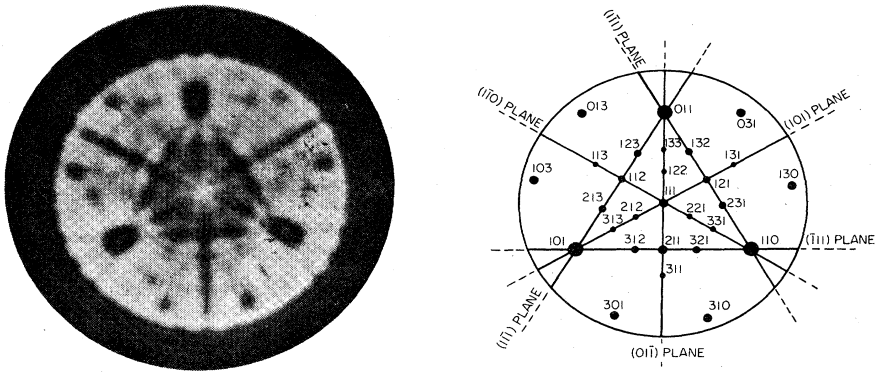

FIG. 72. (a) Photographic reproduction of a ⟨111⟩ Si crystal surface after programmed bombardment with 80-keV Ne^+ ions using the arrangement shown in Fig. 71 [Ne67b]. The dark areas show a minimum of radiation damage where the beam is channeled. (b) Radial projection of the (111) face of an fcc crystal showing the low-index planes for comparison. (Reproduced with permission of J. Mat. Sci., Chapman & Hall, London.)

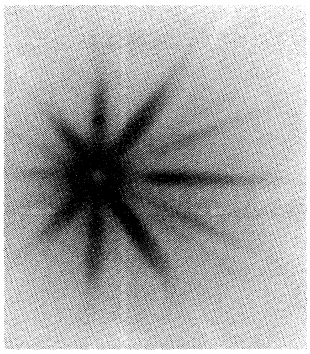

FIG. 73. Star pattern recorded in transmission for 2.43-MeV protons incident along the (110) planar direction and approximately 1.6° from the ⟨110⟩ axis of a Ge crystal 7 μ thick. The dark region corresponds to high particle intensities. (The range of 2.43-MeV protons in amorphous Ge is approximately 43 μ [Gor69].)

current were observed when the beam was aligned with the ⟨110⟩ axial direction. The maxima disappeared after prolonged bombardment with He^+ ions. This was attributed to the formation of dislocation loops which blocked the axial channels.

Dearnaley [De64] made measurements on the energy losses of 2.1-MeV protons transmitted through Si crystals in major axial channeling directions. This was followed by similar measurements by Wegner and co-workers [Weg64; Er64; Ap65; Gi65], who also found evidence for some transmitted particles that had suffered anomalously high energy losses.

4.3a. Star patterns

When the range of the incident beam in the target material exceeds the target thickness, characteristic channeling patterns may be observed as the transmitted beam strikes a photographic plate or a phosphor screen located as shown in Fig. 2. These star patterns were first reported by Schiffer and Holland [Sc65]. Examples are shown in Figs. 4 and 73. The characteristic intersecting planar patterns associated with the major axes are a valuable aid in the alignment of crystals in channeling measurements. The general appearance of these patterns and the distribution of intensity in them are dependent (often in a complicated way) on the magnitudes of several interrelated parameters, e.g., the mass, charge, and energy of the bombarding ions, the beam divergence, the target thickness, the rms multiple scattering angle, the dechanneling rates and critical angles for the various axes and planes involved, and the angle of beam incidence relative to these directions. Thompson [Th68b] has made a detailed theoretical analysis of the dependence of star patterns on many of these factors. The simplest patterns are usually those for fairly thick targets. In these cases, only the high-symmetry directions can be seen. Multiple scattering in the crystal establishes a pseudo-equilibrium between escape from and feeding into the major channeling directions and this results in a "well-behaved" pattern such as that shown in Fig. 4. As the target crystal is made thinner, lower-symmetry directions become observable, the multiple scattering decreases, and, toward large scattering angles, blocking becomes apparent. It is noteworthy that for planar incidence (Fig. 73) the multiple scattering of the channeled beam in the direction along the plane is much less than the normal multiple scattering. Hence the dark planar channeling streak in the center of Fig. 73 turns to a white blocking line well inside the mean angle for random multiple scattering. For crystals thin enough that the multiple scattering of the channeled beam is small compared to the critical angle, the planar channeling pattern exhibits a streak perpendicular to the plane. For very thin and highly perfect crystals, the transmitted patterns observed with tightly collimated incident beams tend to become complex and depend sensitively on the finer details of the channeled trajectories inside the crystal. (These patterns are discussed in Sec. 4.3d).

Star patterns have been investigated by several authors (e.g., [Ge65; Sc65; Ne67a, 68a; Rem67; De68a, b; Ho68; Th68b; Ace68, 70; Ap69; Mark71; So72c]). Perhaps the most extensive studies to date are those of Dearnaley *et al.* [De68a, b]. Nelson *et al.* [Ne67a] were able to obtain some semiquantitative energy analysis as well as the spatial distribution of transmitted ions by using color film to record the star pattern. After developing, the color obtained depended on the depth the ions had penetrated into the different layers of film.

A couple of the features displayed in Fig. 73 are worthy of comment. It can be seen that there is a white spot corresponding to blocking along the ⟨110⟩ axis even though the incident beam direction lies fairly close to this axis. Dearnaley *et al.* [De68a, b] have explained this as being the consequence of a potential barrier existing between the axial direction and the planar direction. In the data shown in Fig. 62 the multiple scattering of the planar channeled beam is not sufficient to overcome this

barrier. Furthermore, the crystal is thin enough that there is negligible feeding of the random component of the beam into the axial channels by multiple scattering.

It was noticed early in the study of star patterns [De68a, b; Ho68] that when a major crystal plane lies at an angle within the region of normal (random) multiple scattering, the corresponding planar streak observed in the transmission pattern on a photographic film becomes asymmetric. The line becomes dark on the side away from the beam direction and light on the side towards the beam. If one follows the white blocking line observed at large angles through the region near the beam direction, it appears that the blocking line bends inward towards the beam direction as it passes by the dark streak, whose length is proportional to the width of the multiple scattering distribution. The resemblance between these patterns and the Kikuchi patterns seen in electron microscopy led to the suggestion (e.g., [Ch66]) that the channeling data could be interpreted in terms of proton Kikuchi patterns. Theoretical analyses by Thompson [Th68b] and by Appleton and Feldman [Ap69] demonstrated that the phenomena seen for protons can be readily understood in classical mechanical terms.

4.3b. Anomalous energy losses

As the list given in Table I indicates, there have been many measurements on the energy losses suffered by channeled ions transmitted through single crystals. In this section we are mostly concerned with measurements on targets thick enough for the channeled beam to reach statistical equilibrium (see Sec. 2.4e). More detailed measurements on thinner targets, noted with the comment *fine structure* in Table I, are discussed in Sec. 4.3c.

We discuss firstly measurements performed at high incident particle velocities (Region I in Fig. 37). Figure 74 shows typical energy-loss spectra for energetic protons transmitted through a crystal (~50 μ thick) in random and axially aligned directions. Reductions in stopping power by factors of up to 3 for major channeling directions have been reported by several authors. There is also good evidence (e.g., [Er64; Gi65; Sa65; Ap67; Rem67]) for the existence of a group of particles transmitted in a channeling direction and having a stopping power higher than the random value. These particles are most probably the ones with transverse energies near to or slightly higher than the critical value for channeling. Evidence for this comes from their dependence on the beam incidence angle (see Fig. 75).

For crystals thick enough for dechanneling to be significant, the spectrum of transmitted energies displays a continuum between the channeled and random peaks. An example is shown in Fig. 76. From the rate of rise of the continuum, one can extract information on the dechanneling rate. In the planar case, this continuum rises approximately exponentially as is predicted by the diffusion model of dechanneling (see, e g., [Ap68; Fel68; Th68b; Mor72]; see also Sec. 2.4e2). Altman *et al.* [Alt70a] have deduced the initial channeled fraction $f_{ch}(0)$ from a calculation fitting their measured energy distribution for 5-MeV protons transmitted through a 60-μ-thick Si crystal in the (110) planar direction. Their results give a value of $[1 - f_{ch}(0)] = 0.12$ at room temperature. The corresponding value of $\chi_{min}(0)$ determined from backscattering experiments is 0.31 [Dav68a]. The large difference between these values is ascribed to initially unchanneled particles with trajectories that yield abnormally high scattering probabilities. The result indicates that substantial errors may be incurred if one simply assumes that $1 - \chi_{min}(0)$ is the initially channeled fraction (see Secs. 2.4e2 and 4.2a). For target thicknesses large compared to the dechanneling distance $x_{1/2}$, feeding-in of particles from the random to the channeled component of the beam occurs. This process has been discussed by Appleton *et al.* [Ap67, 68] and by Morita and Itoh [Mor71b].

The angular half-widths measured for the low-loss component of the transmitted beam as either the inci-

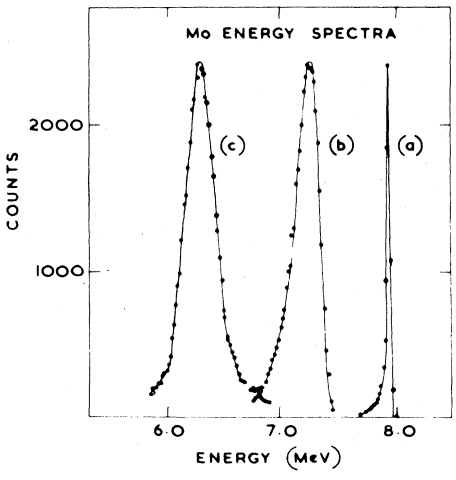

FIG. 74. Energy spectra for 8-MeV protons incident upon a 50 mg/cm² thick Mo crystal [Cl70]. The peaks shown are (a) energy profile of the incident beam, (b) protons transmitted parallel to the ⟨111⟩ axis, and (c) protons transmitted in a random direction.

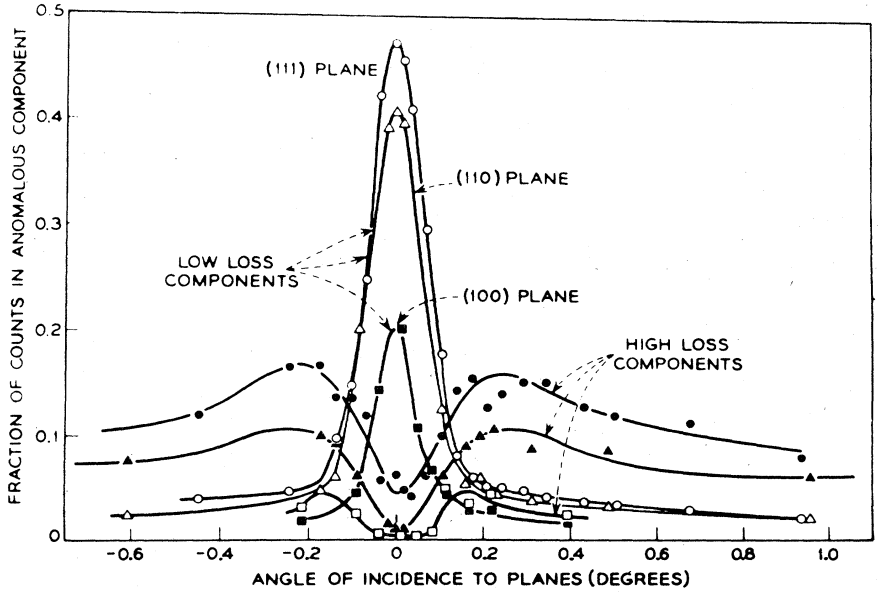

FIG. 75. Fractions of high-loss and low-loss transmitted particles plotted as functions of the incidence angle relative to the (111), (110), and (100) planes for 2.8-MeV protons bombarding a 33-μ-thick Si crystal [Ap67].

TABLE I. Transmission measurements on energy losses of channeled ions.

Reference	Ion	Energy	Crystal	Thickness	Remarks[a]
Alt 70a	p	5 MeV	Si	60 μ	Deduced planar channeling probability
And 65	d	13 keV	Au	700 Å	Angular dependence
And 66a	d	15 keV	Fe	1000 Å	Angular dependence
And 66b	d, ^{4}He	8—25 keV	Au	275—600 Å	Angular dependence; damage effects; charge exchange
Ap 65	p	4.85 MeV	Si	50 μ	Comparison of axial and planar effects
Ap 67	p	3—11 MeV	Si	25—50 μ	Angular dependences; comparison of axial and planar effects
Ap 71	^{16}O ^{127}I	10 MeV 15—22 MeV	Au	5000 Å	Fine structure
Bøtt 69	$7 \leq Z_1 \leq 54$	0.2—1.1 MeV	Au	500—5000 Å	Z_1 oscillations
Ch 68c	p	30 keV	Au	92 Å	Fine structure
Cl 69	p	4 MeV	CsI	90 μ	Comparison with calculations of [Ap 67] and [Lun 68]
Cl 70	p	4—8 MeV	Si, Fe, Mo, Ge, W, NaCl, MgO, CsI	20—100 μ	Comparison of insulators, semiconductors and metals
Da 65a, b	^{79}Br, ^{127}I	20—80 MeV	Au	4000 Å	Energy and angular dependence
Da 69	^{4}He, ^{127}I	3 MeV 60 MeV	Au	7000—9000 Å	Fine structure
Da 70	^{127}I	15—60 MeV	Au	5000—7000 Å	Energy dependence; Fine structure
De 64	p	2.1 MeV	Si	37 μ	First experiment with energy analysis
De 68a, b	p	1—5 MeV	Si, Fe, Al_2, O_3, MgO	1—100 μ	Angular dependence
Del 71, 72	p, d, ^{4}He	0.9—5 MeV	Si	1.5—36 μ	Energy dependence
Ei 66	p	375 keV	Si	2 μ	Comparison of axial and planar effects
Ei 68a	$5 \leq Z_1 \leq 19$	100—500 keV	Si	0.24—1.5 μ	Angular dependence; damage effects; comparison of axial and planar effects; Z_1 oscillations
Ei 71a	p	0.4 MeV	Si	5000—7000 Å	Fine structure
Ei 72a	^{4}He	0.1—18 MeV	Si	0.3—11 μ	Energy dependence
Er 64	p	3 MeV	Si	25 μ	First observation of high-loss particles
Far 65	p	2.5 MeV	Cu	10μ	Angular dependence: temperature dependence
Fuj 69	p	1.5 MeV	Si	26 μ	Temperature dependence
Ge 72a, b	p	3.8 MeV	$BaTiO_3$	3—20 μ	Angular dependences; effects of ferroelectricity
Gi 65	p	5 MeV	Si	50 μ	Angular dependences of low- and high-loss components
Gi 68a	p ^{4}He	0.4 MeV 0.8 MeV	Au	1200—1650 Å	Angular dependences; some fine structure
Gi 72a	^{4}He	1.8 MeV	Au	2750 Å	Fine structure
Ham 66	p	3.55 MeV	Mica	30 μ	Small axial channeling effect
Hi 70	d	20—28 keV	Au	200—300 Å	Energy dependence
Hög 70	p, d ^{4}He, Li	2—54 keV	Au	200—1500 Å	Straggling measurements; some evidence of fine structure

Reference	Ion	Energy	Crystal	Thickness	Remarks[a]
Ib 68	Pb, Tl	116—169 keV	Au	765 Å 1470 Å	Electronic versus nuclear stopping
Kon 69	p	6.72 MeV	NaCl	80 μ	Temperature dependence
Lu 66	^{4}He ^{127}I	3 MeV 60 MeV	Au	5000—7000 Å	Fine structure
Lu 71	^{4}He	2 MeV	Au	1600—3000 Å	Fine structure
Mach 68	p	85 keV	Au	350 Å, 1050 Å	Angular dependence
Mach 70	p	92 keV	Au	500 Å	Angular dependence
Man 68	p	1.5 MeV	Si	10—35 μ	Dependence on target thickness
Man 70	p	1.5 MeV	NaCl, KCl, KBr, KI	10—20 μ	Angular dependence
Rem 67	p	2 MeV	Si	20 μ	Angular dependences of high- and low-loss components
Sa 65	p d	4.25—7.75 MeV 7.63 MeV	Ge	90 μ	Observed high-loss component
Sa 67	p, d	3.3—7.8 MeV	Si, Ge, GaAs	100—150 μ	Angular and velocity dependences
Sa 68a	$p, d, ^3$He	2—13 MeV	SiO_2	30—60 μ	Dependences on ion type and energy
Sa 68b	$p, d, ^3$He	2.5—14 MeV	AlSb, GaSb, InAs, InSb	25—125 μ	Study of zinc-blend lattices; dependences on mass, charge and energy of incident ion
Sh 68a	p	6.72 MeV	Ge	77 μ	Angular dependence
Sh 68b	p	4.7—6.72 MeV	NaCl, KCl, KBr	80—100 μ	Angular dependence; temperature dependence
Weg 64	p ^{4}He	3 MeV 40 MeV	Si	25 μ	Implications for detectors discussed

[a] In all the work cited here energy losses were measured. We remark only on additional features of the measurements. The comment *Fine structure* means the measurement is of the type discussed in Sec. 4.33.

dence angle or the exit angle is varied tend to be somewhat lower than the values of $\psi_{1/2}$ found from backscattering; this was predicted by Lindhard [Li65]. The actual values of the half-widths depend very much on the width and position of the window set on the detected energy spectra; Fig. 89 shows an extreme example where the half-widths for transmission and backscattering differ by a factor of 7 or 8. Where highly perfect target crystals and very small beam divergences are used, the least energy loss observed in axial channeling corresponds to hyperchanneled particles (see Sec. 4.3e). Unless great care is taken, hyperchanneling effects are usually not observed in transmission experiments with moderately thick targets. In the absence of hyperchanneling, the measured energy losses for axial channeling are typical of particles that are free to migrate between axial channels. Under these conditions, the least energy loss in a given axial direction is usually found to be equal to the energy loss characteristic of particles channeled in the most open of the planar channels intersecting in the particular axial direction being studied (e.g., [Ap65, 67; Ei68a; Ge72b]; see also the discussion in Sec 2.6b).

It is interesting to note that, in the ⟨110⟩ axial and (111) planar channels in Si the channeled stopping power for protons in the MeV range is very nearly the same as for Ge. Clark *et al.* [Cl69, 70] suggest that this is because the valence-electron gas density is about the same for crystalline Si and Ge and that the channeled energy loss is predominantly due to interactions with valence electrons. The difference in the values of ε then would come about because the random stopping power is about 1.5 times greater for Ge than for Si at the same incident proton energy.

The temperature dependence of the channeled stopping power has been measured in transmission by several groups (e.g., [Far65; Sh68b; Fuj69; Kon69]). Although dechanneling effects in such measurements are marked, the dependence of ε on temperature is found to be quite weak.

Eisen *et al.* [Ei72a] have studied the energy dependence of the stopping power for ^{4}He ions transmitted through Si crystals in channeling and random directions. Their results are summarized in Fig. 77. The authors express the view that the energy losses determined from the leading edge of the channeled energy spectra correspond to the values for the best-channeled ions. Using the leading-edge values, the stopping power for the ⟨110⟩ axis is lower than for the (111) planes. Using the peak values, however, the two stopping powers are found to be

about the same. Eisen *et al.* find that the values of ε for the various crystal directions all go through a maximum at the same energy as the maximum in the random stopping power. This variation is in sharp contrast with results obtained by Appleton *et al.* [Ap67] and Clark *et al.* [Cl70] for 3- to 11-MeV protons in a variety of crystals. For these proton data, ε is found to decrease only slightly if at all with increasing bombarding energy. Eisen *et al.* attribute the different behavior for ^{4}He ions to the influence of shell corrections (see Sec. 2.6a).

Della Mea *et al.* [Del71, 72] have measured, in transmission, values of ε for Si bombarded by p, d and ^{4}He ions in the energy range 0.9–5.0 MeV. They express the measured stopping powers in terms of an effective stopping number (see also, e.g., [Sa67; Cl70]) defined by

$$B(E)/E = -(dE/dx). \tag{4.6}$$

The experimental value is found from

$$B(\bar{E}) = \frac{1}{t}\int_{E_{ch}}^{E} E'dE' = (E^2 - E_{ch}^2)/2t, \tag{4.7}$$

where $\bar{E}$ is the average energy of the particles traversing the crystal, E_{ch} is the energy of the transmitted channeled particles, and t is the target thickness measured in the beam direction. Values of $B(\bar{E})/M_1 Z_1^{*2}$, where Z_1^* is the effective charge of the incident ion, are shown plotted against $\bar{E}/M_1$ in Fig. 78. When the abscissa is plotted on a logarithmic scale, the data show an approximately linear relationship, c.f. Eq. (2.131), up to some critical incident energy after which the stopping power increases somewhat faster. The authors identify these critical incident energies as the values above which the L shell in Si begins to be ionized even for the best channeled ions (see the discussion in Sec. 2.6b). Using the adiabaticity relation, Eq. (2.137), and the known values of the channel radii, these energies are 6.5, 3.8, and 2.8 MeV/amu for the ⟨110⟩, ⟨112⟩, and ⟨111⟩ axes, respectively.

The transmission of low-energy 10- to 30-keV protons and deuterons through various crystals has been studied by Hines and co-workers [And65, 66a, b; Hi70]. These technically difficult measurements have been performed with target crystals a few hundred angstroms thick. Well-defined reduced energy losses were found in major channeling directions, and the channeled stopping powers were observed to exhibit the expected $E^{1/2}$ dependence on the bombarding energy. Other transmission measurements in the low-energy range (Region III in Fig. 37) have been made using heavy ions (e.g., [Da65a, b; Ei68; Ib68; Bøtt69; Hög70]). Eisen [Ei68] has measured the least energy losses for a variety of heavy ions transmitted through thin (~1 μm) Si crystals along the ⟨110⟩ direction. He found a strong oscillatory Z_1 dependence of the stopping power for ions incident at a fixed velocity. Additionally Eisen determined that the stopping

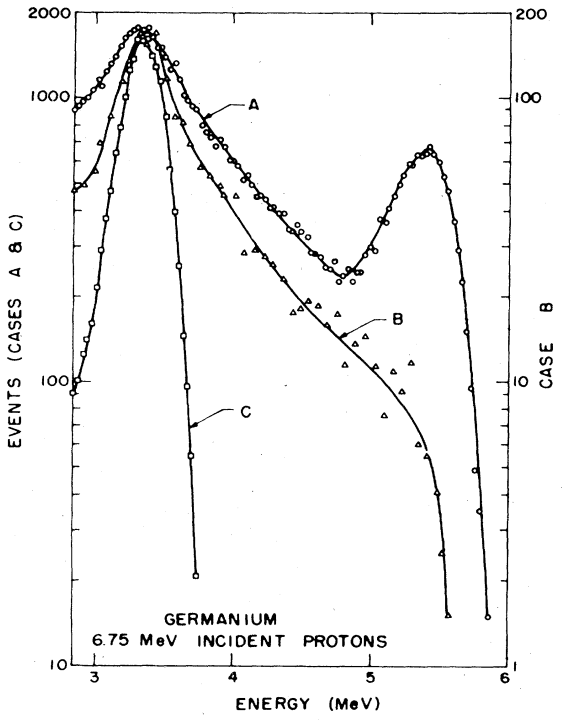

FIG. 76. Spectra of protons incident at 6.75 MeV transmitted through a Ge crystal 90 μ thick [Sa65]: (A) proton beam along ⟨110⟩ axis, detector in beam direction; (B) proton beam along ⟨110⟩ axis, detector 0.86° off the beam direction; (C) protons incident in a random direction, detector in beam direction.

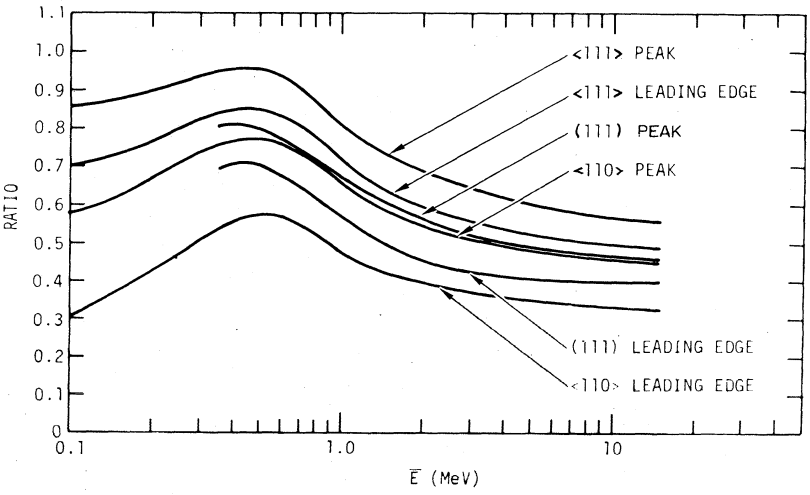

FIG. 77. Ratio ε between channeled and random stopping powers measured for ^{4}He ions transmitted in various channeling directions in thin Si crystals [Ei72a]. The abscissa gives the average value of the energy of the ions in their passage through the crystal. The terms Peak and Leading Edge refer to the method of extracting the energy losses from the measured spectra.

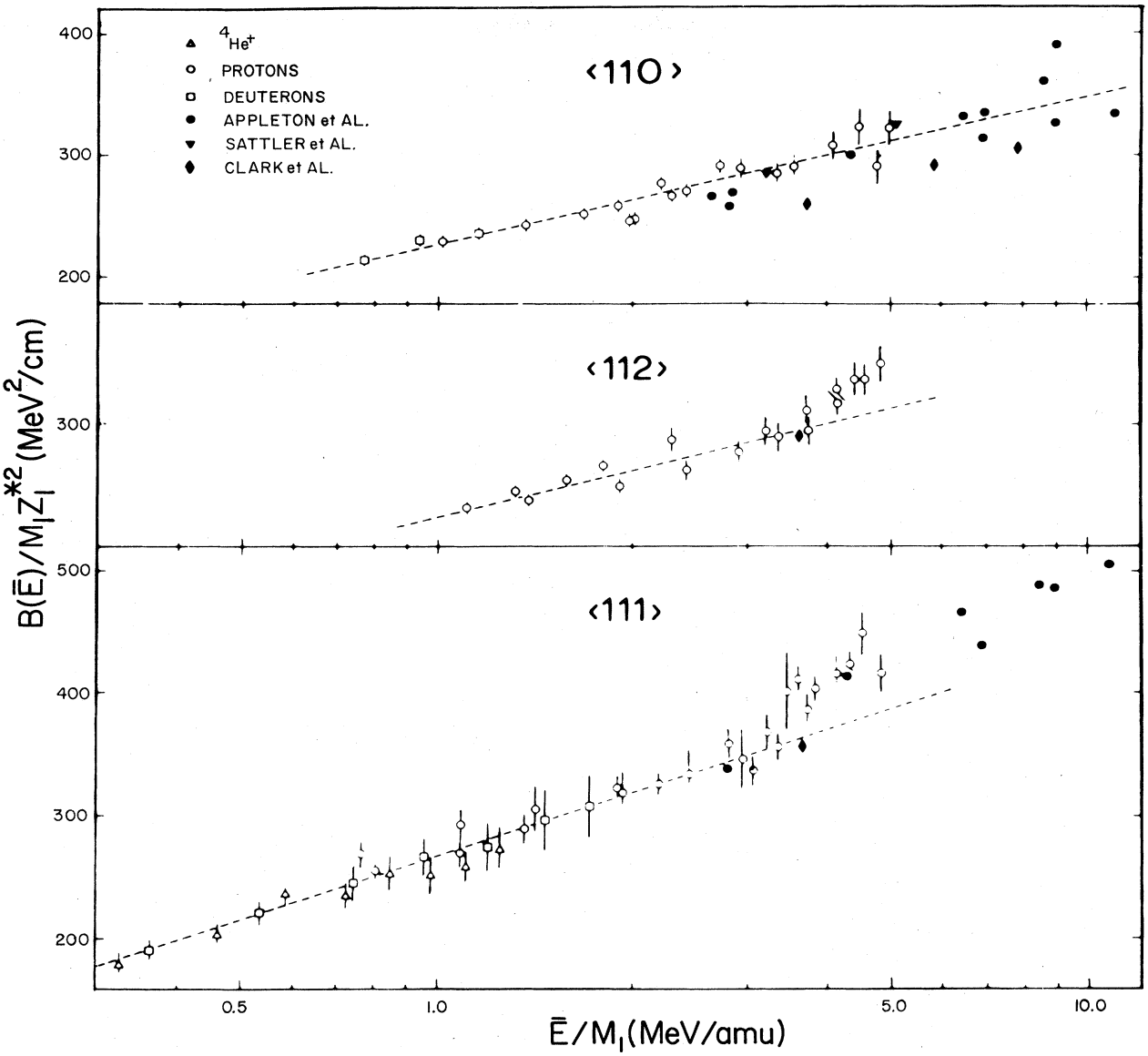

FIG. 78. The quantity $B(\bar{E})/M_1 Z_1^{*2}$ plotted against $\bar{E}/M_1$ [Del72]. See the text for details; note the logarithmic scale for the abscissa. Also shown are data of Appleton *et al.* [Ap67], Sattler and Dearnaley [Sa67], and Clark *et al.* [Cl70].

power showed a dependence on E^p, where the index p was found to oscillate (about the value 0.5) with Z_1, but in opposite phase to the stopping power itself. Later measurements by Bøttiger and Bason [Bøtt69] on thin (~1000 Å) Au crystals extended this type of measurement to higher Z_2 and to a wider range of Z_1. Their data are shown plotted in Fig. 79. It is worthy of note that the minima and maxima in the oscillations occur at values of Z_1 that do not depend much on the value of Z_2 or on whether the target is crystalline or amorphous. The minima occur at Z_1 ~11, 30, and 50. The maxima occur at Z_1 ~8, 20, and 42 (c.f. Fig. 70, see also [Or64, 65; Mac66; Fas66] and Sec. 2.6b). Experiments in which Z_1 is kept fixed and Z_2 is varied are more difficult to perform. There is, however, evidence also for Z_2 oscillations (see, e.g., [Hv71]).

4.3c. Detailed measurements of trajectories and potentials

If the experimental arrangement in a transmission measurement is such that the trajectories of the detected particles do not attain statistical equilibrium in passage through the crystal, then detailed studies of the distributions in emergence angle and energy allow determination of the potentials that govern the channeled motion. Pioneering work in this area has been performed by a group at Oak Ridge National Laboratory (ORNL) (see, e.g., [Lu66; Da69, 70; Ro69, 71a; Ap71]) and has been followed by related studies at several other laboratories [Mach67, 70; Ch68c; Ei68, 71a; Gi68a, 72a; Rog69; Hög70; So70; Lu71]. The ORNL group has measured energy spectra for a variety of ions transmitted through thin (~1000–9000 Å) Au crystals in planar channeling

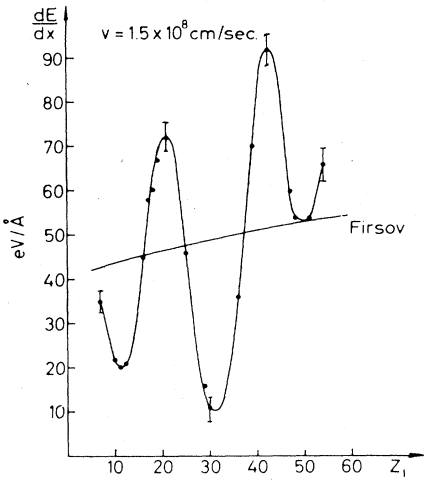

FIG. 79. The Z_1 oscillation in stopping power for various heavy ions channeled in the ⟨110⟩ axial direction of Au [Bøtt69]. The line through the points is merely to guide the eye. The curve labeled *Firsov* is found from Eq. (2.135) using impact parameters, $b = 2.03$Å and $b = 1.44$Å. (The distances from the center of the ⟨110⟩ channel to the rows form the channel walls).

directions. Most of the data have been recorded with a tightly collimated detection system measuring particles transmitted in the direction of the incident beam. Figure 80 shows some results for 60-MeV ^{127}I ions channeled in the (111) planes of Au. The energy spectra display pronounced structure that varies as the target thickness t is changed by rotating the target about an axis normal to the (111) plane and carefully avoiding axial channeling effects. The peaks in the spectra are ascribed to particles that have made an integral number of oscillations in the crystal. Figure 81 illustrates schematically the principle by which selection of trajectories occurs (see also Fig. 21). For the collinear geometry depicted in Fig. 81, only particle trajectories with wavelengths given either by

$$\lambda_{ch}^{(a)} = t/n \tag{4.8a}$$

or by

$$\lambda_{ch}^{(b)} = (t \pm 2|x_0|)/n \tag{4.8b}$$

reach the detector. In Eqs (4.8a, b) n is an integer, and x_0 is a length associated with the phase shifts at the entrance to and exit from the crystal. If the trajectory were sinusoidal with a wavelength $2\pi\lambda_{ch}$, i.e.,

$$z = A \sin(x - x_0)/\lambda_{ch}, \tag{4.9}$$

the value of x_0 would be given by

$$x_0 = \lambda_{ch} \cos^{-1}(\lambda_{ch}\psi_0/A), \tag{4.10}$$

where A is the oscillation amplitude.

The fact that several values of n can contribute to the spectrum of detected particles is a consequence of the anharmonic nature of the interplanar potential. The larger the amplitude of oscillation, the higher the oscillation frequency, and the shorter the wavelength of the associated trajectory. The average stopping power encountered by the planar channeled particles increases with the oscillation amplitude. Since the experimental

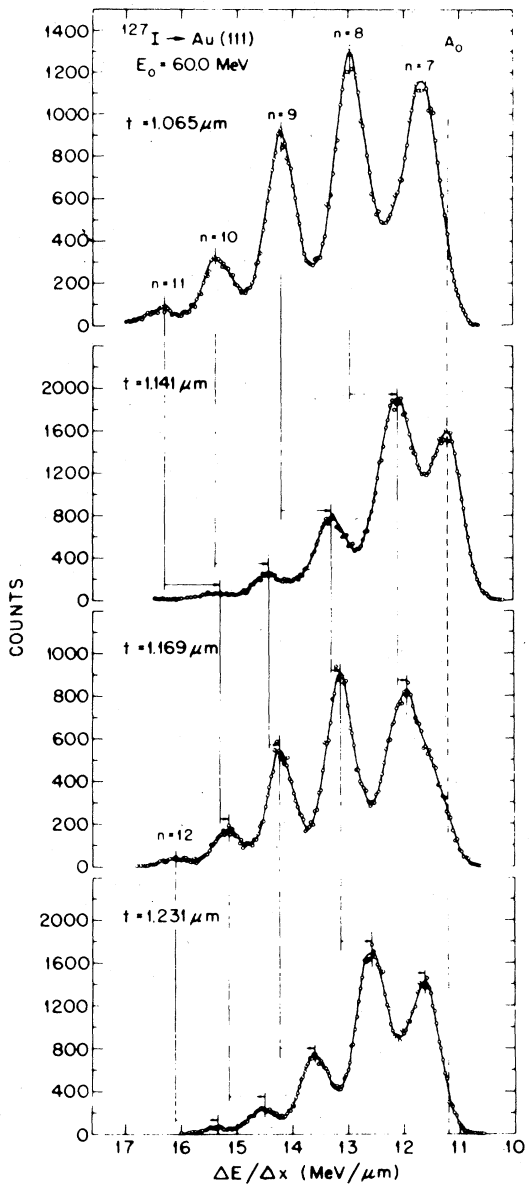

FIG. 80. Energy-loss spectra for 60-MeV ^{127}I ions transmitted in the beam direction after being channeled in the (111) planes of a thin Au crystal [Da70]. The spectra are shown for four different target thicknesses t measured in the beam direction. (The value of $\Delta E/\Delta x$ for a random orientation for a crystal ~1.1 μm thick is roughly 22 MeV/μm.) The spectra shown were obtained for various values of the entrance angle ψ_0 so that the relative peak populations have no significance.

arrangement selects discrete values of $\lambda_{ch}^{(a)}$ and $\lambda_{ch}^{(b)}$, Eq. (4.8), it also, therefore, selects discrete values of the oscillation amplitude and of the average stopping power. This is the reason for the peaks observed in the transmitted particle spectra. The relative population of the peaks in the energy spectra depends among other things on the incidence angle ψ_0. When $\psi_0 = 0$, $\lambda_{ch}^{(a)} = t/n$, and $\lambda_{ch}^{(b)} = t/(n + \frac{1}{2})$. The energy losses for the b groups are then intermediate between the values for the a groups and this results in a filling in of the spectra between the peaks due to particles with type a trajectories. For $\psi_0 = 0$, this causes the spectra to exhibit much less pronounced

structure than shown, for example, in Fig. 80. When $\psi_0 = \psi_e \neq 0$, the values of $\lambda_{ch}^{(a)}$ remain unchanged, but the values of $\lambda_{ch}^{(b)}$ split into two components. In this connection, the influence of mosaic spread in the target is also significant. The mosaic spread (see Sec. 3.2) in effect gives rise to a spread in incidence angles ψ_0. This does not affect the values for $\lambda_{ch}^{(a)}$, but does smear out the already split values of $\lambda_{ch}^{(b)}$. The finite angular divergence of the incident beam has a similar effect. As a result, the energy spectra obtained for $\psi_0 = \psi_e \neq 0$ only display sharp peaks for the type a trajectories. In the remainder of this section, we restrict the discussion to the type a trajectories and drop the use of the superscript. The determination of the values of n for the various peaks in the spectrum is made by varying the thickness t until the stopping power for the $n + 1$ peak at $t = t_2$ is the same as that for the n peak at $t = t_1$. The wavelength for the n group is then given sufficiently accurately by $\lambda_{ch} \approx t_2 - t_1$ to permit a unique assignment of n using Eq. (4.8a). The group labeled A_0 in Fig. 80 is a minimum energy-loss group corresponding to particles confined to trajectories near the channel center, where the potential is almost harmonic. The intensity and definition of the A_0 group depends on both the incidence angle and the angular acceptance of the detector. Within the angular range of the latter, particles in the A_0 group are accepted without regard to integral wavelength conditions.

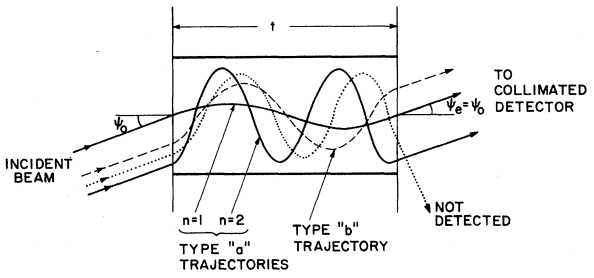

FIG. 81. Possible trajectories of planar channeled particles illustrating the anharmonic nature of the oscillations. The entrance and exit angles are equal. Particles with the trajectories labeled *type a* and *type b* would enter a collimated detector in line with the beam. The dotted curve shows a trajectory for which particles would not be detected.

The ORNL group has made measurements of the type described above for 15- to 22-MeV ^{127}I ions, 60-MeV ^{127}I ions, 10-MeV ^{16}O ions, and 3-MeV ^{4}He ions in the (111) and (100) planes of Au. All of these data exhibit the following linear relationship between the channeled stopping power, corrected to the incident beam energy, and the corresponding channel oscillation "frequency";

$$(-dE/dx)_E = \alpha + \beta\omega, \tag{4.11}$$

where α and β are empirical constants. The oscillation "frequency" ω is determined from the wavelength measurements and is approximately equal to $2\sqrt{E}/\lambda_{ch}$. Figure 82 shows some results for ^{127}I ions. The ^{127}I data are recorded in the velocity-proportional stopping region (Region III in Fig. 37). It is remarkable that a similar relationship also exists for data recorded in velocity regions I and II (Fig. 37), (for the ^{4}He and ^{16}O data, respectively). Although the reason for the simple relationship given in Eq. (4.11) is not yet understood, Robinson [Ro71a] has shown that it implies a definite relationship between the planar channel potential and the distribution of stopping power in the channel. Thus, if the potential were harmonic, Eq. (4.11) would require the stopping power in the channel to be everywhere constant independent of z. For a potential

$$U_2(z) = U_0 \cosh(bz), \tag{4.12}$$

the corresponding stopping power distribution must be of the form

$$S(z, E) = s_0 + s_1[\cosh(bz/2) - 1]. \tag{4.13}$$

Here, $U_2(z)$ is a potential like that given in Eqs. (2.41)–(2.43); b is a screening parameter (the cosh function corresponds to the long-range part of the Molière potential), U_0 is a constant, and s_0 and s_1 are energy-dependent stopping-power parameters determined from experiment. The expressions in Eqs. (4.12) and (4.13) were found by Robinson [Ro69] to give a good fit to the experimental data. It was originally conjectured [Lu66] that $S(z, E)$ should be proportional to the local electron

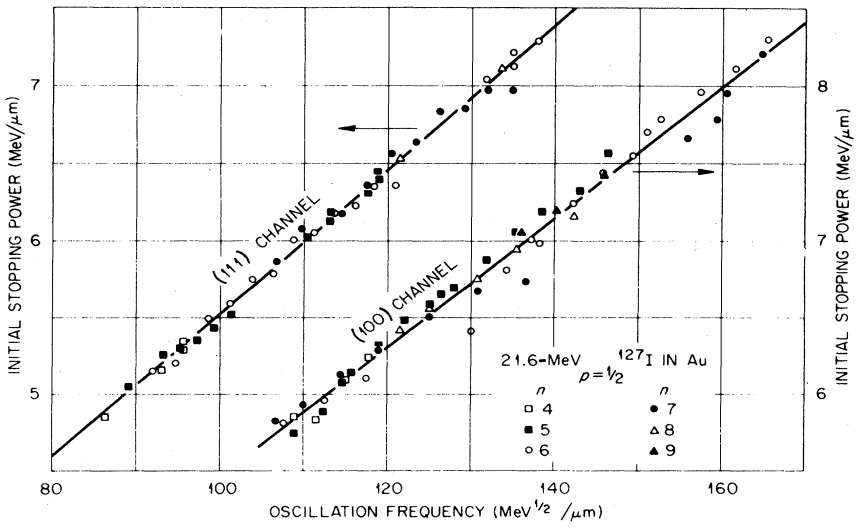

FIG. 82. Initial stopping power as a function of channel oscillation "frequency" for 21.6-MeV ^{127}I ions in the (111) and (100) planar channels of Au [Ap71].

density $n_e(z)$ in the channel and that $n_e(z)$ should, in turn, be related to the potential $U_2(z)$ through Poisson's equation. This would lead to $S(z,E) \propto \cosh(bz)$, which is at variance with the large body of experimental data now available. The fact that the stopping power rises more slowly than the potential as the channel walls are approached may be due to the low probability for nonadiabatic interactions of the ions with the more tightly bound target electrons. Ohtsuki and Kitagawa [Oh72b] have calculated $S(z,E)$ using Firsov's theory [Fi59] [see also Eq. (2.135)] and, for the case of 60-MeV ^{127}I ions, obtained a result in good agreement with Robinson's expression, Eq. (4.13). Based on Eq. (4.11) Robinson has shown that a curvature parameter,

$$y = 4\pi^2(s_0 - \alpha)^2/(\beta^2 d_p), \tag{4.14}$$

evaluated from the experimentally determined values of α, β, and s_0 (d_p is the interplanar spacing), is related to the second derivative (with respect to z) of the potential evaluated at midchannel as follows:

$$y = 2U''_2(0)/d_p. \tag{4.15}$$

Thus data of the type shown in Fig. 82 immediately yield the (harmonic) form of the potential at the channel center. If the ion–atom potential is of the screened Coulomb type, the curvature parameter is

$$y = -8\pi N Z_1^* Z_2^* e^2 b\varphi'(bd_p/2), \tag{4.16}$$

where N is the atomic density of the target, $Z_1^* e$ and $Z_2^* e$ are the effective charges of the incident ions and target atoms, respectively, and φ is the atomic screening function as given in Eq. (2.1) et seq. Using a screening function

$$\varphi(br) = 0.35\exp(-br), \tag{4.17}$$

that is, the long-range term of the Molière potential, Eq. (2.21), and comparing the curvature parameters for the (111) and (100) planes in Au, Appleton *et al.* [Ap71] were able to deduce ionic charges, defined as $Z_1^* Z_2^*/79$, that are in fair agreement with the equilibrium ionic charges measured for the transmitted beam.

A direct method for determining the planar continuum potentials from measurements of the type described above has been given by Gibson and Golovchenko [Gi72a]. Their method is based on the fact that the form of the potential $U_2(z)$ may be deduced from a knowledge of the oscillation period as a function of the transverse energy $E_\perp$ (see, e.g., [Lan60]). In their approach, no relation of the type given in Eq. (4.11) is invoked. In fact, the stopping power only enters insofar as it permits the identification of trajectories with different wavelengths. The transverse energy associated with a given detected wavelength, identified with the index, j, is found by varying the incidence angle ψ_0 while keeping the thickness t fixed. The population of the jth group is proportional to $(dU_2/dz)^{-2}$, where the derivative is evaluated at the point $z_{0,j}$, at which particles in this group enter the planar channel. As ψ_0 is increased from zero, $z_{0,j}$ decreases from $z_{\max,j}$, the maximum amplitude of the jth group (see Fig. 21) until, when $\psi_0 = \psi_{0,j}$, the value of $z_{0,j}$ reaches zero. The population of the jth group then reaches a strong maximum and thereafter, for $\psi_0 > \psi_{0,j}$, abruptly vanishes. This sharp angular behavior, in practice smoothed somewhat by effects due to mosaic spread and multiple scattering, has been observed by Gibson and Golovchenko for 1.8-MeV ^{4}He ions incident along the (111) planar direction in 2750-Å-thick Au crystals. The transverse energy for the jth group is then found from

$$E_{\perp,j} = E\psi_{0,j}^2. \tag{4.18}$$

The wavelength λ_{ch} is a function of both $E_\perp$ and $U_2(z)$. The inverse of the potential can be obtained via the transformation [Lan60]

$$z(U_2) = (8\pi^2 M_1 v)^{-1/2}\int_0^{U_2} \lambda_{ch}(E_\perp, U_2)(U_2 - E_\perp)^{-1/2} dE_\perp. \tag{4.19}$$

For $\lambda_{ch}(E_\perp, U_2)$, Gibson and Golovchenko chose a functional form such that the transformation, Eq. (4.19), yields the physically reasonable potential

$$U_2(z) = \tfrac{1}{2}a_1 z^2 + \tfrac{1}{4}a_2 z^4. \tag{4.20}$$

The constants a_1 and a_2 were determined by a least-squares technique giving the best fit of the function $\lambda_{ch}(E_\perp, U_2)$ to the measured wavelengths and transverse energies. A good fit was found indicating that the potential form in Eq. (4.20) is indeed a reasonable one. The resulting coefficients of the potential are $a_1 = 71.6 \pm 4.6$ eV/Å^2 and $a_2 = 179 \pm 26$ eV/Å^4. The value of a_1 is in good agreement with the value 75.4 ± 3.3 eV/Å^2 obtained from the curvature parameter deduced by Appleton *et al.* [Ap71] from energy-loss measurements and the relations given in Eqs. (2.11)–(4.16).

4.3d. Measurements with super-collimated beams

Measurements on the angular distributions of channeled ions transmitted through very thin ($\lesssim 1$ μm) crystals can provide information of a type that is not obtainable with thicker crystals or in Rutherford backscattering. Studies of this type have been performed by Armstrong *et al.* [Ar71b, 72] using super-collimated beams of 4-MeV H^- ions. The techniques for producing these beams with an angular divergence of ±1.5 mdeg and a spot size of 25 μm, have been described in Sec. 3.1. Related experiments have been performed by Chadderton and Eisen [Ch69b] and Ecker *et al.* [Ec70]. Some of the data recorded photographically by Armstrong *et al.* (with an experimental arrangement like that illustrated in Fig. 2) for the ⟨100⟩ axial direction in Si are reproduced in Fig. 83. Unlike the star patterns observed with thicker crystals (Sec. 4.3a), the patterns are now ring-shaped, the radius of the ring corresponding to the angle between the beam direction and the axial direction of the target crystal. The ring patterns also display azimuthal structure with symmetry properties characteristic of the axis. These patterns are observed when the angle of incidence ψ_0 is less than the critical angle ψ_c for axial channeling.

The main features of the rings can be readily described in terms of the continuum model [Ar72]. The transverse energy $E_\perp$ of a particle entering the crystal is simply $E\psi_0^2 + U_R(\mathbf{r}_0)$, where $U_R(\mathbf{r}_0)$ is the continuum potential, as defined in Eq. (2.30), evaluated at the position of entrance $\mathbf{r}_0$ on the plane normal to the axis under consideration. There is, therefore, at the entrance to the crystal a

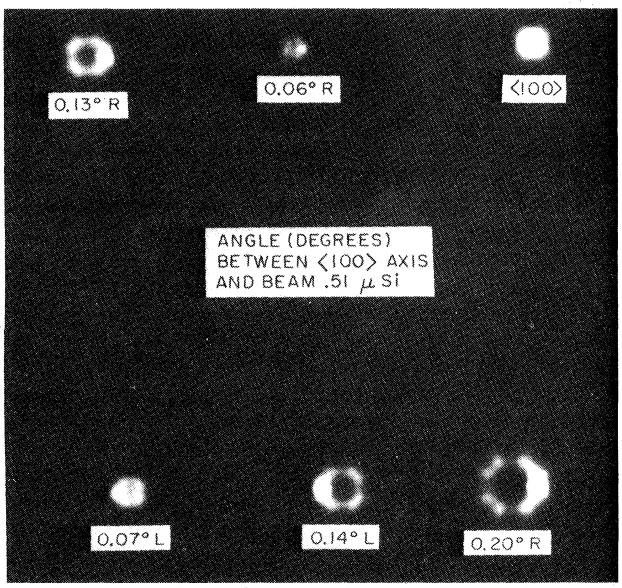

FIG. 83. Photographic recordings of the angular distributions of protons transmitted through a 0.51-μm Si crystal for various entrance angles ($\psi_0 < \psi_c$) relative to the ⟨100⟩ axial direction [Ar71b]. The incident beam energy is 4 MeV. The value of ψ_c is approximately 0.35°. The particle intensities were measured on x-ray film 1.4-m downstream from the target. The exposure times for the different cases are not always the same. In each case, the ⟨100⟩ axis was tilted to the left (L) or right (R) of the beam direction by the angle indicated.

distribution in $E_\perp$ with values ranging between $E\psi_0^2$ and $E\psi_c^2$ for channeled particles. This distribution is sharply peaked towards the lower limit $E\psi_0^2$ because of the geometry at the entrance to the crystal and because of the flat-bottomed nature of the potential $U_R(\mathbf{r})$ at positions between rows. In passage through such thin crystals the initial distribution in transverse energy is approximately preserved. Thus, just before the exit from the crystal the values of $E_\perp$ remain concentrated near $E\psi_0^2$. After emergence, the angle of emission ψ_e relative to the axis for a particle leaving at a transverse position $\mathbf{r}_e$ is $\{[E_\perp - U_R(\mathbf{r}_e)]/E\}^{1/2}$. Again, because of the geometry and the shape of the potential at the exit, the values of ψ_e are concentrated around $(E_\perp/E)^{1/2}$ and thus around ψ_0. The angular distribution of emerging particles is therefore peaked at an angle (relative to the axis) equal to the entrance angle (relative to the axis). That is, the particles emerge mainly on the surface of a cone centered on the axis and with half-angle $\psi_e = \psi_0$. This produces ring-shaped patterns of the type shown in Fig. 83.

The distribution of intensity in the radial direction of the rings is determined primarily by surface transmission effects, mainly at the entrance for $\psi_e > \psi_0$ and mainly at the exit for $\psi_e < \psi_0$. In principle, the distribution in ψ_e is sufficient to determine the continuum potential. There are, however, contributions to the distribution in ψ_e from multiple scattering effects (which change $E_\perp$) and from the finite angular divergence of the incident beam. Armstrong *et al.* have measured the influence of surface oxide layers and of target thickness on the ring patterns. These authors have also measured the emergence patterns by scanning them with a well collimated surface-barrier detector.

The azimuthal distribution, i.e., around the circumference of the ring, in the patterns depends on the extent to which the transverse momentum vector $\mathbf{p}_\perp$ is rotated from its initial direction with respect to the axis. As a channeled particle progresses through the crystal, it collides with many atomic rows, continuum strings, each time changing the direction of $\mathbf{p}_\perp$. If the crystal is thick enough for statistical equilibrium to be reached, a sufficient number of collisions with rows will have occurred to make all orientations of $\mathbf{p}_\perp$ equally likely. In this case no structure in the azimuthal direction of the emergence pattern would be expected. For the thin crystals considered here, however, this stage is not reached. The data of Fig. 83 show that even after many collisions, some azimuthal directions are favored over others. This is explained by Armstrong *et al.* as blocking in the transverse plane. That is, when an axially channeled particle is scattered so that $\mathbf{p}_\perp$ points into a low-index direction in the transverse plane, it will be blocked, i.e., $\mathbf{p}_\perp$ will be rotated away from the low-index direction. Thus, the less intense sections of the azimuthal distributions in Fig. 83 correspond to these low-index directions in the transverse plane; these are planar directions in the three-dimensional crystal.

Another feature of the observed patterns is that for thin crystals and large transverse energies, the intensity around the ring concentrates strongly in the original beam direction. This suggests that there are not enough collisions with rows to randomize the direction of $\mathbf{p}_\perp$. The measurements indicate that statistical equilibrium is not achieved in crystals with thicknesses as much as ten times the mean free path for equilibration estimated by Lindhard [Li65]. Quite possibly the system could be nonergodic, and equilibrium would never be achieved in any distance.

4.3e. Hyperchanneling

The critical value $U_R(\rho_c)$ of the continuum potential for normal axial channeling is usually much larger than the value U_H of the potential at the saddle point between rows; an example is shown in Fig. 8. Consequently, in most axial channeling measurements the majority of the channeled particles have sufficient transverse energy to mount the low potential barrier between adjacent axial channels and to wander freely between channels during passage through the crystal. A few particles with $E_\perp < U_H$ will be confined to one axial channel. These two modes of axial channeling were found by Robinson and Oen [Ro63b] in their early computer calculations. Lindhard [Li65] referred to motion entirely within one channel as proper channeling. In this sense all planar channeled trajectories are proper. To emphasize the distinction for the axial case, Appleton *et al.* [Ap72b] introduced the term *hyperchanneling* meaning proper axial channeling. Eisen [Ei66] observed that a small fraction of an incident beam of 375-keV protons was transmitted through a 2.2-μm-thick Si crystal in the ⟨110⟩ axial direction with an energy loss lower than that for the (111) planar direction, the most open planar direction intersecting in the ⟨110⟩ axis. He attributed these extra-low energy losses to what are now called hyperchanneled particles.

Since the critical angle for hyperchanneling

$$\psi_H \approx (U_H/E)^{1/2} \tag{4.21}$$

is much lower than the normal critical angle ψ_c, hyperchanneling can be observed only for very small angles of incidence, small beam divergences and very thin defect-free crystals. Appleton *et al.* [Ap72a, b] found that, whereas hyperchanneling is difficult to observe for light ions in the Bethe–Bloch stopping region, for heavy-ion beams in the velocity-proportional stopping region hyperchanneling effects can be very pronounced. Some of their data for ^{127}I ions in Ag are shown in Fig. 84. For incidence within about 0.12° of the ⟨011⟩ direction there is a sharply peaked (in angle) group corresponding to hyperchanneled ions. Their rate of energy loss, about 3.15 MeV/μm, is markedly less than that, about 3.8 MeV/μm, for (111) planar channeling. The data shown in Fig. 84 indicate that the (111) planar energy-loss distribution is obtained for $|\psi_0| \geq 0.45° \approx \frac{1}{3}\psi_{1/2}$.

Appleton *et al.* have made a theoretical interpretation of their results. They used the continuum potential illustrated in Fig. 8 and assumed that the ions achieve statistical equilibrium in their passage through the crystal. The measured data are affected by electronic multiple scattering, beam divergence, surface contaminants, mosaic spread, and the acceptance angle of the detector. These factors were therefore also included in the theoretical description. Defects were believed to be of such a low concentration as to have a negligible influence on the results. A good fit to the data was obtained, but it was necessary to assume that there is considerably more multiple scattering than simple estimates give and also that the value of U_H is 120 eV, instead of the 60 eV shown in Fig. 8. The authors conjecture that this latter difficulty could be overcome if Wigner–Seitz, rather than free-atom, boundary conditions were applied to the electron wavefunctions.

4.3f. Charge states of transmitted ions

When fast ions are incident upon an amorphous solid, an equilibrium distribution of ionic charge states is rapidly established (see [Betz72] for a recent review of this topic; see also Sec. 2.6a). This distribution is independent of the initial ionic charge and is achieved after penetrating distances usually on the order of only a hundred angstroms or so. At a given ion velocity, the equilibrium charge-state distribution is maintained by a dynamic balance of the electron capture and loss cross sections. The most probable charge state is that for which the capture and loss cross sections are approximately equal. For higher charge states, the capture cross section dominates and for lower charge states the loss cross section dominates. When the incident ion beam is channeled, it is constrained to move in regions of the target crystal where both the local electron density and velocity are low. As a result, both the capture and the loss cross sections are much reduced, and the distance required to reach equilibrium is correspondingly longer. This effect was first reported by Martin [Mart69] in measurements on charge states of ^{12}C and ^{16}O ions ($E \approx 5 - 35$ MeV) transmitted through Si and Ni crystals. Lutz *et al.* [Lu70] found that 60-MeV ^{127}I ions require approximately 1200 Å to reach charge-state equilibrium when channeled between the (100) planes in Au. The effect of channeling on the most probable charge in the equilibrium distribution depends rather sensitively on the relative reduction factors for the capture and loss cross sections. Thus Martin observed that for ^{12}C and ^{16}O ions the most probable charge increased slightly, whereas for 60-MeV ^{127}I ions in Au, Lutz *et al.* found that the most probable charge was reduced from about 21 (in random orientation) to about 18 for (100) planar channeling. Martin's results showed that for major axial directions in Si, the slower ^{12}C and ^{16}O ions, below about 2-MeV/nucleon, and those incident in low charge states emerge approximately in equilibrium. However, 35-MeV ^{16}O ions incident as 8^+ ions emerge far from equilibrium indicating that the charge-changing cross sections are less than 2×10^{-19} cm^2.

Datz *et al.* [Da72] have studied charge-state distributions of ^{16}O ions (4.45–40 MeV) channeled in Au crystals. They find that for incident energies above 20 MeV, no true equilibrium is observed even for channeled path lengths of 6000 Å. Some of their data are shown in Fig. 85. The random distribution shown in Fig. 85 is representative of charge-state equilibrium since it is independent of path length (in the range 0.143–0.663 μm) in the crystal and is independent of the input charge state, 6^+, 7^+, or 8^+. The channeled distributions are clearly nonequilibrium cases. Using the techniques described in Sec. 4.3c, Datz *et al.* have determined that the larger the oscillation amplitude of planar channeled ^{16}O ions in Au, the closer the measured charge-state distribution approaches the random distribution. By varying the path length for the planar channeling case, they were also able to measure the depth-dependence of the charge-state distributions and so could extract values for the charge-changing cross sections. The results show that all of the cross sections are reduced, but that the electron capture cross sections for 7^+ and 8^+ ions are particularly small. This is the principal cause of the higher charge states for channeled ^{16}O ions and is interpreted by Datz *et al.* in terms of shell effects. In cases such as these where the charge-changing cross sections are so small, it is not possible to achieve true charge-state equilibrium in a distance short enough so that energy loss of the ions does not significantly alter

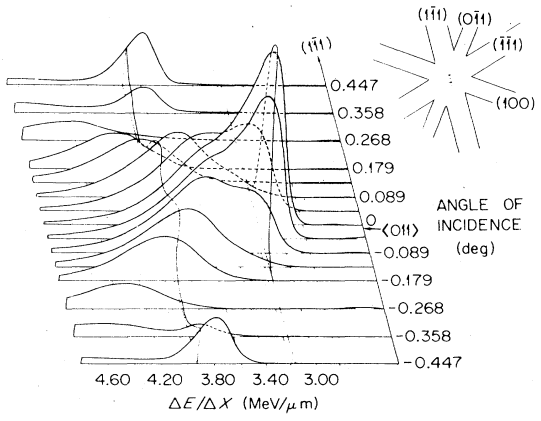

FIG. 84. Energy-loss distribution (normalized for equal numbers of incident ions) measured at various incidence angles ψ_0 relative to the ⟨011⟩ axis for 21.6-MeV ^{127}I ions transmitted through an Ag crystal 0.85 μ thick [Ap72b]. The incident beam direction lies in the (111) plane. The insert shows the angular extent of the measurements (dotted line) and of the hyperchanneling region (central circle). The widths shown for the planar channels are twice the half-angles calculated from Eq. (2.81). The calculated value, Eq. (2.66), of $\psi_{1/2}$ for the ⟨110⟩ axis is 1.2°.

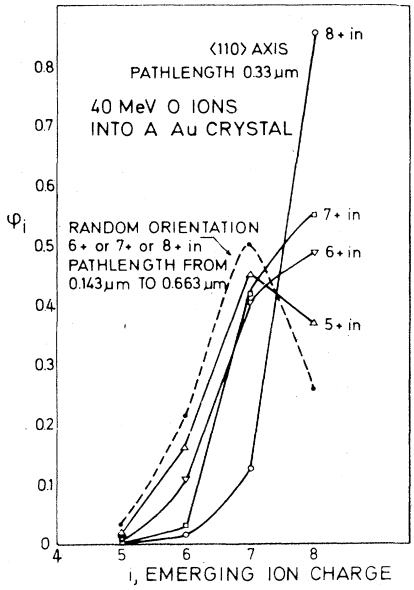

FIG. 85. Charge-state fractions φ_i measured for oxygen ions transmitted through a Au crystal in a random orientation (dashed line) and in the ⟨110⟩ axial channeling direction (solid lines) for various incident ionic charges [Da72]. The incident beam energy in each case was 40 MeV.

the values of the cross sections. (For further work on charge states of channeled ions, see [And66b; Ande70; Kami70].)

4.3g. Light emission from channeled ions

Since channeling can modify the charge-state distributions of channeled ions (Sec. 4.3f), it might be supposed that there could also be an influence on the yield of optical transitions in the ion beam either during or after passage through a crystal. Khan *et al.* [Kh67a] found a channeling dip in the yield of the 1216-Å hydrogen line observed for 25- to 80-keV protons incident near the ⟨110⟩ axial direction of a thick Cu crystal. Similar results were obtained for the 584-Å line of helium. The results were attributed to a reduction in the cross section for electron capture into excited states of the beam ions under channeling conditions. Andersen *et al.* [Ande70] reported strong channeling dips in the integrated spectral intensity of optical transitions observed for beam-foil excited He^+ ions transmitted through Au crystals ~1700 Å thick. The incident He^+ energies lay in the range 200–400 keV. The dominant line observed was believed to be the 1460-Å He II line. Subsequent experiments using a variety of He^+ ion energies in the range 60–940 keV and Au crystal thicknesses in the range 80–1500 Å found no evidence for a channeling effect in the light emission from beam-foil excited ions observed downstream from the target crystal [Po71b, 72b; As72; New72]. Newton *et al.* [New72] also found that there was no effect upon the polarization measured for the 4686-Å line of He II.

Okorokov *et al.* [Oko72] have measured the dependence on the bombarding energy of the yield of the 4686-Å line in He II for He^+ ions transmitted through an 1100-Å-thick Ag crystal under conditions both of random incidence and of ⟨100⟩ axial channeling. For random incidence (3–5° off axis), the yield is a smooth function of bombarding energy in the range 565–590 keV. Under channeling conditions the yield function shows a sharp peak at a bombarding energy of 570 keV. At this energy the channeled ions emerge with an energy of about 530 keV. The authors attribute the peak to the coherent excitation of the 51 eV ($n = 4$) level in He^+ by virtue of a matching between the collision frequency v/d and the transition frequency $(E_{exc} - E_{gnd})/h$; the 4686-Å line arises from transitions between the $n = 4$ level and the $n = 3$ level at 48.4 eV. The incident ion energy at which this match is expected is 526 keV. The fact that the peak occurs when the exit energy of the ion is near this value is in accord with the expectation that if the excitation were to occur inside the target crystal, i.e., at bombarding energies between 526 and 570 keV, the ion would almost immediately be ionized because of the high-loss cross sections for excited electrons (see also [Ga73a]).

4.3h. Channeling of molecular ions

Van de Graaff accelerators can produce intense beams of the molecular ions H_2^+ and H_3^+ and it is of interest to compare channeling effects seen for these beams with those seen for H^+ beams of the same velocity. Caywood *et al.* [Cay71; Tomb73] have compared axial channeling dips obtained for the backscattering from Si of beams of H^+, H_2^+, and H_3^+ ions with energies of 0.8, 1.6, and 2.4 MeV, respectively. The dips measured for the molecular ions are slightly narrower and shallower than those for protons, and the dechanneling rate for molecular ions is significantly larger than the rate for protons. Eisen and Uggerhøj [Ei72b] have observed that axial flux-peaking effects in Si (Yb) are reduced when molecular ion beams are employed. All of these results are in harmony with the idea that the molecular ions are stripped of their binding electrons extremely rapidly ($\sim 10^{-16}$ sec) as they enter the crystal and that there is correspondingly a rapid jump in the transverse energy of the individual protons due to their mutual Coulomb repulsion (the binding energies of H_2^+ and H_3^+ ions are approximately 3 and 4 eV, respectively). Dechanneling and flux peaking effects are expected to be particularly sensitive to such changes in transverse energy.

Poizat and Remillieux [Po72b, c] have measured the transmission of 1-MeV H_2^+ ions through an Au crystal 940 Å thick. In a random orientation the transmission probability for undissociated molecular ions is $\sim 10^{-7}$. Planar channeling strongly enhances the transmission. The transmission probability increases with planar spacing and reaches a maximum of $\sim 10^{-5}$ for large spacings. The mechanism for this process is as yet unclear. It seems likely that the two protons dissociate inside the crystal and that they emerge close enough together that there is a relatively high probability of picking up a binding electron near the exit surface.

4.4. Channeling in nonsimple crystals

Throughout most of this article we are concerned with channeling effects in crystals with simple lattice structures such as those of the bcc and fcc metals and of the common semiconductor materials Si, Ge, etc., having the diamond fcc structure. In this section we briefly consider

channeling in more complicated crystals such as those having complex lattice structures, those with a basis of more than one atom (Si and Ge already fall into this category), polyatomic crystals, and polar crystals. A list of references to measurements on nonsimple crystals is given in Appendix B. It is important to be able to understand the channeling properties of complex crystals since they present a stringent test of any channeling theory. A successful theory would then be able to describe channeling in simple crystals as a special case.

Some of the complicating effects that can arise even in fairly simple monatomic structures may be illustrated by considering the Si lattice. In the ⟨111⟩ axial direction in Si all rows are identical. In each row, there are two atomic spacings, $d^{(a)}$ and $d^{(b)}$, that alternate ($d^{(b)} = 3d^{(a)}$). In the continuum approximation the nuclear and electronic charges are treated as smeared out continuously in the row direction and thus one can use an average spacing, $\bar{d} = 2d^{(a)}$, to calculate quantities such as $\psi_{1/2}$ using, for example, the formulas given in Appendix A. Consider now ⟨111⟩ axial blocking in Si. One knows (see, e.g., Sec. 2.4d1) that the angular width of the blocking pattern is determined mostly by blocking at the nearest-neighbor atom in the row. (For a system consisting only of two stationary atoms a distance d apart, the angular half-width of the blocking pattern is $(4Z_1 Z_2 e^2/dE)^{1/2} = \sqrt{2}\psi_1$.) Thus, one expects the ⟨111⟩ blocking distribution to be the sum of two distributions whose widths correspond to the spacings $d^{(a)}$ and $d^{(b)}$. The rule of reversibility implies that the channeling dip should correspondingly be composed of two contributions. Although thermal vibrations tend to blur the distinction, there is a definite difference between the angular distributions expected in the cases of equal and unequal atomic spacings. This difference has not yet been observed in experiments. A related effect is expected for planar channeling. For the (111) planes in Si there are two interplanar spacings, $d_p^{(a)}$ and $d_p^{(b)}$, that alternate ($d_p^{(b)} = 3d_p^{(a)}$) and that separate equally densely populated planes of atoms. (A similar situation obtains in Si whenever all three Miller indices are odd.) One would expect therefore to be able to observe two components in (111) planar channeling. One of these components should have a smaller value of $\psi_{1/2}$, a faster dechanneling rate, etc. than the other. Thus far, the only reported observation of an effect of this type is the evidence for two dechanneling rates in the transmission of protons through the (111) planar channels of Si

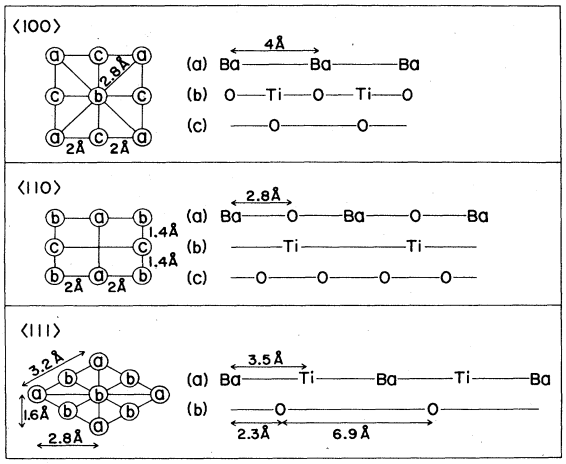

FIG. 86. Atomic arrangements for the ⟨100⟩, ⟨110⟩, and ⟨111⟩ axial directions in cubic $BaTiO_3$ [Ge72b]. The arrangements shown on the left are end views of the channels and the letters refer to the individual rows shown on the right.

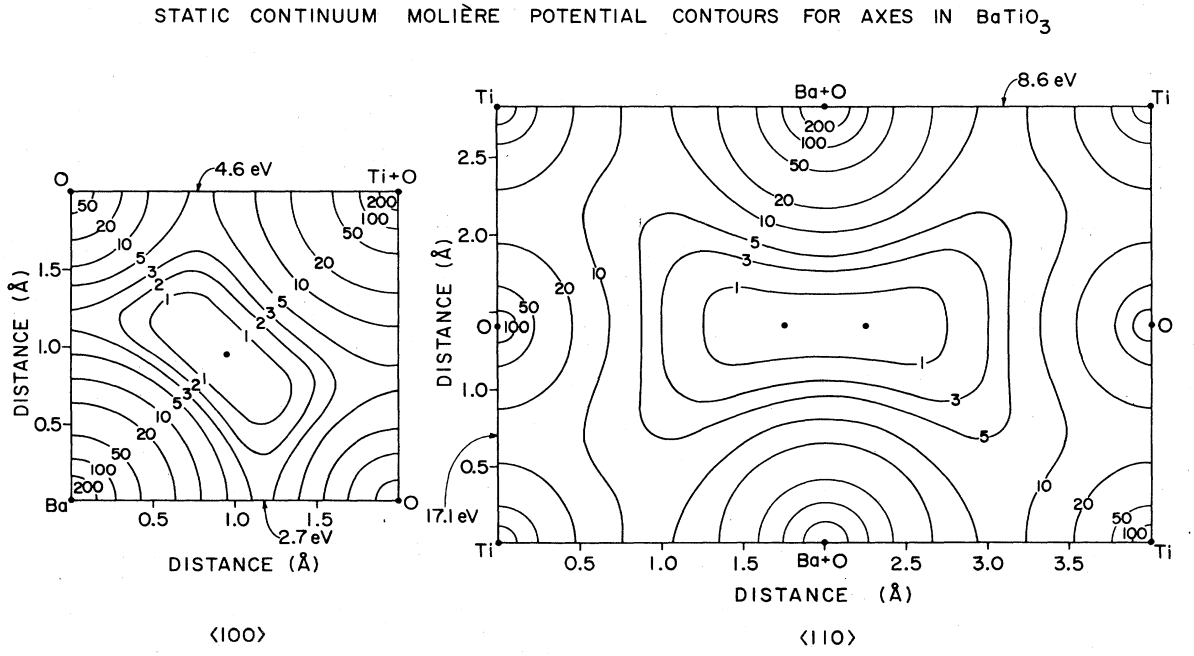

FIG. 87. Potential-energy contour diagrams for ⟨100⟩ and ⟨110⟩ directions in cubic $BaTiO_3$, as calculated from the static continuum form of the Molière potential function, Eqs. (2.15) and (2.18) [Ge72b]. Only one quarter of the cross-sectional area of the unit cell is shown for the ⟨100⟩ direction.

[Ap68]. From these observations it was not clear whether protons leaving the narrower planar channel became random or whether they entered the wider channel (see also [Whi69]).

A further stage of complexity is reached when channeling in polyatomic crystals is considered. In an axial direction in such a structure, not only can each row contain several atomic species and several different spacings between atoms, but there may also be several types of row parallel to one another. Similarly in planar channeling, there may be several types of plane, each type being a particular coplanar mixture of atomic species, and several interplanar spacings. In this connection it is useful to characterize each type of row or plane as weak or strong according to its ability to reflect particles incident at small angles. These considerations are illustrated in Figs. 86–88 for the case of cubic $BaTiO_3$ [Ge72a,b]. (This material has the Perovskite structure which is simple cubic with a basis of 5 atoms. A Ba atom is located at each corner of the unit cell. A Ti atom is in the center, and an O atom is at the center of each face.)

Figure 89 shows a set of data recorded for $\langle 100 \rangle$ axial channeling of 3.8–MeV protons in a thin $BaTiO_3$ crystal. A striking feature of these data is the fact that the angular width of the backscattering dip measured for oxygen is less than one half that for barium. Thus it is apparent that the incident beam can be channeled with respect to a strong row, such as the $\langle 100 \rangle$ barium rows shown in Fig. 86, while traveling randomly with respect to weak rows, e.g., those $\langle 100 \rangle$ rows containing oxygen. An even more pronounced difference in backscattering from oxygen and barium is observed in the (110) planar direction of $BaTiO_3$. Here the barium data show a pronounced channeling dip, whereas in the data for oxygen no evidence for a dip is seen. A reasonably good fit to the measured values of $\psi_{1/2}$ and χ_{min} for $BaTiO_3$ was obtained [Ge72b] based on an extension of Barrett's formulas [Ba71] (see Sec. 2.4d) and with the assumption that each type of row or plane has its own characteristic critical angle. The results show that the channeling characteristics of the weak rows or planes are very much influenced by the presence of the strong ones. Similar conclusions have been reached in channeling studies in crystals of CaF_2 [He71a], quartz [Abel69, 72b, 73], ThO_2 [Cli72], UO_2 [Erik69a], and U_4O_9 [Mat71a].

Another feature of interest in the data shown in Fig. 89 is the small angular width of the peak observed for channeled particles in transmission. Similar widths were seen for planar channeling. The results can be explained as being a consequence of the rapid dechanneling rates encountered by all but the best channeled particles. These high rates are primarily due to encounters with weak rows or planes. Note that in the axial case there are several modes of channeling possible depending on the transverse energy of the particles. For example, in the $\langle 100 \rangle$ direction of $BaTiO_3$ (see Fig. 87) protons will be hyperchanneled if $E_\perp < 2.7$ eV. For $2.7 \text{ eV} < E_\perp < 4.6$ eV, the particles can circulate about the weak rows of oxygen. For $E_\perp > 4.6$ eV, the particles will be normally channeled, i.e., free to wander between rows. For $E_\perp \gtrsim 33$ eV, the protons will be dechanneled with respect to the weak oxygen rows. And so on. For a given initial distribution of transverse energies there will obviously be a rather complex evolution of the relative populations of these various modes as the beam progresses into the crystal. These effects have been studied further by determining the dechanneling rates from measure-

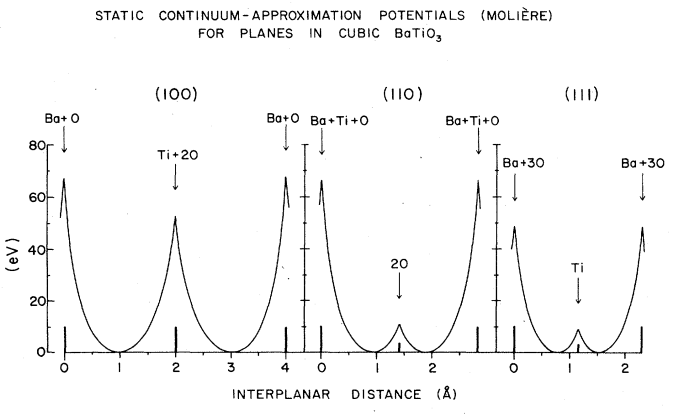

FIG. 88. Continuum-approximation potentials calculated for the (100), (110), and (111) planes in cubic $BaTiO_3$ [Ge72b]. A static lattice is assumed, and the Molière ion–atom potential is used, Eq. (2.2).

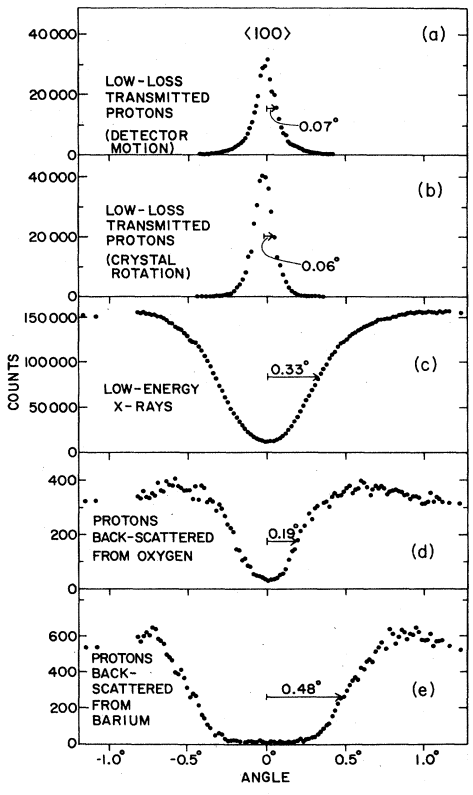

FIG. 89. Angular dependences for channeling of 3.8-MeV protons along the $\langle 100 \rangle$ axis of a 4-μm-thick $BaTiO_3$ crystal at 140°C [Ge72b]. The data show (a) low-loss transmitted protons as a function of exit angle, the incident beam being exactly on axis; (b) low-loss transmitted protons measured in the beam direction as the incidence angle is varied; (c) dip obtained for the Ba L and the Ti K x rays (4–6 keV); (d) and (e) dips obtained for backscattering (157½°) from oxygen and barium, respectively; the scattering region selected is about the first micron of penetration into the crystal.

ments on backscattering from the individual elements in $BaTiO_3$. [Ge72b]

Roth *et al.* [Roth70] have used measurements on characteristic x-ray production to study differences in the channeling behavior of 75-to 200-keV protons along the ⟨100⟩ and ⟨110⟩ axial directions of alkali-halide crystals. In the ⟨100⟩ direction each row consists of an alternating sequence of cations and anions. In the ⟨110⟩ direction there are two types of row each containing only one atomic species. For the ⟨100⟩ direction both x-ray yields showed identical channeling dips. For the ⟨110⟩ directions, the x rays from the element having the lower atomic number showed a shallower and narrower dip than did those from the higher-Z element. These results are in keeping with the ideas outlined above, viz., that the weaker rows have smaller critical angles and that beam particles can become dechanneled with respect to them while remaining channeled with respect to the stronger rows.

Channeling experiments have been performed on a wide variety of polyatomic crystals. The lattice structures studied most frequently have been those homomorphous with the rocksalt structure [Cl70; Dav69; De68a,b; Ec70; Ed70; Fuj71a; Kon69; Man70; Mat67,69,70,71b; Miy72; Mor70b,72; Roth70; Sh68b], with the fluorite structure [Cli72; Dav68,69; Ed70, 72a; Erik69a; He71a,b; Mat67,69,71b], and with the zinc-blende structure [An72; Mor72; Pi69a,b; Sa67, 68b]. Except as noted above most of these studies have chosen channeling orientations that avoid the complications inherent in the existence of several types of row or plane, and of unequal interplanar spacings. In crystal directions where all of the rows, or planar sheets, contain the same mix of atomic species, the experimentally determined values of $\psi_{1/2}$ and χ_{min} can be fairly well fitted with formulas based on the continuum model (e.g., those given in Appendix A) if one uses average values of Z_2, a, d, u_1, etc. Several different methods of averaging have been used. The results are not very sensitive to the choice of method unless the rows or planes contain mixtures of atoms with widely differing values of these parameters. Varelas and Sizmann [Var72] have made analytical computer calculations on the critical angles and distances of closest approach to rows containing mixtures of atoms and having unequal spacings. Their results give good agreement with measured data even when the atoms in a row differ markedly in Z_2, as, for example, in the ⟨100⟩ direction in UC.

There have been relatively few theoretical studies of channeling in complex crystals. Martynenko [Mar71a] and Varelas and Sizmann [Var72] have examined analytically the conditions under which transverse energy is conserved in the scattering of particles from axial rows having nonsimple configurations of atoms. The calculations of Varelas and Sizmann indicate a method for determining the appropriate averages along the row direction and are successful in accounting for the temperature dependent values of $\psi_{1/2}$ measured in many different experiments. Torrens *et al.* [To68,69] have made Monte Carlo calculations on the channeling of protons and of several heavy ions in alkali-halide lattices. Edge *et al.* [Ed72b] have examined theoretically the channeling and blocking of protons along polar lattice directions such as the ⟨111⟩ axial direction in the zinc-blende structure. They suggest that a difference in dechanneling rates should be distinguishable in the two opposite directions. Experiments performed thus far have been unable to detect any difference in channeling behavior for opposing polar directions in crystals such as AlSb, GaP, and GaSb [Sa68b; Pi69a].

It has frequently been speculated that in channeling, for example, along the ⟨100⟩ axial direction of NaCl, the alternating sequences of anions and cations might give rise to some sort of electrostatic strong focussing effect. Nelson [Ne66] has calculated such effects for the ⟨100⟩ axes of NaCl and of CsCl and found them to be negligibly small in both structures. Kononov and Struts [Kon69] have suggested that for the channeling of protons in ionic crystals a dipole interaction between the protons and the anions and cations of the crystal should be important. We conclude this section by remarking that channeling effects have also been measured in crystals that are ferroelectrically polarized [Ge72a,b] and ferromagnetically polarized (see Sec. 6.7).

5. CHANNELING WITH ELECTRONS AND POSITRONS

For electrons and other particles carrying a single negative charge the continuum potential is simply the negative of that governing the motion of protons and positrons. Figure 90 illustrates schematically the differences between the continuum potentials $U^+(z)$ and $U^-(z)$ for planar channeled positrons (β^+) and electrons (β^-), respectively. The minimum of the potential well for electrons lies in the rows or planes of crystal atoms while for positrons (as for protons) it lies between them. Thus, while classically behaving positrons may be expected to exhibit channeling characteristics similar to those of protons, the situation for electrons should be quite different. For example, if a beam of classically behaving electrons is incident on a crystal in a direction parallel to a major plane, most of the beam will become trapped in potential wells of the type shown in Fig. 90(b). A small

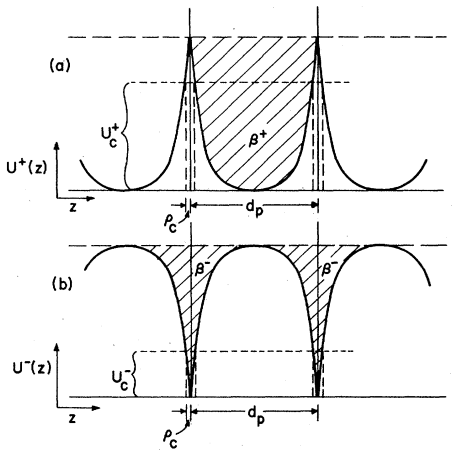

FIG. 90. Schematic illustration of the planar continuum potentials for (a) positrons and (b) electrons. The shaded areas correspond to the potential wells in which channeled particles can move. U_c^+ and U_c^- are the potentials evaluated at the critical distance ρ_c from a plane. Note that U_c^- represents a lower limit for the transverse energy at which stable electron channeling is possible, while U_c^+ is the corresponding upper limit for positrons.

fraction of the beam, those electrons incident at distances $\lesssim \rho_c$ from a plane, will rapidly be scattered into random trajectories. In the remaining channeled fraction of the beam, each electron may be expected to oscillate to and fro through a single plane of atoms. These electrons will therefore experience an anomalously high rate of close encounters with crystal atoms. There will be an associated high rate of multiple scattering leading to pronounced depth-dependent effects. Thus, one expects to see, as a function of angle between the beam direction and the planar direction, a peak in the yield of close-encounter processes and a dip in the transmitted beam intensity. There should be a similar inversion, as compared to the case for positive particles, in electron blocking. For axial electron channeling, there is the added possibility of a rotational bound-state motion about atomic rows (this is discussed further below).

Many of the expected channeling characteristics outlined above for classically behaving electrons have been observed in experiments with electrons having highly relativistic velocities ($E > 1$ MeV, say). However, as has been well established over the last 50 years and as was emphasized in Sec. 2.5, charged particles with masses as light as that of the electron exhibit strong diffraction effects in their interactions with crystals. These effects are especially evident at low velocities.

The relationship between electron diffraction and electron channeling has been examined by several authors (e.g., [Boo67,70; Ch68b,70a; DeW68b,c,70b; Fer70; Fuj72a; How66,68,70a,b; Hum70; Ler67; Li70; New71; Ni72a,b,c,d; Sp70; Whe70a,b] see also Sec. 2.5). At electron energies below about 100 keV, diffraction effects dominate. For thin target crystals the kinematical theory of electron diffraction (see, e.g. [Gev70] for a review) predicts the behavior of the scattered beams. For thicker targets where absorption effects are significant, the dynamical theory based on a Bloch-wave description must be employed (see, e.g. [Whe70a,b] for reviews). When the incident electron velocity is low, usually only two Bloch waves are excited with appreciable intensity. One of these waves has nodes at the atomic sites in the crystal and is thus anomalously transmitted; the other has antinodes at the atoms and is anomalously absorbed. The intensity with which the Bloch waves are excited depends on the match to the incident wave at the crystal surface and thus depends on factors such as the crystal orientation and the incident beam energy. For electrons of 100 keV or less, the best transmission through thick crystals usually occurs at or slightly above the Bragg angle. For electrons and positrons the Bragg angle is given, in degrees, by

$$\theta_B \approx 0.355\,(E^2 + 1.022E)^{-1/2} d_p^{-1}, \qquad (5.1)$$

where the incident energy E is given in MeV and d_p, the distance between equivalent planes, is given in Ångstroms.

Bloch waves with large intensities at the atomic sites can be expected to give rise to anomalously high yields in electron backscattering and in x-ray production. Such effects are indeed observed, the first evidence having been found by Duncumb [Dun62] who used 25-keV electrons to bombard 200-Å-thick gold crystals (see also, e.g., [Bell65; Hal66; Gra68; Kor70]). A related effect is the appearance of bands of contrast superimposed on the normal topographical image obtained in scanning electron micrographs of bulk monocrystalline samples at low magnification [Coa67]. An example is shown in Fig. 91. The width of the bands corresponds to twice the Bragg angle for (110) planar reflections. The intensity distribution in the bands can be explained (e.g., [Boo67,70]) in terms of anomalous absorption and transmission of Bloch waves on the two sides of the Bragg angle; there is a superficial similarity between the star patterns in images of the type shown in Fig. 91 and those seen in heavy positive particle channeling, e.g., Fig. 4. Effects of similar origin are seen in the bend-contour images obtained in transmission electron microscopy. Because of the associated anomalous transmission and absorption, these patterns have come to be known as electron channeling patterns. Their geometrical interpretation has been discussed by Boswarva and Pirouz [Bos72]. Although the patterns look rather like Kikuchi bands their physical origin is quite different (see, e.g., [Wo69]). As the incident electron energy is raised, several Bloch waves can be excited. For 1-MeV electrons it may then happen that, for low-index planes, the best transmission occurs for a high-order Bloch wave excited when the beam is incident parallel to the plane (e.g., [Hum70]).

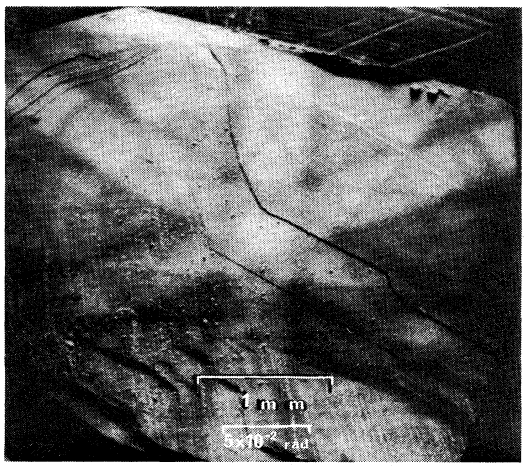

FIG. 91. Low magnification electron scanning micrograph of a thick GaAs crystal [Coa67]. The incident 20-keV electron beam was scanned about the ⟨111⟩ crystal axis. (Reproduced by permission of the Director, RRE, copyright Controller H.B.M.S.O.).

Effects such as those discussed in the preceding paragraph in which one or two particular Bloch waves are anomalously absorbed or transmitted are frequently referred to as Bloch-wave channeling effects. They are of great importance in high-voltage electron microscopy with thick specimens. They are very definitely diffraction effects and generally do not exhibit any of the behavior (such as that described at the beginning of this section) expected of classically channeled particles. Precise comparisons between theory and experiment for low-velocity Bloch-wave channeling are frequently precluded because of difficulties in taking into account multiple scattering effects. At higher electron energies, these problems become less severe. Furthermore, as many Bloch waves become excited the channeling behavior becomes more nearly classical. At the same time, computational difficulties with the many-beam diffraction theory tend to restrict the regions where comparisons with the classical

theory can be made. For a recent review of the multibeam dynamical theory of electron diffraction, the reader is referred to an article by Howie [How70b].

In Sec. 2.5 the criteria governing the applicability of classical and diffraction descriptions of channeling were discussed. It was pointed out there that a necessary condition for a classical model to be valid is that the number of quantum states, n_P (planar case) or n_R (axial case), available to the channeled particles, be large.

The number of states can be estimated by determining semiclassically the total phase-space available to the channeled particles and then dividing by the appropriate power of Planck's constant. That is,

$$n_P = (2\pi\hbar)^{-1} \int p(z)\, dz, \tag{5.2}$$

and

$$n_R = (2\pi\hbar)^{-2} \int [p(\rho)]^2 2\pi\rho\, d\rho, \tag{5.3}$$

where the momentum p is derived classically from the appropriate planar or axial continuum potential. In the planar case it may suffice for the purposes of an estimate of n_P to assume that the interplanar potentials are parabolic in shape. If one does this for positrons and takes as the maximum height of the potential well the value $V_{PS}(0)$ given by Eqs. (2.21) and (2.26), the result is

$$n_P^+ = (0.3\gamma Z_2^{2/3} N d_p^3)^{1/2}, \tag{5.4}$$

where γ is the ratio of the relativistic electron (positron) mass to its rest mass, Z_2 is the atomic number of the target atoms, and N is the number of atoms per unit volume. Note that this is very similar to the estimate given in Sec. 2.5, viz., $n_P^+ = \psi_c/\theta_B$, where ψ_c is the planar critical angle and θ_B is the Bragg angle. If one sets $\psi_c = \psi_a$, given by Eq. (2.23), then Eq. (5.4) results except that the numerical constant is 1.1 instead of 0.3. In terms of the incident positron energy E (given in MeV), Eq. (5.4) becomes

$$n_P^+ = [0.6(E + 0.511) Z_2^{2/3} N d_p^3]^{1/2}. \tag{5.5}$$

Assuming an inverted parabolic potential for the electron case and taking the depth of the potential well to be $V_{PS}(0)$, one obtains

$$n_P^- = (0.03\gamma Z_2^{2/3} N d_p^3)^{1/2} \tag{5.6}$$

$$= [0.06(E + 0.511) Z_2^{2/3} N d_p^3]^{1/2}, \tag{5.7}$$

where E is given in MeV. That is, there are about a factor of 3 fewer quantum states available for planar channeled electrons than for positrons.

For axially channeled positrons a reasonable estimate of the number of states is given by

$$n_R^+ \doteq (2\pi\hbar)^{-2} (p\psi_1)^2 (Nd)^{-1}, \tag{5.8}$$

where p is the momentum of the incident beam, ψ_1 is defined in Eq. (2.12), and d is the interatomic spacing along the rows. (Strictly speaking, n_R^+ can only have a well-defined meaning in connection with proper-channeled positrons. However, the expression given in Eq. (5.8) may still serve as a useful parameter in estimating the extent to which normal positron channeling, in which particles are free to wander between rows, may be treated classically.) This then gives

$$n_R^+ = \gamma Z_2 (\pi N d^2 a_0)^{-1} \tag{5.9}$$

$$= 0.62(E + 0.511) Z_2 (N d^2 a_0)^{-1}, \tag{5.10}$$

where E is in MeV and a_0 is the Bohr radius (0.529 Å). It was suggested in Sec. 2.5 that an estimate for the number of states in the axial case can be found from the relation $n_R \approx n_P^2$, where n_P is the number of states in the most open plane intersecting in the axis. A comparison of Eqs. (5.4) and (5.9) lends support to this. Since the estimates, Eqs. (5.4) and (5.6), for n_P^+ and n_P^- differ by a factor of π, we shall take as an estimate of the number of quantum states available to axially channeled electrons,

$$n_R^- = n_R^+/\pi^2 \tag{5.11}$$

$$= \gamma Z_2 (\pi^3 N d^2 a_0)^{-1} \tag{5.12}$$

$$= 0.063(E + 0.511) Z_2 (N d^2 a_0)^{-1}, \tag{5.13}$$

where E is given in MeV. This estimate differs somewhat from that derived by Lindhard [Li70] using a Hartree potential. It is identical with an estimate obtained by Fujimoto *et al.* [Fuj72a] based on a different set of considerations.

An experimental investigation of the relationship between electron diffraction and classical electron channeling has been performed by Fujimoto *et al.* [Fuj72a]. Some of their transmission patterns recorded photographically for 1-MeV electrons incident on Cu are shown in Fig. 92. The authors classify the axial patterns in terms of two types; flower patterns (like chrysanthema) representative of classical channeling and geometrical patterns representative of the lines and bands typical of diffraction effects (see, e.g., [Tho70]). Data obtained for 0.5 and 1.0-MeV electrons incident on Si, Cu, and Au crystals indicate that the division between the two types of patterns occurs when the number of quantum states n_R^-, Eq. (5.12), is about three. Thus, the data shown in Fig. 92 for Cu indicate a classical channeling behavior for the ⟨110⟩ axis and a diffraction-like behavior for the ⟨111⟩ axis. The ⟨100⟩ and ⟨211⟩ axes exhibit an intermediate behavior. For Au crystals all of the axes studied showed a classical effect, as is to be expected because of the high values of the crystal potential. For Si, where the potential is weaker, only the ⟨110⟩ axis showed a classical pattern and even then, only at the highest of the three bombarding energies used, 0.1, 0.5, and 1.0 MeV. Comparing the data for thin and thick crystals (e.g., Fig. 92), one finds a contrast reversal. For example, the ⟨110⟩ axial peak in intensity shown in Fig. 92(a) becomes a deep minimum in the data for the thicker crystal, Fig. 92(b). This type of contrast reversal from excess to deficit Kikuchi bands is well known in electron diffraction measurements and is thought to be caused by Bloch-wave absorption effects. The classical explanation for the reversal is not so evident. The patterns expected on a classical model correspond to the flower patterns seen with the thicker crystals and, in fact, Fujimoto *et al.* find that the angular half-widths for the axial dips in these cases are always about 0.65 ψ_1, where ψ_1 is calculated from Eqs. (2.12) and (2.45).

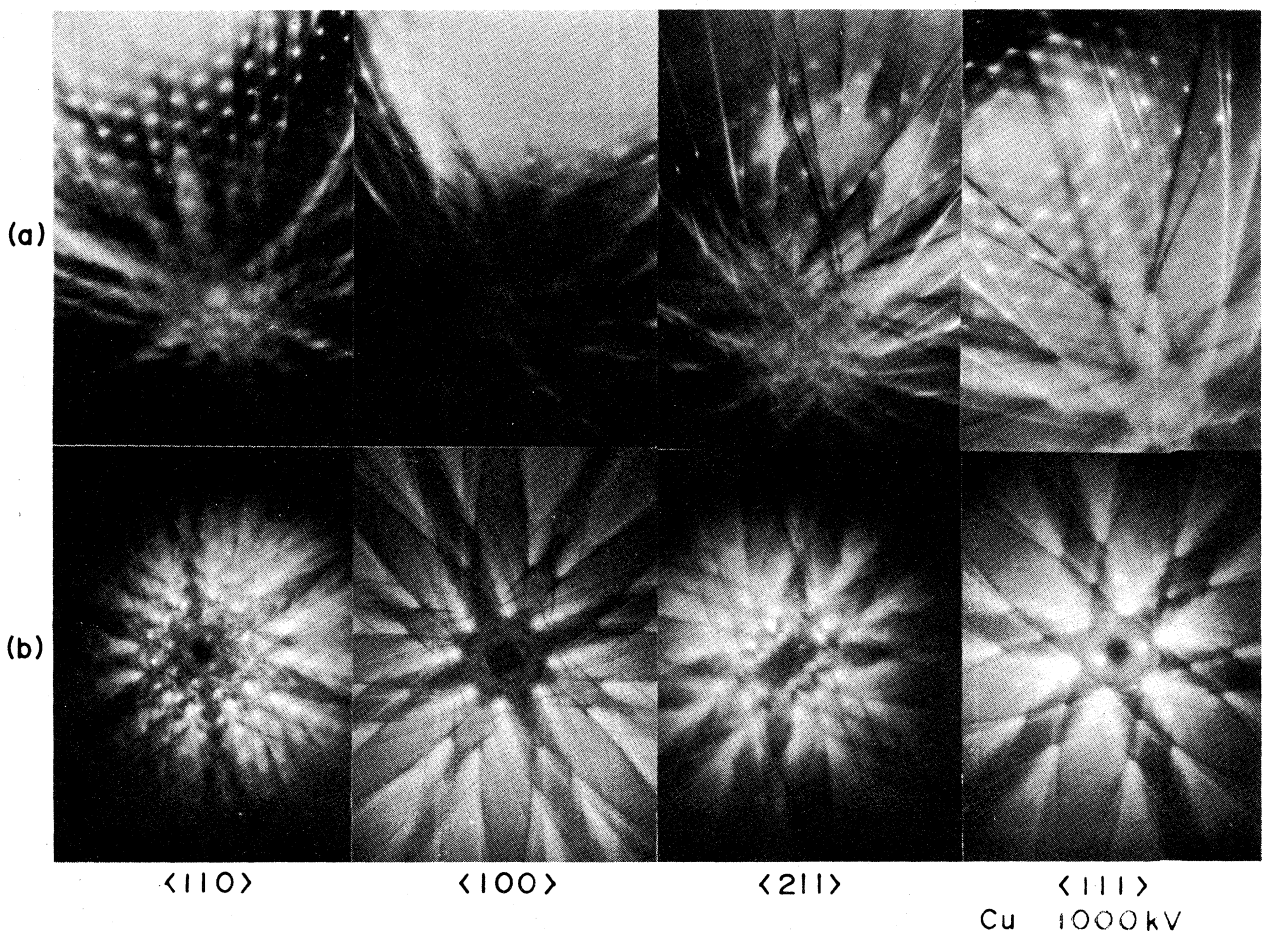

FIG. 92. Transmission patterns recorded for 1-MeV electrons passing through (a) thin (~1 μm) and (b) thick (~5 μm) Cu crystals [Fuj72a]. The data in (a) were recorded with the incident beam a few degrees off axis and in (b) the beam was on axis. Bright regions in the photographs correspond to regions of high electron intensity. The number of quantum states $n_{\bar{R}}$ excitable in the four axial cases are estimated to be approximately 9, 5, 3, and 2 for the ⟨110⟩, ⟨100⟩, ⟨211⟩, and ⟨111⟩ axes, respectively, Eq. (5.13).

It is possible that the central spot seen for thin crystals in cases like the ⟨110⟩ axis for Cu shown in Fig. 92(a) is a manifestation of an effect observed by Kreiner *et al.* [Kr70; Bell72; Kumm72] at higher electron energies. These authors have recorded the forward intensities of electrons transmitted through thin (~8 μm) MgO crystals as the ⟨100⟩ axis is rotated through the beam direction. At the incident energies (5–20 MeV) that were used, $n_{\bar{R}}$ is large. Furthermore, the experimental angular resolution contributed an uncertainty larger than θ_B for the (200) planes. Thus, a classical behavior is expected. Figure 93 shows some results for 20-MeV electrons. The data exhibit the dip expected classically and with a half-width not too different from ψ_1. But a striking feature of the data is the presence of a sharp peak in the center of the dip. Kreiner *et al.* attribute this peak to electrons that are trapped in a spiral motion about the atomic rows and thus have a high transmittivity. They point out that the particle motion in the plane normal to an isolated atomic row is governed by the equivalent one-dimensional potential

$$W(\rho, \mathfrak{L}) = V_R(\rho) + \mathfrak{L}^2/(\gamma m_e \rho^2), \tag{5.14}$$

where ρ is the distance from the row, $\mathfrak{L}$ is the angular momentum of the particle with respect to the row, V_R is the row continuum potential, and γm_e is the relativistic electron mass. The transverse energy of a particle is then given by

$$E_\perp = \tfrac{1}{2}\gamma m_e \dot{\rho}^2 + W(\rho, \mathfrak{L}). \tag{5.15}$$

The values of $E_\perp$ and $\mathfrak{L}$ are considered to be conserved and are determined by the entrance conditions for the particle at the crystal surface. For positive projectiles $E_\perp$ is always positive. However, for negative projectiles $V_R(\rho)$ is negative, and $E_\perp$ can assume positive and negative values. For small distances ρ the potential $W(\rho, \mathfrak{L})$ becomes positive (repulsive) because the ρ dependence of $V_R(\rho)$ is weaker than ρ^{-2}. This led Kreiner *et al.* to suggest that for a certain range of the angular momentum $\mathfrak{L}$ the potential $W(\rho, \mathfrak{L})$ is negative and has a minimum in the range $\rho > \rho_c$. Particles entering the crystal with angular momenta in this range and with negative transverse energies will be trapped in this potential well. That is, they will perform a spiral motion along the row. Projected onto the transverse plane, the motion will execute rosettes, i.e., bound orbits that precess (because of the deviation of the attractive force from a pure ρ^{-2} law). In this motion the particles do not approach closer than a

distance ρ_c to the row, and they therefore enjoy a much reduced scattering. Computer calculations by Kumm *et al.* [Kumm72] indicate that as much as 50% of the incident beam can be captured into this spiral motion. The calculations also show that the mean penetration depths of such particles can be several microns. For smaller values of $\mathfrak{L}$, the rosette motion at its perihelion approaches the row closer than ρ_c and is therefore strongly scattered. For larger values of $\mathfrak{L}$, the potential $W(\rho, \mathfrak{L})$ becomes always positive, and there is no bound state. An estimate of the maximum incidence angle $\psi_0(\max)$ for which bound motion is possible can be found by letting $E_\perp = 0$ and setting $\rho = \rho_c$. This then gives $\psi_0(\max) = \psi_1$ if Lindhard's continuum potential is used. The minima in the transmitted intensity do, in fact, occur at incidence angles of about ψ_1 (see Fig. 93). This theoretical description also predicts for the rosette motion a minimum incidence angle equal to $\psi_c(\rho_c/\rho_0)$, where $\rho_0 = (Nd\pi)^{-1}$. For the case shown in Fig. 93, this angle ($\psi_0 \sim 0.01°$) is so small that the angular resolution does not permit another minimum in the transmitted intensity to be observed near $\psi_0 = 0$; a central minimum has however recently been reported by Bobudaev *et al.* [Bob73] for 2-MeV electrons transmitted through 110 -μm-thick crystals of NaCl. Further evidence for effects like that shown in Fig. 93 has been found by Walker *et al.* [Walk70] in the small-angle scattering of 20-MeV electrons by Si crystals and by Vorobev *et al.* [Vor72a,b; Bob73] in both transmission and wide-angle scattering measurements with 2.26-MeV electrons incident on NaCl crystals. (See also the theoretical discussions of Nip *et al.* [Ni68,70,71a,b,72a,b,c,d] and of Schiebel *et al.* [Schie72].)

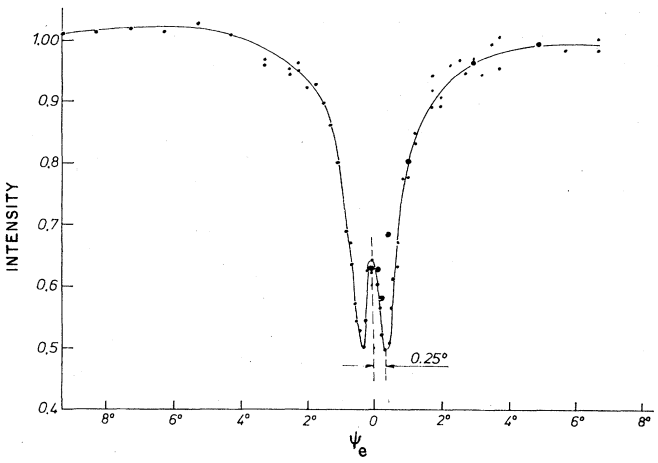

FIG. 93. Intensity of electrons transmitted in the beam direction as a function of the angle ψ_0 between the ⟨100⟩ axial direction of an 8-μm-thick MgO crystal and the incident beam direction [Kumm72]. The bombarding electron energy was 20 MeV, and the beam divergence was ± 0.05°. The small dots are data obtained with a scintillation detector and the large ones are obtained from photographs of the transmitted patterns. The value of ψ_1 is 0.21°.

In 1965 Astner *et al.* [Ast65] reported results on the angular dependence of *K*- and *L*-conversion electrons (45 and 76 keV, respectively) emitted from ^{133}Xe implanted in a Ta crystal, analogous to the experiments of Domeij and Björkquist [Do65a,b] on α-particle emission (see Fig. 61). The data showed pronounced peaks in major crystalline directions. This was the first evidence for a classical behavior in electron channeling, and it demonstrated the expected inversion as compared with the data for positive particles. This was followed by the work of Uggerhøj [Ug66] and Uggerhøj and Anderson [Ug68] who performed rather similar measurements on a Cu crystal doped with ^{64}Cu. Since ^{64}Cu is both a β^- and a β^+ emitter, it was possible to separate these magnetically and to record data simultaneously for both electrons and positrons. Some results are shown in Fig. 94. If one corrects for the β^- and β^+ energy differences, the peaks for β^- are about a factor of two narrower than the corresponding dips for β^+. Another direct comparison of measurements with electrons and positrons has been made by Ok [Ok70]. Transmission measurements were performed with 148-keV β^- and 275-keV β^+ particles incident on thin crystals of Si in the ⟨110⟩ axial direction. The data yielded angular half-widths $\psi_{1/2} \approx 0.53\psi_1$ for both β^- and β^+ particles. Similar results were obtained for anthracene crystals.

Several authors (e.g., [Gra66,68; Ug68,70; Kor70; Kr70; Ok70; Walk70; Kumm72; Nis72; Vor72a,b; Anders73] have studied electron channeling by means of transmission and Rutherford scattering measurements. Figures 95, 96, and 97 illustrate some of the data obtained. It is found that where a classical model is expected to be valid (e.g., $n_R^- \text{ or } n_P^- \gg 1$) , the data do in fact follows the classical behavior; for example, in the axial case, $\psi_{1/2}$ is found to be proportional to ψ_1 with a constant of proportionality of about 0.6. Conversely, when the diffraction picture is expected to be valid, the data do indeed exhibit wave effects; for example, in the planar case, the angular width is found to be proportional

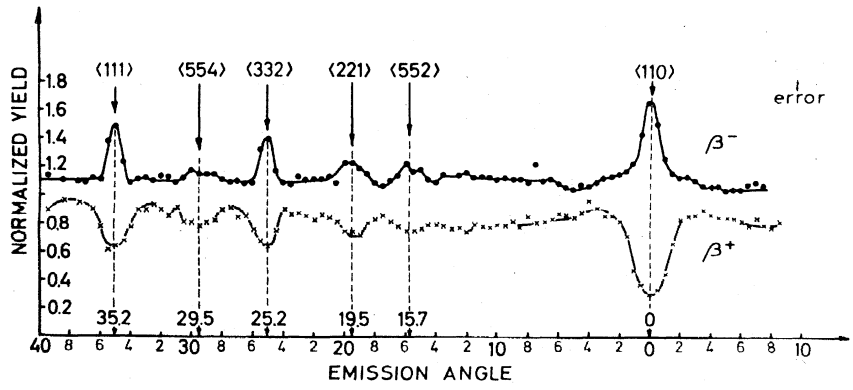

FIG. 94. Angular dependence of the detected yield of β^- (150–250 keV) and β^+ (200–300 keV) particles emitted from ^{64}Cu embedded in a Cu crystal [Ug68]. The tilting plane coincides with the (110) crystal plane.

to d_p^{-1}, rather than to $d_p^{-1/2}$ as in the classical theory, and the data are well reproduced by multibeam dynamical diffraction calculations. Depth-dependent effects have not yet been investigated very much although obviously they play a prominent role in electron channeling (see Figs. 92, 96, and 97). Thus, for example, data obtained in the same fashion as that shown in Fig. 97, but with a thinner crystal (~0.3 μm) exhibit only a single dip instead of the sharp twin peaks, due to Bloch-wave transmission, seen for the 6-μm-thick crystal. Andersen *et al.* [Anders73] have determined that the channeling peaks measured for Rutherford scattering (as the incidence angle is varied) and for electron emission (as the exit angle is varied) are closely the same, indicating that the rule of reversibility (Sec. 2.2) holds for electrons (see also [Pog68]).

Other things being equal, the number of quantum states available for channeled positrons is higher than that for electrons; see Eqs. (5.4) through (5.13). Thus positrons can be expected to behave somewhat more classically than electrons. The first channeling measurements to be made with an external positron beam were those of Behnisch *et al.* [Behn69]. They used a collimated beam from a ^{58}Co source to study the orientation dependence of the rate of production of characteristic K x rays from a RbBr crystal. The results (Fig. 98) show a very pronounced channeling dip with a half-width approximately equal to ψ_1. The authors postulated that the data indicate an anomalously low rate of dechanneling for positrons, about a factor of 10 lower than for protons of the same energy. Vorobev and collaborators [Vor71; Di70; Voro72; Kud73] have also used collimated beams from sources to study the effect of channeling, and also of temperature, on the backscattering and annihilation rates for positrons incident on various alkali-halide crystals. Andersen *et al.* [An71b] and Pedersen *et al.* [Ped72] have studied the orientation dependence of Rutherford scattering from thin Au and Si crystals using a beam obtained by accelerating positrons emitted from a ^{58}Co source in the terminal of a 1-MeV Van de Graaff. This technique has the advantages, as compared to a collimated source, of low background, high intensity, and a small relative energy spread. Some of their data are shown in Figs 99, 100, and 101. The number of quantum states for 1-MeV positrons channeled along the ⟨110⟩ axial direction in Au is large ($n_R^+ \approx 290$). It is therefore gratifying to see the close correspondence between the positron and proton data shown in Fig. 99; the differences in the shoulder regions are thought to be due to the influence of detector acceptance angles. For the positron data shown in Figs. 100 and 101, the values of n_P^+, Eq. (5.4), are 1.5 and 0.14, respectively. Thus while the data for the (110) planes might be expected to bear some resemblance to the classical curve, a classical description should be totally inappropriate for the (115) case. These expectations are fully borne out by the measurements; the classically calculated dip for the (110) case is similar to the diffraction curve shown, but without the "wiggles" In addition, Pedersen *et al.* studied the axial dechanneling rates for positrons in Si and found them to be close to the rates for protons of about the same energy.

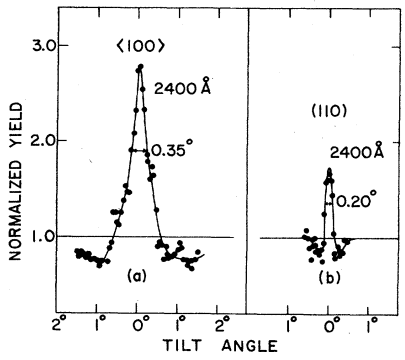

FIG. 95. Normalized Rutherford-scattering yield of 1.5-MeV electrons incident on a 2400-Å-thick Si crystal [Anders73]. The range of scattering angles covered extended from 5° to 10°. Data are shown as a function of the angle between the beam direction and the ⟨100⟩ axial and (100) planar directions.

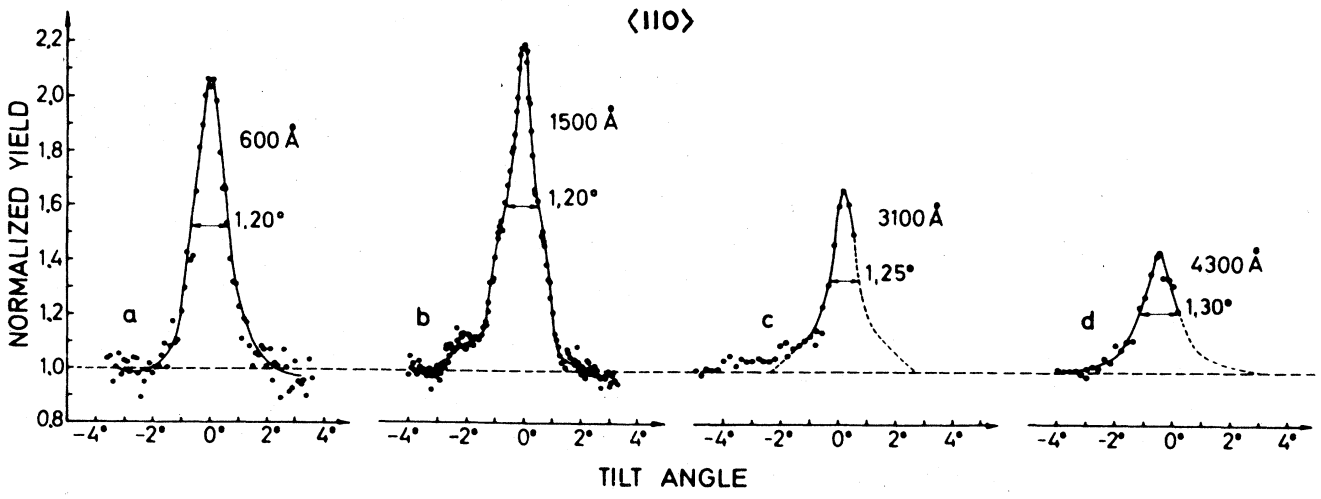

FIG. 96. Target-thickness dependence of the normalized Rutherford-scattering yield for 1-MeV electrons incident on Au crystals [Ug70]. The data are shown as a function of the angle between the beam direction and the ⟨110⟩ crystal axis. The scattering angles covered extended from 15° to 25°.

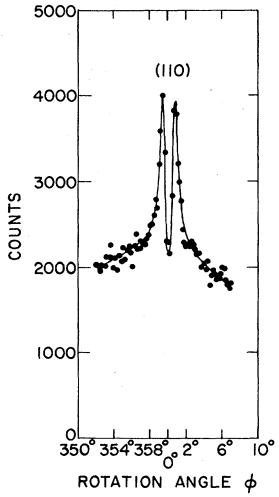

FIG. 97. Number of electrons transmitted in the forward direction as a function of the rotation angle ϕ about the $\langle 110 \rangle$ axis of a 6-μm-thick Si crystal [Anders73]. The incident beam energy was 1.5 MeV. The axis was tilted off the beam direction a few degrees so that the rotation brought the (110) plane through the beam direction. In terms of the angle between the beam direction and the (110) plane, the angular separation of the two peaks in the data is about $2\theta_B$, where $\theta_B = 0.095°$.

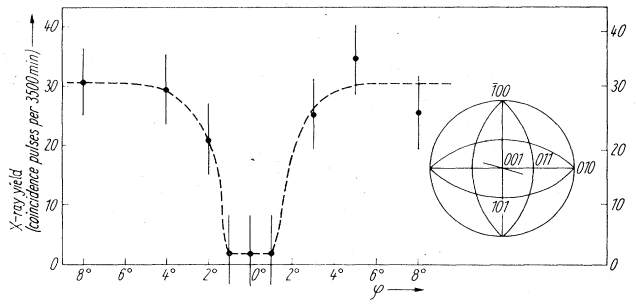

FIG. 98. *K* x-ray yield as a function of the angle between the direction of incidence of a 220-keV positron beam and the $\langle 100 \rangle$ axis of a RbBr crystal [Behn69]. The inserted stereogram shows the line of measured directions.

Walker *et al.* [Walk70] have made channeling measurements on the scattering in Si crystals of positrons and electrons in the energy range 16–28 MeV. The axial angular scans exhibit strong (classical) minima for positrons, while for electrons there is a broad peak with a central depression suggestive of the spiral motion referred to earlier in this section. These authors also measured the channeling dependence of the bremstrahlung intensity in the forward direction. This is shown in Fig. 102. Walker *et al.* suggest that the low-energy part of the bremsstrahlung spectrum, contributing to the data in Fig. 102(a), but not 102(b), has a component caused by coherent bremsstrahlung effects. This may cause the broad humps for both β^+ and β^- particles in Fig. 102(a). Such effects would occur in addition to channeling effects. The mechanism for coherent bremsstrahlung production does not necessitate the particles being channeled. Morokhovskii *et al.* [Mor72] have made similar observations (Fig. 103) at the very much higher energy of 1 GeV. (For discussions on the orientation dependence of bremsstrahlung produced in crystals, see, for example, [Bely71; Ni71a; Kal72] and references contained therein.)

Following the first measurements by Duncumb [Dun62], the orientation dependence of production rates for characteristic x rays arising from crystals bombarded by electrons has been studied by several groups (e.g.,

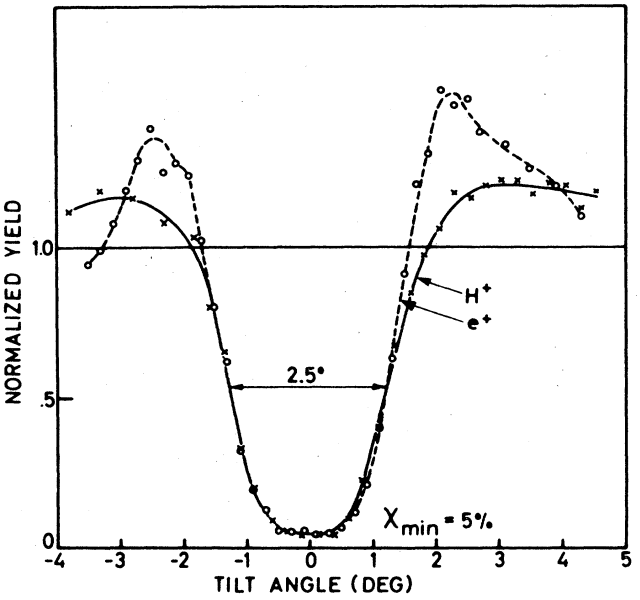

FIG. 99. Comparison of dips in Rutherford scattering measured for the $\langle 110 \rangle$ axial channeling in Au of 1-MeV positrons and 0.670-MeV protons; i.e., positrons and protons with the same value of kE, Eq. (2.45), [An71b]. The proton data were obtained by appropriate scaling of data measured for 1-MeV protons.

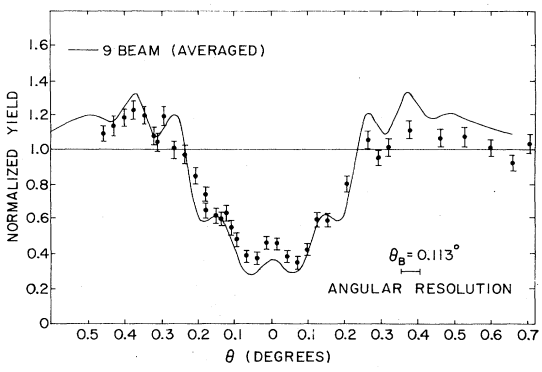

FIG. 100. Channeling dip measured for Rutherford scattering of 1.2-MeV positrons incident along the (110) planes of a Si crystal (~1 μm thick) [Ped72]. The solid line represents the result of a 9-beam dynamical diffraction calculation into which the experimental energy spread and angular resolution have been folded

[Bell65; Gra66; Hal66; Bro69,72; Kor70]). All of these measurements, except for those of Bronder and Jakschik [Bro69, 72], were performed at incident energies of less than 100 keV and consequently are dominated by diffraction effects. The data of Bronder and Jakschik (an example is shown in Fig. 104) were recorded for electrons incident at 350 keV and exhibit somewhat more classical features (cf. Fig. 98).

Makin [Mak70] has examined the orientation dependence of the damage rate in Cu crystals bombarded with 600-keV electrons and finds a marked decrease in channeling, i.e., anomalous transmission, directions. The influence of lattice vacancies on the channeling of 25-keV electrons in NaCl has been studied by Choudhury *et al.*

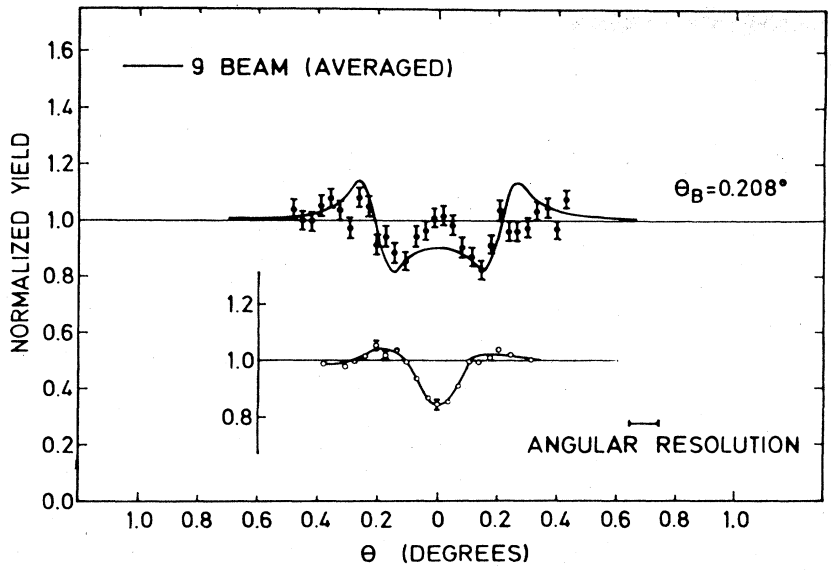

FIG. 101 Comparison of (115) planar dips obtained for Rutherford scattering of 1.2-MeV positrons (solid circles) and 0.78-MeV protons (open circles) from a thin (~1 μm) Si crystal [Ped72]. Positrons and protons at these energies have the same value of kE, Eq. (2.45). The solid curve through the positron data is the result of a 9-beam calculation with the experimental energy spread and angular resolution folded in. θ_B is the (115) Bragg angle.

[Cho71]. The measurements were made by determining the depths of F-center coloration along various axial directions. The results indicate that negative-ion vacancies induced by heat treatment cause a reduction in the range of channeled electrons.

6. APPLICATIONS

A variety of practical uses have been found for channeling effects. By far the most widespread application is presently in the area of semiconductor physics, where channeling techniques have become an essential tool in, for example, determining the lattice location of dopant atoms, and studying defects. In this section, we briefly outline some applications, the intent being to illustrate the diversity of the various fields in which channeling has found a use, rather than to provide a complete catalogue of all known applications. In particular, it is not feasible to give here more than a cursory review of the very extensive literature concerning applications in semiconductor physics. Fortunately there do exist already some comprehensive reviews of this topic (see, e.g., [De69a; May70,72; Dav72b] and references contained therein) and also several conference proceedings to which the reader may refer [e.g., *Proceedings of the Second International Conference on Ion Implantation in Semiconductors*,

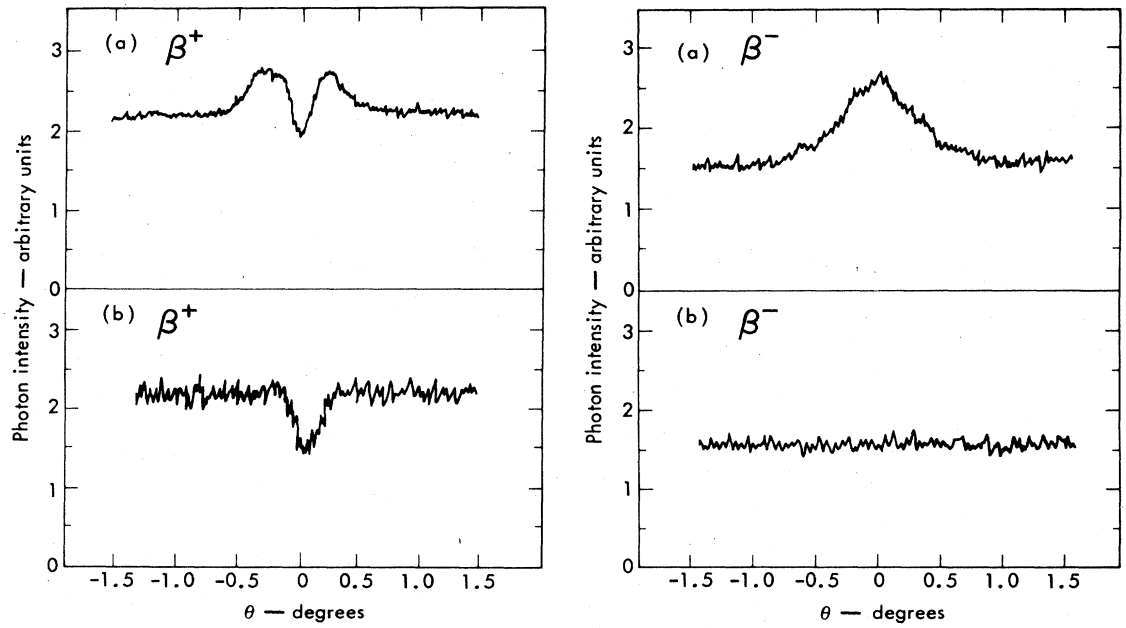

FIG. 102. Effect of channeling on the forward (± 0.1°) bremsstrahlung intensity produced by 28-MeV positrons (left-hand set of data) and electrons (right-hand set of data) incident on a 53-μm-thick Si crystal [Walk70]. θ is the angle between the ⟨110⟩ axis and the beam direction. Curves (a) are for the unfiltered bremsstrahlung; curves (b) are measured with 1/2 in. lead absorber between target crystal and detector. The beam divergence was approximately 0.2°.

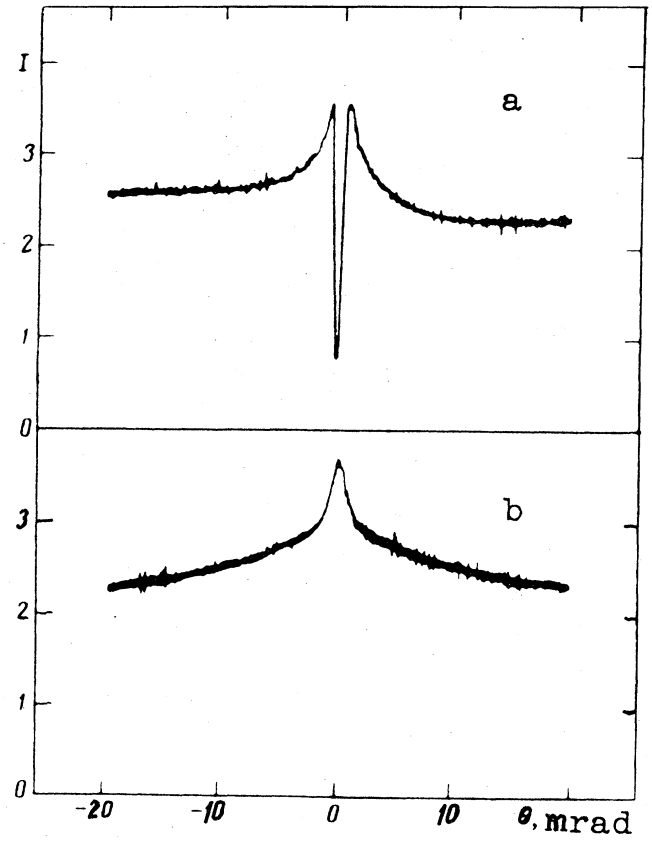

FIG. 103. Bremsstrahlung energy flux as a function of the angle between the direction of 1-GeV beams of (a) positrons and (b) electrons and the ⟨110⟩ axial direction of a Si crystal 0.64 mm thick [Moro72]. The beam divergence was approximately 0.2 mrad. The measured value of $\psi_{1/2}$ is ~0.3 mrad ($\psi_1 \approx$ 0.5mrad).

edited by I. Ruge and J. Graul (Springer, Berlin, 1971) and *Hyperfine Interactions in Excited Nuclei*, edited by G. Goldring and R. Kalish (Gordon and Breach, New York, 1971)] .

6.1. Ion implantation

In the last few years there have been rapid advances in the technology and understanding of electronic devices prepared by ion implantation in semiconductors [May70]. Ion implantation offers the advantages, as compared, for example, with thermal diffusion, of permitting the doping of semiconductors with a large variety of elements and to concentrations exceeding the solubility limit. The depth and distribution of dopant atoms can be flexibly controlled by adjusting the bombarding energy, incident beam direction, temperature, etc. Devices can be fabricated with a high packing density by "writing" in a very precise fashion, in depth as well as across the surface, with tightly collimated ion beams. The chief disadvantage associated with the technique is the radiation damage accompanying the implantation. This damage can easily produce a high enough concentration of electrically active defects to completely mask the effects due to the implanted ions. Thus some annealing treatment is almost invariably required in order to reduce the defect concentration to an acceptable level.

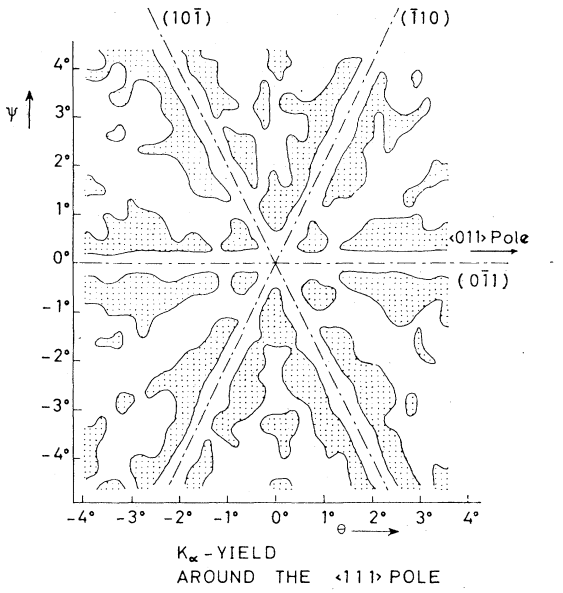

FIG. 104. Contour map of the distribution of normalized intensity for K_α x rays detected around the ⟨111⟩ axis of a Ge crystal bombarded with 350-keV electrons [Bro72]. The angles θ and ψ represent deviations of the crystal axis from the beam directions. The shaded areas depict intensities below normal, and in the unshaded areas the intensity is above normal. The Bragg angle for the (220) planes is $\theta_B \approx 0.26°$. For the ⟨111⟩ axis, $n_{\bar{R}} = 3.1$ and for the (110) planes, $n_{\bar{P}} = 0.43$ [See Eqs. (5.12) and (5.16)].

Channeling effects find their use much more in the characterization of implanted materials (see Secs. 6.2 and 6.3) than in their actual preparation. However, by channeling the beam during implantation, the final depth reached by the ions can be increased for a given incident energy. Furthermore, the radiation damage in the region traversed by the beam is very much reduced for channeling, as compared with random incidence directions. Figures 67 and 68 illustrate the range distributions observed for various implantation conditions. For a well-aligned beam incident along a major axial direction in a crystal at low temperature, i.e., good channeling conditions, the range distribution frequently exhibits two peaks, one due to those ions initially dechanneled and one due to ions remaining channeled for a large part of their path in the crystal. The range distribution obtained is very sensitive to dechanneling effects; Fig. 68 illustrates the strong influence of temperature on the dechanneling rate. Since these effects are both large and to some degree unpredictable (e.g., as when dechanneling is caused by defects introduced during implantation) they represent one of the most significant factors limiting the usefulness of channeling during ion implantation.

For further discussion of the channeling process in ion implantation, the reader is referred to the following, by no means complete, list of references: [Gi68b; May68, 70,71,72; De69a,b; Ne69d; Goo70; Jo70; Ch71a,b; Ei71b; Wh71; Dav72b; Pav72] (see also [Sea73] for a recent selective bibliography on ion implantation).

6.2. Location of dopant and impurity atoms

Following the discovery of the channeling effect, it was quickly realized that it represented a unique new tool for determining the lattice location of dopant and impurity

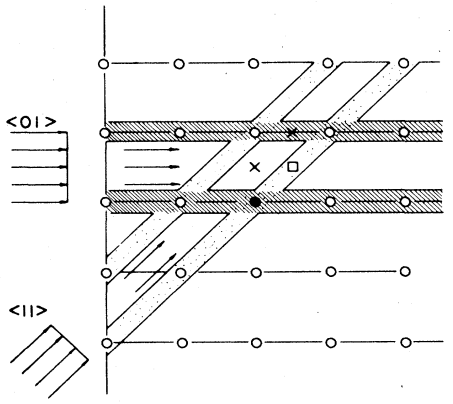

	DIRECTIONAL EFFECT ?		
	●	×	□
<01>	YES	50%	NO
<11>	YES	NO	YES

FIG. 105. Two-dimensional model illustrating how the channeling effect can be used to locate foreign atoms in a crystal [Dav72b]. As shown by the table, three typical sites for a foreign atom indicated by the crosses, solid circle, and square can be uniquely distinguished by studying the channeling behavior firstly along the ⟨01⟩ and then along the ⟨11⟩ axial direction. The atoms of the host crystal are indicated by the open circles. The 50% entry in the table is intended to point out that, when located in the lattice positions shown by the crosses, only half of the impurity atoms are shadowed in the ⟨01⟩ direction. The comments in the table are over-simplified; for example, flux-peaking effects are ignored.

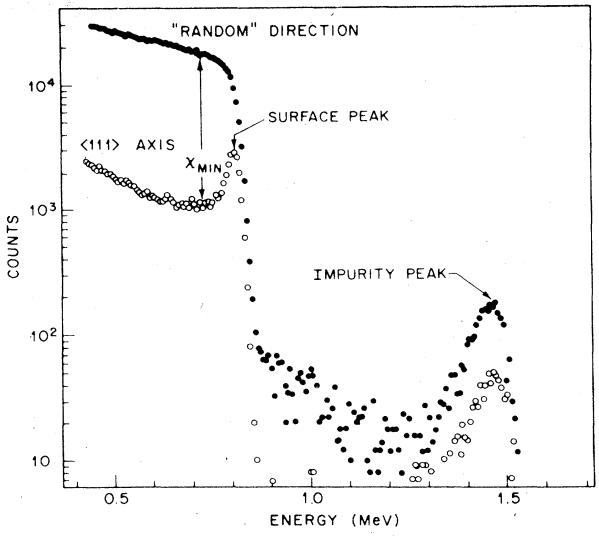

FIG. 106. Energy spectra of backscattered ^{12}C ions incident at 2.0 MeV in channeling (open circles) and nonchanneling (closed circles) directions on an Fe single crystal implanted with 2×10^{14} Pb atoms/cm^2 at 100 keV [Fel71].

atoms in crystals. The principle of the method (illustrated in Fig. 105) is that interstitial impurity atoms experience a particle flux that depends, often very strongly, on the channeling orientation, whereas substitutional impurity atoms experience approximately the same flux as that experienced by the atoms of the host crystal for all crystal orientations. The first measurements implementing these ideas were the blocking experiments (alpha-particle emission from ^{222}Rn implanted in W) of Domeij and Björkquist [Do65a,b, 66]. These were followed by measurements using external beams. For example, Bøgh [Bø67c] studied the location of ^{169}Tm implanted into Si, and Matzke and Davies [Mat67] studied the backscattering of 3-MeV protons from KCl in which 40-keV ^{132}Xe ions had previously been implanted. Since then, the technique has been extensively developed and is now in widespread use as one of the standard tools of solid-state physics research. The method can make use of any close-encounter process that shows a strong channeling effect. The choice is usually determined by the relative masses of the host and impurity atoms. Thus, for impurity atoms much heavier than the host atoms, Rutherford backscattering is normally the most attractive possibility since the energy differences due to kinematical effects permit one to distinguish between scattering from host and impurity atoms; sometimes a heavy-ion beam is necessary in order to make this distinction. An example is shown in Fig. 106. If the impurity atoms have a mass lower than that of the host atoms, nuclear reactions, especially those with a high positive Q value, such as the ^{11}B (p,α) reaction, for example, offer a means of distinguishing some of the more common dopants (see, e.g., [Gi68b; Fis69; Nort 70a; Fl70; An72b]). Characteristic x rays may also be used (e.g., [Cai68, 71]) although the depth resolution obtained is usually poor. If the host crystal can be implanted with radioisotopes that emit charged particles, this offers another possibility. Several authors have used this technique to study alpha emission (e.g., [Do65a,b, 66; Mat67,69]) and electron and positron emission (e.g., [Tom68; Ug69; How70a]).

In order to be able to locate impurity atoms accurately, it is essential to know the distribution of the flux of beam particles inside the crystal. As has been discussed in previous sections, this flux distribution depends sensitively on such factors as depth within the crystal, beam incidence angle, beam divergence, shape of the channeling continuum potential, the presence of crystal defects, and surface layers. (see Secs. 2.4e, 2.4f, and 4.2a). If all of these various factors are taken into account to the fullest extent possible and if detailed angular scans are made for both the host and the impurity atoms, then present channeling techniques are capable of determining the lattice location of impurity atoms to an accuracy typically of one or two tenths of an angstrom. One of the most significant factors limiting measurements of this type is the production of defects by the incident beam used in the channeling analysis. For low concentrations of impurity atoms, large incident beam fluxes are necessary to obtain adequate counting statistics. The attendant high concentrations of beam-induced defects modify both the flux distribution and the dechanneling rate in a manner difficult to assess. Another important factor limiting the sensitivity of the method is the rate-dependant background due to pulse pile-up in the detector. Usually antipile-up circuits in the associated electronics are essential. The importance of measuring the complete angular dependence for a given channeling direction is of particular significance; this is demonstrated by the calculations shown in Fig. 36. The shape of the angular dip or peak, or sometimes both, measured for the impurity atoms can often be very narrow or exhibit a complicated shape for

certain interstitial positions or for certain mixtures of positions. The first experimental evidence for the large and sharply peaked (in angle) yields associated with flux peaking effects was observed by Iferov *et al.* [If67] for interstitially dissolved deuterium in Nb. An example from some more recent work is shown in Fig. 107.

In the absence of experimental limitations, such as radiation damage and pulse pile-up, the sensitivity of the channeling technique is limited by the value of χ_{min} for the host atoms. For major axial channeling directions this is on the order of 1%. The sensitivity can be improved by using double alignment techniques (see Sec. 4.2b). This then permits lattice-location measurements for impurity atom concentrations about 10^{-4} to 10^{-3} of the host atom concentration. Figure 108 shows a comparison of angular scans obtained with single and double alignment. The reader is referred to the following work on lattice location: [Dav67b; Bø69; Erik69b; Fel69,70b,71,72a; Fis69; Fl69, 70; Ap70,71; Bj70; Do70; May70,72; Al71,72; An71a; Ei71c,72b; Fuj71c,72; Gy71; Si71; Dav72b; Ed72b; Iu72; Rim72b; Kau73; Poa73]. See also *Hyperfine Interactions in Excited Nuclei*, edited by G. Goldring and R. Kalish (Gordon and Breach, New York, 1971).

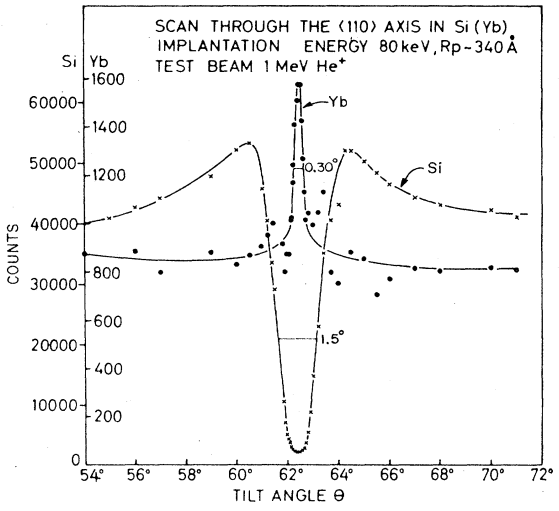

FIG. 107. Example showing how flux peaking influences the backscattering yield of 1-MeV alpha particles from Yb atoms (solid dots) implanted in Si (crosses) [Ei72b]. The data shown are for a depth 0–500 Å. The abscissa represents the angle between the beam direction and the ⟨110⟩ axis of the Si crystal. 3×10^{14} Yb ions/cm^2 had previously been implanted at 80 keV and at a temperature of 450°C.

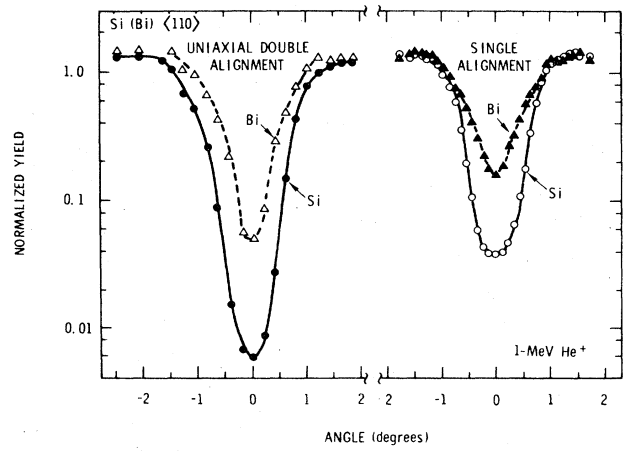

FIG. 108. Comparison of angular scans obtained for Rutherford scattering in single alignment and uniaxial double alignment for 1-MeV He^+ ions incident along the ⟨110⟩ axial direction of a Si crystal implanted with Bi atoms [Pi72a].

6.3. Studies of lattice disorder

A natural extension of the applications discussed in the previous section is to the case where the impurity atoms are identical with the atoms of the host crystal. That is, the channeling effect may be used to study lattice disorder and imperfections in crystals. It has been pointed out earlier (e.g., Secs. 2.4d, 2.4e, 2.4f, and 4.2) that several channeling characteristics, such as dechanneling rates, minimum yields, and flux-peaking effects, depend sensitively upon the degree of crystallinity of the sample. It is not surprising, therefore, that channeling techniques are currently in widespread use in studies of lattice disorder, especially in connection with ion-implantation applications. The reader is referred to the following recent reviews of the rather extensive published literature on the subject: [Bø69; Ne69b; May70,72; Dav72b]. See also *Proceedings of the Second International Conference on Ion Implantation in Semiconductors*, edited by I. Ruge and J. Graul (Springer, Berlin, 1971).

Figure 109 shows the effect of various doses of im-

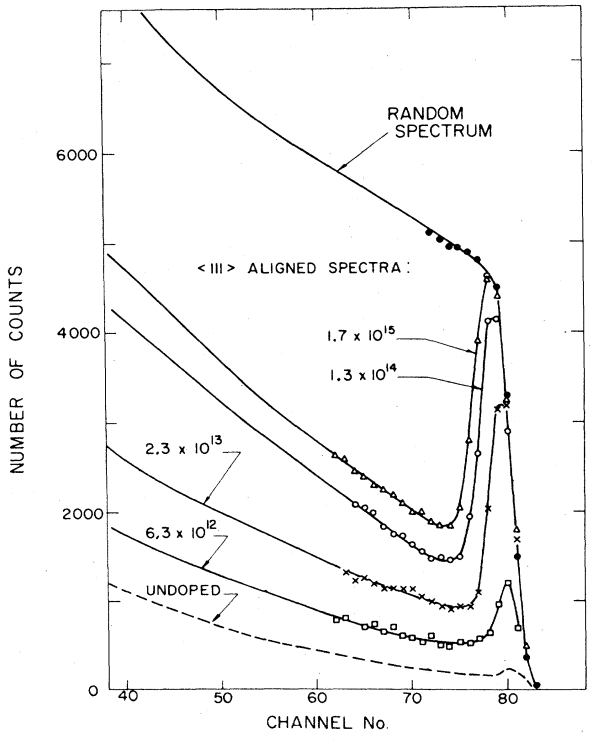

FIG. 109. Aligned (⟨111⟩ axis) and random backscattering spectra for 1-MeV ^{4}He ions incident on Ge crystals implanted at room temperature with various doses of 40-keV In ions [May68]. To simplify the figure, data points have been omitted except in the more important regions of the spectra. The high-energy part of the spectra, corresponding to scattering off the In atoms, is not shown.

planted In ions upon the backscattering spectra obtained for axially aligned Ge crystals. The damaged region near the crystal surface causes a higher surface peak and also results in a higher dechanneled fraction of the beam entering the deeper regions of the crystal. There is also a higher dechanneling rate because in the damaged region the transverse energy distribution is modified towards higher values. The data shown in Fig. 109 were obtained with a surface-barrier detector. The resolution, ~10 – 15 keV, is not sufficient to separate scattering in the region of high damage near the end of the range of the In ions from the normal surface peak. Bøgh [Bø68a,b,71] has overcome this limitation by using as a detector a magnetic spectrograph with resolution about a factor of ten better than that obtainable with solid-state detectors. Figure 110 shows some of his data. The magnetic spectrograph is particularly useful for examining small depths, e.g., damaged regions caused by ions implanted at low energies, where energy straggling does not spoil the depth resolution attainable.

Methods for quantitative analysis of data of the type shown in Figs. 109 and 110 have been given by several authors (e.g., [Bø68a,b,71; Wes69,70; Ei70; Fel70a; Har70; Zi72b]). Most analyses are based upon that of Bøgh [Bø68b]. In this approach, the effect of displaced atoms is considered to increase the backscattering yield in two ways. Firstly, they can cause channeled particles to be deflected out of the channel and thereafter to contribute to the yield in the same way as randomly travelling particles. Secondly, there may be direct scattering from the displaced atoms. The relative sizes of these two contributing factors depend upon the defect concentration. The sensitivity for detection of displaced atoms can be improved by using double alignment techniques as discussed in Secs. 4.2b and 6.2.

Extensive studies on dechanneling caused by dislocations and stacking faults in crystals have been performed by Mory, Quére, and collaborators [Dels70; Let71; Mory69,70,71a,b,72; Qu68a,b,70]. These authors have developed techniques using α particles and fission products emitted from radioactive sources. A related theoretical investigation using computer simulation has been carried out by Van Vliet [Va70]. For further work on channeling studies of lattice disorder, see [Ander65; Dav67b; May68; Ne69c; Mak70; Mars70; Baru71; Cho71; Fuj71a; Od71; Pi71,73a; Wei71; Ca72c; Gran72; Marc72; Mer73; Sak73].

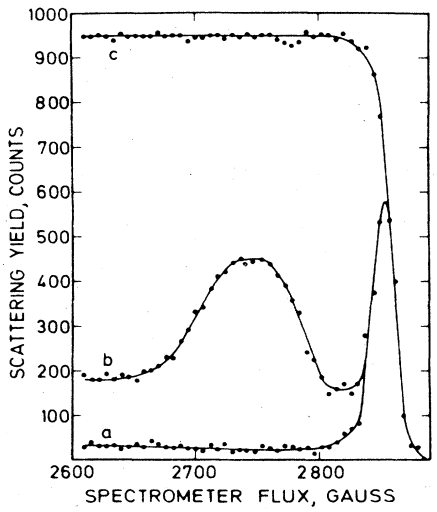

FIG. 110. Aligned (⟨111⟩ axis) and random spectra obtained for backscattering of 1.0-MeV ^{4}He ions from Sb-implanted Si. The data were obtained by Bøgh using a magnetic spectrograph. The aligned spectrum for an unimplanted crystal (curve a) is included for comparison. The mean depth of the disorder peak in curve b is about 500 Å [Dav72b].

6.4. Studies of surfaces and epitaxial layers

If the surface of the target crystal in a channeling experiment is clean, then the scattering yield in the surface peak (see Secs. 2.4e1 and 4.2a) measured in various channeling orientations can give quantitative information on the crystal structure in the immediate vicinity of the surface. From the scattering yield in the surface peak, one can readily deduce the effective number of surface layers contributing. This number may then be compared with calculations (e.g., [Ba71]; see also Sec. 2.4d1 and Fig. 20). The measured value will normally somewhat exceed the calculated value because of modifications of the lattice structure at the surface. By determining this difference in several channeling orientations, the surface structure can be elucidated. Similarly, the lattice location of impurity atoms sitting in a monolayer on the crystal surface may be determined by measuring their influence on the surface peak for the host crystal in various channeling directions. These sorts of measurements have not yet been applied very much, mainly because of the technical difficulties involved in performing channeling experiments in ultrahigh vacuum. However, such difficulties can be surmounted, and several laboratories either are now using or have under construction apparatus capable of providing the required vacuum conditions.

The influence of amorphous surface layers on channeling has been studied by several authors (e.g., [Mat69b; Mit71; Rim71,72a; Me72; Lug73]; see Fig. 57). Such layers cause the minimum yield and the dechanneling rate to increase, and thus studies of the changes in these quantities can be used to infer properties of the surface layers. If the amorphous surface layer is thick enough to give an observable peak, or peaks, in the spectrum of backscattered particles, both the stoichiometry and the thickness of the layer can be deduced (see, e g., [Gy70]). The sensitivity of this technique can be greatly improved by using double alignment [e.g., Bø68a].

An important application of channeling is to the study of epitaxial layers. This has recently been elegantly demonstrated in the work of Picraux [Pi72b,73a,b] who has examined heteroepitaxial layers of Si grown on polished substrates of spinel ($Al_2O_3 \cdot MgO$) and of sapphire (α-alumina). Some of his data are shown in Fig. 111. From an analysis of data of this type, the crystalline quality of the Si can be determined. It is found that the density of defects is greatest near the Si/spinel or Si/sapphire interface and that the Si more nearly approaches perfect crystallinity as the distance from the interface increases. By correlating the results of channeling and of electron microscopy, not only the depth profile of the density of imperfections but also the nature of the

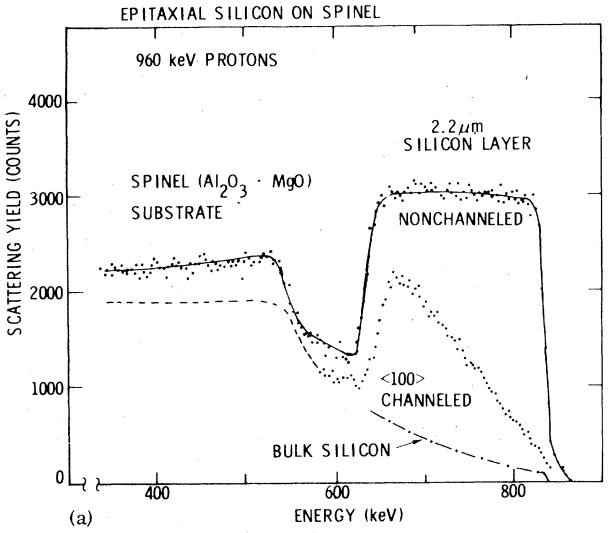

FIG. 111. Proton backscattering spectra recorded for ⟨100⟩ and random orientations of heteroepitaxial (100) Si/spinel and bulk Si [Pi73a]. The thickness of the Si layer is 2.2 μm. The incident proton energy is 960 keV.

imperfections, in this case, mainly stacking faults and microtwins, can be determined. (For further work on surface studies, see [Fuj71a; Zi71; Dav72b; Dal72; Hub72; May72; Po72b; Lin73; Sko73].)

6.5. Crystallography

Crystallographic applications of channeling effects vary from simple uses in ascertaining crystal orientations to more complex problems of structure determination. Orientation techniques have been developed using transmission patterns (e.g., [De67]), backscattering yields (e.g., [Bord70]) and blocking patterns (e.g., [Ne67c; Liv68; En70]). Several authors have demonstrated the usefulness of radioactive sources in such applications (e.g., [Mory69; Je70,72; Sk70; Dels71; Ni72e]) Although channeling techniques do not presently match x-ray diffraction as far as precision and richness of detailed information about crystal structure is concerned, there are some applications where channeling provides information difficult to obtain otherwise. For example, x-ray techniques often encounter problems in locating light atoms in crystals containing many heavy atoms which dominate the x-ray scattering. In such instances, channeling measurements can provide a useful supplement to the x-ray data. An example of structure determination by channeling techniques is the work of Matzke *et al.* [Mat71a] on U_4O_9, a compound that can be reached by dissolving excess oxygen in the fluorite structure UO_2. Using backscattering of He ions from uranium and the reaction $^{16}O\,(d,p)\,^{17}O$ to identify oxygen, Matzke *et al.* were able to measure the lattice position of the excess oxygen and to determine its influence on the UO_2 structure. Akhmetova *et al.* [Ak69] used the blocking effect to measure the change in the structure (from cubic to tetragonal) of $BaTiO_3$ as it is cooled through the Curie temperature (120° C). Miyagawa *et al.* [Miy72] have studied lattice distortions in mixed single crystals of KCl–KBr by measuring the dechanneling rates for 1.5-MeV protons. Considerable structure information can be extracted from the study of blocking patterns (e.g.,[Barr68, 69a,b,70; En70; Mu70; Gv72] see also Sec. 4.2b). Thus, for example, SiC is known to exist in over 50 different structure types. Yet, by recording a blocking pattern photographically, Barret *et al.* [Barr70] were able to make positive identifications of the particular structures existing in spots irradiated by a beam of 100-keV protons. Figure 112 shows a comparison of proton blocking patterns obtained by Barrett *et al.* [Barr69a] for the hcp structures, ζ Cu-Ge and Co, and for the wurtzite structures, CdSe and CdS. It was found that the planar blocking intensities in data of the type shown in Fig. 112 could be well explained in terms of the structure factors commonly used in x-ray crystallography [Barr69b] Mueller *et al.* [Mu70] have studied blocking patterns obtained for crystals of nearly identical structure (e.g , Pt and Au) and have attributed the rather pronounced differences in planar blocking intensities to differences in thermal vibrational amplitudes. Huber *et al.* [Hub72] have studied the structure of ice at various temperatures by employing backscattering techniques with 100-keV protons.

6.6. Measurement of nuclear lifetimes

When the blocking effect in crystals was discovered, it was immediately suggested [Ge65, Tu65a] that the phenomenon could be applied to the measurement of short nuclear lifetimes. Figure 113 illustrates the principle involved. When a compound nucleus is formed by interaction of the incident beam with one of the nuclei in the target crystal, it recoils from the lattice site with a velocity typically in the range $10^8 - 10^9$ cm/sec. If the compound nucleus decays by charged-particle emission and if the lifetime is so short that the decays occur before the compound nucleus has recoiled more than about 0.1 Å, i.e., about the thermal vibration amplitude, the full blocking effect will be observed with a detector measuring particles emitted in directions close to a major axis or plane of the crystal (c.f. Figs. 5, 6, 60, and 61). If, on the other hand, most of the decays occur at a time when the compound nucleus has recoiled into the open channel between atomic rows or planes, the blocking effect observed in the detector will be much weaker. A rough upper limit on the lifetimes for which the blocking effect may be used as a measuring tool is set by the lattice spacing. Thus, the technique should be applicable in the approximate range of lifetimes, $10^{-18} - 10^{-16}$ sec. This range is of considerable interest in nuclear physics and is one for which other measuring techniques are not readily available. Doppler-shift measurements on electromagnetic transitions presently extend down to about 10^{-14} sec., and lifetimes inferred from energy-width measurements and application of the uncertainty principle extend up to about $10^{-18} - 10^{-17}$ sec. Melikov *et al.* [Mel68] have discussed methods of extending the technique to shorter lifetimes by measuring asymmetries in axial blocking patterns.

Several years before channeling effects in crystals were known, Treacy [Tr60] made an unsuccessful attempt to measure a compound nuclear lifetime in the $^{12}C\,(d,p)$ reaction by a recoil technique. He used as a target a thin hexacosane ($C_{26}H_{54}$) crystal. Unfortunately, such organic

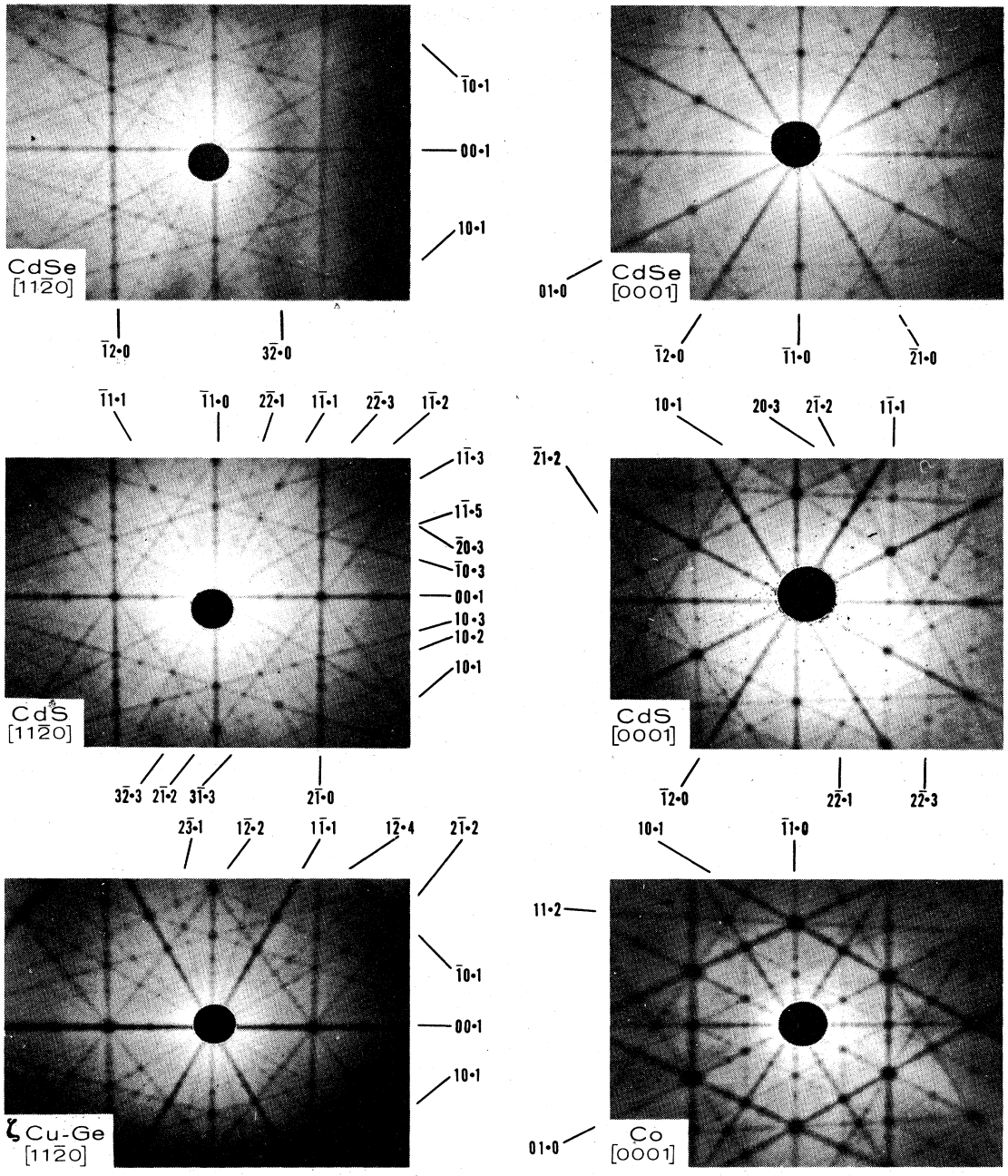

FIG. 112. Blocking patterns for 100-keV protons incident on thick single crystals of CdSe, CdS, ζCu-Ge, and Co [Barr69a]. The beam was incident a few degrees off the normal to the (1120) or (0001) surfaces, and the film positioned closely parallel to these surfaces. The black spots near the center of the photographs are due to holes in the film to permit passage of the incident beam.

crystals are extremely susceptible to radiation damage, and this is the probable reason for the negative result. The first successful application of blocking techniques to lifetime measurements was that of Brown *et al.* [Brow68]. These authors studied blocking patterns for fission fragments emerging from UO_2 crystals irradiated by thermal neutrons and by 12-MeV protons. The patterns, measured with plastic-sheet detectors (see Sec. 3.1), were closely the same for both neutron and proton beams. From this, it was deduced that for the proton-induced fission, the lifetime must be less than $\sim 2 \times 10^{-17}$ sec. Further work on proton induced fission in UO_2 crystals was performed by Gibson and Nielson [Gi69, 70] who found that at bombarding energies of 9 and 12 MeV, the effective lifetime was very short ($< 1.3 \times 10^{-16}$ sec), but that at 10 MeV, the lifetime was long enough ($\sim 1.4 \times 10^{-16}$ sec) to result in a measureably shallower blocking dip. It was postulated that this energy dependence of the lifetime could be explained in terms of second-chance fission. That is, at $E \approx 10$ MeV, the primary compound nucleus ^{239}Np can emit a neutron leaving a secondary compound nucleus ^{238}Np in a state of relatively low

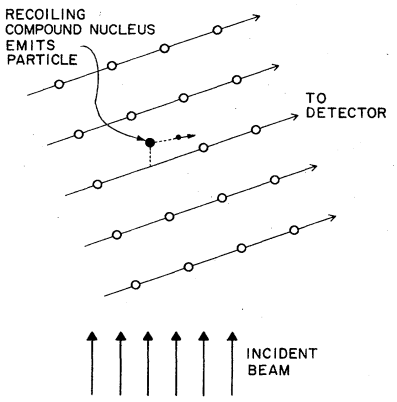

FIG. 113. Illustration of the principle involved in measuring short nuclear lifetimes by blocking techniques.

excitation and thus of relatively long lifetime. At $E \approx 9$ MeV, this process is not energetically possible, and all the fission fragments come from highly excited (short-lived) ^{239}Np. At $E_p \approx 12$ MeV, the nucleus ^{238}Np is also left in a state of high excitation resulting again in a short lifetime.

Gibson and Nielsen developed an analysis procedure that has been used in several subsequent lifetime measurements. The procedure assumes that for particles emitted at recoil distances greater than some cutoff distance, the yield detected along an axial blocking direction is not affected by the crystalline nature of the target. For recoil distances less than the cutoff distance, it is assumed that the yield measured on axis is given by a formula like Eq. (2.67), except that a weighting factor is introduced to allow for the exponential decay of the compound nucleus with time and that instead of u_2, the recoil distance is used. By integrating over recoil distances and adding in contributions from thermal vibrations and from multiple-scattering effects, Gibson and Nielsen derived an expression that relates the difference between a "delayed" $\chi_{\min}$ and a "prompt" $\chi_{\min}$ to the compound nuclear lifetime, the recoil velocity, and the cutoff distance. The recoil velocity is easily calculated. On the basis of Andersen's calculations [An67], Gibson and Nielsen estimated that the cutoff distance should lie in the range 3–5 times the Thomas–Fermi screening distance, a.

Following these first experiments, the blocking technique has been used by several groups to measure fission lifetimes. For example, ^{238}U(n,f) has been studied by Melikov *et al.* [Mel72] and by Noelpp *et al.* [Noe72]. Melikov *et al.* also measured ^{238}U(α,f) at $E = 25$ MeV. Heavy-ion induced fission, for example, W (^{22}Ne,f) at energies $E = 98$ and 174 MeV, has been studied intensively by a group at Dubna [Kar70,71a,b; Kam72a,b] and is now under active investigation at several other laboratories.

A number of groups (e.g., [Maru69,70; Cl71,72; Fuj71d; Tem71; Gi72b]) have used the blocking technique to measure compound nuclear lifetimes in inelastic proton scattering. The first such measurements were those of Maruyama *et al.* [Maru69] who studied the reactions ^{28}Si (p,p'), ^{70}Ge (p,p'), and ^{72}Ge (p,p') and found lifetimes on the order of 10^{-17} sec. In all blocking lifetime determinations, it is important to determine the "prompt" as well as the "delayed" blocking dips. Proton scattering experiments have the convenient feature that the Rutherford elastic scattering is prompt and the associated dip can easily be measured for reference purposes. Figure 114 shows dips obtained for elastic and inelastic proton scattering on a Ge crystal. The compound nuclear lifetime calculated by Clark *et al.* [Cl71] for the inelastic reaction illustrated in Fig. 114 is $(1.92 \pm 0.36) \times 10^{-17}$ sec. Clark *et al.* were able to observe a sharp reduction in the compound nuclear lifetime in the ^{72}Ge (p,p') reaction as the incident proton energy was raised up over the threshold for the ^{72}Ge (p,n) reaction. Recently Gibson *et al.* [Gi72b] made measurements using very thin ($\sim$1.5 μm) Ge crystals. For 5-MeV protons this target thickness corresponds to an energy loss of about 30 keV. With these targets Gibson *et al.* were able to measure such fine details as the enhancement (speeding-up) of the decay rate for compound nuclei formed for bombarding energies corresponding to isobaric analogue resonances. In addition, evidence was found for the influence of residual spin and structure factors on the compound nuclear lifetime.

The blocking technique has also been used to study sharp resonances in (p,α) reactions. For example, Komaki *et al.* [Ko72] have measured the ^{27}Al (p,α) ^{24}Mg reaction at the resonance energies $E = 0.633$ MeV and $E = 1.183$ MeV (see also [Na73]). From previous measurements, the widths of these resonances were known to be $\Gamma < 30$ eV and $\Gamma = 650 \pm 150$ eV, corresponding to $\tau > 2 \times 10^{-17}$ sec and $\tau \sim 10^{-18}$ sec, respectively. The blocking measurements gave for the 0.633-MeV reso-

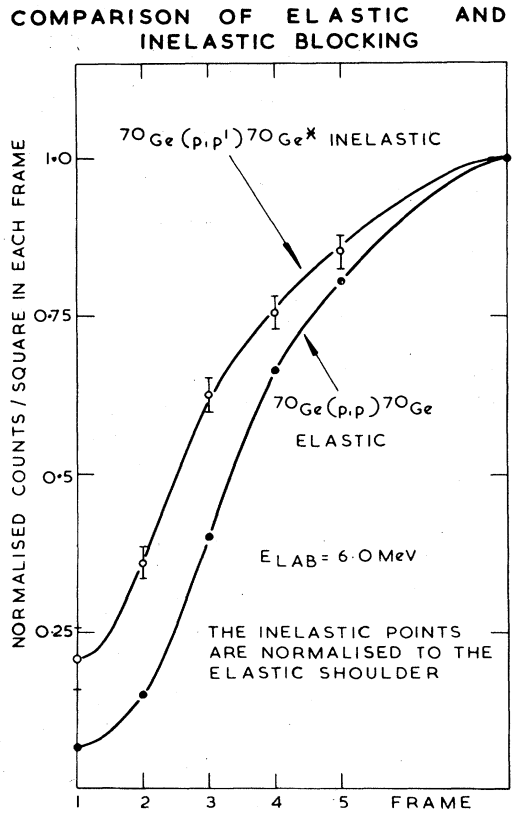

FIG. 114. A comparison of the ⟨110⟩ axial blocking dips obtained for the reactions ^{70}Ge$(p,p)^{70}$Ge and ^{70}Ge$(p,p')^{70}$Ge* (1.04 MeV) at a bombarding proton energy of 6.0 MeV [Cl71]. The abscissa is a measure of angular deviation from the ⟨110⟩ axial direction.

nance $\tau = 1.4 \times 10^{-16}$ (corresponding to $\Gamma \sim 5$ eV) and showed the 1.183-MeV resonance to be prompt, i.e., $\tau \lesssim 10^{-18}$ sec. Sharma *et al.* [Sha71] have made similar sorts of measurements on the ^{31}P (p, α) ^{28}Si reaction at the resonant proton energies of 0.641 MeV and 1.510 MeV. They used a GaP crystal and found for the 0.641-MeV resonance, $\tau \sim 1.4 \times 10^{-16}$ sec($\Gamma \sim 5$ eV) and found the 1.510-MeV resonance to be prompt, consistent with width measurements that give $\Gamma \sim 7$ keV for this resonance.

There is presently considerable effort being invested into improving the analysis techniques for extracting lifetime information from the blocking data. The simple model and analysis procedures developed by Gibson and Nielsen [Gi69, 70] have obvious limitations. For example, flux peaking effects are not taken into account. Yet it is known that they can be large (see Secs. 2.4f and 6.2; see also [Has73]). Furthermore, the influences of dechanneling and multiple scattering need to be incorporated in a more precise fashion. Figure 61 shows how multiple scattering can lead to the presence of channeled components emerging in blocking directions (see also [Fuj71d]). The minimum yield in a blocking dip is clearly not the only quantity affected by lifetime effects. The width and other details of the shape contain a lot of additional information; some groups use the dip area as the measured parameter from which the lifetime is extracted. Several authors have used Monte Carlo computing techniques to determine the influence of lifetime effects on blocking and to extract lifetimes more precisely from experimental data. (For discussions of these and other analysis techniques, see [Gi69,70; Ko69,70; Ma70; Maru70; Mo70c; Son70; Cl71,72; Fuj71d; Mal71; Fu72; Pi72; Mel72; Ry72; Ve72; Has73; Kar73])

6.7 Production of polarized beams

Kaminsky [Kami69,71] has demonstrated a method for producing polarized deuterium beams using channeling techniques. The experimental arrangement is shown schematically in Fig. 115. A tightly collimated D^+ beam is incident along the $\langle 110 \rangle$ axial direction of a thin ($\sim$1–2 μm) monocrystalline Ni foil magnetized in the plane of the foil. After transmission through the Ni, the charged components of the beam are removed by electrostatic deflection. A set of restrictive collimators selects the best-channeled neutral component emerging from the foil. This neutral fraction, after leaving the foil, passes through a weak transverse magnetic field ($\sim$10 G) and impinges upon a tritiated titanium target. By observing the asymmetry of the angular distribution for α particles emitted from the reaction T (d, n) ^{4}He occurring in this target, the nuclear polarization of the D° beam can be deduced. The energy of the incident D^+ beam is chosen so that the channeled component of the beam emerging from the Ni foil has an energy ($\sim$100 – 130 keV) optimum for employing the T(d, n) ^{4}He reaction as a polarization analyzer. The random component of the transmitted beam then has an energy of a few keV and does not affect the polarization measurement. The idea behind the experiment is that those emerging neutrals that were channeled in the Ni, will have captured electrons from the outermost (e.g., 3*d*) states of Ni and that these electrons will have spins pointing preferentially in one direction along the magnetic field lines. During the time of passage ($\sim 10^{-7}$ sec) through the weak field region, part of the electron polarization may be transferred to the nucleus by hyperfine interaction. Kaminsky's measurements gave a value for the tensor polarization of $P_{zz} = -0.32 \pm 0.01$. This result is remarkable in that it implies that 98% of the analyzed deuterium atoms emerge from the foil with electron spins oriented parallel to the magnetic field direction.

The magnitude of the effect is somewhat surprising since the effective magneton number of Ni is 0.6. The experimental result therefore implies that 9.4 of the ten possible 3*d* states in Ni are occupied. If only electrons in the outermost shells (3*d* and 4*s*) were picked up to form neutral deuterium atoms, one would expect the maximum fraction of spin-up electrons to be about 53%, assuming that the capture probabilities for spin-up and spin-down electrons are simply proportional to their relative population in the crystal. Feldman *et al.* [Fel72b] have also made polarization measurements with an experimental arrangement (Fig. 115) very similar to that of Kaminsky. Their data qualitatively agree with Kaminsky's. Although the effect observed was not so strong [their result implies an electron spin-up fraction of 71($\pm$10)%] it is much larger than the 53% expected assuming a spin-independent capture mechanism. No effect is seen for polycrystalline foils.

Ebel [Eb70] was able to explain the high observed polarization by postulating that once a deuteron has captured a spin-up electron inside the crystal, the probability of its losing that electron would be small since the spin-up 3*d*-band states are filled. A captured spin-down electron, on the other hand, could readily be lost since the spin-down 3*d*-band states in the crystal are not filled. This would give rise to a pumping of electrons from spin-down to spin-up atomic states of deuterium. Brandt and Sizmann [Br71], however, pointed out that there cannot exist stable bound electronic states in deuterium atoms passing through metals at these velocities. They proposed instead that the electron capture takes place in the tail of the electron density distribution at the crystal surface where the density is low enough for bound states to be stable. (With this assumption, it is possible to account for the measured neutral fractions of protons and deuterons emerging from solids over a wide range of velocities.) Thus the electron polarization in the neutral beam would be determined by the polarization of the electrons avail-

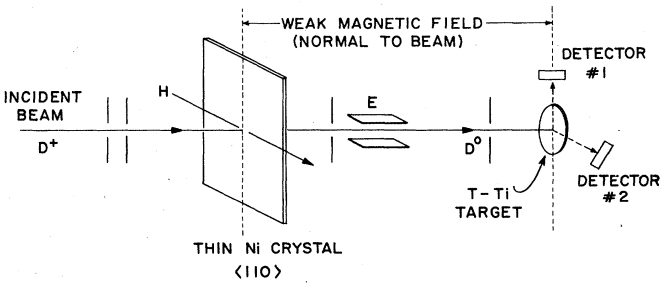

FIG. 115. Schematic diagram illustrating the experimental arrangement used in polarization measurements on deuterium beams transmitted through thin magnetized Ni crystals in the $\langle 110 \rangle$ axial channeling direction [Kami69; Fel72b].

able at the surface. Electron field-emission experiments [Gl71] on Ni have shown that the orientation of electron spins at the surface depends strongly on the crystal axis, e.g., electrons field-emitted along the ⟨100⟩ and ⟨110⟩ directions have predominantly spin-up, but are spin-down along the ⟨111⟩. Rau and Sizmann [Rau73] have recently made measurements which lend strength to this explanation. They have measured the polarization, also using the T $(d,n)^4$He reaction, of the nuclei in neutral deuterium atoms created by electron capture during reflection of a 150-keV D^+ beam incident at glancing angles ($< 0.4°$) upon the surface of magnetized Ni crystals. The results show that the electron spin orientation is predominantly parallel to the magnetizing field for electrons in the (100), (110), and (111) surfaces and antiparallel in the (120) surface. Rau and Sizmann found that a vacuum of 2×10^{-8} Torr was necessary in order to see polarization effects. If the vacuum was allowed to deteriorate to 5×10^{-6} Torr, the polarization gradually vanished, presumably as a result of the build-up of thin layers of surface contaminants. Feldman *et al.* [Fel72b] also have studied the influence of surface oxide layers and the deleterious effects of radiation damage in the transmission arrangement shown in Fig. 115. In addition, these authors attempted to observe an effect using thin polycrystalline foils of Fe; Fe has an effect magneton number of 2.2 and thus might be expected to show a stronger polarization effect than Ni. No effect was seen, possibly because of the presence of fairly thick (50–to 100-Å) surface oxide layers.

6.8. Particle detectors

Many particle detectors operate by measuring the energy deposited by charged particles traversing single crystals. Such detectors range from scintillators such as NaI (Tl) and anthracene to semiconductor counters such as Si and Ge. Channeling effects in these devices can be extremely important. This is particularly true in connection with thin ("dE/dx") detectors, where only a small fraction of each particle's energy is deposited, usually for identification purposes. In order to minimize complicating effects due to channeling, care must be taken to avoid crystal orientations in which the detected particles are incident in major channeling directions (e.g., [Mad64; Weg64]). The influence of channeling on the scintillation response of various crystals is discussed in Sec. 4.2g. Provided that energetic light ions such as protons and alpha particles are completely stopped in the sensitive volume of semiconductor counters, the number of electron–hole pairs created does not depend measurably on whether the ions are channeled or not. This is not true, however, for heavy ions. Moak *et al.* [Moa66] have shown that when fast ^{127}I and ^{40}Ar ions are channeled in a Si detector, the pulse-height defect normally observed for heavy ions is reduced by more than a factor of 10 and the resolution in the pulse-height spectrum is substantially improved. These effects are attributed to the much lower contribution from nuclear energy-loss processes (see Sec. 2.6a) at the end of the ranges of the ions.

ACKNOWLEDGMENTS

It is a pleasure to acknowledge many stimulating conversations with Dr. R. E. Holland and Dr. J.-C. Poizat during the course of preparing this article. Thanks are also gratefully extended to the many colleagues and authors who have given permission to reproduce their data.

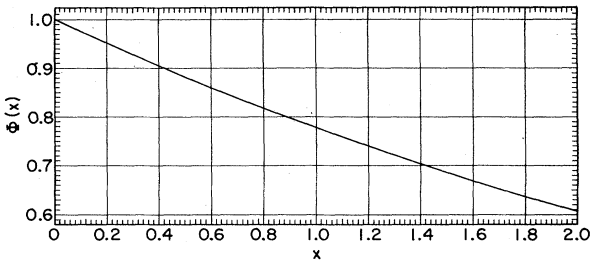

FIG. 116. Graph of the Debye function $\Phi(x) = (1/x)\int_0^x [\xi d\xi/(e^\xi - 1)]$.

APPENDIX A: USEFUL DATA FOR QUICK ESTIMATES OF CHANNELING PROPERTIES

We give here and in Appendix B graphs and tables of the various quantities needed to make quick estimates of surface values of half-angles and minimum yields for axial channeling and of half-angles for planar channeling. We use the empirical formulas of Barrett [Ba71], viz., Eqs. (2.66), (2.67), (2.68), (2.69), and (2.81). (For an alternative method of estimating axial half-angles, see [Var72].) These estimates apply to the ψ_1-region; see Eqs. (2.27), (2.28), and (2.29). At lower energies, i.e., in the ψ_2-region, the estimate given in Eq. (2.28) may be used. Note that when relativistic effects are expected to be important, the value kE, where k is defined in Eq. (2.45), should be used in the following formulae in place of the incident energy E. The estimates for the half-angles $\psi_{1/2}$ require the prior calculation of the Thomas–Fermi screening radius a, Eq. (2.3), and the one-directional rms thermal vibration amplitude u_1, Eq. (2.4d). From Eq. (2.3) one has

$$a = 0.4685 Z_2^{-1/3} \text{ Å}, \tag{A1a}$$

if the incident ion is fully ionized and

$$a = 0.4685(\sqrt{Z_1} + \sqrt{Z_2})^{-2/3} \text{ Å}, \tag{A1b}$$

if the incident ion is not fully ionized. The thermal vibration amplitude may be estimated from the Debye approximation (e.g., [Blac55]) as follows:

$$u_1 = 12.1\{[\Phi(x)/x + \tfrac{1}{4}]/M_2\Theta\}^{1/2} \text{ Å}, \tag{A2}$$

where $\Phi(x)$ is the Debye function shown plotted in Fig. 116, M_2 is the atomic weight (amu) of the crystal atoms, Θ is the Debye temperature (°K) and x is given by

$$x = \Theta/T, \tag{A3}$$

where T is the crystal temperature (°K). Values of M_2 and Θ for the most commonly studied crystals are given in Appendix B.

A.1 Axial case

From Eq. (2.66) one has

$$\psi_{1/2} = 0.80 F_{RS}(1.2u_1/a)\psi_1, \tag{A4}$$

where the function $F_{RS}(\xi)$ is defined in Eqs. (2.36), (2.18),

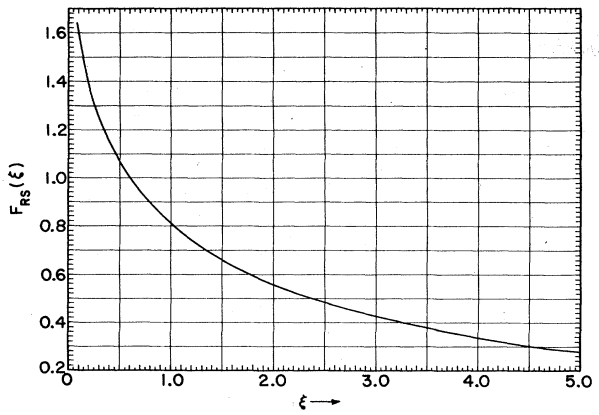

FIG. 117. Graph of the function $F_{RS}(\xi)$ as defined in Eq. (2.36) and using Molière's potential.

and (2.2) (Molière potential) and graphed in Fig. 117. The angle ψ_1, Eq. (2.12), can be written

$$\psi_1 \approx 0.307(Z_1 Z_2/dE)^{1/2} \text{ degrees}, \tag{A5}$$

where d is the atomic spacing along the row (in angstroms) and E is the bombarding energy (in MeV).

For the minimum yield, Eq. (2.68) gives, assuming no effects due to beam divergence, surface layers, etc.,

$$\chi_{\min} = 18.8 N d u_1^2 (1 + \zeta^{-2})^{1/2}. \tag{A6}$$

Here N is the number of crystal atoms per unit volume and

$$\zeta = 126 u_1/(\psi_{1/2} d), \tag{A7}$$

where $\psi_{1/2}$ is given in degrees. At energies high enough so that $\psi_{1/2} \ll \sin^{-1}(u_1/d)$, Eq. (A6) becomes

$$\chi_{\min} = 18.8 N d u_1^2. \tag{A8}$$

A.2 Planar case

From Eq. (2.81) one obtains

$$\psi_{1/2} = 0.72 F_{PS}(1.6u_1/a, d_p/a)\psi_a, \tag{A9}$$

where the function $F_{PS}(\xi, \eta)$ is defined in Eqs. (2.43), (2.25), and (2.2) (Molière potential) and graphed in Fig. 118. The angle ψ_a, Eq (2.23), can be written

$$\psi_a \approx 0.545(nZ_1 Z_2 a/E)^{1/2} \text{ degrees}, \tag{A10}$$

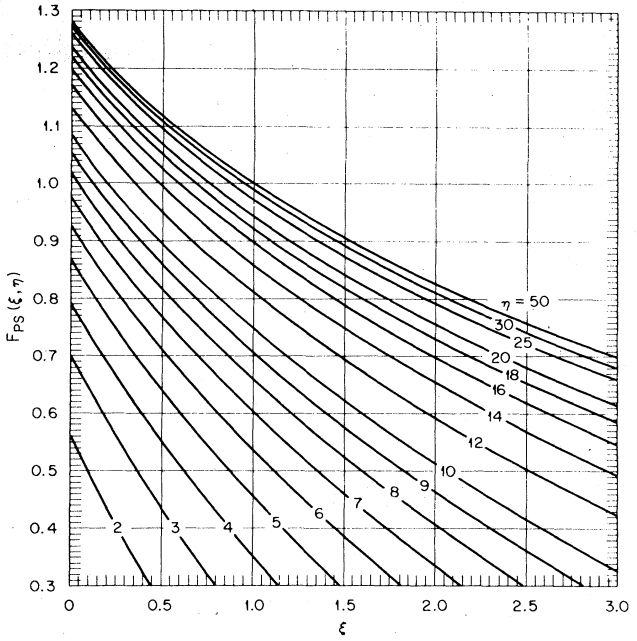

FIG. 118. Graphs of the function $F_{PS}(\xi, \eta)$ as defined in Eq (2.43) and using Molière's potential. Values are given as functions of ξ for various η [Ba71].

where n is the atomic density in the planes [atoms/ (Å)^2], a is given by Eq. (A1), and E is in MeV.

A.3 Examples

(a) Axial channeling of 1.0-MeV ^{4}He ions along the ⟨110⟩ direction in Ge at 20 °C. From Table IV (Appendix B) we find the lattice spacing of Ge is 5.657 Å and the Debye temperature is 290 °K. From Eqs. (A1) and (A2) the values of a and u_1 are found to be 0.148 Å and 0.085 Å, respectively. Using Table II we see that the atomic spacing in the ⟨110⟩ direction of Ge is 4.00 Å. Equation (A5) then gives $\psi_1 = 1.23°$. From Fig. 117 the value of $F_{RS}(0.689)$ can be read off as 0.95. Then from Eq. (A4) we find $\psi_{1/2} = 0.93°$ (Picraux *et al.* [Pi69a] measured $\psi_{1/2} = 0.95°$). To calculate the minimum yield, we first evaluate Eq. (A7) and find $\zeta = 2.86$. Next we compute $N = 8/(5.657)^3 = 0.0442$ atoms/(Å)^3. Then Eq. (A6) gives $\chi_{\min} = 0.025$ (the measured value [Pi69a] is 0.03).

(b) Planar channeling of 20-MeV ^{35}Cl ions along the (111) direction in Au at 25 °C. From Table IV (Appendix B), we find the lattice spacing of Au is 4.078 Å and the Debye temperature is 170° K. From Eqs. (A1) and (A2) the values of a and u_1 are found to be 0.0847 Å and 0.088 Å, respectively. The interplanar spacing d_p for (111) planes (see Table II) is 2.354 Å. The areal density of atoms in the planes is simply $Nd_p = 4 \times 2.354/(4.078)^3 = 0.1389$ atoms/(A)^2. Then Eq. (A10) gives $\psi_a = 0.484°$. From Fig. 118, one reads off for $F_{PS}(1.66, 27.8)$ the value 0.86. Then from Eq. (A9), we find $\psi_{1/2} = 0.30°$ (the value measured by Davies *et al.* [Dav68a] is 0.32°).

TABLE II. Values by which the lattice constant must be multiplied to compute the interatomic spacings d in axial directions and the interplanar spacings d_p for planar directions in the simplest (monatomic) cubic structures.

Structure	Atoms per unit cell	Axis ⟨100⟩	Axis ⟨110⟩	Axis ⟨111⟩	Plane (100)	Plane (110)	Plane (111)
fcc	4	1	$1/\sqrt{2}$	$\sqrt{3}$	1/2	$1/2\sqrt{2}$	$1/\sqrt{3}$
bcc	2	1	$\sqrt{2}$	$\sqrt{3}/2$	1/2	$1/\sqrt{2}$	$1/2\sqrt{3}$
fcc (diamond)	8	1	$1/\sqrt{2}$	$\sqrt{3}/4, 3\sqrt{3}/4$	1/4	$1/2\sqrt{2}$	$1/4\sqrt{3}, \sqrt{3}/4$

TABLE III. Values by which the lattice constant must be multiplied to compute the interatomic spacings d in axial directions and the interplanar spacings d_p for planar directions in the most common simple diatomic compounds (atoms labeled A and B) having cubic structures.[a]

Structure	Atoms per unit cell	Axis ⟨100⟩	Axis ⟨110⟩	Axis ⟨111⟩	Plane (100)	Plane (110)	Plane (111)
Rocksalt (like NaCl)	4A + 4B	ABAB··· 1/2	pure $1/\sqrt{2}$	ABAB··· $\sqrt{3}/2$	mixed 1/2	mixed $1/2\sqrt{2}$	pure ABAB··· $1/2\sqrt{3}$
Fluorite (like CaF_2)	4A + 8B	pure 1(A), 1/2(B)	pure $1/\sqrt{2}$	BAB···BAB··· $\sqrt{3}/4, \sqrt{3}/2$	pure ABAB·· 1/4	mixed $1/2\sqrt{2}$	pure BAB··BAB·· $1/4\sqrt{3}, \sqrt{3}/4$
Zinc blend (like ZnS)	4A + 4B	pure 1	pure $1/\sqrt{2}$	AB···AB··· $\sqrt{3}/4, 3\sqrt{3}/4$	pure ABAB·· 1/4	mixed $1/2\sqrt{2}$	pure AB··AB·· $1/4\sqrt{3}, \sqrt{3}/4$

[a] For the axial case, the term *pure* indicates that each row contains only one atomic species. For rows containing both species, the ordering in the row is given. For the planar case, the term *pure* indicates that each sheet of atoms contains only one atomic species and the way in which the sheets are ordered is shown. The term *mixed* refers to cases where each planar sheet of atoms contains both atomic species.

APPENDIX B: GUIDE TO CHANNELING MEASUREMENTS PERFORMED ON VARIOUS TARGET CRYSTALS.

In Tables IV, V and VI we list some of the properties of the more commonly studied crystals together with references to published literature describing channeling experiments with these crystals. Because of the great amount of work done with crystals of Si, Cu, Ge, W, and Au, references for these materials are listed separately below Table IV. Unless a different reference is specified, the Debye temperatures are taken from [Lo48, 62]. The lattice constants are taken from [Wy63] and pertain to room temperature.

TABLE IV. Most commonly studied elements having cubic structures at room temperature.

Z_2	M_2	Name	Structure	$0.4685 Z_2^{-1/3}$ (Å)	Θ(°K)	u_1(293°K) (Å)	Lattice constant (Å)	References
6	12.01	C	fcc (diamond)	0.258	2000	0.04	3.567	Pi69a
13	26.98	Al	fcc	0.199	390	0.105	4.050	An65;Barr68;Blan69; Bø64, 65b;Br65, 68; Dav69;Kh66, 67b;Ko72; Let71;Se66
14	28.09	Si	fcc (diamond)	0.194	543 [Bat62]	0.075	5.431	See Footnote a.
23	50.94	V	bcc	0.165	360	0.082	3.024	Po68b
24	52.00	Cr	bcc	0.162	485	0.061	2.884	Barr68;Mu70
26	55.85	Fe	bcc	0.158	420	0.068	2.867	Abel72a;Al71;An72a, b; And66a;Bø69;Cl70; De68b;Fel71, 72a
28	58.71	Ni	fcc	0.154	425	0.065	3.524	An72a;Fel72b;Kami69, 71; Kau73;Mart69;Rau73
29	63.54	Cu	fcc	0.152	315	0.084	3.615	See Footnote b.
32	72.59	Ge	fcc (diamond)	0.148	290	0.085	5.657	See Footnote c.
41	92.91	Nb	bcc	0.136	275	0.079	3.300	Beh71, 72
42	95.94	Mo	bcc	0.135	380	0.057	3.147	Cl70;Tu65d
45	102.91	Rh	fcc	0.132	340	0.061	3.803	Mu70
46	106.4	Pd	fcc	0.131	275	0.074	3.890	Mu70;Nis72
47	107.87	Ag	fcc	0.130	215	0.093	4.086	An72a;Anders73;Ap72a, b;Bro69;How70a;Kami70; Mu70;Tom68
73	180.95	Ta	bcc	0.112	245	0.064	3.306	An72a;Ast65;Barr68; Bø65a, b;Do65b
74	183.85	W	bcc	0.112	310	0.050	3.165	See Footnote d.
78	195.09	Pt	fcc	0.110	225	0.066	3.923	Mu70
79	196.97	Au	fcc	0.109	170	0.087	4.078	See Footnote e.
82	207.19	Pb	fcc	0.108	88	0.164	4.951	How70a;Tom68

[a] References for Si: Ace69, 70; Alt70a; An71a, 72a; Ana69b; Anders73; Ap65, 67; Ar71b, 72; Barr68; Bel72c; Bø64, 68b, 69, 72; Bulg71; Ca70, 72a, b, c; Cai68; Cay71; Cl70; Dav67b, 68a, 69; De64, 68b; Del71, 72; Dem72; Do70; Ei66, 68a, 71a, 72a, b; Er64; Erik69b; Fel70a; Fl70; Fon72; Fot69, 70b, 71; Fuj69, 70, 71a, b, c, d, 72a; Ge65, 71; Ger72; Gi65, 68b; Gr72; Gv72; Gy70; Har70; Ho68; Iu72; Je70; Jo69; Kon70; Lug73; Man68; Marc72; Mart69; Maru69, 70; Mit71; Moa66; Mor71c, 72; Moro72; Ne67a, b; Nort70a; Ok70; Pav72; Ped72; Pi69a, b, 72a, b, 73a, b; Red72; Rem67; Rim71, 72a, b; Sa67; Sh68a; Si71; Sk70; So71a, b, 72; Walk 70; Weg64; Wes69; Wo69; Zi73.

[b] References for Cu: Al71, 72; An72a; Anders73; Barr68; Bell65; Br65, 68; Cai72; Eli70; Far65; Fis69;Fuj72a; Gra66, 68; Ja72; Kami70; Kh66, 67a, b; Liv68; Mak70; Mars69; Pan72; Sar69; Shu71; Th64; Ug66, 68.

[c] References for Ge: Ab69; An72a; Ap67, 70; Barr68; Bro 72; Ca71, 72a, b, c; Cl70, 71, 72; Fuj 71d, 72a; Ge71; Gi72b; Ho68; Kor70; Marc72; Maru69, 70; Mor70, 71a, b, c; Pi69a,b; Sa65, 67; Sh68a.

[d] References for W: Ace69; An68, 72a b; Ap70; Barr68; Berg68; Bø67a, b, 68b, 72; Cl70; Dav68a, 69, 72a; Do65a, b, 66; Erik67a, b; Far70; Kam72; Kar70, 71a,b; Kh67b; Kul67; Marw72; Mel68; Pan72; Tu65a, b, c.

[e] References for Au: An71b, 72a; And65, 55b; Ande70; Anders73; Ap71b; Al72; Barr68; Bøtt69; Ch68c, 69b; Da65a, b, 69, 70, 72; Dav68a; Fuj72a; Gi68a, 72a; Hi70; Hög70; How70a, 71; Ib68; Lu66, 70, 71; Mach68, 70; Mark71; Mory71a, b; Mu70; Ne69a; New72; No66, 69; Oko72; Po71b, 72b, c: Reu69; Schob69a; Ug68, 70; Wh67; Wij69.

TABLE V. Commonly studied diatomic compounds having cubic lattice structures at room temperature.

Name	Structure	Lattice constant (Å)	References	Name	Structure	Lattice constant (Å)	References
AlSb	ZnS	6.135	Sa68b	KI	NaCl	7.066	Alt73;Di70;Man70; Roth70;Vor71
BaF_2	CaF_2	6.200	Ed72a;He71b	LiF	NaCl	4.017	Ed70;Mat71b
$BaTiO_3$	Perovskite (> 120 °C)	3.996	Ak69;Ge72a, b	MgO	NaCl	4.211	Cl70;De68b;Ho68; Kr70;Kumm72; Mat71b
CaF_2	CaF_2	5.463	Ato70;Ed72a, He71a, b;Mat67	NaF	NaCl	4.620	Mat71b
CsI	CsCl	4.567	Cl69, 70;Kule72	NaCl	NaCl	5.640	Cho71;Cl70;Kon69; Man70;Mat71b; Mor72;Roth70; Sh68b;Vor72a, b; Voro72
GaP	ZnS	5.451	Dav69;Fel70b; Kob68;Mor72; Pi69a, b;Shá71	NaI	NaCl	6.473	Alt70b, 73
GaAs	ZnS	5.654	Mars69;Maz69; Pi69a;Sa67	PbS	NaCl	5.936	An72a
GaSb	ZnS	6.118	Dav69;Pi69a; Sa68b	RbBr	NaCl	6.854	Behn69
InAs	ZnS	6.036	Sa68b	SrF_2	CaF_2	5.800	Mat71b
InSb	ZnS	6.478	Sa68b	ThO_2	CaF_2	5.600	Cli72;Mars69
KCl	NaCl	6.293	Di70;Fuj71a;Hu71; Man70;Mat67, 71b; Miy72;Mor72; Roth70;Sh68b; Vor71	UC	NaCl	4.959	Mars69;Mat69a, b, 70, 71b
				UO_2	CaF_2	5.468	Brow68;Dav68a, 69;Erik69a;Gi69, 70;Mars69;Mat67, 69, 71a, b;Mel72; Noe72
KBr	NaCl	6.600	Di70;Man70;Miy72; Mor70b, 72; Sh68b;Vor71				

TABLE VI. References to work on non-cubic and complex structures.

Crystal	References
Al_2O_3	De68b
Anthracene	Br68;Ok70;Wick67
Bi	El67;En70
CdS	Barr69a
CdSe	Barr69a
Co	Barr69a
Ice (H_2O)	Hub72
Mica	Ham66;Se66
Quartz (SiO_2)	Abel69, 72b;Sa68a
SiC	Barr70;Mat71b
Sn	Mi73
U_4O_9	Mat71a
Zn	Howe71
ZnO	Ap70, 71;Fel69
Zr	Mars69

Abel 69 Abel, F., G. Amsel, M. Bruneaux, and E. d'Artemare, J. Phys. Chem. Solids **30**, 687 (1969).

Abel 72a Abel F., G. Amsel, M. Bruneaux, and C. Cohen, Phys. Lett. A **42**, 165 (1972).

Abel 72b Abel, F., G. Amsel, B. Bruneaux, and C. Cohen, Radiat Eff. **12**, 35 (1972).

Abel 73 Abel, F., G. Amsel, M. Bruneaux, and C. Cohen, C. R. Acad. Sci. B **276** 267 (1973).

Ab 69 Abroyan, I. A., V. A. Koryukin, N. N. Ushakov, and L. A. Tsekhnovicher, Fiz. Tverd. Tela **11**, 3376 (1969) [Sov. Phys.—Solid State **11**, 2745 (1970)].

Ace 69 Acerbi, E., C. Birattari, B. Candoni, M. Castiglioni, G. Dutto, G. Fait, and C. Sutti, Nuovo Cimento Lett. **2**, 805 (1969).

Ace 70 Acerbi, E., C Birattari, B. Candoni, A. M. Castiglioni, G. Dutto, G. Fait, and C. Succi, Nuovo Cimento Lett. **3**, 569 (1970).

Aka 73 Akasaka, Y., and K. Horie, J. Appl. Phys. **44**, 3372 (1973).

Ak 69 Akhmetova, B. G., Y. M. Plets, and A. F. Tulinov, Zh. Eksp. Teor. Fiz. **56**, 813 (1969) [Sov. Phys.—JETP **29**, 442 (1969)].

Al 70 Alexander, R. B., G. Dearnaley, D. V. Morgan, and J. M. Poate, Phys. Lett. A **32**, 365 (1970).

Al 71 Alexander, R. B., Harwell Report No. AERE-R6849 (1971).

Al 72 Alexander, R. B., and J. M. Poate, Radiat. Eff. **12**, 211 (1972).

Alm 61 Almén, O., and G. Bruce, Nucl. Instrum. Methods **11**, 279 (1961).

Alt 70a Altman, M. R., L. C. Feldman, and W. M. Gibson, Phys. Rev. Lett. **24**, 464 (1970).

Alt 70b Altman, M. R., H. B. Dietrich, and R. B. Murray, Phys. Lett. A **32**, 423 (1970).

Alt 73 Altman, M. R., H. B. Dietrich, R. B. Murray, and T. J. Rock, Phys. Rev. B **7**, 1743 (1973).

Am 70 Amberger, R. W., Z. Phys. **236**, 352 (1970).

Ana 69a Anastassiades, A., G. Andritsopoulos, S. Filippakis, and N. H. Gangas, Nucl. Instrum. Methods **67**, 240 (1969).

Ana 69b Anastassiades, A. J., S. E. Filippakis, N. H. Gangas, and E. T. Sarris, Nucl. Instrum. Methods **75**, 48 (1969).

Ander 65 Andersen, H. H. and P. Sigmund, Nucl. Instrum. Methods **38**, 238 (1965).

An 65 Andersen, J. U., J. A. Davies, K. O. Nielsen, and S. L. Andersen, Nucl. Instrum. Methods **38**, 210 (1965).

An 67 Andersen, J. U., K. Dan. Vidensk. Selsk, Mat.-Fys. Medd. **36**, No. 7 (1967).

An 68 Andersen, J. U. and E. Uggerhøj, Can. J. Phys. **46**, 517 (1968).

An 70 Andersen, J. U. and L. C. Feldman, Phys. Rev. B **1**, 2063 (1970).

An 71a Andersen, J. U., O. Andreasen, J. A. Davies, and E. Uggerhøju, Radiat. Eff. **7**, 25 (1971).

An 71b Andersen, J. U., W. M. Augustyniak, and E. Uggerhøj, Phys. Rev. B **3**, 705 (1971).

An 72a Andersen, J. U. and E. Laegsgaard, Radiat. Eff. **12**, 3 (1972).

An 72b Andersen, J. U., E. Laegsgaard, and L. C. Feldman, Radiat. Eff. **12**, 219 (1972).

Anders 73 Andersen, S. K., F. Bell, F. Fransden, and E. Uggerhøj, Phys. Rev. B **8**, 4913 (1973).

Ande 70 Andersen, T., S. Datz, P. Hvelplund, and G. Sorensen, Phys. Lett. A **33**, 121 (1970).

And 65 Andreen, C. J., R. L. Hines, W. Morris, and D. Weber, Phys. Lett. **19**, 116 (1965).

And 66a Andreen, C. J., E. F. Wasserman, and R. L. Hines, Phys. Rev. Lett. **16**, 782 (1966).

And 66b Andreen, C. J. and R. L. Hines, Phys. Rev. **151**, 341 (1966).

Ap 65 Appleton, B. R., C. Erginsoy, H. E. Wegner, and W. M. Gibson, Phys. Lett. **19**, 185 (1965).

Ap 67 Appleton, B. R., C. Erginsoy, and W. M. Gibson, Phys. Rev. **161**, 330 (1967).

Ap 68 Appleton, B. R., L. C. Feldman, and W. L. Brown, in *Solid State Physics Research with Accelerators*, Brookhaven National Laboratory Report No. BNL-50083, p. 45 (1968).

Ap 69 Appleton, B. R. and L. C. Feldman, Radiat. Eff. **2**, 65 (1969).

Ap 70 Appleton, B. R. and L. C. Feldman, in *Atomic Collision Phenomena in Solids*, edited by (North-Holland, Amsterdam, 1970), p. 417.

Ap 71 Appleton, B. R., S. Datz, C. D. Moak, and M. T. Robinson, Phys. Rev. B **4**, 1452 (1971).

Ap 72a Appleton, B. R., J. H. Barrett, T. S. Noggle, and C. D. Moak, Radiat. Eff. **13**, 171 (1972).

Ap 72b Appleton, B. R., C. D. Moak, T. S. Noggle, and J. H. Barrett, Phys. Rev. Lett. **28**, 1307 (1972).

Ap 72c Appleton, B. R. and L. C Feldman, J. Phys. Chem. Solids **33**, 507 (1972).

Ari 72 Arifov, U. A., D. D. Gruich, G. E. Ermakov, and E. Khalmirzayev, Radiat. Eff. **12**, 181 (1972).

Ar 71a Armstrong, D. D. and H. E. Wegner, Rev. Sci. Instrum. **42**, 40 (1971).

Ar 71b Armstrong, D. D., W. M. Gibson, and H. E. Wegner, Radiat. Eff. **11**, 241 (1971).

Ar 72 Armstrong, D. D., W. M. Gibson, A. Goland, J. A. Golovchenko, R. A. Levesque, R. L. Meek, and H. E. Wegner, Radiat. Eff. **12**, 143 (1972).

Ast 65 Astner, G., I. Bergström, B. Domeij, L. Eriksson, and Å. Persson, Phys. Lett. **14**, 308 (1965).

As 72 Astrup, G. and J. S. Olsen, Radiat. Eff. **15**, 205 (1972).

Ato 70 Ato, Y., S. Miyagawa, and R. Huzimura, J. Phys. Soc. Jap. **28**, 1383 (1970).

Ba 68 Barrett, J. H., Phys. Rev. **166**, 219 (1968).

Ba 71 Barrett, J. H., Phys. Rev. B **3**, 1527 (1971).

Bang 59 Bang, J., and J. M. Hansteen, K. Dan. Vidensk. Selsk. Mat.-Fys. Medd. **31**, No. 13 (1959).

Bar 72 Barat, M., and W. Lichten, Phys. Rev. A **6**, 211 (1972).

Barr 68 Barrett, C. S., R. M. Mueller, and W. White, J. Appl. Phys. **39**, 4695 (1968).

Barr 69a Barrett, C. S., R. M. Mueller, and W. White, Trans. Metall. Soc. AIME **245**, 427 (1969).

Barr 69b Barrett, C. S., Trans. Metall. Soc. AIME **245**, 429 (1969).

Barr 70 Barret, C. S., M. A Barrett, R. M. Mueller, and W. White, J. Appl. Phys. **41**, 2727 (1970).

Baru 71 Baruch, P., F. Abel, C. Cohen, M. Bruneaux, D. W. Palmer, and H. Pabst, Radiat. Eff. **9**, 211 (1971).

Bas 59 Bassett, G. A., and D. W. Pashley, J. Inst. Met. **87**, 449 (1959).

Bat 62 Batterman, B. W., and D. R. Chipman, Phys. Rev. **127**, 690 (1962).

Bat 64 Batterman, B. W., and H. Cole, Rev. Mod. Phys. **36**, 681 (1964).

Bea 67 Bearden, J. A., Rev. Mod. Phys. **31**, 49 (1967).

Be 30 Bethe, H. A., Ann. Physik **5**, 325 (1930).

Beh 68 Behrisch, R., Can. J. Phys. **46**, 527 (1968).

Beh 69 Behrisch, R., G. Mühlbauer, and B. M. U. Scherzer, J. Phys. E (Sci. Instr.) **2**, 381 (1969).

Beh 71 Behrisch, R., B. M. U. Scherzer, and H. Schulze, Phys. Lett. A **35**, 181 (1971).

Beh 72 Behrisch, R., B. M. U. Scherzer, and H. Schulze, Radiat. Eff. **13**, 33 (1972).

Behn 69 Behnisch, R., F. Bell, and R. Sizmann, Phys. Status Solidi **33**, 375 (1969).

Bel 72a Beloshitsky, V. V., M. A. Kumakhov, and V. A Muralev, Radiat. Eff. **13**, 9 (1972).

Bel 72b Beloshitsky, V. V., and M. A Kumakhov, Zh. Eksp. Teor. Fiz. **62**, 1144 (1972) [Sov. Phys.—JETP **35**, 605 (1972)].

Bel 72c Beloshitsky, V. V., Y. V. Bulgakov, and M. A. Kumakhov, Phys. Lett. A **40**, 181 (1972).

Bell 65 Bell, F., and R. Sizmann, Phys. Lett. **19**, 171 (1965).

Bell 72 Bell, F., H. J. Kreiner and R. Sizmann, Phys. Lett. A **38**, 373 (1972).

Bely 71 Belyakov, V. A., Zh. Eksp. Teor. Fiz. Pis'ma Red. **13**, 254 (1971) [JETP Lett. **13**, 179 (1971)].

Berg 68 Bergström, I., K. Bjorkquist, B. Domeij, and G. Fladda, Can. J. Phys. **46**, 2679 (1968).

Berk 64 Berkhan, E., Z. Phys **178**, 101 (1964).

Betz 72 Betz, H. D., Rev. Mod. Phys. **44**, 465 (1972).

Bh 68 Bhalla, C. P., and J. N. Bradford, Phys. Lett. A **27**, 318 (1968).

Bh 70 Bhalla, C. P., J. N. Bradford, and G. Reese, in *Atomic Collision Phenomena in Solids* (North-Holland, Amsterdam, 1970), p. 361.

Bi 73 Biersack, J. P., and D. Fink, Nucl. Instrum. Methods **108**, 397 (1973).

Bir 64 Birks, J. B., *The Theory and Practice of Scintillation Counting* (Pergamon, New York, 1964).

Bj 70 Björkquist, K., D. Sigurd, G. Fladda, and G. Bjarnholt, Radiat. Eff. **6**, 141 (1970).

Bj 72 Björkquist, K., B. Cartling, and B. Domeij, Radiat. Eff. **12**, 267 (1972).

Bl 52 Blatt, J. M., and V. F Weisskopf, *Theoretical Nuclear Physics* (Wiley, New York), p. 336 (1952).

Blac 55 Blackman, M., in *Encyclopedia of Physics*, edited by S. Flügge (Springer, Berlin, 1955), Part I, Vol. 7, p. 377.

Blan 69 Blanchin, D., J.-C. Poizat, J. Remillieux, and A. Sarazin, Nucl. Instrum. Methods **70**, 98 (1969).

Blo 33a Bloch, F., Ann. Physik **16**, 285 (1933).

Blo 33b Bloch, F., Z. Phys. **81**, 363 (1933).

Bo 41 Borrmann, G., Phys. Z. **42**, 157 (1941).

Bø 64 Bøgh, E., J. A. Davies, and K. O. Nielsen, Phys. Lett. **12**, 129 (1964).

Bø 65a Bøgh, E., and E. Uggerhøj, Phys. Lett. **17**, 116 (1965).

Bø 65b Bøgh, E., and E. Uggerhøj, Nucl. Instrum. Methods **38**, 216 (1965).

Bø 67a Bøgh, E., Phys. Rev. Lett. **19**, 61 (1967).

Bø 67b Bøgh, E., and J. L. Whitton, Phys. Rev. Lett. **19**, 553 (1967)

Bø 67c Bøgh, E., in *Interaction of Radiation with Solids*, edited by (Plenum, New York, 1967), p. 361.

Bø 68a Bøgh, E., in *Solid State Physics Research with Accelerators*, Brookhaven National Laboratory Report No. BNL-50083, p. 76 (1968).

Bø 68b Bøgh, E., Can. J. Phys. **46**, 653 (1968).

Bø 69 Bøgh, E., Proc. R. Soc. Lond. A **311**, 35 (1969).

Bø 71 Bøgh, E., P. Høgild, and I. Stensgaard, Radiat. Eff. **7**, 115 (1971).

Bø 72 Bøgh, E., Radiat. Eff. **12**, 13 (1972).

Bob 73 Bobudaev, A. J., V. V. Kaplin, and S. A. Vorobeev, Phys. Lett. A 45, 71 (1973).

Boh 13 Bohr, N., Phil. Mag. **25**, 10 (1913)

Boh 40 Bohr, N., Phys. Rev. **58**, 654 (1940).

Boh 41 Bohr, N., Phys Rev. **59**, 270 (1941).

Boh 48 Bohr, N., K. Dan. Vidensk. Selsk. Mat.-Fys. Medd. **18**, No. 8 (1948).

Bon 69 Bonsignori, F., and A. DeSalvo, Nuovo Cimento Lett. **1**, 589 (1969).

Bon 70 Bonsignori, F., and A. DeSalvo, J. Phys. Chem. Solids **31**, 2191 (1970).

Bond 72 Bonderup, E., H. Esbensen, J. U. Andersen, and H. E. Schiøtt, Radiat. Eff. **12**, 261 (1972).

Boo 67 Booker, G. R., A. M. B. Shaw, M. J. Whelan, and P. B. Hirsch, Phil. Mag. **16**, 1185 (1967).

Boo 70 Booker, G. R., in *Modern Diffraction and Imaging Techniques in Material Science* edited by (North-Holland, Amsterdam, 1970), p. 613.

Bor 32 Born, M., and J. E. Mayer, Z. Phys. **75**, 1 (1932).

Bord 70 Borders, J. A., and S. T. Picraux, Rev. Sci. Instrum. **41**, 1230 (1970).

Bos 72 Boswarva, I. M., and P. Pirouz, J. Phys. C **5**, 2117 (1972).

Bøtt 69 Bøttiger, J., and F. Bason, Radiat. Eff. **2**, 105 (1969).

Br 65 Brandt, W., J. M. Khan, D. L. Potter, R. D. Worley, and H. P. Smith, Phys. Rev. Lett. **14**, 42 (1965).

Br 68 Brandt, W., R. Dobrin, H. Jack, R. Laubert, and S. Roth, Can. J. Phys. **46**, 537 (1968).

Br 70a Brandt, W., and J. Reinheimer, Phys. Rev. B **2**, 3104 (1970).

Br 70b Brandt, W., and R. Laubert, Phys. Rev. Lett. **24**, 1037 (1970).

Br 71 Brandt, W., and R. Sizmann, Phys. Lett. A **37**, 115 (1971).

Br 73a Brandt, W., K. W. Jones, and H. W. Kraner, Phys. Rev. Lett. **30**, 351 (1973).

Br 73b Brandt, W., R. Laubert, M. Mourino, and A. Schwarzschild, Phys. Rev. Lett. **30**, 358 (1973).

Bri 68 Brice, D. K., Phys. Rev. **165**, 475 (1968).

Bro 69 Bronder, Th., and J. Jakschik, Phys. Lett. A **29**, 580 (1969).

Bro 72 Bronder, Th., and J. Jakschik, Radiat. Eff. **13**, 209 (1972).

Brow 68 Brown, F., D. A. Marsden, and R. D. Werner, Phys. Rev. Lett. **20**, 1449 (1968).

Bu 71 Bulckaen, V., and L. Paganini, Rev. Sci. Instrum. **42**, 1687 (1971).

Bulg 71 Bulgakov, Y. V., T. I. Kolomenskaya, and M. A. Kumakhov, Phys. Status Solidi A **5**, 591 (1971).

Ca 70 Campisano, S. U., G. Foti, F. Grasso, R. Quattrocchi, and E. Rimini, Phys. Lett. A **33**, 433 (1970).

Ca 71 Campisano, S. U., F. Grasso, and E. Rimini, Radiat. Eff. **9**, 153 (1971).

Ca 72a Campisano, S. U., G. Foti, F. Grasso, M. Lo Savio, and E. Rimini, Radiat. Eff **13**, 157 (1972).

Ca 72b Campisano, S. U., G. Foti, F. Grasso, I. F. Quercia, and E. Rimini, Radiat. Eff. **13**, 23 (1972).

Ca 72c Campisano, S. U., G. Foti, F. Grasso, and E. Rimini, Appl. Phys. Lett. **21**, 425 (1972).

Cai 68 Cairns, J. A., and R. S. Nelson, Phys. Lett. A **27**, 14 (1968).

Cai 71 Cairns, J. A., R. S. Nelson and J. S. Briggs in *Ion Implantation in Semiconductors*, edited by (Springer, Berlin, 1970), p. 299.

Cai 72 Cairns, J. A., A. D. Marwick, R. S. Nelson, and J. S. Briggs, Radiat. Eff. **12**, 7 (1972).

Car 72 Carstanjen, H. D., and R. Sizmann, Radiat. Eff. **12**, 225 (1972).

Cay 71 Caywood, J. M., T. A. Tombrello, and T. A. Weaver, Phys. Lett. A **37**, 350 (1971).

Ch 66 Chadderton, L. T., Phys. Lett. **23**, 303 (1966).

Ch 68a Chadderton, L. T., Thin Films **1**, 157 (1968).

Ch 68b Chadderton, L. T., Phil. Mag. **18**, 1017 (1968).

Ch 68c Chadderton, L. T., and M. G. Anderson, Phys. Lett. A **27**, 665 (1968).

Ch 69a Chadderton, L. T., and M. G. Anderson, Thin Films **1**, 229 (1969).

Ch 69b Chadderton, L. T., and F. H. Eisen, Phil. Mag. **20**, 195 (1969).

Ch 70a Chadderton, L. T., J. Appl. Crystallogr. **3**, 429 (1970).

Ch 70b Chadderton, L. T., and F. G. Krajenbrink, in *Atomic Collision Phenomena in Solids*, edited by (North-Holland, Amsterdam, 1968), p. 456.

Ch 71a Chadderton, L. T., and F. H. Eisen, Radiat. Eff. **7**, 129 (1971).

Ch 71b Chadderton, L. T., Radiat. Eff. **8**, 77 (1971).

Chap 72 Chapman, G. E., B. W. Farmery, M. W. Thompson, and I. H. Wilson, Radiat. Eff. **13**, 121 (1972).

Che 68 Cheshire, I. M., G. Dearnaley, and J. M. Poate, Phys. Lett. A **27**, 304 (1968).

Che 69 Cheshire, I. M., G. Dearnaley, and J. M. Poate, Proc. R. Soc. Lond. A **311**, 47 (1969).

Che 70 Cheshire, I. M., and J. M. Poate, in *Atomic Collision Phenomena in Solids*, edited by (North-Holland, Amsterdam, 1970), p. 351.

Cho 71 Choudhury, A., S. Chaudhuri, K. Goswamy, and H. B. De, Phys. Status Solidi B **47**, K103 (1971).

Cl 69 Clark, G. J., G. Dearnaley, D. V. Morgan, and J. M. Poate, Phys. Lett. A **30**, 11 (1969).

Cl 70 Clark, G. J., D. V. Morgan, and J. M. Poate, in *Atomic Collision Phenomena in Solids*, edited by (North-Holland, Amsterdam), p. 388. (1970).

Cl 71 Clark, G. J., J. M. Poate, E. Fuschini, C. Maroni, I. G. Massa, A. Uguzzoni, and E. Verondini, Nucl. Phys. A **173**, 73 (1971).

Cl 72 Clark, G. J., E. Fuschini, C. Maroni, I. G. Massa, F. Malaguti, A. Uguzzoni, E. Verondini, and D. Wilmore, in *Statistical Properties of Nuclei*, edited by (Plenum Press, New York, 1972), p. 535.

Cli 72 Clinard, F. W., and M. W. Sanders, J. Appl. Phys. **43**, 4937 (1972).

Co 68 Cowley, J. M., Phys. Lett. A **26**, 623 (1968).

Coa 67 Coates, D. G., Phil Mag. **16**, 1179 (1967).

Col 69 Colombie, N., B. Fagot, and C. Fert, Radiat. Eff. **2**, 31 (1969).

Cou 51 Courant, E. D., Rev. Sci. Instrum. **33**, 1003 (1951).

Da 65a Datz, S., T. S. Noggle, and C. D. Moak, Nucl. Instrum. Methods **38**, 221 (1965).

Da 65b Datz, S., T. S. Noggle, and C. D. Moak, Phys. Rev. Lett. **15**, 254 (1965).

Da 67 Datz, S., C. Erginsoy, G. Leibfried, and H. O. Lutz, Ann. Rev. Nucl. Sci. **17**, 129 (1967).

Da 69 Datz, S., C. D. Moak, T. S. Noggle, B. R. Appleton, and H. O. Lutz, Phys. Rev. **179**, 315 (1969).

Da 70 Datz, S., C. D. Moak, B. R. Appleton, M. T. Robinson, and O. S. Oen, in *Atomic Collisions in Solids*, edited by (North-Holland, Amsterdam, 1970), p. 374.

Da 71 Datz, S., C. D. Moak, B. R. Appleton, and T. A. Carlson, Phys. Rev. Lett. **27**, 363 (1971).

Da 72 Datz, S., F. W. Martin, C. D. Moak, B. R. Appleton, and L. B. Bridwell, Radiat. Eff. **12**, 163 (1972).

Dal 72 Dale, E. B., G. C. Poole, S. Özkök, and H. Goldberg, Radiat. Eff. **13**, 3 (1972).

Dav 60a Davies, J. A., J. Friesen, and J. D. McIntyre, Can. J. Chem. **38**, 1526 (1960).

Dav 60b Davies, J. A., J. D. McIntyre, R. L. Cushing, and M. Lounsbury, Can. J. Chem. **38**, 1535 (1960).

Dav 67a Davies, J. A., Chalk River Report No. AECL-2757 (1967).

Dav 67b Davies, J. A., J. Denhartog, L. Eriksson, and J. W. Mayer, Can. J. Phys. **45**, 4053 (1967).

Dav 68a Davies, J. A., J. Denhartog, and J. L. Whitton, Phys. Rev. **165**, 345 (1968).

Dav 68b Davies, J. A., L. Eriksson, and J. L. Whitton, Can. J. Phys. **46**, 573 (1968).

Dav 69 Davies, J. A., L. Eriksson, N. G. E. Johansson, and I. V. Mitchell, Phys. Rev. **181**, 548 (1969).

Dav 72a Davies, J. A., L. M. Howe, D. A. Marsden, and J. L. Whitton, Radiat. Eff. **12**, 247 (1972).

Dav 72b Davies, J. A., in *The Structure of Nuclei*, edited by (International Atomic Energy Agency, Vienna, 1972), p. 457.

De 64 Dearnaley, G., IEEE Trans. Nucl. Sci. **NS-11**, 249 (1964).

De 67 Dearnaley, G., and M. A. Wilkins, J. Sci. Instrum. **44**, 880 (1967).

De 68a Dearnaley, G., B. W. Farmery, I. V. Mitchell, R. S. Nelson, and M. W. Thompson, in *Solid State Physics Research with Accelerators*, Brookhaven National Laboratory Report No. BNL-50083, p. 125 (1968).

De 68b Dearnaley, G., I. V. Mitchell, R. S. Nelson, B. W. Farmery, and M. W. Thompson, Phil. Mag. **18**, 985 (1968).

De 68c Dearnaley, G., J. H. Freeman, G. A. Ward, and M. A. Wilkins, Can. J. Phys. **46**, 587 (1968).

De 69a Dearnaley, G., Rep. Prog. Phys. **32**, 405 (1969).

De 69b Dearnaley, G., Proc. R. Soc. Lond. A **311**, 21 (1969).

Del 71 Della Mea, G., A. V. Drigo, S. Lo Russo, P. Mazzoldi, and G. G. Bentini, Phys. Rev. Lett. **27**, 1194 (1971).

Del 72 Della Mea, G., A. V. Drigo, S. Lo Russo, P. Mazzoldi, and G. G. Bentini, Radiat. Eff. **13**, 115 (1972).

Del 73 Della Mea, G., A. V. Drigo, S. Lo Russo, P. Mazzoldi, A. DeSalvo, and R. Rosa, Phys. Rev B **7**, 4029 (1973).

Dels 70 Delsarte, G., J. C. Jousset, J. Mory, and Y. Quéré, in *Atomic Collision Phenomena in Solids*, edited by (North-Holland, Amsterdam, 1970), p. 501.

Dels 71 Delsarte, G., G. Désarmot, and J. Mory, Phys. Status Solidi A **5**, 683 (1971).

Dem 72 Demichelis, F., R. Liscia, and A. Tartaglia, Nuovo Cimento Lett. **5**, 918 (1972).

DeS 68 DeSalvo, A., Phys. Lett. A **26**, 608 (1968).

DeW 66 DeWames, R. E., W. F. Hall, and G. W. Lehman, Phys. Rev. **148**, 181 (1966).

DeW 67 DeWames, R. E., W. F. Hall, and L. T. Chadderton, Phys. Lett. A **24**, 686 (1967).

DeW 68a DeWames, R. E., W. F. Hall, and L. T. Chadderton, in *Solid State Physics Research with Accelerators*, Brookhaven National Laboratory Report No. BNL-50083, p. 3 (1968).

DeW 68b DeWames, R. E., W. F. Hall, and G. W. Lehman, Phys. Rev. **174**, 392 (1968).

DeW 68c DeWames, R. E., and W. F. Hall, Acta Crystallogr. A **24**, 206 (1968).

DeW 70a DeWames, R. E., L. T. Chadderton, and E. R. Cohen, Radiat. Eff. **5**, 195 (1970).

DeW 70b DeWames, R. E., and W. F. Hall, Radiat. Eff. **5**, 197 (1970).

Di 70 Didenko, A. I., S. A. Vorob'ev, and I. A. Tsekhanovskii, Zh. Eksp. Teor. Fiz. Pis'ma Red. **12**, 310 (1970) [JETP Lett. **12**, 209 (1970)].

Do 65a Domeij, B., and K. Björkquist, Phys. Lett. **14**, 127 (1965).

Do 65b Domeij, B., Nucl. Instrum. Methods **38**, 207 (1965).

Do 66 Domeij, B., Ark. Fys. **32**, 179 (1966).

Do 70 Domeij, B., G. Fladda, and N. G. E. Johansson, Radiat. Eff. **6**, 155 (1970).

Du 64 Dupouy, G., and F. Perrier, J. Microsc. **3**, 233 (1964).

Dun 62 Duncumb, P., Phil. Mag. **7**, 2101 (1962).

Eb 70 Ebel, M. E., Phys. Rev. Lett. **24**, 1395 (1970).

Ec 70 Ecker, K., V. Lottner, S. F. Schmid, and R. Sizmann, in *Atomic Collision Phenomena in Solids*, edited by (North-Holland, Amsterdam, 1970), p. 455.

Ed 70 Edge, R. D., and R. L. Dixon, in *Atomic Collision Phenomena in Solids*, edited by (North-Holland, Amsterdam, 1970), p. 435.

Ed 72a Edge, R. D., W. R. Hedrick, and R. L. Dixon, Radiat. Eff. **12**, 97 (1972).

Ed 72b Edge, R. E., C. Varelas, and R. Sizmann, Radiat. Eff. **16**, 95 (1972).

Ei 66 Eisen, F. H., Phys. Lett. **23**, 401 (1966).

Ei 68 Eisen, F. H., Can. J. Phys. **46**, 561 (1968).

Ei 70 Eisen, F. H., B. Welch, J. E. Westmoreland, and J. W. Mayer, in *Atomic Collision Phenomena in Solids*, edited by (North-Holland, Amsterdam, 1970), p. 111.

Ei 71a Eisen, F. H., and M. T. Robinson, Phys. Rev. B **4**, 1457 (1971).

Ei 71b Eisen, F. H., and B. Welch, Radiat. Eff. **7**, 143 (1971)

Ei 71c Eisen, F. H., in *Ion Implantation in Semiconductors*, edited by (Springer, Berlin), p. 287 (1971).

Ei 72a Eisen, F. H., G. J. Clark, J. Bøttiger, and J. M. Poate, Radiat. Eff. **13**, 93 (1972).

Ei 72b Eisen, F. H., and E. Uggerhøj, Radiat. Eff. **12**, 233 (1972).

El 67 Ellegaard, C., and N. O. Lassen, K. Dan. Vidensk. Selsk. Mat.-Fys. Medd. **35**, No. 16 (1967).

El-H 68 El-Hoshy, A. H., and J. F. Gibbons, Phys. Rev. **173**, 454 (1968).

Eli 70 Elich, J. J. P., and H. E. Roosendaal, Phys. Lett. A **33**, 235 (1970).

Elt 70 Eltekov, V. A., D. S. Karpuzov, Y. V. Martynenko, and V. E. Yurasova, in *Atomic Collision Phenomena in Solids*, edited by (North-Holland, Amsterdam, 1970), p. 657.

Elt 72 Eltekov, V. A., D. S. Karpuzov, Y. V. Martynenko, E. A. Rubakha, V. A. Simonov, and V. E. Yurasova, Radiat. Eff. **13**, 237 (1972).

En 70 Engelmohr, G. O., R. M. Mueller, and W. White, Nucl. Instrum. Methods **83**, 160 (1970).

Er 64 Erginsoy, C., H. E. Wegner, and W. M. Gibson, Phys. Rev. Lett. **13**, 530 (1964).

Er 65 Erginsoy, C., Phys. Rev. Lett. **15**, 360 (1965).

Er 68 Erginsoy, C., in *Solid State Physics Research with Accelerators*, Brookhaven National Laboratory Report No. BNL-50083, p. 30 (1968).

Erik 67a Eriksson, L., J. A. Davies, and P. Jespersgaard, Phys. Rev. **161**, 219 (1967).

Erik 67b Eriksson, L., Phys. Rev. **161**, 235 (1967).

Erik 69a Eriksson, L., and J. A. Davies, Ark. Fys. **39**, 439 (1969).

Erik 69b Eriksson, L., J. A. Davies, N. G. E. Johansson, and

J. W. Mayer, J. Appl. Phys. **40**, 842 (1969).
Ev 55 Everhart, E., G. Stone, and R. J. Carbone, Phys. Rev. **99**, 1287 (1955).
Fa 63 Fano, U., Annu. Rev. Nucl. Sci. **13**, 1 (1963).
Fa 65 Fano, U., and W. Lichten, Phys. Rev. Lett. **14**, 627 (1965).
Far 65 Farmery, B. W., R. S. Nelson, R. Sizmann, and M. W. Thompson, Nucl. Instrum. Methods **38**, 231 (1965).
Far 70 Farmery, B. W., A. D. Marwick, and M. W. Thompson, in *Atomic Collision Phenomena in Solids*, edited by (North-Holland, Amsterdam), p. 589.
Fas 66 Fastrup, B., P. Hvelplund, and C. A. Sautter, K. Dan. Vidensk. Sels. Mat.-Fys. Medd. **35**, No. 10 (1966).
Fe 47 Fermi, E., and E. Teller, Phys. Rev. **72**, 399 (1947).
Fei 73 Feijen, H. H. W., L. K. Verhey and A. L. Boers, Phys. Lett. A **45**, 31 (1973).
Fel 68 Feldman, L. C., B. R. Appleton, and W. L. Brown, in *Solid State Physics Research with Accelerators*, Brookhaven National Laboratory Report No. BNL-50083, p. 58 (1968).
Fel 69 Feldman, L. C., and B. R. Appleton, Appl. Phys. Lett. **15**, 305 (1969).
Fel 70a Feldman, L. C., and J. W. Rodgers, J. Appl. Phys. **41**, 3776 (1970).
Fel 70b Feldman, L. C., W. M. Augustyniak, and J. L. Merz, Radiat. Eff. **6**, 293 (1970).
Fel 71 Feldman, L. C., E. N. Kaufmann, D. W. Mingay, and W. M. Augustyniak, Phys. Rev. Lett. **27**, 1145 (1971).
Fel 72a Feldman, L. C., and D. E. Murnick, Phys. Rev. B **5**, 1 (1972).
Fel 72b Feldman, L. C., D. W. Mingay, and J. P. F. Sellschop, Radiat. Eff. **13**, 145 (1972).
Fer 70 Ferretti, B., in *Evolution of Particle Physics*, edited by (Academic Press, New York, 1970), p. 88.
Fi 57 Firsov, O. B., Zh. Eksp. Teor. Fiz. **33**, 696 (1957) [Sov. Phys.-JETP **6**, 534 (1958)].
Fi 59 Firsov, O. B., Zh. Eksp. Teor. Fiz. **36**, 1517 (1959) [Sov. Phys.-JETP **9**, 1076 (1959)].
Fi 69 Firsov, O. B., Dokl. Akad. Nauk SSSR **189**, 302 (1969) [Sov. Phys.-Dokl. **14**, 1092 (1970)].
Fi 70 Firsov, O. B., in *Atomic Collision Phenomena in Solids*, edited by (North-Holland, Amsterdam, 1970), p. 301.
Fin 70 Fink, D., and U. Fischmann, Nucl. Instrum. Methods **100**, 549 (1972).
Fis 69 Fischer, H., R. Sizmann, and F. Bell, Z. Phys. **224**, 135 (1969).
Fl 69 Fladda, G., P. Mazzoldi, E. Rimini, D. Sigurd, and L. Eriksson, Radiat. Eff. **1**, 249 (1969).
Fl 70 Fladda, G., K. Björkquist, L. Eriksson, and D. Sigurd, Appl. Phys. Lett. **16**, 313 (1970).
Flu 64 Fluit, J. M., and P. K. Rol, Physica **30**, 857 (1964).
Fo 67 Fowler, H. A., and C. Erginsoy, Phys. Lett. A **24**, 390 (1967).
Fon 72 Fontell, A., E. Arminen, and E. Leminen, Radiat. Eff. **12**, 255 (1972).
For 69 Fortner, R. J., B. P. Curry, R. C. Der, T. M. Kavanagh, and J. M. Khan, Phys. Rev. **185**, 164 (1969).
Fot 69 Foti, G., F. Grasso, and E. Rimini, Nuovo Cimento Lett. **1**, 941 (1969).
Fot 70a Foti, G., F. Grasso, R. Quattrocchi, I. F. Quercia, and E. Rimini, Nuovo Cimento Lett. **4**, 707 (1970).
Fot 70b Foti, G., F. Grasso, R. Quattrocchi, I. F. Quercia, and E. Rimini, Phys. Lett. A **31**, 214 (1970).
Fot 71 Foti, G., F. Grasso, R. Quattrocchi, and E. Rimini, Phys. Rev. B **3**, 2169 (1971).
Fr 70 Francken, L., and D. Onderdelinden, in *Atomic Collision Phenomena in Solids*, edited by (North-Holland, Amsterdam, 1970), p. 266.
Fu 71 Fuschini, E., C. Maroni, I. Massa, A. Uguzzoni, and E. Verondini, Nucl. Instrum. Methods **91**, 487 (1971).
Fu 72 Fuschini, E., F. Malaguti, C. Maroni, I. Massa, A. Uguzzoni, E. Verondini, and G. J. Clark, Nuovc Cimento A **10**, 177 (1972).
Fuj 69 Fujimoto, F., K. Komaki, K. Ozawa, M. Mannami, and T. Sakurai, Phys. Lett. A **29**, 332 (1969).
Fuj 70 Fujimoto, F., K. Komaki, H. Nakayama, and M. Ishii, Phys. Lett. A **33**, 432 (1970).
Fuj 71a Fujimoto, F., K. Komaki, and H. Nakayama, Phys. Status Solidi A **5**, 725 (1971).
Fuj 71b Fujimoto, F., K. Komaki, H. Nakayama, and M. Ishii, Phys. Status Solidi A **6**, 623 (1971).
Fuj 71c Fujimoto, F., K. Komaki, K. Hisatake, and H. Nakayama, Phys. Status Solidi A **5**, 737 (1971).
Fuj 71d Fujimoto, F., K. Komaki, M. Maruyama, K. Tsukada, K. Ozawa, M. Mannami, and T. Sakurai, Phys. Status Solidi A **4**, 485 (1971).
Fuj 72a Fujimoto, F., S. Takagi, K. Komaki, H. Koike, and Y. Uchida, Radiat. Eff. **12**, 153 (1972).
Fuj 72b Fujimoto, F., K. Komaki, H. Nakayama, and M. Ishii, Radiat. Eff. **13**, 43 (1972).
Ga 73a Gaillard, M. J., J.-C. Poizat, J. Remillieux, and M. L. Gaillard, Phys. Lett. A **45**, 306 (1973).
Ga 73b Gaillard, M. J., J.-C. Poizat, and J. Remillieux, Phys. Lett. A **45**, 325 (1973).
Ge 65 Gemmell, D. S., and R. E. Holland, Phys. Rev. Lett. **14**, 945 (1965).
Ge 71 Gemmell, D. S., and J. N. Worthington, Nucl. Instrum. Methods **91**, 1 (1971).
Ge 72a Gemmell, D. S., and R. C. Mikkelson, Radiat. Eff. **12**, 21 (1972).
Ge 72b Gemmell, D. S., and R. C. Mikkelson, Phys. Rev. B **6**, 1613 (1972).
Ger 72 Gerasimov, A. I., E. I. Zorin, P. V. Pavlov, and D. I. Tetelbaum, Phys. Status Solidi **12**, 679 (1972).
Gev 70 Gevers, R., 1970, in *Modern Diffraction and Imaging Techniques in Material Science*, edited by (North-Holland, Amsterdam), p. 1.
Gi 65 Gibson, W. M., C. Erginsoy, H. E. Wegner, and B. R. Appleton, Phys. Rev. Lett. **15**, 357 (1965).
Gi 68a Gibson, W. M., J. B. Rasmussen, P. Ambrosias-Olesen, and C. J. Andreen, Can. J. Phys. **46**, 551 (1968); erratum, Can. J. Phys. **47**, 1756 (1969).
Gi 68b Gibson, W. M., F. W. Martin, R. Stensgaard, F. P. Jensen, N. I. Meyer, G. Galster, A. Johansen, and J. S. Olsen, Can. J. Phys. **46**, 675 (1968).
Gi 69 Gibson, W. M., and K. O. Nielsen, in *Physics and Chemistry of Fission* (International Atomic Energy Agency, Vienna, 1969), p. 861.
Gi 70 Gibson, W. M., and K. O. Nielsen, Phys. Rev. Lett. **24**, 114 (1970).
Gi 72a Gibson, W. M., and J. Golovchenko, Phys. Rev. Lett. **28**, 1301 (1972).
Gi 72b Gibson, W. M., Y. Hashimoto, R. J. Keddy, M. Maruyama, and G. M. Temmer, Phys. Rev. Lett. **29**, 74 (1972).
Gi 71 Gleich, W., G. Regenfus and R. Sizmann, Phys. Rev. Lett. **27**, 1066 (1971).
Go 56 Gombas, P., in *Handbuch der Physik*, edited by (Springer, Berlin, 1956), Vol. 36, p. 109.
Goo 70 Goode, P. D., M. A. Wilkins, and G. Dearnaley, Radiat. Eff. **6**, 237 (1970).
Gor 69 Gorodetzky, S., A. Pape, E. L. Cooperman, A. Chevallier, J. C. Sens, and R. Armbruster, Nucl. Instrum. Methods **70**, 11 (1969).
Gori 66 Goringe, M. J., A. Howie, and M. J. Whelan, Phil. Mag. **14**, 217 (1966).
Gr 72 Grasso, F., M. Lo Savio, and E. Rimini, Radiat. Eff. **12**, 149 (1972).
Gra 66 Grachev, B. D., A. P. Komar, Y. S. Korobochko and V. I. Mineev, Zh. Eksp. Teor. Fiz, Pis'ma Red. **4**, 241 (1966) [JETP Lett. **4**, 163 (1966)].
Gra 68 Grachev, B. D., A. P. Komar, Y. S. Korobochko, and V. I. Mineev, Fiz. Tverd. Tela **10**, 2408 (1968) [Sov. Phys.-Solid State **10**, 1894 (1969)].
Gran 72 Grant, W. A., and J. N. Baruah, Radiat. Eff. **14**, 261 (1972).
Gray 63 *American Institute of Physics Handbook*, edited by D. E. Gray (McGraw-Hill, New York), pp. 4–61 (1963).
Gu 70 Gurvich, L. G., and U. Yarkulov, Fiz. Tverd. Tela

12, 1427 (1970) [Sov. Phys.-Solid State **12**, 1121 (1970)].

Gv 72 Gverdtsiteli, I. G., A. L. Guldamashvili, E. M. Diasamidze, A. N. Kalinin, and Y. W. Martynenko, Radiat. Eff. **12**, 73 (1972).

Gy 70 Gyulai, J., O. Meyer, J. W. Mayer and V. Rodriguez, Appl. Phys. Lett. **16**, 232 (1970).

Gy 71 Gyulai, J., O. Meyer, R. D. Pashley, and J. W. Mayer, Radiat. Eff. **7**, 17 (1971).

Ha 68 Harrison, D. E., Appl. Phys. Lett. **13**, 277 (1968).

Hal 66 Hall, C. R., Proc. R. Soc. A **295**, 140 (1966).

Ham 66 Hamilton, G. F., and A. R. Quinton, Phys. Lett. **22**, 312 (1966).

Han 72 Hansteen, J. M., and O. P. Mosebekk, in *Proceedings of the International Conference on Inner Shell Ionization Phenomena and Future Applications, Atlanta, Georgia, 17–22 April 1972*, U. S. Atomic Energy Commission Report No. CONF-720404, Vol. 2, p. 936.

Har 70 Hart, R. R., Radiat. Eff. **6**, 51 (1970).

Has 73 Hashimoto, Y., J. H. Barrett, and W. M. Gibson, Phys. Rev. Lett. **30**, 995 (1973).

He 71a Hellborg, R., Physica Scripta **3**, 279 (1971).

He 71b Hellborg, R., Physica Scripta **4**, 75 (1971).

He 73 Hellborg, R., Physica Scripta **7**, 289 (1973).

Hi 70 Hines, R. L., Phys. Lett. A **33**, 348 (1970).

Hir 65 Hirsch, P. B., A. Howie, R. B. Nicholson, D. W. Pashley, and M. J. Whelan, *Electron Microscopy of Thin Crystals* (Butterworths, London, 1965).

Ho 68 Holland, R. E., and D. S. Gemmell, Phys. Rev. **173**, 344 (1968).

Hög 70 Högberg, G., H. Nordén, and R. Skoog, Phys. Status Solidi **42**, 441 (1970).

How 66 Howie, A., Phil. Mag. **14**, 223 (1966).

How 68 Howie, A., in *Solid State Physics Research with Accelerators*, Brookhaven National Laboratory Report No. BNL-50083, p. 15 (1968).

How 70a Howie, A., M. S. Spring, and P. N. Tomlinson, in *Atomic Collision Phenomena in Solids*, edited by (North-Holland, Amsterdam, 1970), p. 34.

How 70b Howie, A., in *Modern Diffraction and Imaging Techniques in Material Science* (North-Holland, Amsterdam, 1970), p. 295.

Howe 71 Howe, L. M., and S. Schmid, Can. J. Phys. **49**, 2321 (1971).

Hu 71 Huzimura, R., Y. Ato, and S. Miyagawa, Phys. Lett. A **37**, 81 (1971).

Hub 72 Huber, H., C. Jaccard, and M. Roulet, Radiat. Eff. **12**, 241 (1972).

Hum 70 Humphreys, C. J., and J. S. Lally, J. Appl. Phys. **41**, 232 (1970).

Hv 71 Hvelplund, P., K. Dan. Vidensk. Selsk. Mat.-Fys. Medd. **38**, No. 4 (1971).

Ib 68 Ibel, K., and R. Sizmann, Phys. Status Solidi **29**, 403 (1968).

If 67 Iferov, G. A., G. P. Pokhil, and A. F. Tulinov, Zh. Eksp. Teor. Fiz. Pis'ma Red. **5**, 250 (1967) [JETP Lett. **5**, 250 (1967)].

Is 72 Ishitani, T., R. Shimizu, and K. Murata, Phys. Status Solidi B **50**, 681 (1972).

Iu 72 Iue, N., N. Matsunami, K. Morita, N. Itoh, M. Yoshida, and S. Hirota, Radiat. Eff. **14**, 191 (1972).

Ja 72 Jack, H. E., Radiat. Eff. **13**, 101 (1972).

Je 70 Jech, C., Phys. Status Solidi A **3**, 579 (1970).

Je 72 Jech, C., Phys. Lett. A **39**, 417 (1972).

Jo 69 Johansen, A., J. S. Olsen, S. Steenstrup, and J. Koch, Radiat. Eff. **2**, 19 (1969).

Jo 70 Johansen, A., J. S. Olsen, L. Sarholt-Kristensen, and F. W. Martin, Radiat. Eff. **3**, 65 (1970).

Joy 69 Joy, D. C., E. M. Schulson, J. P. Jakubovics, and C. G. Van Essen, Phil. Mag. **20**, 843 (1969).

Ka 70 Kagan, Y., and Y. V Kononets, Zh. Eksp. Teor. Fiz. **58**, 226 (1970) [Sov. Phys.—JETP **31**, 124 (1970)].

Kal 68 Kalashnikov, N. P., M. I. Ryazanov, and F. N. Chukhovskii, Zh. Eksp. Teor. Fiz. **54**, 822 (1968) [Sov. Phys.—JETP **27**, 441 (1968)].

Kal 72 Kalashnikov, N. P., E. A. Koptelov, and M I. Ryazanov, Fiz. Tverd. Tela **14**, 1211 (1972) [Sov. Phys.—Solid State **14**, 1033 (1972)].

Kam 72a Kamanin, V. V., S. A. Karamyan, F. Normuratov, and S. P. Tret'yakova, Yad. Fiz. **16**, 447 (1972) [Sov. J. Nucl. Phys. **16**, 249 (1973)].

Kam 72b Kamanin, V. V., S. A. Karamyan, A. M. Kucher, F. Normuratov, and Y. T. Oganesyan, Yad. Fiz. **16**, 252 (1972) [Sov. J. Nucl. Phys. **16**, 140 (1973)].

Kami 69 Kaminsky, M., Phys. Rev. Lett. **23**, 819 (1969).

Kami 70 Kaminsky, M., in *Recent Developments in Mass Spectrometry*, edited by (University of Tokyo Press, Tokyo, 1970), p. 1167.

Kami 71 Kaminsky, M., in *Polarization Phenomena in Nuclear Reactions*, edited by (University of Wisconsin Press, Madison, Wisconsin), p. 803 (1971).

Kar 70 Karamyan, S. A., Y. V. Melikov, F. Normuratov, O. Otgonsuren, and G. M. Solovieva, Dubna Report No. P7-5300 (1970).

Kar 71a Karamyan, S. A., Y. V. Melikov, F. Normuratov, O. Otgonsuren, and G. M. Solovieva, Yad. Fiz. **13**, 944 (1971) [Sov. J. Nucl. Phys. **13**, 543 (1971)].

Kar 71b Karamyan, S. A., Y. T. Oganesyan, and F. Normuratov, Yad. Fiz. **14**, 499 (1971) [Sov. J. Nucl. Phys. **14**, 279 (1972)].

Ka 73 Karamyan, S. A., Y. V. Melikov, and A. F. Tulinov, Fiz. El. Chast. Atom. Yad., (1973) **4**, 456 [Sov. J. Particles Nucl., **4**, 196 (1973)].

Kau 73 Kaufman, E. N., J. M. Poate, and W. M. Augustyniak, Phys. Rev. B **7**, 951 (1973).

Ke 71 Kessel'man, V. S., Zh. Tekh. Fiz. **41**, 1708 (1971) [Sov. Phys.—Tech. Phys. **16**, 1346 (1972)].

Ke 72 Kessel'man, V. S., Zh. Tekh. Fiz. **42**, 1161 (1972) [Sov. Phys.—Tech. Phys. **17**, 923 (1972)].

Kei 60 Keil, E., E. Zeitler, and W. Zinn, Z. Naturforsch. A **15**, 1031 (1960).

Kh 66 Khan, J. M., D. L. Potter, R. D. Worley, and H. P. Smith, Phys. Rev. **148**, 413 (1966).

Kh 67a Khan, J. M., D. L. Potter, R. D. Worley, S. I. Salem, and H. P. Smith, Phys. Rev. Lett. **19**, 950 (1967).

Kh 67b Khan, J. M., D. L. Potter, R. D. Worley, and H. P. Smith, Phys. Rev. **163**, 81 (1967).

Ki 72 Kitagawa, M., and Y. H. Ohtsuki, Phys. Rev. B **5**, 3418 (1972).

Kir 72 Kirsch, R., Thesis, University of Lyon, France, (1972).

Kn 70 Knox, K. C., Nucl. Instrum. Methods **81**, 202 (1970).

Ko 69 Komaki, K., and F. Fujimoto, Phys. Lett A **29**, 544 (1969).

Ko 70 Komaki, K., and F. Fujimoto, Phys. Status Solidi **2**, 875 (1970).

Ko 72 Komaki, K., F. Fujimoto, H. Nakayama, M. Ishii, and K. Hisatake, Phys. Lett. B **38**, 218 (1972).

Kob 68 Kobayakawa, M., H. Niwa, S. Tanemura, K. Suzuki, and K. Shinzi, J. Phys. Soc. Jap. **24**, 645 (1968).

Kob 70 Kobayakawa, M., H. Niwa, S. Tanemura, K. Suzuki, and K. Shinzi, J. Phys. Soc. Jap. **28**, 250 (1970).

Kom 73 Komarov, F. F., and M. A. Kumakhov, Phys. Status Solidi B **58**, 389 (1973).

Kon 69 Kononov, B. A., and V. K. Struts, Fiz. Tverd. Tela **11**, 3577 (1969) [Sov. Phys.—Solid State **11**, 2994 (1970)].

Kon 70 Kononov, V. A., and B. K. Struts, Izv. VUZ. Fiz **6**, 60 (1970) [Sov. Phys. J. **6** (1970)].

Kor 70 Korobochko, Y. S., B. D. Grachev, and V. I. Mineev, Fiz. Tverd. Tela **12**, 3450 (1970) [Sov. Phys.—Solid State **12**, 2802 (1971)].

Kr 47 Kramers, H. A., Physica **13**, 401 (1947).

Ku 69 Kuvakin, M. V., and O. A. Romanyuk, Izvest. Akad. Nauk SSR, Ser. Fiz. **33**, 694 (1969) [Bull. Acad. Sci. USSR, Phys. Ser. **33**, 752 (1969)].

Kub 73 Kubota, Y., and Y. H. Ohtsuki, Phys. Lett. A **43**, 521 (1973).

Kud 73 Kudrin, V. V., Y. A. Timoshnikov and S. A. Vorobev, Phys. Status Solidi B **58**, 409 (1973).

Kul 67 Kulikauskas, V. S., M. M. Malov, and A. F. Tulinov, Zh. Eksp. Teor. Fiz. **53**, 487 (1967) [Sov. Phys. JETP **26**, 321 (1968)].

Kule 72 Kuleshov, E. A., V. A. Stupak, and E. T. Shipatov, Fiz. Tverd. Tela **14**, 258 (1972) [Sov. Phys.—Solid State **14**, 209 (1972)].

Kum 68a Kumakhov, M. A., Fiz. Tverd. Tela **10**, 2854 (1968) [Sov. Phys.—Solid State **10**, 2254 (1969)].

Kum 68b Kumakhov, M. A., Phys. Status Solidi **30**, 379 (1968).

Kum 69 Kumakhov, M. A., Phys. Lett. A **29**, 243 (1969).

Kum 70a Kumakov, M. A., Phys. Lett. A **33**, 133 (1970).

Kum 70b Kumakhov, M. A., Phys. Lett. A **32**, 538 (1970).

Kum 71 Kumakhov, M. A., Phys. Lett. A **37**, 153 (1971).

Kum 72a Kumakhov, M. A., Radiat. Eff. **15**, 85 (1972).

Kum 72b Kumakhov, M. A., Phys. Lett. A **39**, 191 (1972).

Kum 72c Kumakhov, M. A., Dokl. Akad. Nauk SSSR **203**, 794 (1972) [Sov. Phys.—Dokl. **17**, 348 (1972)].

Kum 72d Kumakhov, M. A., Fiz. Tverd. Tela **14**, 1126 (1972) [Sov. Phys.—Solid State **14**, 963 (1972)].

Kumm 72 Kumm, K., F. Bell, R. Sizmann, H. J. Kreiner, and D. Harder, Radiat. Eff. **12**, 53 (1972).

Kun 69 Kunstreich, S., and A. Otto, Optics Commun. **1**, 45 (1969).

Kr 70 Kreiner, H. J., F. Bell, R. Sizmann, D. Harder, and W. Hüttl, Phys. Lett. A **33**, 135 (1970).

La 40 Lamb, W. E., Phys Rev. **58**, 96 (1940).

Laeg 72a Laegsgaard, E., J. U. Andersen, and L. C. Feldman, Phys. Rev. Lett. **29**, 1206 (1972).

Laeg 72b Laegsgaard, E., J. U. Andersen, and L. C. Feldman, *Proceedings of the International Conference on Inner Shell Ionization Phenomena and Future Applications, Atlanta, Georgia, 17–22 April 1972*, U. S. Atomic Energy Commission Report No. CONF-720404, Vol. 2, p. 1019 (1972).

Lan 60 Landau, L. D., and E. M. Lifshitz, *Mechanics* (Pergamon, New York), p. 27 (1960).

Le 63 Lehmann, C., and G. Leibfried, J. Appl. Phys. **34**, 2821 (1963).

Ler 67 Lervig, P., J. Lindhard, and V. Nielsen, Nucl. Phys. A **96**, 481 (1967).

Let 71 Leteutre, J., N. Housseau, and Y. Quéré, J. Phys. (Paris) **32**, 205 (1971).

Li 54 Lindhard, J., K. Dan. Vidensk. Selsk. Mat.-Fys. Medd. **28**, No. 8 (1954).

Li 61 Lindhard, J., and M. Scharff, Phys. Rev. **124**, 128 (1961).

Li 63 Lindhard, J., M. Scharff, and H. E. Schiøtt, K. Dan. Vidensk. Selsk. Mat.-Fys. Medd. **33**, No. 14 (1963).

Li 64a Lindhard, J., Phys. Lett. **12**, 126 (1964).

Li 64b Lindhard, J., and A. Winther, K. Dan. Vidensk. Selsk. Mat.-Fys. Medd. **34**, No. 4 (1964).

Li 65 Lindhard, J., K. Dan. Vidensk. Selsk. Mat.-Fys. Medd. **34**, No. 14 (1965).

Li 68 Lindhard, J., V. Nielsen, and M. Scharff, K. Dan. Vidensk. Selsk. Mat.-Fys. Medd. **36**, No. 10 (1968).

Li 69 Lindhard, J., Proc. R. Soc. Lond. A **311**, 11 (1969).

Li 70 Lindhard, J., in *Atomic Collision Phenomena in Solids*, edited by (North-Holland, Amsterdam), p. 1 (1970).

Lin 73 Linker, G., O. Meyer, and W. Scherber, Phys. Status Solidi A **16**, 377 (1973).

Liv 68 Livesey, R. G., and G. Butcher, J. Phys. E **1**, 820 (1968).

Lo 48 Lonsdale, K., Acta Crystallogr. **1**, 142 (1948).

Lo 62 Lonsdale, K., editor, *International Tables for X-Ray Crystallography* (Kynoch, Birmingham, England, 1962), Vol. III, p. 234.

Lu 63 Lutz, H. O., and R. Sizmann, Phys. Lett. **5**, 113 (1963).

Lu 66 Lutz, H. O., S. Datz, C. D. Moak, and T. S. Noggle, Phys. Rev. Lett. **17**, 285 (1966).

Lu 70 Lutz, H. O., S. Datz, C. D. Moak, and T. S. Noggle, Phys. Lett. A **33**, 309 (1970).

Lu 71 Lutz, H. O., R. Ambros, C. Mayer-Böricke, K. Reichelt, and M. Rogge, Z. Naturforsch. A **26**, 1105 (1971).

Lug 73 Lugujjo, E., and J. W. Mayer, Phys. Rev. B **7**, 1782 (1973).

Lun 68 Luntz, M., and R. H. Bartram, Phys. Rev. **175**, 468 (1968).

Lun 72 Luntz, M. and G. M. Heymsfield, Phys. Rev. B **6**, 2530 (1972).

Ma 70 Massa, I., Nuovo Cimento Lett. **3**, 186 (1970).

Mac 66 Macdonald, J. R., J. H. Ormrod, and H. E. Duckworth, Z. Naturforsch. A **21**, 130 (1966).

Mach 67 Machlin, E. S., Phys. Lett. A **24**, 173 (1967).

Mach 68 Machlin, E. S., S. Petralia, A. DeSalvo, G. F. Missiroli, and F. Zignani, Nuovo Cimento B **55**, 263 (1968).

Mach 70 Machlin, E. S., S. Petralia, A. DeSalvo, R. Rosa, and F. Zignani, Phil. Mag. **22**, 101 (1970).

Mad 64 Madden, T. C., and W. M. Gibson, IEEE Trans. Nucl. Sci **NS-11**, 254 (1964).

Mak 70 Makin, M. J., in *Atomic Collision Phenomena in Solids*, edited by (North-Holland, Amsterdam, 1970), p. 205.

Mal 71 Malaguti, F., A. Uguzzoni, and E. Verondini, Nuovo Cimento Lett. **2**, 629 (1971).

Man 68 Mannami, M., F. Fujimoto, and K. Ozawa, Phys. Lett. A **26**, 201 (1968).

Man 70 Mannami, M., T. Sakurai, K. Ozawa, F. Fujimoto, and K. Komaki, Phys. Status Solidi **38**, K1 (1970).

Mar 70 Martynenko, Y. V., in *Atomic Collision Phenomena in Solids*, edited by (North-Holland, Amsterdam), p. 400 (1970).

Mar 71a Martynenko, Y. V., Fiz. Tverd. Tela **13**, 1055 (1971) [Sov. Phys.—Solid State **13**, 876 (1971)].

Mar 71b Martynenko, Y. V., Fiz. Tverd. Tela **13**, 2580 (1971) [Sov. Phys.—Solid State **13**, 2166 (1972)].

Marc 72 Marcus, G. H., N. T. Olson, and J. L. Ryan, Radiat. Eff. **15**, 51 (1972).

Mark 71 Markus, A. M., Y. E. Geguzin, and A. L. Fainshtein, Zh. Eksp. Teor. Fiz. **61**, 332 (1971) [Sov. Phys.—JETP **34**, 175 (1972)].

Mars 69 Marsden, D. A., N. G. E. Johansson, and G. R. Bellavance, Nucl. Instrum. Methods **70**, 291 (1969).

Mars 70 Marsden, D. A., and J. L. Whitton, Radiat. Eff. **6**, 181 (1970).

Mart 69 Martin, F. W., Phys. Rev. Lett. **22**, 329 (1969).

Maru 69 Maruyama, M., K. Tsukada, K. Ozawa, F. Fujimoto, K. Komaki, M. Mannami, and T. Sakurai, Phys. Lett. B **29**, 414 (1969).

Maru 70 Maruyama, M., K. Tsukada, K. Ozawa, F. Fujimoto, K. Komaki, M. Mannami, and T. Sakurai, Nucl. Phys. A **145**, 581 (1970).

Marw 71 Marwick, A. D., M. W. Thompson, B. W. Farmery, and G. S. Harbinson, Radiat. Eff. **10**, 49 (1971).

Marw 72 Marwick, A. D., M. W. Thompson, B. W. Farmery, and G. S. Harbinson, Radiat. Eff. **15**, 195 (1972).

Mas 73 Masay, R. B., M. R. Altman, Kh. B. Dietrich and D. J. Rokk, Izv. Akad. Nauk SSSR Ser. Fiz. **37**, 690 (1973) [Bull. Acad. Sci. USSR, Phys. Ser. **37**, No. 4.]

Mash 70 Mashkova, E. S., V. A. Molchanov, Y. G. Skripka, V. A. Snisar, and W. Soshka, in *Atomic Collision Phenomena in Solids*, edited by (North-Holland, Amsterdam, 1970), p. 606.

Mash 72 Mashkova, E. S., and V. A. Molchanov, Radiat. Eff. **13**, 131 (1972).

Mat 67 Matzke, Hj., and J. A. Davies, J. Appl. Phys. **38**, 805 (1967).

Mat 69a Matzke, Hj., J. Nucl. Mater. **30**, 110 (1969).

Mat 69b Matzke, Hj., J. Appl. Phys. **40**, 3819 (1969).

Mat 70 Matzke, Hj., J. Mat. Sci **5**, 777 (1970).

Mat 71a Matzke, Hj., J. A. Davies, and N. G. E. Johansson, Can. J. Phys. **49**, 2215 (1971).

Mat 71b Matzke, Hj., Phys. Status Solidi A **8**, 99 (1971).

Mats 73 Matsunami, N., and N. Itoh, Phys. Lett. A **43**, 435 (1973).

May 68 Mayer, J. W., L. Eriksson, S. T. Picraux, and J. A. Davies, Can. J. Phys. **46**, 663 (1968).

May 70 Mayer, J. W., L. Eriksson, and J. A. Davies, *Ion Implantation in Semiconductors* (Academic, New York, 1970).

May 71 Mayer, J. W., Radiat. Eff. **8**, 269 (1971).
May 72 Mayer, J. W., Radiat. Eff. **12**, 183 (1972).
Maz 69 Mazey, D. J., and R. S. Nelson, Radiat. Eff. **1**, 229 (1969).
McC 63 McCargo, M., J. A. Davies, and F. Brown, Can. J. Phys. **41**, 1231 (1963).
Me 71a Meek, R. L., W. M. Gibson, and J. P. F. Sellschop, Appl. Phys. Lett. **18**, 535 (1971).
Me 71b Meek, R. L., W. M. Gibson, and R. H. Braun, Nucl. Instrum. Methods **94**, 435 (1971).
Me 72 Meek, R. L., and W. M. Gibson, Nucl. Instrum. Methods **98**, 375 (1972).
Mel 68 Melikov, Y. V., Y. D. Otstavnov, A. A. Puzanov, and A. F. Tulinov, Zh. Eksp. Teor. Fiz. **55**, 1690 (1968) [Sov. Phys.—JETP **28**, 888 (1969)].
Mel 72 Melikov, Y. V., Y. D. Otstavnov, A. F. Tulinov, and N. G. Chetchenin, Nucl. Phys. A **180**, 241 (1972).
Mer 70 Merkle, K. L., in *Atomic Collision Phenomena in Solids*, edited by (North-Holland, Amsterdam, 1970), p. 192.
Mer 73 Merkle, K. L., P. P. Pronko, D. S. Gemmell, R. C. Mikkelson and J. R. Wrobel, Phys. Rev. B. **8**, 1002 (1973).
Mey 71 Meyer, L., Phys. Status Solidi B **44**, 253 (1971).
Mi 73 Mikkelson, R. C., J. W. Miller, R. E. Holland, and D. S. Gemmell, J. Appl. Phys. **44**, 935 (1973).
Mit 71 Mitchell, I. V., M. Kamoshida, and J. W. Mayer, Phys. Lett. A **35**, 21 (1971).
Miy 72 Miyagawa, S., K. Morita, N. Matsunami, K. Tachibana, and N. Itoh, Radiat. Eff. **13**, 271 (1972).
Mo 68 Morgan, D. V., and D. VanVliet, Can J. Phys. **46**, 503 (1968).
Mo 70a Morgan, D. V., and D. VanVliet, in *Atomic Collision Phenomena in Solids*, edited by (North-Holland, Amsterdam), p. 476 (1970).
Mo 70b Morgan, D. V., and D. VanVliet, AERE Report No. R6283 (1970).
Mo 70c Morgan, D. V., and D. VanVliet, Radiat. Eff. **5**, 157 (1970).
Mo 71 Morgan, D. V., and D. VanVliet, Radiat. Eff. **8**, 51 (1971).
Mo 72 Morgan, D. V., and D. VanVliet, Radiat. Eff. **12**, 203 (1972).
Moa 66 Moak, C. D., J. W. T. Dabbs, and W. W. Walker, Rev. Sci. Instrum. **37**, 1131 (1966).
Mol 47 Molière, G., Z. Naturforsch. A **2**, 133 (1947).
Mor 70a Morita, K., and N. Itoh, Phys. Lett. A **31**, 283 (1970).
Mor 70b Morita, K., K. Tachibana, and N. Itoh, Phys. Lett. A **33**, 257 (1970).
Mor 71a Morita, K., and N. Itoh, Phys. Lett. A **34**, 359 (1971).
Mor 71b Morita, K., and N. Itoh, J. Phys. Soc. Jap. **30**, 1430 (1971).
Mor 71c Morita, K., N. Kobayashi, and N. Itoh, J. Phys. Soc. Jap., **31**, 313 (1971).
Mor 72 Morita, K., Radiat. Eff. **14**, 195 (1972).
Moro 72 Morokhovskii, V. L., G. D. Kovalenko, I. A. Grishaev, A. N. Fisun, V. I. Kasilov, B. I. Shramenko, and A. N. Krinitsyn, Zh. Eksp. Teor. Fiz. Pis'ma Red. **16**, 162 (1972) [JETP Lett. **16**, 112 (1972)].
Mory 69 Mory, J., and G. Delsarte, Radiat. Eff. **1**, 1 (1969).
Mory 70 Mory, J., D. DeGuillebon, and G. Delsarte, Radiat. Eff. **5**, 37 (1970).
Mory 71a Mory, J., J. Phys. (Paris) **32**, 41 (1971).
Mory 71b Mory, J., Radiat. Eff. **8**, 139 (1971).
Mory 72 Mory, J., and Y. Quéré, Radiat. Eff. **13**, 57 (1972).
Mott 31 Mott, N. F., Proc. Camb. Philos. Soc. **27**, 553 (1931).
Mott 52 Mott, N. F., and H. S. W. Massey, *The Theory of Atomic Collisions*, (Clarendon, Oxford) (1952) 2nd ed.
Mu 70 Mueller, R. M., and W. White, Phys. Lett. A **31**, 431 (1970).
Na 73 Nakayama, H., M. Ishii, K. Hisatake, F. Fujimoto, and K. Komaki, Nucl. Phys. A **208**, 545 (1973).
Ne 63 Nelson, R. S., and M. W. Thompson, Phil. Mag. **8**, 1677 (1963); erratum: Phil. Mag. **9**, 1069 (1964).
Ne 66 Nelson, R. S., Phil. Mag. **14**, 637 (1966).
Ne 67a Nelson, R. S., B. W. Farmery, G. Dearnaley, and I. V. Mitchell, J. Mater. Sci. **2**, 171 (1967).
Ne 67b Nelson, R. S., and D. J. Mazey, J. Mater. Sci. **2**, 211 (1967).
Ne 67c Nelson, R. S., Phil. Mag. **15**, 845 (1967).
Ne 68a Nelson, R. S., *The Observation of Atomic Collisions in Crystalline Solids* (North-Holland, Amsterdam) (1968).
Ne 68b Nelson, R. S., and D. J. Mazey, Can. J. Phys. **46**, 689 (1968).
Ne 69a Nelson, R. S., Phys. Lett. A **28**, 676 (1969).
Ne 69b Nelson, R. S., in *Vacancies and Interstitials in Metals* (North-Holland, Amsterdam), p. 637 (1969).
Ne 69c Nelson, R. S., Proc. R. Soc. A **311**, 53 (1969).
Ne 69d Nelson, R. S., Radiat. Eff. **2**, 47 (1969).
New 71 Newton, C. S., and L. T. Chadderton, Radiat. Eff. **10**, 33 (1971).
New 72 Newton, C. S., R. J. MacDonald, C. J. Sofield, and H. J. Hay, Phys. Lett. A **42**, 47 (1972).
Ni 68 Nip, H. C. H., M. J. Hollis, and J. C. Kelly, Phys. Lett. A **28**, 324 (1968).
Ni 70 Nip, H. C. H., and J. C. Kelly, in *Atomic Collision Phenomena in Solids* (North-Holland, Amsterdam), p. 50 (1970).
Ni 71a Nip, H. C. H., and J. C. Kelly, Phys Rev. B **3**, 2884 (1971).
Ni 71b Nip, H. C. H., R. L. Dalglish, A. P. M. Chang, and J. C. Kelly, Phys. Lett. A **34**, 257 (1971).
Ni 72a Nip, H. C. H., and J. C. Kelly, Phys. Rev. B **5**, 813 (1972).
Ni 72b Nip, H. C. H., and J. C. Kelly, Phys. Rev. B **5**, 1797 (1972).
Ni 72c Nip, H. C. H., and J. C. Kelly, Phys. Rev. B **5**, 2425 (1972).
Ni 72d Nip, H. C. H., R. L. Dalglish, and J. C. Kelly, Acta Crystallogr. A **28**, 97 (1972).
Ni 72e Nip, H. C. H., and J. S. Williams, Radiat. Eff. **12**, 171 (1972).
Nis 72 Nishihard, H., Phys. Lett. A **39**, 299 (1972).
No 66 Noggle, T. S., and O. S. Oen, Phys. Rev. Lett. **16**, 395 (1966).
No 67 Noggle, T. S., and J. H. Barrett, Brookhaven National Laboratory Report No BNL-50083, p. 402 (unpublished).
No 69 Noggle, T. S., and J. H. Barrett, Phys. Status Solidi **36**, 761 (1969).
No 72 Noggle, T. S., Nucl. Instrum. Methods **102**, 539 (1972).
Noe 72 Noelpp, U., R. Abegg, J. Schacher, and R. Wagner, Helv. Phys. Acta **45**, 55 (1972).
Nor 63 Northcliffe, L. C., Annu. Rev. Nucl. Sci. **13**, 67 (1963).
Nor 70 Northcliffe, L. C., and R. F. Schilling, Nucl. Data Tables A **7**, 233 (1970).
Nort 70a North, J. C., and W. M. Gibson, Appl. Phys. Lett. **16**, 126 (1970).
Nort 70b North, J. C., and W. M. Gibson, Radiat. Eff. **6**, 199 (1970).
Od 71 Odintsov, D. D., Fiz. Tverd. Tela **13**, 3451 (1971) [Sov. Phys.—Solid State **13**, 2916 (1972)].
Oe 65 Oen, O. S., Phys. Lett. **19**, 358 (1965).
Oh 71a Ohtsuki, Y. H., Phys. Lett. A **34**, 104 (1971).
Oh 71b Ohtsuki, Y. H., M. Mizuno, and M. Kitagawa, J. Phys. Soc. Jap. **31**, 1109 (1971).
Oh 72a Ohtsuki, Y. H., M. Kitagawa, and M. Mizuno, Phys. Status Solidi B **51**, K19 (1972).
Oh 72b Ohtsuki, Y. H., and M. Kitagawa, Phys. Lett. A **40**, 313 (1972).
Oh 73 Ohtsuki, Y. H., J. Phys. Soc. Jap. **34**, 473 (1973).
Ok 70 Ok, H. H. A., Z. Phys. **240**, 314 (1970).
Oko 72 Okorokov, V. V., D. L. Tolchenkov, I. S. Khizhnyakov, Y. U. Cheblukov, Y. Y. Lapitskii, G. A. Iferov, and Y. I. Zhukova, Zh. Eksp. Teor. Fiz. Pis'ma Red. **16**, 588 (1972) [JETP Lett. **16**, 415 (1972)].
On 68 Onderdelinden, D., Can. J. Phys. **46**, 739 (1968).
Or 63 Ormrod, J. H., and H. E. Duckworth, Can. J. Phys. **41**, 1424 (1963).

Or 65 Ormrod, J. H., J. R. Macdonald, and H. E. Duckworth, Can. J. Phys. **43**, 275 (1965).

Pa 70 Pathak, A. P., and M. Yussouff, Phys. Rev. B **2**, 4723 (1970).

Pa 72 Pathak, A. P., and M. Yussouff, Radiat. Eff. **16**, 1 (1972).

Pal 68 Palmer, D. W., and E. d'Artemare, Phil. Mag. **17**, 1195 (1968).

Pan 72 Panin, S. D., S. Y. Lebedev and V. E. Dubinskii, Fiz. Tverd. Tela **14**, 2452 (1972); [Sov. Phys.—Solid State **14**, 2123 (1973)].

Pav 72 Pavlov, P. V., E. I. Zorin, D. I. Tetel'baum, A. S. Baronova, and V. K. Vasil'ev, Radiat. Eff. **13**, 153 (1972).

Pe 72 Pegoraro, A., and G. Quirci, Nucl. Instrum. Methods **103**, 417 (1972).

Ped 72 Pedersen, M. J., J. U. Andersen, and W. M. Augustyniak, Radiat. Eff. **12**, 47 (1972).

Pi 69a Picraux, S. T., J. A. Davies, L. Eriksson, N. G. E. Johansson, and J. W. Mayer, Phys. Rev. **180**, 873 (1969).

Pi 69b Picraux, S. T., and J. U. Andersen, Phys. Rev. **186**, 267 (1969).

Pi 71 Picraux, S. T., W. H. Weisenberger, and F. L. Vook, Radiat. Eff. **7**, 101 (1971).

Pi 72a Picraux, S. T., W. L. Brown, and W. M. Gibson, Phys. Rev. B **6**, 1382 (1972).

Pi 72b Picraux, S. T., Appl. Phys. Lett. **20**, 91 (1972).

Pi 73a Picraux, S. T., J. Appl. Phys. **44**, 587 (1973).

Pi 73b Picraux, S. T., and G. J. Thomas, J. Appl. Phys. **44**, 594 (1973)

Pie 63 Piercy, G. R., F. Brown, J. A. Davies, and M. McCargo, Phys. Rev. Lett. **10**, 399 (1963).

Pie 64 Piercy, G. R., M. McCargo, F. Brown, and J. A. Davies, Can. J. Phys. **42**, 1116 (1964).

Pin 64 Pines, D., *Elementary Excitations in Solids* (Benjamin, Inc., New York) (1964).

Po 68a Poizat, J.-C., J. Remillieux, and A. Sarazin, Nucl. Instrum. Methods **59**, 333 (1968).

Po 68b Poizat, J.-C., J. Remillieux, and A. Sarazin, Nucl. Instrum. Methods **59**, 272 (1968).

Po 71a Poizat, J.-C., and J. Remillieux, Phys. Rev. Lett **27**, 6 (1971).

Po 71b Poizat, J.-C., J. Remillieux, and J. Desesquelles, Phys. Lett. A **37**, 427 (1971).

Po 72a Poizat, J.-C., and J. Remillieux, Radiat. Eff. **13**, 51 (1972).

Po 72b Poizat, J.-C., and J. Remillieux, J. Phys. (Paris) **33** 1013 (1972).

Po 72c Poizat, J.-C., and J. Remillieux, J. Phys. B **5**, L94 (1972).

Poa 73 Poate, J. M., T. M. Buck and B. Schwartz, J. Phys. Chem. Solids **34**, 779 (1973).

Pog 68 Pogany, A. P., and P. S. Turner, Acta Crystallogr. A **24**, 103 (1968).

Pok 72 Pokhil, G. P., and A. F. Tulinov, Fiz. Tverd. Tela **14**, 1927 (1972) [Sov. Phys.—Solid State **14**, 1669 (1973)].

Pr 69 Przyborski, W., J. Roed, J. Lippert, and L. Sarholt-Kristensen, Radiat. Eff. **1**, 33 (1969).

Qu 68a Quéré, Y., Phys. Status Solidi **30**, 713 (1968).

Qu 68b Quéré, Y., Phys. Lett. A **26**, 578 (1968).

Qu 70 Quéré, Y., Ann. Phys. (Paris) **5**, 105 (1970).

Rau 73 Rau, C., and R. Sizmann, Phys. Lett. A **43**, 317 (1973).

Re 69 Resmini, F. G., A. D. Bacher, D. J. Clark, E. A. McClatchie, and R. DeSwiniarski, Nucl. Instrum. Methods **74**, 261 (1969).

Red 72 Reddi, V. G. K., and J. D. Sansbury, Appl. Phys. Lett. **20**, 30 (1972).

Red 73 Reddi, V. G. K., and J. D. Sansbury, J. Appl. Phys. **44**, 2951 (1973).

Rei 71 Reichelt, K., and H. O. Lutz, J. Crystal Growth **10**, 103 (1971).

Rem 67 Remillieux, J., J. J. Samueli, and A. Sarazin, J. Phys. (Paris) **28**, 832 (1967).

Reu 69 Reuther, E., and J. N. Bradford, Phys. Rev. **188**, 654 (1969).

Ri 62 Rickey, M. E., and R. Smythe, Nucl. Instrum. Methods **18**, 67 (1962).

Rim 71 Rimini, E., E. Lugujjo, and J. W. Mayer, Phys. Lett. A **37**, 157 (1971).

Rim 72a Rimini, E., E. Lugujjo, and J. W. Mayer, Phys. Rev. B **6**, 718 (1972).

Rim 72b Rimini, E., J. Haskell, and J. W. Mayer, Appl. Phys. Lett. **20**, 237 (1972).

Ro 62 Robinson, M. T., Appl. Phys. Lett. **1**, 49 (1962).

Ro 63a Robinson, M. T., and O. S. Oen, Appl. Phys. Lett. **2**, 30 (1963).

Ro 63b Robinson, M. T., and O. S. Oen, Phys. Rev. **132**, 2385 (1963).

Ro 69 Robinson, M. T., Phys. Rev. **179**, 327 (1969).

Ro 70 Robinson, M. T., in *Atomic Collision Phenomena in Solids*, edited by (North-Holland, Amsterdam), p. 66 (1970).

Ro 71a Robinson, M. T., Phys. Rev. B **4**, 1461 (1971).

Ro 71b Robinson, M. T., in *Proceedings of the Battelle Colloquium on Interatomic Potentials and Simulation of Lattice Defects, 14–19 June* (Plenum, New York, 1971), p. 281.

Rog 69 Rogge, M., W. Dünnweber, and C. Mayer-Böricke, Z. Naturforsch. A **24**, 660 (1969).

Rol 60 Rol, P. K., J. M. Fluit, F. P. Viehböck and M. De Jong, *Proc. Fourth Inter. Conf. on Ionization Phenomena in Gases*, edited by N. R. Nilsson (North-Holland, Amsterdam, 1960), p. 257.

Roth 70 Roth, S., R. Sizmann, R. Coutelle, and F. Bell, Phys. Lett. A **32**, 119 (1970).

Ry 68 Ryabov, V. A., Fiz. Tverd. Tela **10**, 3436 (1968) [Sov. Phys.—Solid State **10**, 2720 (1969)].

Ry 70 Ryabov, V. A., Phys. Status Solidi **38**, 63 (1970).

Ry 72 Ryabov, V. A., Phys. Status Solidi B **49**, 467 (1972).

Sa 65 Sattler, A. R., and G. Dearnaley, Phys. Rev. Lett. **15**, 59 (1965).

Sa 67 Sattler, A. R., and G. Dearnaley, Phys. Rev. **161**, 244 (1967).

Sa 68a Sattler, A. R., and D. K. Brice, *Solid State Physics Research with Accelerators*, Brookhaven National Laboratory Report No. BNL-50083, p. 96 (1968).

Sa 68b Sattler, A. R., and F. L. Vook, Phys. Rev. **175**, 526 (1968).

Sak 73 Sakurai, T., J. Phys. Soc. Jap. **35**, 113 (1973).

Sar 69 Saris, F. W., W. F. V. D. Weg, and D. Onderdelinden, Radiat. Eff. **1**, 137 (1969).

Sau 72 Sauter, G. D., and S. D. Bloom, Phys. Rev. B. **6**, 699 (1972).

Sc 65 Schiffer, J. P., and R. E. Holland, Bull. Am. Phys. Soc. **10**, 54 (1965).

Scher 69 Scherzer, B. M. U., Institut für Plasmaphysik, Garching b. München, Report No. IPP2/80, (June 1969).

Schie 72 Schiebel, U., A. Neufert, and G. Clausnitzer, Phys Lett. A **42**, 45 (1972).

Schiø73 Schiøtt, H. E., in *Interaction of Energetic Charged Particles with Solids*, Brookhaven National Laboratory Report No. BNL-50336, p. 6 (1973).

Schob 68 Schober, T., and R. W. Balluffi, Phys. Status Solidi **27**, 195 (1968).

Schob 69a Schober, T., and R. W. Balluffi, Can. J. Phys. **47**, 1221 (1969).

Schob 69b Schober, T., L. E. Thomas, and R. W. Balluffi, Radiat. Eff. **1**, 279 (1969).

Schol 72 Scholz, W., A. Li-Scholz, R. Collé, and I. L. Preiss, Phys. Rev. Lett. **29**, 761 (1972).

Se 66 Selig, O., and R. Sizmann, Nukleonik **8**, 303 (1966).

Sea 73 Seager, D. K., Sandia Laboratories Report, SC-B-710148 (1971) and Supplement (1973).

Sh 68a Shipatov, E. T., Fiz. Tekh. Poluprovodn. **2**, 1690 (1968) [Sov. Phys.—Semicond. **2**, 1408 (1969)].

Sh 68b Shipatov, E. T., Fiz. Tverd. Tela **10**, 2709 (1968) [Sov. Phys.—Solid State **10**, 2132 (1969)].

Sh 73 Shipatov, E. T., Izv. Vyssh Uchebn Zaved Fiz. (USSR) No. **3**, 139 (1973) [Sov. Phys. J. No. 3.].

Sha 71 Sharma, R. P., J. U. Andersen, and K. O. Nielsen, (data presented at the International Conference on Atomic Collisions in Solids, Gausdal, Norway, Sept. 1971).

Shu 71 Shulga, V. I., I. G. Bunin, V. E. Yurasova, V. V. Andreev, and B. M. Mamaev, Phys. Lett. A **37**, 181 (1971).

Si 71 Sigurd, D., and B. Domeij, Phys. Lett. A **36**, 81 (1971).

Sk 70 Skvortsov, V. V., and I. P. Bogdanovskaya, Zh. Eksp. Teor. Fiz. Pis'ma Red. **11**, 3 (1970) [JETP Letters **11**, 1 (1970)].

Sko 73 Skog, G., and R. Hellborg, Phys. Scr. **7**, 285, (1973).

So 70 Sone, K., Jap. J. Appl. Phys. **9**, 1533 (1970).

So 71a Sone, K., N. Natsuaki, and F. Fukuzawa, Mem. Fac. Eng. Kyoto Univ. **33**, 174 (1971).

So 71b Sone, K., M. Teramoto, and F. Fukuzawa, Phys. Lett. A **35**, 445 (1971).

So 72a Sone, K., and F. Fukuzawa, Phys. Lett. A **40**, 11 (1972).

So 72b Sone, K., and F. Fukuzawa, Mem. Fac. Eng. Kyoto Univ. **34**, 315 (1972).

So 72c Sone, K., and F. Fukuzawa, Mem. Fac. Eng. Kyoto Univ. **34**, 325 (1972).

Son 70 Sona, P., Nuovo Cimento A **66**, 663 (1970).

Sp 70 Spring, M. S., Phys. Lett. A **31**, 421 (1970).

St 12a Stark, J., and G. Wendt, Ann. Physik **38**, 921 (1912).

St 12b Stark, J., Phys. Z. **13**, 973 (1912).

Ste 70 Stein, H. J., H. O. Lutz, P. H. Mokler, K. Sistemich, and P. Armbruster, Phys. Rev. Lett. **24**, 701 (1970).

Te 62 Teplova, Y. A., V. S. Nikolaev, I. S. Dmitriev, and L. N. Fateeva, Zh. Eksp. Teor. Fiz. **42**, 44 (1962) [Sov. Phys.—JETP **15**, 31 (1962)].

Tem 71 Temmer, G. M., M. Maruyama, D. W. Mingay, M. Petrascu, and R. VanBree, Phys. Rev. Lett. **26**, 1341 (1971).

Th 64 Thompson, M. W., Phys. Rev. Lett. **13**, 756 (1964).

Th 68a Thompson, M. W., Contemp. Phys. **9**, 375 (1968).

Th 68b Thompson, M. W., in *Solid State Physics Research with Accelerators*, Brookhaven National Laboratory Report No. BNL-50083, p. 106 (1968).

Tho 69 Thomas, L. E., T. Schober, and R. W. Balluffi, Radiat. Eff. **1**, 257, 269 (1969).

Tho 70 Thomas, L. E., and C. J. Humphries, Phys. Status Solidi A **3**, 599 (1970).

To 67 Torrens, I. M., and L. T. Chadderton, Phys. Lett. A **25**, 575 (1967).

To 68 Torrens, I. M., and L. T. Chadderton, Can. J. Phys. **46**, 1303 (1968).

To 69 Torrens, I. M., L. T. Chadderton, and M. G. Anderson, Radiat. Eff. **1**, 47 (1969).

Tom 68 Tomlinson, P. N., and A. Howie, Phys. Lett. **27**, 491 (1968).

Tomb 73 Tombrello, T. A., and J. M. Caywood, Phys. Rev. B **8**, 3065 (1973).

Tr 60 Treacy, P. B., Aust. J. Sci. **22**, 334 (1960).

Tu 65a Tulinov, A. F., Dokl. Akad. Nauk SSSR **162**, 546 (1965) [Sov. Phys.—Dokl. **10**, 463 (1965)].

Tu 65b Tulinov, A. F., V. S. Kulikauskas, and M. M. Malov, Phys. Lett. **18**, 304 (1965).

Tu 65c Tulinov, A. F., Usp. Fiz. Nauk **87**, 585 (1965) [Sov. Phys.—Usp. **8**, 864 (1966)].

Tu 65d Tulinov, A. F., B. G. Akhmetova, A. A. Puzanov, and A. A. Bednyakov, Zh. Eksp. Teor. Fiz. Pis'ma Red. **2**, 48 (1965) [JETP Letters **2**, 30 (1965)]

Tuc 69 Tucker, T. C., L. D. Roberts, C. W. Nestor, T. A. Carlson, and F. B. Malik, Phys. Rev. **178**, 998 (1969).

Ug 66 Uggerhøj, E., Phys. Lett. **22**, 382 (1966).

Ug 68 Uggerhøj, E., and J. U. Andersen, Can. J. Phys. **46**, 543 (1968).

Ug 70 Uggerhøj, E., and F. Fransden, Phys. Rev. B **2**, 582 (1970).

Va 70 VanVliet, D., Phys. Status Solidi A **2**, 521 (1970).

Va 71 VanVliet, D., Radiat. Effects **10**, 137 (1971).

Var 70 Varelas, C., and J. Biersack, Nucl. Instrum. Methods **79**, 213 (1970).

Var 72 Varelas, C., and R. Sizmann, Radiat. Eff. **16**, 211 (1972).

Ve 72 Verondini, E., Phys. Lett. A **40**, 341 (1972).

von J 67 vonJan, R., Phys. Rev. Lett. **18**, 303 (1967).

von J 68 vonJan, R., Phys. Status Solidi **29**, 755 (1968).

Vor 71 Vorobev, A. A., A. N. Didenko, S. A. Vorobev, and I. A. Tsekhanovskii, Phys. Status Solidi A **6**, 389 (1971).

Vor 72a Vorobev, A. A., A. Ya. Bobudaev, S. A. Vorobev, and V. V. Kaplin, Phys. Lett. A **40**, 105 (1972).

Vor 72b Vorobev, A. A., A. Y. Bobudaev, S. A. Vorobev, and V. V. Kaplin, Fiz. Tverd. Tela **14**, 2157 (1972) [Sov. Phys.—Solid State **14**, 1864 (1973)].

Voro 72 Vorobev, S. A., and I. A. Tsekhanovskii, Phys. Status Solidi, A **14**, K89 (1972).

Wa 58 Watson, G. N., *Theory of Bessel Functions* (Cambridge U. P., Cambridge, England, 1958).

Wal 52 Walske, M., Phys. Rev. **88**, 1283 (1952).

Wal 56 Walske, M., Phys. Rev. **101**, 940 (1956).

Walk 70 Walker, R. L., B. L. Berman, R. C. Der, T. M. Kavanagh, and J. M. Khan, Phys. Rev. Lett. **25**, 5 (1970).

We 69 Wedepohl, P. T., Radiat. Eff. **1**, 77 (1969).

Weg 64 Wegner, H. E., C. Erginsoy, and W. M. Gibson, IEEE Trans. Nucl. Sci. **NS-12**, 240 (1965).

Wei 71 Weisenberger, W. H., S. T. Picraux, and F. L. Vook, Radiat. Eff. **9**, 121 (1971).

Wes 69 Westmoreland, J. E., J. W. Mayer, F. H. Eisen, and B. Welch, Appl. Phys. Lett. **15**, 308 (1969).

Wes 70 Westmoreland, J. E., J W. Mayer, F. H. Eisen, and B. Welch, Radiat. Eff. **6**, 161 (1970).

Wh 67 Whitton, J. L., Can. J. Phys. **45**, 1947 (1967).

Wh 68 Whitton, J. L., Can. J. Phys. **46**, 581 (1968).

Wh 69 Whitton, J. L., Proc. R. Soc. Lond. A **311**, 63 (1969).

Wh 71 Whitton, J. L., and G. R. Bellavance, Radiat. Eff. **9**, 127 (1971).

Whe 70a Whelan, M. J., in *Atomic Collision Phenomena in Solids* (North-Holland, Amsterdam), p. 3 (1970).

Whe 70b Whelan, M. J., in *Modern Diffraction and Imaging Techniques in Material Science* (North-Holland, Amsterdam, 1970), p. 35.

Whi 69 White, W., and R. M. Mueller, Phys. Lett. A **28**, 651 (1969).

Wi 68 Winterbon, K. B., Can. J. Phys. **46**, 2429 (1968).

Wick 67 Wick, K., and A. Flammersfeld, Z. Phys. **204**, 164 (1967).

Wij 69 Wijngaarden, A. van, E. Reuther, and J. N. Bradford, Can. J. Phys. **47**, 411 (1969).

Wil 66 Williamson, C. F., J.-P. Boujot, and J. Picard, Saclay Report No. R3042 (unpublished) (1966).

Wo 69 Wolf, E. D., and T. E. Everhart, Appl. Phys. Lett. **14**, 299 (1969).

Wy 63 Wyckoff, R. W. G., *Crystal Structures* (Interscience, New York) (1963).

Yu 68 Yurasova, V. E., V. I. Shulga, and D. S. Karpuzov, Can. J. Phys. **46**, 759 (1968).

Yu 72 Yurasova, V. E., I. G. Bunin, V. I. Shulga, and B. M. Mamaev, Radiat. Eff. **12**, 175 (1972).

Zi 71 Ziegler, J. F., and J. E. E. Baglin, J. Appl. Phys. **42**, 2031 (1971).

Zi 72a Ziegler, J. F., and B. L. Crowder, Appl. Phys. Lett. **20**, 178 (1972); erratum, Appl. Phys. Lett. **22**, 347 (1973).

Zi 72b Ziegler, J. F., J. Appl. Phys. **43**, 2973 (1972).

Zi 73 Ziegler, J. F., and M. H. Brodsky, J. Appl. Phys. **44**, 188 (1973).

Zig 68 Zignani, F., G. F. Missiroli, A. DeSalvo, and S. Petralia, Nuovo Cimento B **55**, 539 (1968).

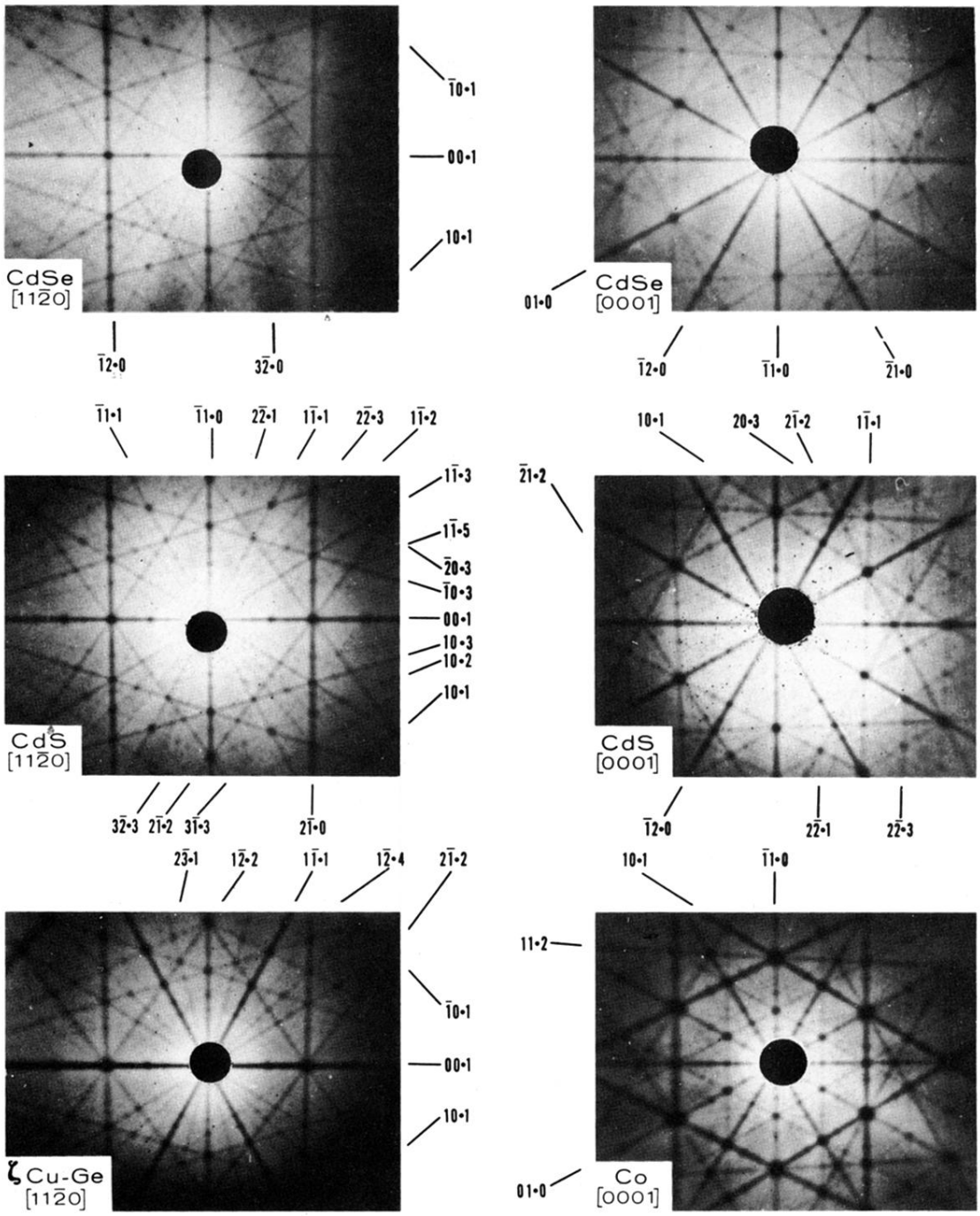

FIG. 112. Blocking patterns for 100-keV protons incident on thick single crystals of CdSe, CdS, ζCu-Ge, and Co [Barr69a]. The beam was incident a few degrees off the normal to the (1120) or (0001) surfaces, and the film positioned closely parallel to these surfaces. The black spots near the center of the photographs are due to holes in the film to permit passage of the incident beam.

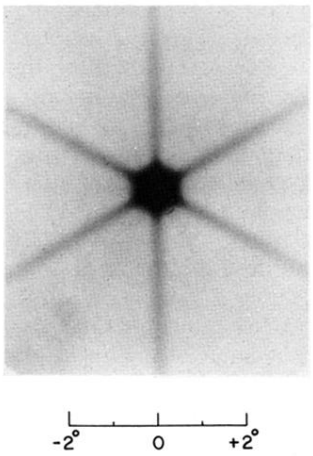

FIG. 4. Star pattern recorded in transmission (see Fig. 2) for 2.43-MeV protons incident along the ⟨111⟩ direction of a 60-μm-thick Ge crystal. The dark regions in the figure correspond to regions of high particle intensity. The range of 2.43-MeV protons in amorphous Ge is approximately 43 μm [Gor69].

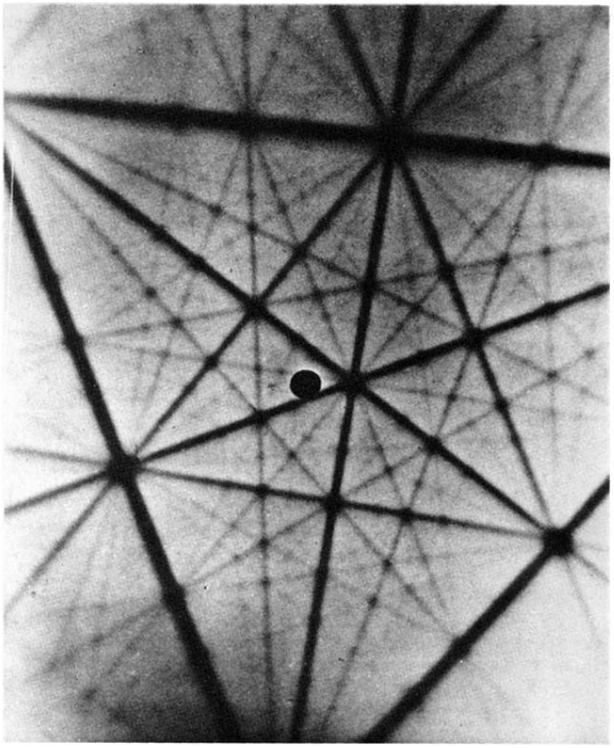

FIG. 62. Backscattering blocking pattern recorded for 150-keV protons incident on a Bi crystal near the ⟨111⟩ axial direction [En70]. The hole near the center of the picture is to permit the passage of the incident beam.

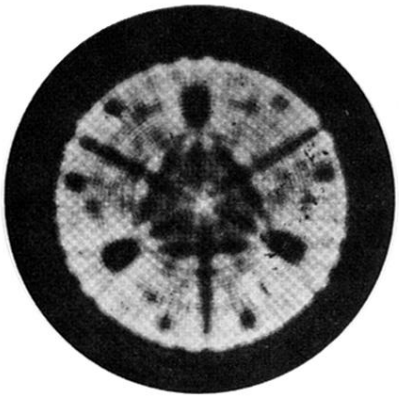

(a)

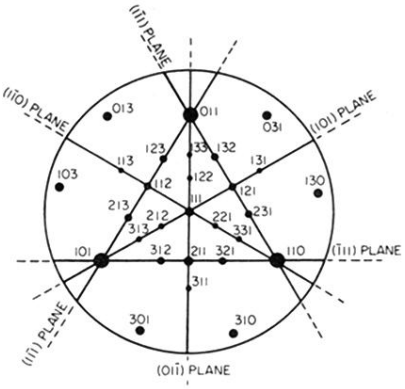

(b)

FIG. 72. (a) Photographic reproduction of a ⟨111⟩ Si crystal surface after programmed bombardment with 80-keV Ne^+ ions using the arrangement shown in Fig. 71 [Ne67b]. The dark areas show a minimum of radiation damage where the beam is channeled. (b) Radial projection of the (111) face of an fcc crystal showing the low-index planes for comparison. (Reproduced with permission of J. Mat. Sci., Chapman & Hall, London.)

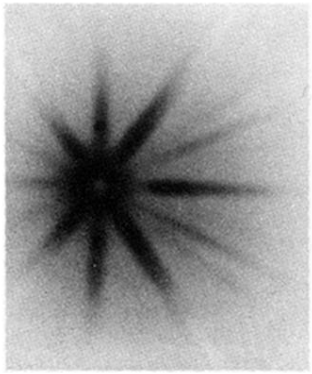

FIG. 73. Star pattern recorded in transmission for 2.43-MeV protons incident along the (110) planar direction and approximately 1.6° from the ⟨110⟩ axis of a Ge crystal 7 μ thick. The dark region corresponds to high particle intensities. (The range of 2.43-MeV protons in amorphous Ge is approximately 43 μ [Gor69].)

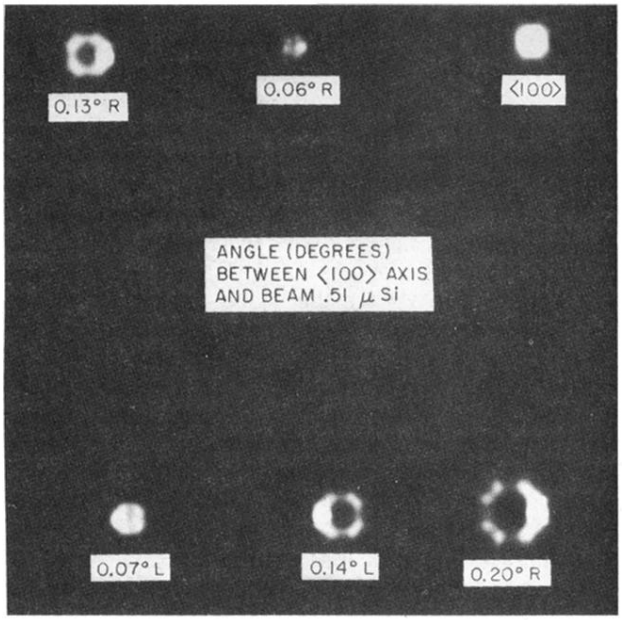

FIG. 83. Photographic recordings of the angular distributions of protons transmitted through a 0.51-μm Si crystal for various entrance angles ($\psi_0 < \psi_c$) relative to the $\langle 100 \rangle$ axial direction [Ar71b]. The incident beam energy is 4 MeV. The value of ψ_c is approximately 0.35°. The particle intensities were measured on x-ray film 1.4-m downstream from the target. The exposure times for the different cases are not always the same. In each case, the $\langle 100 \rangle$ axis was tilted to the left (L) or right (R) of the beam direction by the angle indicated.

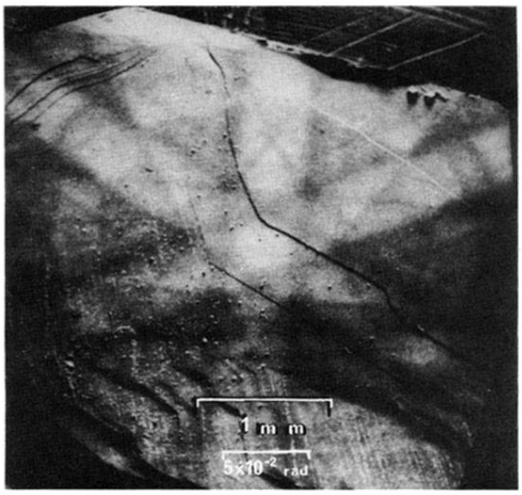

FIG. 91. Low magnification electron scanning micrograph of a thick GaAs crystal [Coa67]. The incident 20-keV electron beam was scanned about the ⟨111⟩ crystal axis. (Reproduced by permission of the Director, RRE, copyright Controller H.B.M.S.O.).

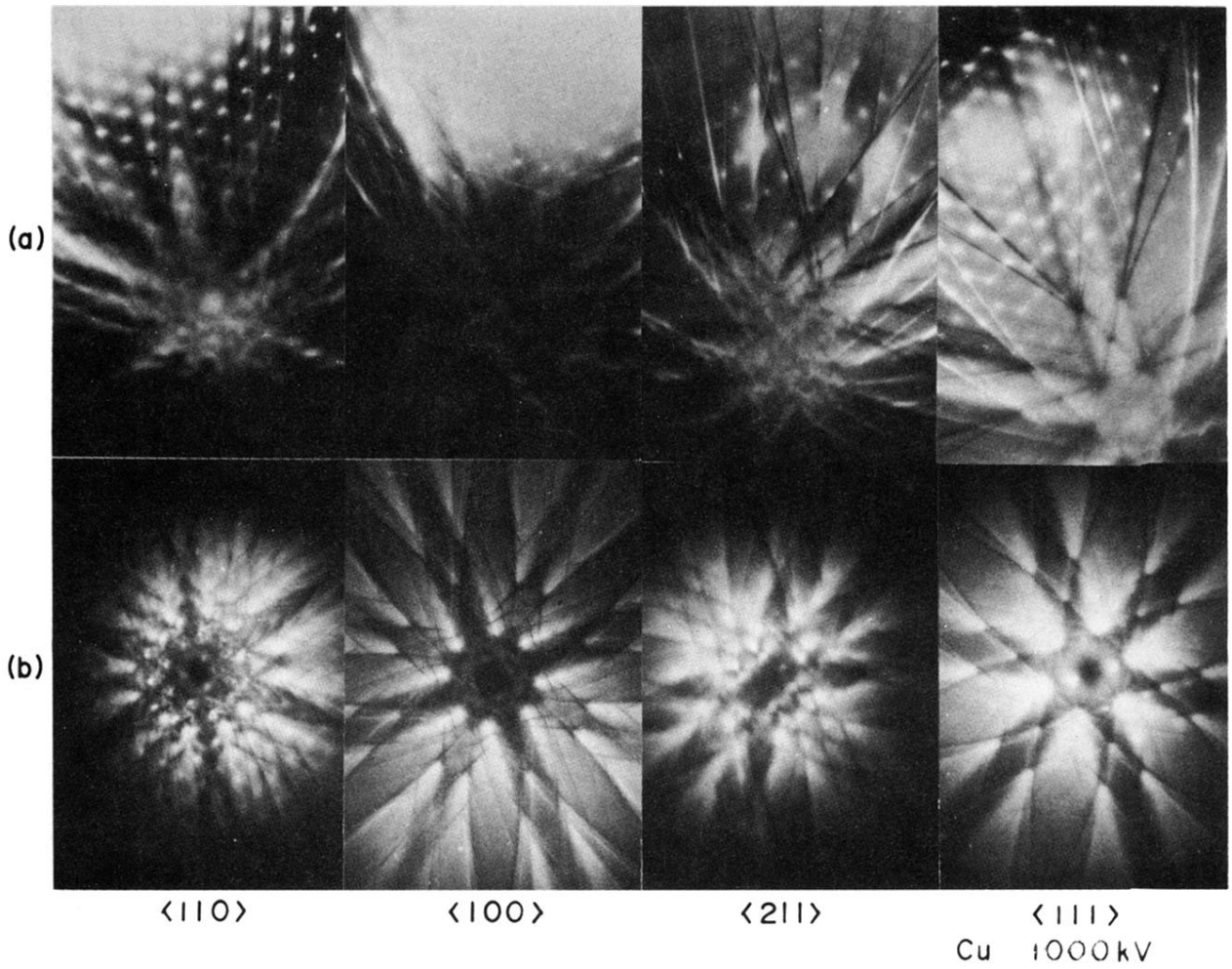

FIG. 92. Transmission patterns recorded for 1-MeV electrons passing through (a) thin (~1 μm) and (b) thick (~5 μm) Cu crystals [Fuj72a]. The data in (a) were recorded with the incident beam a few degrees off axis and in (b) the beam was on axis. Bright regions in the photographs correspond to regions of high electron intensity. The number of quantum states n_R^- excitable in the four axial cases are estimated to be approximately 9, 5, 3, and 2 for the ⟨110⟩, ⟨100⟩, ⟨211⟩, and ⟨111⟩ axes, respectively, Eq. (5.13).